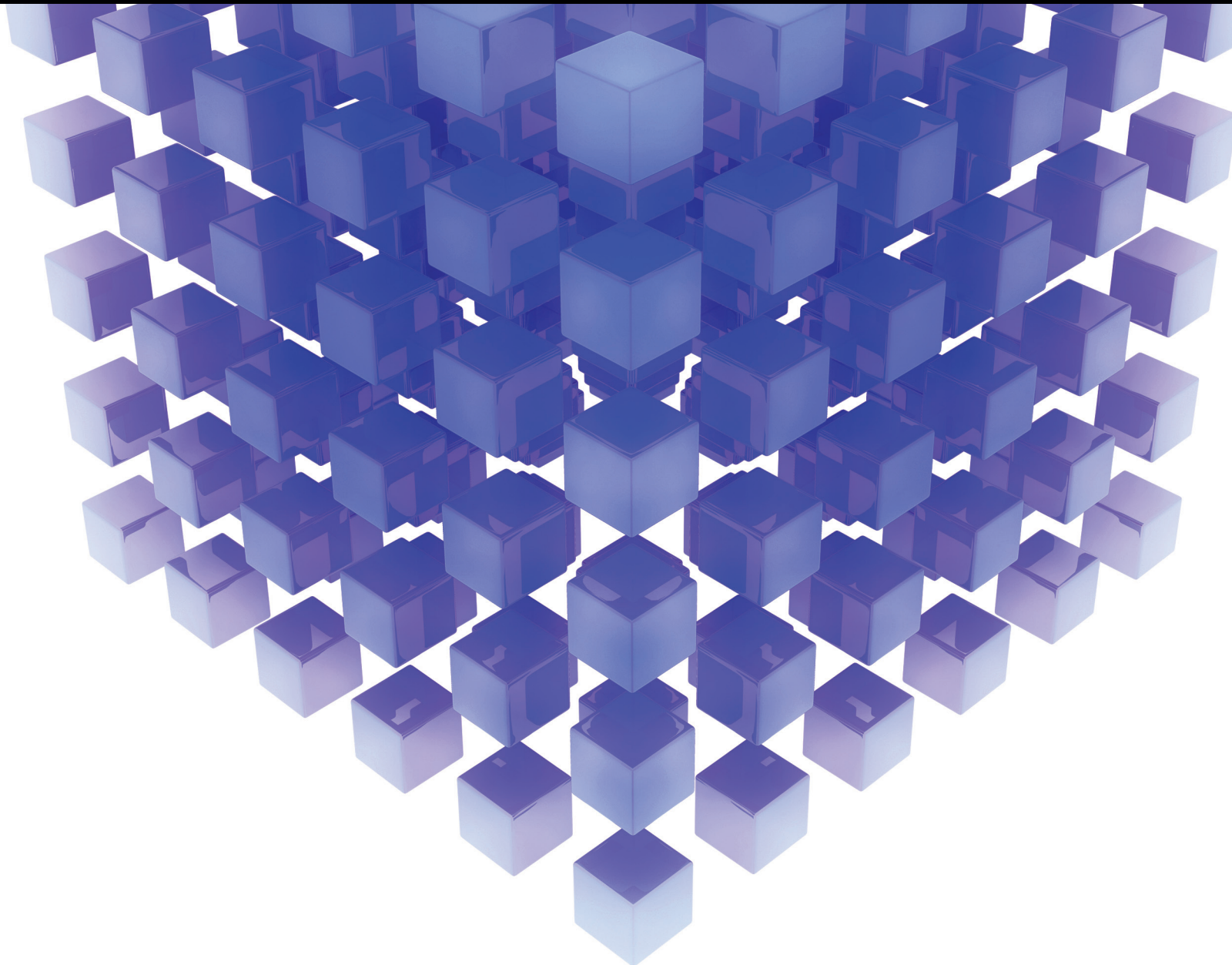


Mathematical Problems in Engineering

Shape and Topology Optimization for Complicated Engineering Structures

Guest Editors: Ji-Hong Zhu, Pierre Beckers, Marc Dahan, Jun Yan,
and Chao Jiang





Shape and Topology Optimization for Complicated Engineering Structures

Mathematical Problems in Engineering

Shape and Topology Optimization for Complicated Engineering Structures

Guest Editors: Ji-Hong Zhu, Pierre Beckers, Marc Dahan,
Jun Yan, and Chao Jiang



Copyright © 2015 Hindawi Publishing Corporation. All rights reserved.

This is a special issue published in “Mathematical Problems in Engineering.” All articles are open access articles distributed under the Creative Commons Attribution License, which permits unrestricted use, distribution, and reproduction in any medium, provided the original work is properly cited.

Editorial Board

Mohamed Abd El Aziz, Egypt
Farid Abed-Meraim, France
Silvia Abrahão, Spain
Paolo Addresso, Italy
Claudia Adduce, Italy
Ramesh Agarwal, USA
Juan C. Agüero, Australia
Ricardo Aguilar-López, Mexico
Tarek Ahmed-Ali, France
Hamid Akbarzadeh, Canada
Muhammad N. Akram, Norway
Mohammad-Reza Alam, USA
Salvatore Alfonzetti, Italy
Francisco Alhama, Spain
Juan A. Almendral, Spain
Lionel Amodeo, France
Igor Andrianov, Germany
Sebastian Anita, Romania
Renata Archetti, Italy
Felice Arena, Italy
Sabri Arik, Turkey
Fumihiko Ashida, Japan
Hassan Askari, Canada
Mohsen Asle Zaeem, USA
Francesco Aymerich, Italy
Seungik Baek, USA
Khaled Bahlali, France
Laurent Bako, France
Stefan Balint, Romania
Alfonso Banos, Spain
Roberto Baratti, Italy
Martino Bardi, Italy
Azeddine Beghdadi, France
Abdel-Hakim Bendada, Canada
Ivano Benedetti, Italy
Elena Benvenuti, Italy
Jamal Berakdar, Germany
Enrique Berjano, Spain
Jean-Charles Beugnot, France
Simone Bianco, Italy
David Bigaud, France
Jonathan N. Blakely, USA
Paul Bogdan, USA
Daniela Boso, Italy
Abdel-Ouahab Boudraa, France
Francesco Braghin, Italy
M. J. Brennan, UK
Maurizio Brocchini, Italy
Julien Bruchon, France
Javier Bulduú, Spain
Tito Busani, USA
Pierfrancesco Cacciola, UK
Salvatore Caddemi, Italy
Jose E. Capilla, Spain
Ana Carpio, Spain
Miguel E. Cerrolaza, Spain
Mohammed Chadli, France
Gregory Chagnon, France
Ching-Ter Chang, Taiwan
Michael J. Chappell, UK
Kacem Chehdi, France
Chunlin Chen, China
Xinkai Chen, Japan
Francisco Chicano, Spain
Hung-Yuan Chung, Taiwan
Joaquim Ciurana, Spain
John D. Clayton, USA
Carlo Cosentino, Italy
Paolo Crippa, Italy
Erik Cuevas, Mexico
Peter Dabnichki, Australia
Luca D'Acerno, Italy
Weizhong Dai, USA
Purushothaman Damodaran, USA
Farhang Daneshmand, Canada
Fabio De Angelis, Italy
Stefano de Miranda, Italy
Filippo de Monte, Italy
Xavier Delorme, France
Luca Deseri, USA
Yannis Dimakopoulos, Greece
Zhengtao Ding, UK
Ralph B. Dinwiddie, USA
Mohamed Djemai, France
Alexandre B. Dolgui, France
George S. Dulikravich, USA
Bogdan Dumitrescu, Finland
Horst Ecker, Austria
Ahmed El Hajjaji, France
Fouad Erchiqui, Canada
Anders Eriksson, Sweden
Giovanni Falsone, Italy
Hua Fan, China
Yann Favennec, France
Giuseppe Fedele, Italy
Roberto Fedele, Italy
Jacques Ferland, Canada
Jose R. Fernandez, Spain
Simme Douwe Flapper, Netherlands
Thierry Floquet, France
Eric Florentin, France
Francesco Franco, Italy
Tomonari Furukawa, USA
Mohamed Gadala, Canada
Matteo Gaeta, Italy
Zoran Gajic, USA
Ciprian G. Gal, USA
Ugo Galvanetto, Italy
Akemi Gálvez, Spain
Rita Gamberini, Italy
Maria Gandarias, Spain
Arman Ganji, Canada
Xin-Lin Gao, USA
Zhong-Ke Gao, China
Giovanni Garcea, Italy
Fernando Garcia, Spain
Laura Gardini, Italy
Alessandro Gasparetto, Italy
Vincenzo Gattulli, Italy
Oleg V. Gendelman, Israel
Mergen H. Ghayesh, Australia
Anna M. Gil-Lafuente, Spain
Hector Gómez, Spain
Rama S. R. Gorla, USA
Oded Gottlieb, Israel
Antoine Grall, France
Jason Gu, Canada
Quang Phuc Ha, Australia
Ofer Hadar, Israel
Masoud Hajarian, Iran
Frédéric Hamelin, France
Zhen-Lai Han, China
Thomas Hanne, Switzerland
Takashi Hasuike, Japan
Xiao-Qiao He, China

M.I. Herreros, Spain
Vincent Hilaire, France
Eckhard Hitzer, Japan
Jaromir Horacek, Czech Republic
Muneo Hori, Japan
András Horváth, Italy
Gordon Huang, Canada
Sajid Hussain, Canada
Asier Ibeas, Spain
Giacomo Innocenti, Italy
Emilio Insfran, Spain
Nazrul Islam, USA
Payman Jalali, Finland
Reza Jazar, Australia
Khalide Jbilou, France
Linni Jian, China
Bin Jiang, China
Zhongping Jiang, USA
Ningde Jin, China
Grand R. Joldes, Australia
Joaquim Joao Judice, Portugal
Tadeusz Kaczorek, Poland
Tamas Kalmar-Nagy, Hungary
Tomasz Kapitaniak, Poland
Haranath Kar, India
Konstantinos Karamanos, Belgium
C. M. Khalique, South Africa
Do Wan Kim, Korea
Nam-Il Kim, Korea
Oleg Kirillov, Germany
Manfred Krafczyk, Germany
Frederic Kratz, France
Jurgen Kurths, Germany
Kyandoghere Kyamakya, Austria
Davide La Torre, Italy
Risto Lahdelma, Finland
Hak-Keung Lam, UK
Antonino Laudani, Italy
Aime' Lay-Ekuakille, Italy
Marek Lefik, Poland
Yaguo Lei, China
Thibault Lemaire, France
Stefano Lenci, Italy
Roman Lewandowski, Poland
Qing Q. Liang, Australia
Panos Liatsis, UK
Peide Liu, China
Peter Liu, Taiwan

Wanquan Liu, Australia
Yan-Jun Liu, China
Jean J. Loiseau, France
Paolo Lonetti, Italy
Luis M. López-Ochoa, Spain
Vassilios C. Loukopoulos, Greece
Valentin Lychagin, Norway
Fazal M. Mahomed, South Africa
Yassir T. Makkawi, UK
Noureddine Manamanni, France
Didier Maquin, France
Paolo Maria Mariano, Italy
Benoit Marx, France
Geérard A. Maugin, France
Driss Mehdi, France
Roderick Melnik, Canada
Pasquale Memmolo, Italy
Xiangyu Meng, Canada
Jose Merodio, Spain
Luciano Mescia, Italy
Laurent Mevel, France
Y. V. Mikhlin, Ukraine
Aki Mikkola, Finland
Hiroyuki Mino, Japan
Pablo Mira, Spain
Vito Mocella, Italy
Roberto Montanini, Italy
Gisele Mophou, France
Rafael Morales, Spain
Aziz Moukrim, France
Emiliano Mucchi, Italy
Domenico Mundo, Italy
Jose J. Muñoz, Spain
Giuseppe Muscolino, Italy
Marco Mussetta, Italy
Hakim Naceur, France
Hassane Naji, France
Dong Ngoduy, UK
Tatsushi Nishi, Japan
Ben T. Nohara, Japan
Mohammed Nouari, France
Mustapha Nourelfath, Canada
Sotiris K. Ntuyas, Greece
Roger Ohayon, France
Mitsuhiro Okayasu, Japan
Javier Ortega-Garcia, Spain
A. Ortega-Moñux, Spain
Naohisa Otsuka, Japan

Erika Ottaviano, Italy
Alkiviadis Paipetis, Greece
Alessandro Palmeri, UK
Anna Pandolfi, Italy
Elena Panteley, France
Manuel Pastor, Spain
P. N. Pathirana, Australia
Francesco Pellicano, Italy
Haipeng Peng, China
Mingshu Peng, China
Zhike Peng, China
Marzio Pennisi, Italy
Matjaz Perc, Slovenia
Francesco Pesavento, Italy
M. do Rosário Pinho, Portugal
Antonina Pirrotta, Italy
Vicent Pla, Spain
Javier Plaza, Spain
J.-C. Ponsart, France
Mauro Pontani, Italy
Stanislav Potapenko, Canada
Sergio Preidikman, USA
C. Pretty, New Zealand
Carsten Proppe, Germany
Luca Pugi, Italy
Yuming Qin, China
Dane Quinn, USA
Jose Ragot, France
K. R. Rajagopal, USA
Gianluca Ranzi, Australia
Sivaguru Ravindran, USA
Alessandro Reali, Italy
Oscar Reinoso, Spain
Nidhal Rezg, France
Ricardo Riaza, Spain
Gerasimos Rigatos, Greece
José Rodellar, Spain
R. Rodriguez-Lopez, Spain
Ignacio Rojas, Spain
Carla Roque, Portugal
Aline Roumy, France
Debasish Roy, India
R. Ruiz Garcia, Spain
A. Ruiz-Cortes, Spain
Ivan D. Rukhlenko, Australia
Mazen Saad, France
Kishin Sadarangani, Spain
Mehrddad Saif, Canada

Miguel A. Salido, Spain
Roque J. Salterén, Spain
F. J. Salvador, Spain
Alessandro Salvini, Italy
Maura Sandri, Italy
Miguel A. F. Sanjuan, Spain
Juan F. San-Juan, Spain
Roberta Santoro, Italy
I. Ferreira Santos, Denmark
José A. Sanz-Herrera, Spain
Nickolas S. Sapidis, Greece
E. J. Sapountzakis, Greece
Andrey V. Savkin, Australia
Valery Sbitnev, Russia
Thomas Schuster, Germany
Mohammed Seaid, UK
Lotfi Senhadji, France
Joan Serra-Sagrasta, Spain
Leonid Shaikhet, Ukraine
Hassan M. Shanechi, USA
Sanjay K. Sharma, India
Bo Shen, Germany
Babak Shotorban, USA
Zhan Shu, UK
Dan Simon, USA
Luciano Simoni, Italy
C. H. Skiadas, Greece
Michael Small, Australia
Francesco Soldovieri, Italy
Raffaele Solimene, Italy
Ruben Specogna, Italy

Sri Sridharan, USA
Ivanka Stamova, USA
Yakov Strelniker, Israel
Sergey A. Suslov, Australia
Thomas Svensson, Sweden
Andrzej Swierniak, Poland
Yang Tang, Germany
Sergio Teggi, Italy
Alexander Timokha, Norway
Rafael Toledo, Spain
Gisella Tomasini, Italy
Francesco Tornabene, Italy
Antonio Tornambe, Italy
Fernando Torres, Spain
Fabio Tramontana, Italy
Sébastien Tremblay, Canada
Irina N. Trendafilova, UK
George Tsiatas, Greece
Antonios Tsourdos, UK
Vladimir Turetsky, Israel
Mustafa Tutar, Spain
Efstratios Tzirtzilakis, Greece
Filippo Ubertini, Italy
Francesco Ubertini, Italy
Hassan Ugail, UK
Giuseppe Vairo, Italy
Kuppalapalle Vajravelu, USA
Robertt A. Valente, Portugal
Pandian Vasant, Malaysia
M. E. Vázquez-Méndez, Spain
Josep Vehi, Spain

Kalyana C. Veluvolu, Korea
Fons J. Verbeek, Netherlands
Franck J. Vernerey, USA
Georgios Veronis, USA
Anna Vila, Spain
Rafael J. Villanueva, Spain
Uchechukwu E. Vincent, UK
Mirko Viroli, Italy
Michael Vynnycky, Sweden
Junwu Wang, China
Shuming Wang, Singapore
Yan-Wu Wang, China
Yongqi Wang, Germany
Desheng D. Wu, Canada
Yuqiang Wu, China
Guangming Xie, China
Xuejun Xie, China
Gen Qi Xu, China
Hang Xu, China
Xinggang Yan, UK
Luis J. Yebra, Spain
Peng-Yeng Yin, Taiwan
Ibrahim Zeid, USA
Huaguang Zhang, China
Qingling Zhang, China
Jian Guo Zhou, UK
Quanxin Zhu, China
Mustapha Zidi, France
Alessandro Zona, Italy

Contents

Shape and Topology Optimization for Complicated Engineering Structures, Ji-Hong Zhu, Pierre Beckers, Marc Dahan, Jun Yan, and Chao Jiang
Volume 2015, Article ID 723897, 2 pages

Multidisciplinary Inverse Reliability Analysis Based on Collaborative Optimization with Combination of Linear Approximations, Xin-Jia Meng, Shi-Kai Jing, Ye-Dong Wang, Jing-Tao Zhou, Li-Xiang Zhang, and Ji-Hong Liu
Volume 2015, Article ID 964238, 11 pages

Optimization of the Turbulence Model on Numerical Simulations of Flow Field within a Hydrocyclone, Yan Xu, Zunce Wang, Lin Ke, Sen Li, and Jinglong Zhang
Volume 2015, Article ID 604379, 7 pages

Improved Reliability-Based Optimization with Support Vector Machines and Its Application in Aircraft Wing Design, Yu Wang, Xiongqing Yu, and Xiaoping Du
Volume 2015, Article ID 569016, 14 pages

Improved Genetic Algorithm with Two-Level Approximation Method for Laminate Stacking Sequence Optimization by Considering Engineering Requirements, Haichao An, Shenyang Chen, and Hai Huang
Volume 2015, Article ID 595484, 13 pages

Reliability-Based Topology Optimization Using Stochastic Response Surface Method with Sparse Grid Design, Qinghai Zhao, Xiaokai Chen, Zheng-Dong Ma, and Yi Lin
Volume 2015, Article ID 487686, 13 pages

Improved Genetic Algorithm with Two-Level Approximation for Truss Optimization by Using Discrete Shape Variables, Shen-yan Chen, Xiao-fang Shui, Dong-fang Li, and Hai Huang
Volume 2015, Article ID 521482, 11 pages

Reliability Analysis of High Rockfill Dam Stability, Ping Yi, Jun Liu, and Chunlei Xu
Volume 2015, Article ID 512648, 8 pages

Structural Response Analysis under Dependent Variables Based on Probability Boxes, Z. Xiao and G. Yang
Volume 2015, Article ID 484615, 11 pages

Editorial

Shape and Topology Optimization for Complicated Engineering Structures

Ji-Hong Zhu,¹ Pierre Beckers,² Marc Dahan,³ Jun Yan,⁴ and Chao Jiang⁵

¹*Engineering Simulation and Aerospace Computing, Northwestern Polytechnical University, Xi'an 710072, China*

²*LTAS-Infographie, University of Liege, 4000 Liege, Belgium*

³*Department of Applied Mechanics, The University of Franche-Comté, 25000 Besançon, France*

⁴*State Key Laboratory of Structural Analysis for Industrial Equipment, Department of Engineering Mechanics, Dalian University of Technology, Dalian 116024, China*

⁵*State Key Laboratory of Advanced Design and Manufacturing for Vehicle Body, College of Mechanical and Automotive Engineering, Hunan University, Changsha 410082, China*

Correspondence should be addressed to Ji-Hong Zhu; jh.zhu@nwpu.edu.cn

Received 17 May 2015; Accepted 31 May 2015

Copyright © 2015 Ji-Hong Zhu et al. This is an open access article distributed under the Creative Commons Attribution License, which permits unrestricted use, distribution, and reproduction in any medium, provided the original work is properly cited.

Advanced optimization methods have been addressed as the most promising techniques for least-weight and performance design of engineering structures (e.g., Martinez et al. [1], Vitali et al. [2], Hansen and Horst [3], Grihon et al. [4], and Chintapalli et al. [5]). During the last 30 years, many theoretical achievements have been obtained both mechanically and mathematically, which was addressed in the survey papers such as Guo and Cheng [6], Sigmund and Maute [7], and Deaton and Grandhi [8]. Nowadays, the great challenge lies in solving more complicated engineering design problems with multidisciplinary objectives or complex structural systems (see Zhu et al. [9]).

Another important issue in structural optimization is the reliability-based optimization, where uncertainties in geometric dimensions, material properties, loads, boundary conditions, and so forth existing in practical engineering problems are considered. Different effective methods such as the probability methods and the interval methods have been proposed till now (see Jiang and Han [10]).

Focusing on the above mentioned topics, 8 research papers have been published in this special issue. The contents are summarized as follows.

The paper titled “Structural Response Analysis under Dependent Variables Based on Probability Boxes” by Z. Xiao and G. Yang proposed a sampling-based method to calculate

uncertainty structural responses. They used a sampling strategy to consider the random intervals from dependent probability boxes. Different structural interval response problems were then solved with the metamodel-based optimization method.

In the paper titled “Reliability-Based Topology Optimization Using Stochastic Response Surface Method with Sparse Grid Design” by Q. Zhao et al., performance measure approach (PMA) and the sequential optimization and reliability assessment (SORA) were used to deal with the reliability-based topology optimization problems. Stochastic response surface method (SRSM) and the sparse grid design (SGD) are used to enhance the computational efficiencies.

The paper titled “Reliability Analysis of High Rockfill Dam Stability” by P. Yi et al. introduced the slope stability analysis and reliability analysis which were combined in a program to deal with the stability reliability analysis of concrete faced rockfill dams. The safety factor of the critical slip surface was calculated using the limit equilibrium method.

The paper titled “Improved Genetic Algorithm with Two-Level Approximation for Truss Optimization by Using Discrete Shape Variables” by S. Chen et al. presented a simultaneous optimization procedure with size, shape, and topology variables. In the two-level approximation strategy,

genetic algorithm was well applied to deal with mixed and even discretized variables.

The paper titled “Improved Reliability-Based Optimization with Support Vector Machines and Its Application in Aircraft Wing Design” by Y. Wang et al. proposed a new reliability-based design optimization method based on Support Vector Machines (SVM) and the Most Probable Point (MPP). Importance Sampling (IS) is used to calculate the failure probability based on the surrogate model. The improved method was then proved to be more accurate and efficient in numerical examples.

The paper titled “Improved Genetic Algorithm with Two-Level Approximation Method for Laminate Stacking Sequence Optimization by Considering Engineering Requirements” by H. An et al. used genetic algorithm to optimize the stacking sequences of laminated composites. With a new two-level strategy, random initial designs were provided to present better optimization design. The efficiency and feasibility of these improvements were verified with illustrative and industrial examples.

The paper titled “Optimization of the Turbulence Model on Numerical Simulations of Flow Field within a Hydrocyclone” by Y. Xu et al. used Reynolds Stress Model and Large Eddy Simulation to, respectively, perform numerical simulation for the flow field of a hydrocyclone. Compared with the Laser Doppler Velocimeter test results, the results obtained from Large Eddy Simulation were proved to be more accurate and reliable.

In the paper titled “Multidisciplinary Inverse Reliability Analysis Based on Collaborative Optimization with Combination of Linear Approximations” by X.-J. Meng et al., the multidisciplinary reliability assessment problem was transformed into a most probable failure point problem which will be solved later with combination of linear approximations. The proposed method is highly efficient and very convenient in treating nonnormal distribution variables.

Acknowledgments

We would like to express our faithful gratitude to all the contributors to this special issue for their support and to all the reviewers for their constructive and timely comments.

Ji-Hong Zhu
 Pierre Beckers
 Marc Dahan
 Jun Yan
 Chao Jiang

References

- [1] M. P. Martinez, A. Messac, and M. Rais-Rohani, “Manufacturability-based optimization of aircraft structures using physical programming,” *AIAA journal*, vol. 39, no. 3, pp. 517–525, 2001.
- [2] R. Vitali, O. Park, R. T. Haftka, B. V. Sankar, and C. A. Rose, “Structural optimization of a hat-stiffened panel using response surfaces,” *Journal of Aircraft*, vol. 39, no. 1, pp. 158–166, 2002.
- [3] L. U. Hansen and P. Horst, “Multilevel optimization in aircraft structural design evaluation,” *Computers & Structures*, vol. 86, no. 1-2, pp. 104–118, 2008.
- [4] S. Grihon, L. Krog, and D. Bassir, “Numerical Optimization applied to structure sizing at AIRBUS: a multi-step process,” *International Journal for Simulation and Multidisciplinary Design Optimization*, vol. 3, no. 4, pp. 432–442, 2009.
- [5] S. Chintapalli, M. S. A. Elsayed, R. Sedaghati, and M. Abdo, “The development of a preliminary structural design optimization method of an aircraft wing-box skin-stringer panels,” *Aerospace Science and Technology*, vol. 14, no. 3, pp. 188–198, 2010.
- [6] X. Guo and G.-D. Cheng, “Recent development in structural design and optimization,” *Acta Mechanica Sinica*, vol. 26, no. 6, pp. 807–823, 2010.
- [7] O. Sigmund and K. Maute, “Topology optimization approaches,” *Structural and Multidisciplinary Optimization*, vol. 48, no. 6, pp. 1031–1055, 2013.
- [8] J. D. Deaton and R. V. Grandhi, “A survey of structural and multidisciplinary continuum topology optimization: post 2000,” *Structural and Multidisciplinary Optimization*, vol. 49, no. 1, pp. 1–38, 2014.
- [9] J. H. Zhu, W. H. Zhang, and L. Xia, “Topology optimization in aircraft and aerospace structures design,” *Archives of Computational Methods in Engineering*, 2015.
- [10] C. Jiang and X. Han, “A new uncertain optimization method based on intervals and an approximation management model,” *Computer Modeling in Engineering and Sciences*, vol. 22, no. 2, pp. 97–118, 2007.

Research Article

Multidisciplinary Inverse Reliability Analysis Based on Collaborative Optimization with Combination of Linear Approximations

Xin-Jia Meng,¹ Shi-Kai Jing,¹ Ye-Dong Wang,¹ Jing-Tao Zhou,²
Li-Xiang Zhang,³ and Ji-Hong Liu⁴

¹School of Mechanical Engineering, Beijing Institute of Technology, Beijing 100081, China

²School of Mechatronics, Northwestern Polytechnical University, Xi'an 710072, China

³Mechanical and Electrical Engineering Institute, Hebei University of Engineering, Handan 056038, China

⁴School of Mechanical Engineering and Automation, Beihang University, Beijing 100191, China

Correspondence should be addressed to Shi-Kai Jing; jingshikai@bit.edu.cn

Received 22 October 2014; Revised 24 April 2015; Accepted 2 May 2015

Academic Editor: P. Beckers

Copyright © 2015 Xin-Jia Meng et al. This is an open access article distributed under the Creative Commons Attribution License, which permits unrestricted use, distribution, and reproduction in any medium, provided the original work is properly cited.

Multidisciplinary reliability is an important part of the reliability-based multidisciplinary design optimization (RBMDO). However, it usually has a considerable amount of calculation. The purpose of this paper is to improve the computational efficiency of multidisciplinary inverse reliability analysis. A multidisciplinary inverse reliability analysis method based on collaborative optimization with combination of linear approximations (CLA-CO) is proposed in this paper. In the proposed method, the multidisciplinary reliability assessment problem is first transformed into a problem of most probable failure point (MPP) search of inverse reliability, and then the process of searching for MPP of multidisciplinary inverse reliability is performed based on the framework of CLA-CO. This method improves the MPP searching process through two elements. One is treating the discipline analyses as the equality constraints in the subsystem optimization, and the other is using linear approximations corresponding to subsystem responses as the replacement of the consistency equality constraint in system optimization. With these two elements, the proposed method realizes the parallel analysis of each discipline, and it also has a higher computational efficiency. Additionally, there are no difficulties in applying the proposed method to problems with nonnormal distribution variables. One mathematical test problem and an electronic packaging problem are used to demonstrate the effectiveness of the proposed method.

1. Introduction

Reliability-based design optimization (RBDO) is a brand new optimum design method developed on the basis of conventional optimization method. It organically combines the reliability analysis theory and mathematical programming methods [1, 2]. The RBDO of mechanical products is a computing method which takes the reliability of the products as the target or constraint conditions and gets the optimum design in the sense of probability using appropriate optimization method. Similar to the RBDO, RBMDO is a multidisciplinary design optimization considering the influence of random uncertainty on optimization results, and it includes two important parts, multidisciplinary design optimization

(MDO) and multidisciplinary reliability analysis (MRA). Due to the increasingly complicated modern products, the RBMDO has been developed rapidly in recent years [3, 4].

However, the classical RBMDO has a large amount of calculation due to the multilayer nested loops. Both efficient MRA method and reasonable decouple strategy of the MDO are effective ways to improve the computational efficiency of RBMDO. For the reasonable decouple strategy of the MDO, Sues and Cesare [5] proposed a single circular order RBMDO framework, which separated the reliability analysis from the optimization calculation. Padmanabhan and Batill [6] proposed a concurrent subspace method of RBMDO, which was on the basis of the concurrent subspace optimization (CSSO) strategy and reliability index approach (RIA). Du et al. [7]

presented an efficient RBMDO method, where a relationship was established between deterministic optimization part and reliability analysis part. Their method is on the basis of sequence optimization and reliability assessment (SORA). Sun et al. [8] put forward a multidisciplinary reliability design optimization with the integration of collaborative optimization (CO) strategy and performance measurement approach (PMA).

For the multidisciplinary reliability analysis part of RBMDO, because the analyzed object is the multidisciplinary system with couplings, the amount of calculation is also very large. To improve the efficiency of the multidisciplinary reliability analysis, many scholars proposed various analysis methods. Du and Chen [9] proposed collaborative multidisciplinary reliability analysis method, which combined individual discipline feasible (IDF) method and RIA method of reliability analysis. On the basis of decoupling, Liu et al. [10] presented a sequential reliability analysis method for multidisciplinary system, and CSSO and PMA were reasonably combined in the method. Huang et al. [11] established collaborative optimization method with inverse reliability analysis using CO strategy. The multidisciplinary reliability analysis methods mentioned above are mostly aimed at multidisciplinary inverse reliability analysis. This is because most RBMDO frameworks are based on SORA method. The SORA method has a high computational efficiency and strong practicability [12, 13]. The relationship of deterministic and uncertain constraints in the SORA was set up by the most probable point (MPP) of the inverse reliability analysis.

The CO strategy is proposed to solve the multidisciplinary inverse reliability analysis problems in the literature [11]. In this method, the disciplinary analysis and optimization are performed concurrently. Therefore, the computational efficiency is higher than the directly adopting multidisciplinary inverse reliability analysis based on the strategy of multidisciplinary disciplinary feasible (MDF). However, the computational efficiency of traditional CO strategy is still limited due to the inherent problems [14–16], the system level constraint Jacobian does not exist at the solution, the Lagrange multipliers either are zero or converge to zero in the subsystem level, and the system level constraints are nonsmooth functions. These existing problems may make the multidisciplinary inverse reliability analysis of integrated collaborative optimization strategy inefficient.

Recently, an alternative formulation of CO named CLA-CO is proposed by Li et al. [17]. In CLA-CO framework, the equality consistency constraints are replaced by accumulative linear approximations with the response of subsystem level. Some application cases have validated the efficiency of CLA-CO. In this study, on the basis of this method, we propose a multidisciplinary inverse reliability analysis method based on the CLA-CO. In the proposed method, each disciplinary analysis is treated as a form of equality constraint for each subsystem optimization. As the optimization process goes on, the approximations to subsystem responses are continually added to system level as the replacement of the consistency equality constraint. The disciplines analyses are implemented in parallel with the CLA-CO, and the system level constraints

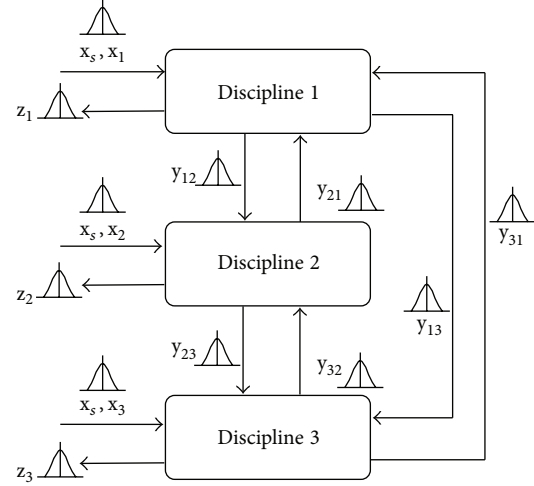


FIGURE 1: A three-discipline system with random variables.

are no longer the subsystem object function. The multidisciplinary inverse reliability method based on the CLA-CO, which is proposed in this study, further improves the efficiency of multidisciplinary inverse reliability analysis.

The remainder of this paper is organized as follows. In Section 2, the multidisciplinary reliability analysis based on the probability model is introduced, including RIA and PMA. In Section 3, the CLA-CO is briefly introduced. Then, the proposed multidisciplinary inverse reliability analysis is provided in Section 4. In Section 5, two test problems are used to demonstrate the effectiveness of the proposed method, and conclusions are in Section 6.

2. Multidisciplinary Reliability Analysis (MRA)

For simplicity, a three-discipline system [18] is used to present the MRA. Figure 1 shows the three-coupled-discipline system with random variables, where each box represents the discipline analysis. In this system, x_s the vector of the shared design variables, and x_i ($i = 1, 2$, and 3) are the vector of the input variables of disciplinary i ; $y = (y_{21}, y_{31}, y_{12}, y_{32}, y_{13}, y_{23})$ are the vector of the coupling variables, and the notation y_{ij} is the vector of the general representation of the coupling variables, which are the vector of the output of discipline i and the input of discipline j ; z_i are the outputs of discipline i . Each coupling variable can be obtained through solving the following system of equations:

$$\begin{aligned}
 y_{12} &= Y_{12}(x_s, x_1, y_{21}, y_{31}), \\
 y_{13} &= Y_{13}(x_s, x_1, y_{21}, y_{31}), \\
 y_{21} &= Y_{21}(x_s, x_2, y_{12}, y_{32}), \\
 y_{23} &= Y_{23}(x_s, x_2, y_{12}, y_{32}), \\
 y_{31} &= Y_{31}(x_s, x_3, y_{13}, y_{23}), \\
 y_{32} &= Y_{32}(x_s, x_3, y_{13}, y_{23}).
 \end{aligned} \tag{1}$$

Figure 1 also shows the propagation of the random uncertainty in multidisciplinary system. Due to the uncertainty of the input variable, the coupling variables and the output of system are no longer determinate. The multidisciplinary reliability analysis is to evaluate whether the output of system satisfies the design requirement under the uncertainty. In RBMDO the design requirement under the uncertainty is given by the form of constraint: that is,

$$\Pr \{z_i(x_s, x_i, y_{\bullet i}) \geq 0\} \geq R_i, \quad (2)$$

where \Pr represents the probability and Z is the limit state function. Consider $y_{\bullet i} = \{y_{ij}, j = 1, 2, 3, j \neq i\}$, and R_i is desired probability.

The left-hand side of (2) is the reliability R , and it can be written as

$$R = \Pr \{z_i(x_s, x_i, y_{\bullet i}) \geq 0\}. \quad (3)$$

The reliability is generally calculated by the following integral:

$$\Pr \{z_i(x_s, x_i, y_{\bullet i}) \geq 0\} = \int_{z_i(x_s, x_i, y_{\bullet i}) \geq 0} f_X(X), \quad (4)$$

where $f_X(X)$ denotes the joint probability density function (PDF) and $X = (x_s, x_i, y_{\bullet i})$.

Due to the multidimensional random variables and nonlinear integration boundary in engineering, it is very difficult or even impossible to obtain an analytical solution to the probability integration in (4); therefore, presently the first order reliability method (FORM) [19, 20] is still a main technique for its approximate solution [21]. In the FORM, the original random variables and the limit state function need to be transformed to standard normal space (U space) [22]:

$$\Phi(U) = F_X(X), \quad (5)$$

$$U = \Phi^{-1}[F_X(X)],$$

$$z_i(X) = z_i[T(U)] = G(U), \quad (6)$$

where $\Phi(\bullet)$ is the cumulative distribution function (CDF) of standard normal distribution and F_X is the CDF of X . Φ^{-1} is the inverse of normal distribution, and T represents a probability transformation function based on (5).

The integration in (4) is now rewritten as

$$\Pr \{z_i(x_s, x_i, y_{\bullet i}) \geq 0\} = \int_{G_i(U) \geq 0} f_U(U), \quad (7)$$

where $f_U(U)$ is PDF of the standard normal variables U .

To easily compute the above integration, the reliability index β , which is defined as the shortest distance from the origin to a point on the limit state surface in U space, is used to assess reliability. Then, the reliability can be expressed as

$$R = \Phi(\beta). \quad (8)$$

Both RIA and PMA are well-known approaches to search β .

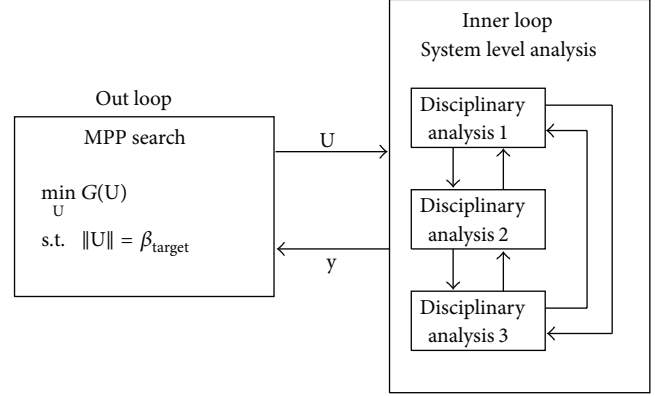


FIGURE 2: Inverse reliability MPP search using MDF method.

2.1. Reliability Index Approach (RIA). In RIA, the most probable point (MPP) is searched on the limit state surface. It can be formulated as a minimization problem as

$$\beta = \min_U \|U\| \quad (9)$$

$$\text{s.t. } G(U) = 0,$$

where $G(U) = 0$ is the limit state equation. It should be noted that, for multidisciplinary system, solving optimization problem (9) needs the inner loop of discipline analysis to obtain the coupling variables $y_{\bullet i}$. The inner loop that solves the coupling is given by the following system of simultaneous equations:

$$y_{\bullet i} = y_{\bullet i}(u_s, u_i, y_{ji} \mid i, j = 1, 2, 3, j \neq i). \quad (10)$$

2.2. Performance Measurement Approach (PMA). The reliability analysis in PMA is formulated as the inverse of reliability analysis in RIA; namely,

$$\min_U G(U) \quad (11)$$

$$\text{s.t. } \|U\| = \beta_{\text{target}},$$

where β_{target} is the target reliability index and the percentile performance $G(U)$ is the function value at the solution U_{MPP}^* [23]. For multidisciplinary system, solving the optimization problem (11) also needs the inner loop procedure which is given by (10). This direct integration of MPP search and inner loop is usually called MPP search using MDF method. The inverse reliability MPP search with multidisciplinary systems is shown in Figure 2.

PMA is superior to RIA at the computational robustness, efficiency, and convenience of sensitivity analysis; therefore, it is widely used in reliability-based design optimization [24, 25]. In this paper, we mainly pay attention to the multidisciplinary inverse reliability analysis. Nonetheless, the proposed method is also applicable to the multidisciplinary reliability analysis in RIA.

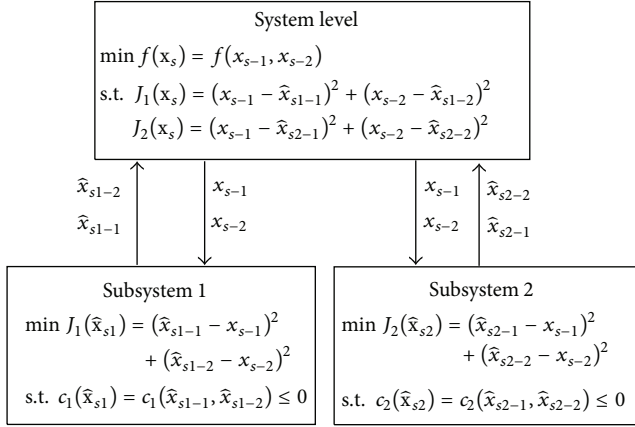


FIGURE 3: Framework of CO for problem (12).

3. Collaborative Optimization with Combination of Linear Approximations (CLA-CO)

3.1. *The Framework of CO.* For a clear understanding of geometric and intrinsic properties, the simple one is the best choice compared with the practical MDO problem [16, 26]. The simple optimization problem is stated as follows:

$$\begin{aligned} \min \quad & f(x_1, x_2) \\ \text{s.t.} \quad & c_1(x_1, x_2) \leq 0 \\ & c_2(x_1, x_2) \leq 0. \end{aligned} \quad (12)$$

Problem (12) is decomposed into a bilevel CO architecture as shown in Figure 3. In the system level, the design variables x_1 and x_2 of problem (12) are denoted by x_{s-1} and x_{s-2} , respectively, and the vector form of system level variables is denoted by x_s . The object function is still the object function of initial problem (12). However, the constraints of system level optimization are no longer the constraints of problem (12), c_1 and c_2 . It is the consistency constraints to the response of subsystem. In the subsystem level, there are two independent optimization problems; the design variables x_1 and x_2 of problem (12) are denoted by \hat{x}_{s1-1} and \hat{x}_{s1-2} in subsystem 1 and denoted by \hat{x}_{s2-1} and \hat{x}_{s2-2} in subsystem 2. The vector form of variables for subsystem 1 and subsystem 2 is denoted by \hat{x}_{s1} and \hat{x}_{s2} , respectively. The original constraints of problem (12), c_1 and c_2 , are assigned to subsystem 1 and subsystem 2, respectively. For each subsystem, the object is as much as possible to meet the consistency, which is as the constraints in system level. In some sense, the consistency constraint is the bridge between system level and subsystem level.

3.2. *The Geometric Analysis of CO.* Figure 4 shows the geometry of the above two subsystem optimizations at the k th iteration. For any subsystem in Figure 4, the object function J_i and constraint c_i share the same tangent line denoted as L_i at the optimal point \hat{x}_{si}^* . L_i is the linear approximation of c_i .

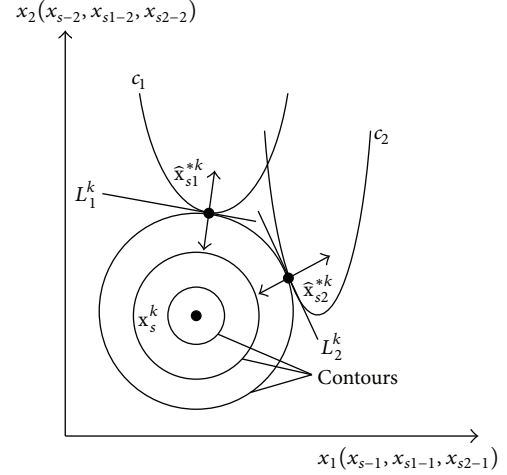


FIGURE 4: Geometry of the subsystem optimizations.

The constraint and object function should satisfy the Kuhn tucker condition at the optimal point:

$$\nabla J_i + \mu \nabla c_i = 0, \quad (13)$$

where μ is a real number that represents the relation between the modules of the two gradient vectors.

At the optimum point of the subsystem, the linear approximation of constraint c_i can be approximated by Taylor's theorem as follows:

$$L_i(x_s) = c_i(\hat{x}_{si}^*) + \nabla^T c_i * (x_s - \hat{x}_{si}^*). \quad (14)$$

At the optimum point of the subsystem in Figure 4, the value of the objective function $c_i(\hat{x}_{0i}^*)$ is equal to zero. Therefore, the linear approximation in the subsystem can be written as follows:

$$L_i(x_s) = \nabla^T c_i * (x_s - \hat{x}_{si}^*) = \frac{1}{\mu} \nabla^T J_i * (\hat{x}_{si}^* - x_s). \quad (15)$$

For the subsystem objective functions that have uniform expressions, that is, the sum of squared terms, the gradients of the subsystem objective functions can be obtained by the following equation:

$$\nabla J_i = \frac{\partial J_i}{\partial x} = 2(\hat{x}_{si} - x_s). \quad (16)$$

Instead of the consistency constraint, the linear approximation as the constraint is added to the system level. The linear approximation constraint is expressed as follows:

$$L_i(x_s) = \frac{1}{\mu} \nabla^T J_i * (\hat{x}_{si}^* - x_s) \leq 0. \quad (17)$$

Given that μ is a positive parameter, μ can be eliminated in (17) in the calculation process; that is,

$$L_i(x_s) = \nabla^T J_i * (\hat{x}_{si}^* - x_s) \leq 0. \quad (18)$$

3.3. *The Formulation of CLA-CO.* On the basis of the analysis in Section 3.2, the formulation of CLA-CO is stated in (19a) and (19b). In the system level of the CLA-CO, the constraints are no longer nonsmooth function, and the inconsistencies are treated explicitly by the accumulation of the linear approximations. The system optimization is restored back to the initial design optimization within the accumulative linear approximations. Thus, the computational efficiency of CLA-CO is very high.

System level is

$$\begin{aligned} \min \quad & f(x_s, \hat{x}_1, \hat{x}_2, \dots, \hat{x}_N) \\ \text{s.t.} \quad & \bigcup_{i=1}^N [L_i^{(1)}(x_s, \hat{x}_i) \leq 0, L_i^{(2)}(x_s, \hat{x}_i) \leq 0, \dots, L_i^{(k)}(x_s, \hat{x}_i) \leq 0], \end{aligned} \quad (19a)$$

where f is the global object; x_s is the vector of shared design variables, and \hat{x}_i are copies of the local design variables passed to the system level; N and k are the number of the subsystem and the iteration, respectively, and $L_i^{(k)}$ stands for the linear approximation of k th iteration in subsystem i .

Subsystem level is

$$\begin{aligned} \min \quad & J_i = \|\hat{x}_{si} - x_s\|^2 + \|x_i - \hat{x}_i\|^2 \\ \text{s.t.} \quad & c_i(\hat{x}_{si}, x_i) \leq 0, \end{aligned} \quad (19b)$$

where \hat{x}_{si} are copies of the shared design variables passed to subsystem i and x_i is the vector of the local design variables

of subsystem i ; $c_i(\hat{x}_{si}, x_i)$ is the vector of the constraints in subsystem i .

It should be noted that, when the optimal values of subsystem are equal to the allocated target values of system, the gradients of the subsystem objection function do not exist. For this situation, no linear approximation can be constructed due to no information of the constraint bound, and no linear approximation can be added to system level.

4. Multidisciplinary Inverse Reliability Analysis under the Framework of CLA-CO

In order to improve the efficiency of multidisciplinary inverse reliability analysis, a multidisciplinary inverse reliability analysis, which combines inverse reliability analysis with CLA-CO, is proposed in this section. It has also to be noted that elements of all the random variables are assumed to be independent in our proposed method.

4.1. *Model of Multidisciplinary Inverse Reliability Analysis with CAL-CO.* The proposed multidisciplinary inverse reliability analysis based on CLA-CO and PMA can be formulated as follows.

System level is

$$\begin{aligned} \min \quad & z(u_s, \hat{u}_1, \dots, \hat{u}_n, \hat{y}) \\ \text{DV} \quad & u_s, \hat{u}_1, \dots, \hat{u}_n, \hat{y} \\ \text{s.t.} \quad & \sqrt{u_s^2 + \hat{u}_1^2 + \dots + \hat{u}_n^2} = \beta_{\text{target}} \\ & \bigcup_{i=1}^n [L_i^{(1)}(x_s, \hat{x}_i, \hat{y}_{i\bullet}) \leq 0, L_i^{(2)}(x_s, \hat{x}_i, \hat{y}_{i\bullet}) \leq 0, \dots, L_i^{(k)}(x_s, \hat{x}_i, \hat{y}_{i\bullet}) \leq 0]. \end{aligned} \quad (20a)$$

Subsystem level is

$$\begin{aligned} \min \quad & J_i = (\hat{u}_{si} - u_s)^2 + (u_i - \hat{u}_i)^2 + (y_{i\bullet} - \hat{y}_{i\bullet})^2 \\ \text{DV} \quad & \hat{u}_{si}, u_i \\ \text{s.t.} \quad & y_{i\bullet} = y_{i\bullet}(u_{si}, u_i, \hat{y}_{j\neq i,i}). \end{aligned} \quad (20b)$$

In the system level, the gradients of the subsystem objective functions for the linear approximation can be obtained by the following equation:

$$\nabla J_i = \frac{\partial J_i}{\partial x} = [2(\hat{x}_{si} - x_s), 2(x_i - \hat{x}_i), 2(y_{i\bullet} - \hat{y}_{i\bullet})]^T. \quad (21)$$

In the proposed method, the coupled multidisciplinary analysis is decomposed into several individual disciplinary analyses. Each disciplinary analysis belongs to a subsystem (or disciplinary) optimization and is treated as a form of

equality constraint in the belonging subsystem optimization. The disciplinary analysis is conducted independently and in parallel. The system level optimization is to search the MPP of the inverse reliability, and it is under the constraints of the target reliability index and the cumulative linear approximation to the subsystem responses. Therefore, the computational difficulty of multidisciplinary inverse reliability analysis with CO strategy is solved. The proposed method not only decomposes coupling among disciplines, but also can improve the computational efficiency of searching the MPP of multidisciplinary inverse reliability. The model of the integration of CLA-CO and inverse reliability for MPP is shown in Figure 5.

4.2. *Procedures of Multidisciplinary Inverse Reliability Analysis with CAL-CO.* The procedures of the proposed method are shown in Figure 6. Details of the procedures are described in six steps.

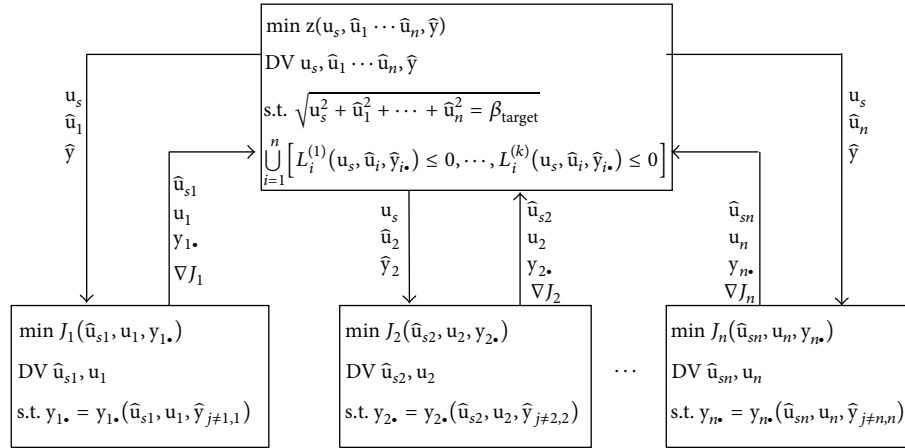


FIGURE 5: Model of the integration of CLA-CO and inverse reliability for MPP.

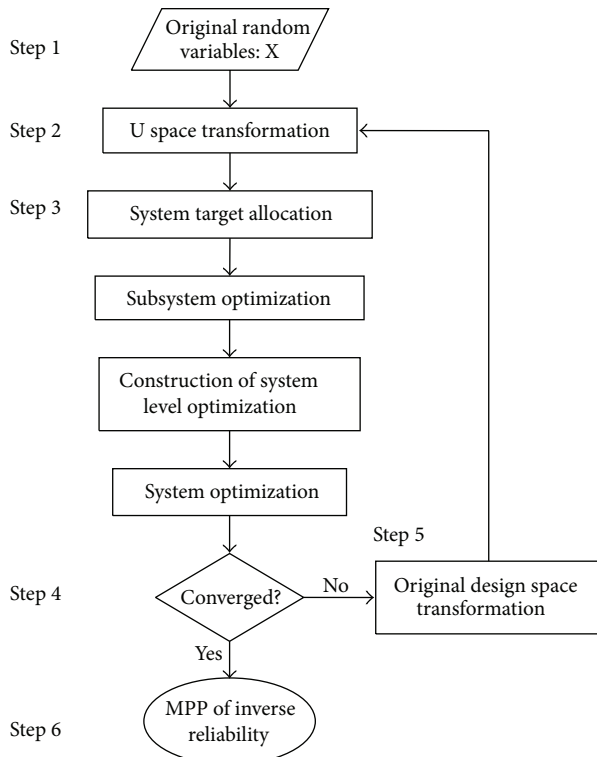


FIGURE 6: Procedures of multidisciplinary inverse reliability analysis with CLA-CO.

Step 1 (initialization). Provide original random variables $X = \{x_s, x_1, \dots, x_n\}$, coupling relationship of multidiscipline system, and distribution parameters of the original random variables.

Step 2 (U space transformation). When the original random variables $X = \{x_s, x_1, \dots, x_n\}$ (in the original design space) all follow normal distribution, the random variables can be

transformed into a set of normalized random variables $U = \{u_s, u_1, \dots, u_n\}$ (in U space) by the following equation:

$$u_i = \frac{x_i - \mu_{x_i}}{\sigma_{x_i}}, \quad (22)$$

where μ_{x_i} and σ_{x_i} are the mean value and standard deviation of x_i , respectively.

Notably, the distributions of random variables are varied and include the uniform, Weibull, and normal distributions. The normal distribution is among the most widely used ones, and other distributions can be converted into it using a certain approach [27]. The most commonly used transformation is given by Rackwitz and Flessler [28] as

$$\begin{aligned} \mu_N &= x^* - \sigma_N \cdot \Phi^{-1} [F_X(x^*)], \\ \sigma_N &= \frac{\phi [\Phi^{-1} (F_X(x^*))]}{f_X(x^*)}, \end{aligned} \quad (23)$$

where x^* presents the specified point which is needed to perform transformation, μ_N and σ_N are the mean value and standard deviation of normal distribution, respectively, and $\phi(\cdot)$ and $f_X(x^*)$ are the PDF of normal distribution and PDF of original random variables.

Therefore, for the original random variable which does not follow the normal distribution, it can be converted into normal distribution through (23), and then the obtained normal distribution variable can be converted into a normalized random variable through (22).

After the transformation, each element of U follows the standard normal distribution.

Step 3 (searching for MPP). With the transformation of Step 2, the original multidisciplinary reliability assessment problem (in the original design space) is transformed into a multidisciplinary optimization problem (in U space). Based

on the CLA-CO method the MPP in U space can be quickly found. The circulation of Step 3 is listed as follows:

- Input: initial value of the parameters in U space
 Output: MPP of multidisciplinary inverse reliability in U space
 Repeat
- 3.1: Distribute system level objectives to each subsystem
 For each subsystem (or disciplinary) i (in parallel), do
 - 3.2: Subsystem optimization
- End for
- 3.3: Construct the system level constraint.
 At each subsystem optimization point, construct linear approximations of the responses of subsystem, and add them to system level.
 - 3.4: Do system level optimization with constructed constraint

Until 3.4 \rightarrow 3.1: System optimization has converged

Step 4 (checking convergence). The convergence criterion of the procedures is set as follows:

$$\left| \frac{z^{(k)} - z^{(k-1)}}{z^{(k)}} \right| \leq \varepsilon, \quad (24)$$

where $z^{(k)}$ and $z^{(k-1)}$ are the k th and the $(k-1)$ th iteration system level optimal objective values, respectively, and ε is a predetermined small positive parameter.

If the obtained MPP satisfies (24), go to Step 6. Otherwise, go to Step 5.

Step 5 (original design space transformation). In this step, the obtained MPP from Step 4 is transformed into the original design space by the following equation:

$$x_i = \mu_{x_i} + u_i \sigma_{x_i}. \quad (25)$$

It has also to be noted that if the original random variables are normally distributed variables, this transformation actually does not need to be performed, because the transformation of Step 5 and transformation of Step 2 are mutual transformation for normally distributed variables.

Step 6 (multidisciplinary reliability assessment). With the obtained MPP, the percentile performance $g(x) = g(x_{\text{MPP}}^*)$ (where $g(x)$ stands for the limit state function) can be calculated at the MPP, and the reliability of the multidisciplinary system can be assessed through the percentile performance. The reliability assessment by percentile performance is given as follows.

For a given reliability assessment

$$\text{Prob} \{g(x) \leq 0\} = R_{\text{target}}, \quad (26)$$

where R_{target} is the target or required reliability while $\text{Prob}\{\bullet\}$ denotes a probability.

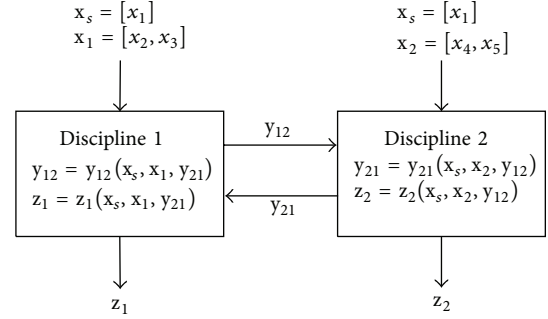


FIGURE 7: Two-discipline system of the example numerical.

If the percentile performance $g(x_{\text{MPP}}^*) \geq 0$, it stands for the fact that the limit state function $g(x)$ satisfies the reliability requirement at the specified design point x ; otherwise, the limit state function will not satisfy the reliability requirement.

5. Illustrative Examples

In this section, two test problems are used to demonstrate the proposed method. To verify the effectiveness of the proposed method, two aspects, efficiency and accuracy, are mainly considered. In each example, the total number of individual disciplinary analyses needed for the MDF method and CO method is compared with those for the proposed method, and the results of the reliability analysis from the proposed method, MDF method, and CO method are also compared in computational accuracy. The sequential quadratic program (SQP) algorithm is adopted as the optimizer.

5.1. Mathematical Test Problem. This numerical example is modified from [29]. It includes five random variables and two disciplines. The two-discipline system is as shown in Figure 7.

In discipline 1, the functional relationships are represented as

$$\begin{aligned} x_s &= [x_1], \\ x_1 &= [x_2, x_3], \\ y_{12} &= x_1^2 + 2x_2 - x_3 + 2\sqrt{y_{21}}, \\ z_1 &= (x_1^2 + 2x_2 - x_3 + x_2 e^{-y_{21}}) - 6. \end{aligned} \quad (27)$$

In discipline 2, the functional relationships are represented as

$$\begin{aligned} x_s &= [x_1], \\ x_1 &= [x_4, x_5], \\ y_{21} &= x_1 x_4 + x_4^2 + x_5 + y_{12}, \\ z_2 &= \sqrt{x_1} + x_4 + x_5 (0.4x_1). \end{aligned} \quad (28)$$

The design point $x = [x_1, x_2, x_3, x_4, x_5]$ is selected for the reliability analysis. In order to show the ability of handling nonnormal distribution variables, in this example, it

is assumed that the design variable x_2 follows a lognormal distribution with logarithmic mean value $\lambda = -0.005$ and logarithmic standard deviation $\zeta = 0.0998$; the design variable x_4 follows a type I extreme value distribution with distribution parameter $u = 0.955$ and $\alpha = 12.8255$; the design variables x_1, x_3 , and x_5 are normally distributed with $[x_1, x_3, x_5] \sim N(1, 0.1^2)$. The system output z_1 is treated as the limit state function. The target reliability index β_{target} is 3. The proposed method is utilized to perform the multidisciplinary reliability analysis.

For simplification of presentation, only the transformations of nonnormal distribution variable are presented as follows.

The transformation of design variable x_2 is obtained through (23) and represented as

$$\begin{aligned}\mu_{N_{x_2}} &= x_2^* - \sigma_{N_{x_2}} \cdot \Phi^{-1} [F_{X_2}(x_2^*)] \\ &= x_2^* (1 - \ln x_2^* + \lambda), \\ \sigma_{N_{x_2}} &= \frac{\phi [\Phi^{-1}(F_{X_2}(x_2^*))]}{f_{X_2}(x_2^*)} = x_2^* \zeta,\end{aligned}\quad (29)$$

where F_{X_2} is the CDF of lognormal distribution and is given by

$$F_{X_2}(x_2) = \frac{1}{\zeta \sqrt{2\pi}} \int_0^{x_2} \frac{1}{t} \exp\left(-\frac{(\ln t - \lambda)^2}{2\zeta^2}\right) dt. \quad (30)$$

f_{X_2} is the PDF of lognormal distribution and is given by

$$f_{X_2}(x_2) = \frac{1}{\zeta x_2 \sqrt{2\pi}} \exp\left(-\frac{(\ln x_2 - \lambda)^2}{2\zeta^2}\right). \quad (31)$$

The transformation of design variable x_4 is obtained through (23) and represented as

$$\begin{aligned}\mu_{N_{x_4}} &= x_4^* - \sigma_{N_{x_4}} \cdot \Phi^{-1} [F_{X_4}(x_4^*)], \\ \sigma_{N_{x_4}} &= \frac{\phi [\Phi^{-1}(F_{X_4}(x_4^*))]}{f_{X_4}(x_4^*)},\end{aligned}\quad (32)$$

where F_{X_4} is the CDF of type I extreme value distribution and is given by

$$F_{X_4}(x_4) = \exp\{-\exp[-\alpha(x_4 - u)]\}. \quad (33)$$

f_{X_4} is the PDF of type I extreme value distribution and is given by

$$f_{X_4}(x_4) = \alpha \exp\{-\alpha(x_4 - u) - \exp[-\alpha(x_4 - u)]\}. \quad (34)$$

After the above transformations all the design variables are normal distribution variables, and then these design variables can be transformed into a set of normalized random variables through (22). Therefore, the formulations of the system and subsystem for our proposed model are obtained as follows.

System level is

$$\begin{aligned}\min \quad z_1 &= \left[(1 + 0.1u_1)^2 + 2(\mu_{N_{x_2}} + \hat{u}_2\sigma_{N_{x_2}}) - (1 + 0.1\hat{u}_3) + (\mu_{N_{x_2}} + \hat{u}_2\sigma_{N_{x_2}}) e^{-\hat{y}_{21}^2} \right] - 6 \\ \text{s.t.} \quad &\sqrt{u_1^2 + u_2^2 + u_3^2 + u_4^2 + u_5^2} = \beta_{\text{target}} \\ &L_1^{(1)} \leq 0, L_1^{(2)} \leq 0, \dots, L_1^{(k)} \leq 0 \\ &L_2^{(1)} \leq 0, L_2^{(2)} \leq 0, \dots, L_2^{(k)} \leq 0.\end{aligned}\quad (35)$$

Subsystem 1 is

$$\begin{aligned}\min \quad J_1 &= (\hat{u}_{11} - u_1)^2 + (u_2 - \hat{u}_2)^2 + (u_3 - \hat{u}_3)^2 \\ &\quad + [y_{12}(\hat{u}_{11}, u_2, u_3, \hat{y}_{21}) - \hat{y}_{12}]^2 \\ \text{s.t.} \quad y_{12} &= (1 + 0.1\hat{u}_{11})^2 + 2(\mu_{N_{x_2}} + u_2\sigma_{N_{x_2}}) \\ &\quad - (1 + 0.1 \times u_3) + 2\sqrt{\hat{y}_{21}}.\end{aligned}\quad (36)$$

Subsystem 2 is

$$\begin{aligned}\min \quad J_2 &= (\hat{u}_{12} - u_1)^2 + (u_4 - \hat{u}_4)^2 + (u_5 - \hat{u}_5)^2 \\ &\quad + [y_{21}(\hat{u}_{12}, u_4, u_5, \hat{y}_{12}) - \hat{y}_{21}]^2 \\ \text{s.t.} \quad y_{21} &= (1 + 0.1\hat{u}_{12}) \times (\mu_{N_{x_4}} + u_4\sigma_{N_{x_4}}) \\ &\quad + (\mu_{N_{x_4}} + u_4\sigma_{N_{x_4}})^2 + (1 + 0.1u_5) + \hat{y}_{21}.\end{aligned}\quad (37)$$

The solutions of this example from the proposed method are $x_{\text{MPP}}^* = (0.8065, 0.8180, 1.1215, 0.9838, 0.9998)$ and $z_1(x_{\text{MPP}}^*) = -4.8319$. For comparisons, the results from MDF

TABLE 1: Results for numerical Example 1 from different methods.

Method	$x_{MPP}^* = (x_1, x_2, x_3, x_4, x_5)$	$z_1(x_{MPP}^*)$	Number of DA ^a
MDF	(0.8066, 0.8186, 1.1196, 0.9838, 0.9998)	-4.8318	862
CO	(0.8066, 0.8178, 1.1217, 0.9841, 0.9999)	-4.8314	520
CLA-CO	(0.8065, 0.8180, 1.1215, 0.9838, 0.9998)	-4.8319	86

^aDA: disciplinary analyses (subsystem).

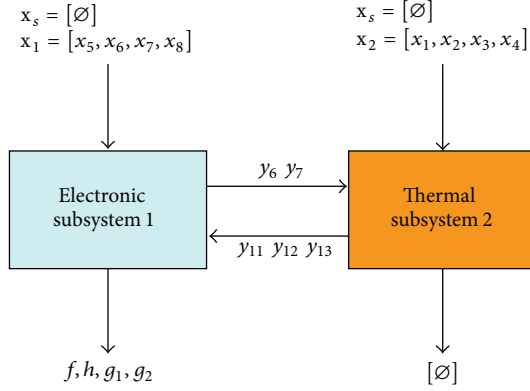


FIGURE 8: The two-coupling-discipline system of electronic packaging problem.

method, CO method, and the proposed method are listed in Table 1.

From Table 1, the solutions of three methods (MDF, CO, and CLA-CO) are almost identical. Both the solutions of CO method and CLA-CO method are very close to that of MDF. However, from the number of discipline analyses, the computational efficiencies of the three methods are quite different. The computational efficiency of those methods from low to high is MDF, CO, and CLA-CO. This indicates that the proposed method is more efficient than the other two methods.

5.2. Electronic Packaging Problem. The electronic packaging problem is a classical MDO numerical problem [30]. This electronic packaging problem has been modified into multidisciplinary reliability assessment problem in [9]. In this test example, it is modified into a multidisciplinary inverse reliability assessment problem to test our proposed method. The multidiscipline system contains two coupling disciplines which is shown in Figure 8:

in electronic discipline 1:

input variables: $x_s = [\emptyset]$, $x_1 = [x_5, x_6, x_7, x_8]$,

linking variables: $y_{12} = [y_6, y_7]$,

outputs: $z_1 = [f, h, g_1, g_2]$;

in thermal discipline 2:

input variables: $x_s = [\emptyset]$, $x_2 = [x_1, x_2, x_3, x_4]$,

linking variables: $y_{21} = [y_{11}, y_{12}, y_{13}]$,

outputs: $z_2 = [\emptyset]$.

TABLE 2: Reliability analysis result for electronic packaging problem for limit state function.

Method	$g_1(x)$	$g_2(x)$	Number of DA (g_1/g_2)
MDF	-0.8615	0.1135	343/496
CO	-0.8256	0.1034	278/382
CLA-CO	-0.8027	0.1012	116/201

The state variables (linking variables) can be obtained by performing multidisciplinary analysis, which is to solve 13 equations. The 13 equations can be easily found from [9].

In this example, g_1 and g_2 are treated as the limit state function, and specified reliability β_{target} is 3; it also assumes that uncertainties are associated with all the input variables, and all the input variables are described by normal distributions with the variation coefficient (the ratio between the standard deviation and the mean value) $c_v = 0.1$.

For simplification of presentation, the formulation of the proposed method is not provided, which can be constructed easily by reference to (20a) and (20b). The specified design point is $x = [x_1, x_2, x_3, x_4, x_5, x_6, x_7, x_8] = [0.08, 0.08, 0.055, 0.0275, 505.0, 0.0065, 505.0, 0.065]$. For comparisons, the MDF method and CO method are also used to solve this reverse reliability issue, respectively. The reliability analysis results from the adopted three methods are listed in Table 2.

For the reliability assessment of limit state function g_1 , the results of MDF, CO, and CLA-CO are -0.8615, -0.8256, and -0.8027, respectively. These results are all smaller than zero, and therefore the limit state function g_1 does not satisfy reliability requirement at the specified design point. From Table 2, the solution of CO is much closer to that of MDF compared with CLA-CO; however, the minimal number of disciplinary analysis comes from the proposed method.

For the reliability assessment of limit state function g_2 , the results of MDF, CO, and CLA-CO are 0.1135, 0.1034, and 0.1012, respectively. These results are all larger than zero, and therefore the limit state function g_1 satisfies reliability requirement at the specified design point. For the comparisons of computational accuracy and efficiency, we have similar conclusion as the reliability assessment of limit state function g_1 .

Through the above analysis, it indicates that any one of the adopted three methods is qualified for the reliability assessment task, and although the proposed approach is slightly deficient in the accuracy, the proposed approach has a high computational efficiency.

6. Conclusions

In this paper, a multidisciplinary inverse reliability analysis method is proposed based on PMA and CLA-CO. In the proposed method, each disciplinary analysis is assigned to a subsystem-level optimization and treated as an equality constraint, and the approximations to subsystem responses are continually added to system level as the optimization process goes on. The method proposed by this paper not

only can realize the parallel analysis of each discipline, but also has a higher computational efficiency. In addition, through transforming nonnormal distribution variables into the normal distribution, the proposed method can effectively address problems with nonnormal distribution variables. Results of examples illustrate that the proposed method is much more efficient than the multidisciplinary inverse reliability analysis method which is combined with the MDF method or CO method. The method has further enriched the solving strategy for multidisciplinary reliability analysis.

Although a high computational efficiency for multidisciplinary inverse reliability analysis can be obtained using the proposed method, there are still two aspects needing to be further developed. (1) The accuracy of the proposed method can be further improved. As shown in electronic packaging problem, the proposed approach is slightly deficient in the accuracy compared with MDF method or CO method. This is mainly because of the adopted linear approximations, and for improving accuracy, other high precision approximation approaches are potential solutions to this difficulty. (2) The application of the proposed method with statistically correlated variables needs to be developed. In our proposed method, all input random variables are assumed to be independent. However, in practice, there always exists the case where the input random variables are statistically correlated. For developing this application, the main difficulty is to develop a multidisciplinary analysis approach for statistically correlated variables. Additionally, to extend the present multidisciplinary inverse reliability analysis method into the RBMDO problems has been our future research plan.

Conflict of Interests

The authors declare that there is no conflict of interests regarding the publication of this paper.

Acknowledgments

This work is partially supported by National Natural Science Foundation of China (NSFC), Grant no. 51175019, and National Defense Basic Research Program of China, Grant no. JSZL2014210B001. The authors thank the academic editor and anonymous reviewers for their valuable comments.

References

- [1] X. C. H. Agarwal, J. E. Renaud, J. C. Lee, and L. T. Watson, "A unilevel method for reliability based design optimization," in *Proceedings of the 45th AIAA/ASME/ASCE/AHS/ASC Structures, Structural Dynamics & Materials Conference, Probabilistic Methods and Reliability Based Optimization*, Palm Springs, Calif, USA, April 2004.
- [2] Y. Wang, S. K. Zeng, and J. B. Guo, "Time-dependent reliability-based design optimization utilizing nonintrusive polynomial chaos," *Journal of Applied Mathematics*, vol. 2013, Article ID 513261, 16 pages, 2013.
- [3] W. Yao, X. Chen, Q. Ouyang, and M. van Tooren, "A reliability-based multidisciplinary design optimization procedure based on combined probability and evidence theory," *Structural and Multidisciplinary Optimization*, vol. 48, no. 2, pp. 339–354, 2013.
- [4] L. S. Li, J. H. Liu, and S. H. Liu, "An efficient strategy for multidisciplinary reliability design and optimization based on CSSO and PMA in SORA framework," *Structural and Multidisciplinary Optimization*, vol. 49, no. 2, pp. 239–252, 2014.
- [5] R. H. Sues and M. A. Cesare, "An innovative framework for reliability-based MDO," in *Proceedings of the 41st Structures, Structural Dynamics, and Materials Conference and Exhibit*, Atlanta, Ga, USA, April 2000.
- [6] D. Padmanabhan and S. M. Batill, "Decomposition strategies for reliability based optimization in multidisciplinary system design," in *Proceedings of the 9th AIAA/ISSMO Symposium on Multidisciplinary Analysis and Optimization*, Atlanta, Ga, USA, September 2002.
- [7] X. P. Du, J. Guo, and H. Beeram, "Sequential optimization and reliability assessment for multidisciplinary systems design," *Structural and Multidisciplinary Optimization*, vol. 35, no. 2, pp. 117–130, 2008.
- [8] J. X. Sun, L. Q. Zhang, J. J. Chen, J. Liu, and L. Li, "Reliability-based multidisciplinary design optimization integrating collaborative optimization strategy and performance measurement approach," *Journal of Computer-Aided Design & Computer Graphics*, vol. 23, no. 8, pp. 1373–1379, 2011.
- [9] X. P. Du and W. Chen, "Collaborative reliability analysis under the framework of multidisciplinary systems design," *Optimization and Engineering*, vol. 6, no. 1, pp. 63–84, 2005.
- [10] S.-H. Liu, L.-S. Li, and J.-H. Liu, "Performance measure approach based sequential reliability analysis of multidisciplinary systems," *Computer Integrated Manufacturing Systems*, vol. 16, no. 11, pp. 2399–2404, 2010.
- [11] H.-Z. Huang, H. Yu, X. Zhang, S. Zeng, and Z. Wang, "Collaborative optimization with inverse reliability for multidisciplinary systems uncertainty analysis," *Engineering Optimization*, vol. 42, no. 8, pp. 763–773, 2010.
- [12] T. M. Cho and B. C. Lee, "Reliability-based design optimization using a family of methods of moving asymptotes," *Structural and Multidisciplinary Optimization*, vol. 42, no. 2, pp. 255–268, 2010.
- [13] H.-Z. Huang, X. D. Zhang, D.-B. Meng, Z. L. Wang, and Y. Liu, "An efficient approach to reliability-based design optimization within the enhanced sequential optimization and reliability assessment framework," *Journal of Mechanical Science and Technology*, vol. 27, no. 6, pp. 1781–1789, 2013.
- [14] B. D. Roth and I. M. Kroo, "Enhanced Collaborative Optimization: a decomposition-based method for multidisciplinary design," in *Proceedings of the ASME International Design Engineering Technical Conferences & Computers and Information in Engineering Conference*, Brooklyn, NY, USA, 2008.
- [15] S. I. Yi, J. K. Shin, and G. J. Park, "Comparison of MDO methods with mathematical examples," *Structural and Multidisciplinary Optimization*, vol. 35, no. 5, pp. 391–402, 2008.
- [16] N. M. Alexandrov and R. M. Lewis, "Analytical and computational aspects of collaborative optimization for multidisciplinary design," *AIAA Journal*, vol. 40, no. 2, pp. 301–309, 2002.
- [17] X. Li, C. G. Liu, W. J. Li, and T. Long, "An alternative formulation of collaborative optimization based on geometric analysis," *Journal of Mechanical Design*, vol. 133, no. 5, Article ID 051005, 2011.
- [18] X. Du, J. Guo, and H. Beeram, "Sequential optimization and reliability assessment for multidisciplinary systems design,"

- Structural and Multidisciplinary Optimization*, vol. 35, no. 2, pp. 117–130, 2008.
- [19] A. M. Hasofer and N. C. Lind, “xact and invariant second-moment code format,” *Journal of the Engineering Mechanics Division*, vol. 100, no. 1, pp. 111–121, 1974.
- [20] F.-K. Huang, G. S. Wang, and Y.-L. Tsai, “Rainfall reliability evaluation for stability of municipal solid waste landfills on slope,” *Mathematical Problems in Engineering*, vol. 2013, Article ID 653282, 10 pages, 2013.
- [21] C. Jiang, W. X. Li, X. Han, L. X. Liu, and P. H. Le, “Structural reliability analysis based on random distributions with interval parameters,” *Computers and Structures*, vol. 89, no. 23-24, pp. 2292–2302, 2011.
- [22] H. O. Madsen, S. Krenk, and N. C. Lind, *Methods of Structural Safety*, Prentice Hall, Englewood Cliffs, NJ, USA, 1986.
- [23] X. Du, A. Sudjianto, and W. Chen, “An integrated framework for optimization under uncertainty using inverse reliability strategy,” *Journal of Mechanical Design, Transactions of the ASME*, vol. 126, no. 4, pp. 562–570, 2004.
- [24] B. D. Youn and K. K. Choi, “Selecting probabilistic approaches for reliability-based design optimization,” *AIAA Journal*, vol. 42, no. 1, pp. 124–131, 2004.
- [25] Y. Aoues and A. Chateaufneuf, “Benchmark study of numerical methods for reliability-based design optimization,” *Structural and Multidisciplinary Optimization*, vol. 41, no. 2, pp. 277–294, 2010.
- [26] X. Li, W. Li, and C. Liu, “Geometric analysis of collaborative optimization,” *Structural and Multidisciplinary Optimization*, vol. 35, no. 4, pp. 301–313, 2008.
- [27] X. J. Meng, S. K. Jing, L. X. Zhang, J. H. Liu, and H. C. Yang, “A new sampling approach for response surface method based reliability analysis and its application,” *Advances in Mechanical Engineering*, vol. 7, no. 1, pp. 1–10, 2015.
- [28] R. Rackwitz and B. Flessler, “Structural reliability under combined random load sequences,” *Computers and Structures*, vol. 9, no. 5, pp. 489–494, 1978.
- [29] X. P. Du and W. Chen, “Efficient uncertainty analysis methods for multidisciplinary robust design,” *AIAA Journal*, vol. 40, no. 3, pp. 545–552, 2002.
- [30] S. Kodiyalam, “Evaluation of methods for multidisciplinary design optimization,” Tech. Rep. NASA/CR-208716, 1998.

Research Article

Optimization of the Turbulence Model on Numerical Simulations of Flow Field within a Hydrocyclone

Yan Xu, Zunce Wang, Lin Ke, Sen Li, and Jinglong Zhang

School of Mechanical Science and Engineering, Northeast Petroleum University, Developing Road, P.O. Box 199, High-Tech District, Daqing, Heilongjiang 163318, China

Correspondence should be addressed to Zunce Wang; wangzc@nepu.edu.cn

Received 25 September 2014; Revised 26 January 2015; Accepted 13 April 2015

Academic Editor: Marc Dahan

Copyright © 2015 Yan Xu et al. This is an open access article distributed under the Creative Commons Attribution License, which permits unrestricted use, distribution, and reproduction in any medium, provided the original work is properly cited.

Reynolds Stress Model and Large Eddy Simulation are used to respectively perform numerical simulation for the flow field of a hydrocyclone. The three-dimensional hexahedral computational grids were generated. Turbulence intensity, vorticity, and the velocity distribution of different cross sections were gained. The velocity simulation results were compared with the LDV test results, and the results indicated that Large Eddy Simulation was more close to LDV experimental data. Large Eddy Simulation was a relatively appropriate method for simulation of flow field within a hydrocyclone.

1. Introduction

As separation equipment, a hydrocyclone is widely used in petroleum industry, marine industry, and water treatment industry. The fidelity of CFD predictions for turbulent flows is highly dependent upon the quality of the turbulence modelling. This is especially true when it comes to the flow in hydrocyclone, because the salient features include high swirl, three-dimensional boundary layers with strong streamline curvature. The studies of the turbulence model on numerical simulations of a hydrocyclone indicate that different degrees of defects exist in mixed length model, normal $k-\varepsilon$ model, and various modified $k-\varepsilon$ model established based on eddy viscosity hypothesis. The basic solution to solve the defects of aforementioned different models lies in giving up turbulence model established on isotropic eddy viscosity hypothesis, while adopting anisotropic Reynolds Stress Model (RSM) and Large Eddy Simulation (LES) instead [1–3].

For the past few years, LES has been applied to the numerical investigation of flow within a hydrocyclone. Delgadillo and Rajamani [4, 5] used LES, RSM, and renormalization group $k-\varepsilon$ turbulence model to simulate the flow of a hydrocyclone. By comparison of their results and experimental data, this showed that LES was more accurate. Schmidt et al. [6] adopted LES to process unsteady characteristics of the fluid

and gained good results. Souza et al. [4, 7, 8] used LES to simulate the flow field of a hydrocyclone; the results showed, although LES need more computational cost, they all got very precise velocity distribution, especially for the tangential velocity.

RSM and LES were, respectively, used in this paper to conduct numerical simulations for the three-dimensional flow field of a hydrocyclone, and the simulation results were compared with the experimental data. The distribution of flow field in a hydrocyclone was gained.

2. RSM Control Equations

2.1. Basic Governing Equations. For incompressible flow, the Reynolds-averaged Navier-Stokes equations:

$$\begin{aligned} \frac{\partial u_i}{\partial x_i} &= 0 \\ \frac{\partial \rho u_i}{\partial t} + \rho \frac{\partial}{\partial x_j} (u_i u_j) &= -\frac{\partial p}{\partial x_i} + \frac{\partial}{\partial x_j} \left(\mu \frac{\partial u_i}{\partial x_j} - \overline{\rho u'_i u'_j} \right). \end{aligned} \quad (1)$$

In these equations, x_i ($i = 1, 2, 3$) is coordinate component, u_i, u_j ($i, j = 1, 2, 3$) is the time-mean velocity component, p is the time-mean average pressure, μ is dynamic viscosity of

the fluid, ρ is the fluid density, and $\overline{u'_i u'_j}$ is the Reynolds stress component.

2.2. *RSM Turbulence Model.* Solve the Reynolds stress equations to get closed equations. One has

$$\frac{\partial}{\partial t} (\overline{\rho u'_i u'_j}) + \frac{\partial}{\partial x_k} (\overline{\rho u_k u'_i u'_j}) = D_{ij} + P_{ij} + \varphi_{ij} + \varepsilon_{ij}. \quad (2)$$

In the equation, every concrete form in the right hand is as follows:

$$D_{ij} = \frac{\partial}{\partial x_k} \left(\frac{\mu_t}{\sigma_k} \frac{\partial \overline{u'_i u'_j}}{\partial x_k} + \mu \frac{\partial \overline{u'_i u'_j}}{\partial x_k} \right), \quad (3)$$

where μ_t is the turbulent viscosity, $\sigma_k = 0.82$. Consider

$$P_{ij} = -\rho \left(\overline{u'_i u'_j} \frac{\partial u_j}{\partial x_k} + \overline{u'_j u'_k} \frac{\partial u_i}{\partial x_k} \right) \quad (4)$$

$$\varphi_{ij} = -C_1 \rho \frac{\varepsilon}{k} \left(\overline{u'_i u'_j} - \frac{2}{3} k \delta_{ij} \right) - C_2 \left(P_{ij} - \frac{1}{3} P_{kk} \delta_{ij} \right),$$

where $C_1 = 1.8$, δ_{ij} is Kronecker delta, k is turbulence energy, ε is turbulent dissipation rate, and $\varepsilon_{ij} = -(2/3)\rho\varepsilon\delta_{ij}$.

Then the closed Reynolds stress equations are got.

3. LES Control Equations

3.1. *Basic Governing Equations.* In LES, the governing equations are obtained by spatially filtering the Navier-Stokes equations. The large turbulent scales are computed explicitly, while the small scales are modelled using Subgrid Scale (SGS) models. The SGS models describe interactions between the resolved and unresolved scales.

For incompressible flow, the governing equations employed for LES are obtained by filtering the time-dependent; applying the filtering operation to the continuity and momentum equations gives

$$\begin{aligned} \frac{\partial \rho}{\partial t} + \frac{\partial}{\partial x_i} (\rho \overline{u}_i) &= 0 \\ \frac{\partial}{\partial t} (\rho \overline{u}_i) + \frac{\partial}{\partial x_j} (\rho \overline{u}_i \overline{u}_j) \\ &= -\frac{\partial \overline{p}}{\partial x_i} + \mu \frac{\partial^2 \overline{u}_i}{\partial x_j \partial x_j} + \frac{\partial}{\partial x_j} \left(\rho (\overline{u}_i \overline{u}_j - \overline{u}_i u_j) \right). \end{aligned} \quad (5)$$

$\overline{\tau}_{ij} = \overline{u}_i \overline{u}_j - \overline{u}_i u_j$ is SGS stress and is computed to close the model.

3.2. *Subgrid Scale Model.* The subgrid scale turbulence models employ the Boussinesq hypothesis as in the RANS models, computing subgrid scale turbulent stresses from

$$\tau_{ij} - \frac{1}{3} \tau_{kk} \delta_{ij} = -2\mu_t \overline{S}_{ij}, \quad (6)$$

where μ_t is subgrid scale turbulent viscosity and \overline{S}_{ij} is the rate-of-strain tensor for the resolved scale defined by:

$$\overline{S}_{ij} \equiv \frac{1}{2} \left(\frac{\partial \overline{u}_i}{\partial x_j} + \frac{\partial \overline{u}_j}{\partial x_i} \right). \quad (7)$$

Kinetic Energy Transport Subgrid Scale Model was proposed by Kim and Menon [9], which acquired favorable application on complex flow of nonequilibrium turbulence. This paper adopted the Kinetic Energy Transport model to calculate the complex flow in hydrocyclone. In the Kinetic Energy Transport model, the eddy viscosity is modeled by

$$\mu_t = C_k \rho k_{sgs}^{1/2} \Delta_f, \quad (8)$$

where Subgrid Scale Kinetic Energy is computed using

$$k_{sgs} = \frac{1}{2} (\overline{u_k^2} - \overline{u_k}^2), \quad (9)$$

where Δ_f is the filter size computed from $\Delta_f = V^{1/3}$; SGS stress can then be written as

$$\tau_{ij} - \frac{2}{3} \rho k_{sgs} \delta_{ij} = -2C_k \rho k_{sgs}^{1/2} \Delta_f \overline{S}_{ij}. \quad (10)$$

k_{sgs} is obtained by solving its transport equation. Consider

$$\begin{aligned} \rho \frac{\partial \overline{k}_{sgs}}{\partial t} + \rho \frac{\partial \overline{u}_j \overline{k}_{sgs}}{\partial x_j} &= -\tau_{ij} \frac{\partial \overline{u}_i}{\partial x_j} - C_\varepsilon \rho \frac{k_{sgs}^{3/2}}{\Delta_f} \\ &+ \frac{\partial}{\partial x_j} \left(\frac{\mu_t}{\sigma_k} \frac{\partial \overline{k}_{sgs}}{\partial x_j} \right). \end{aligned} \quad (11)$$

In the above equations, the model constants, C_k and C_ε , are determined dynamically; σ_k is hardwired to 1.0.

4. The Numerical Calculation Model of Flow Field within a Hydrocyclone

4.1. *Calculation Domain and the Grid.* Double conical hydrocyclone was selected as the research object in this paper. Its main diameter $D = 56$ mm. The fluid that flowed into the hydrocyclone through two inlets located at the tangential direction formed strong swirl turbulence in it and then outflowed from two outlets of underflow and overflow. The geometry is shown in Figure 1.

The hexahedral computational grids were generated using the grid generator ICFM CFD, and the pipe center adopts an O-block grid. In order to guarantee the solution requirement of LES on the viscous sublayer, the grid height of the first layer is $L = 2.0 \times 10^{-5}$ m, and the grid extends in a radial direction with the scaling factor of 1.08. The final grid had about 2.0×10^6 cells. The near wall grid satisfies $y^+ = O(1)$, which guarantees the accurate seizing of a small scale eddy in the flow field. The grid is shown in Figure 2.

4.2. *Boundary Conditions.* In this paper, the velocity u of two inlets is 0.5 m/s, with the hydraulic diameter of 16.6 mm.

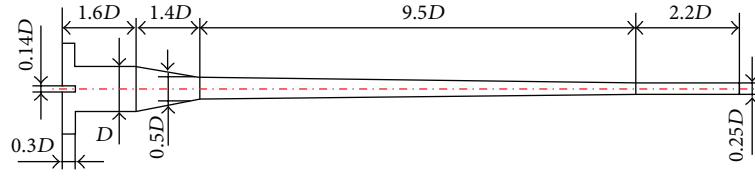


FIGURE 1: Geometry of the double conical hydrocyclone.



FIGURE 2: Graphics display of grid.



FIGURE 4: Experiment equipment.

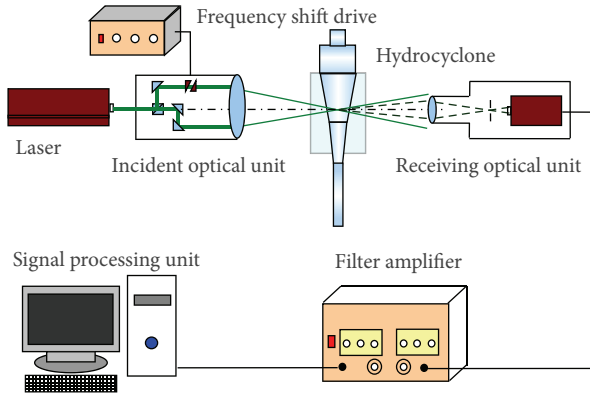


FIGURE 3: Schematic diagram of LDV.

TABLE 1: Numerical calculation method of RSM and LES simulations.

Analogy method	RSM	LES
Grid quantity	9.0×10^5	2.0×10^6
Pressure-velocity coupling method	SIMPLEC	PISO
Gradient interpolation	Least square method	Least square method
Pressure interpolation	PRESTO!	Standard
Convection interpolation	QUICK	Second Order Upwind
Convergence precision	1×10^{-5}	1×10^{-5}

According to $I = 0.16(\text{Re})^{-1/8}$, the turbulence intensity I is 5.18%. According to the formula, $k = 3/2(U * I)^2$, the turbulence energy k can be obtained as $0.001 \text{ m}^2/\text{s}^2$. The underflow and overflow are disposed as the full developed $\partial\Phi/\partial z = 0$, and the split ratio is 95% and 5%, respectively. The boundary conditions of wall are set as no slip wall, whose velocity components are $u = 0, v = 0$, and $w = 0$. In the RSM simulation, Nonequilibrium Wall Functions were used. In the LES, Wall Functions were not used.

4.3. Numerical Calculation Method. ANSYS FLUENT 14.5 was used on a 12 Core CPU 2.67 GHz workstation. Control equations are dispersed in space by finite volume method. Detailed numerical calculation methods of RSM and LES are shown in Table 1. In the LES method, courant number (courant number = time step size/(unit grid length/the velocity in the grid)) is approximately equal to 1. The time step size is calculated by the courant number. The simulation was run until steady state. After steady state was reached, a real time of one second was simulated with a time step of

0.0001 sec. An average of over one thousand time steps was taken to record the velocity profile and other results.

5. The Flow Field Velocity Test Experiment

The flow field test apparatus is established in the ratio of 1:1 according to the simulated hydrocyclone. SCD-23 two-dimensional Laser Doppler Velocimeter (LDV) of Tsinghua University is used to conduct a LDV test on the internal flow field. Speed measuring precision is $\pm 0.5\%$. This process consists of a supply tank, a power pump, flowmeters, pressure metering devices, a control valve, a hydrocyclone, the LDV, and so forth. A screw pump is used to feed fluid in cycle, and the test fluids use running water. The LDV system and the experimental apparatus are shown in Figures 3 and 4. The inlet velocity is 0.5 m/s in experiment process. The values of tangential and axial velocities of three sections with $z = 150 \text{ mm}$, $z = 200 \text{ mm}$, and $z = 300 \text{ mm}$ in hydrocyclone are

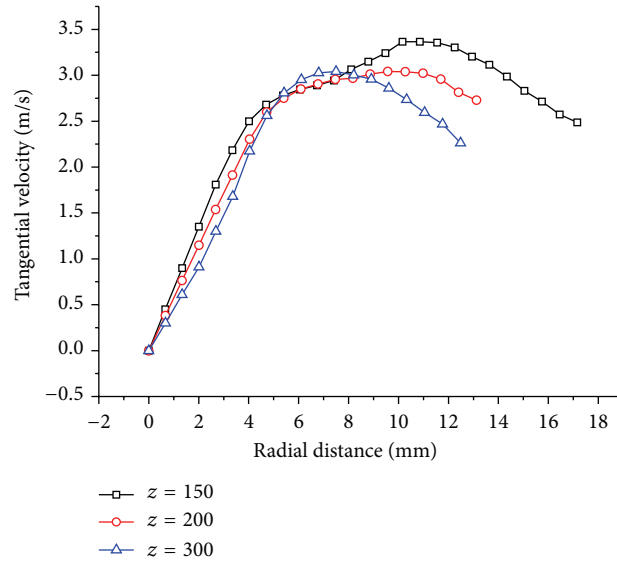


FIGURE 5: Tangential velocity distribution.

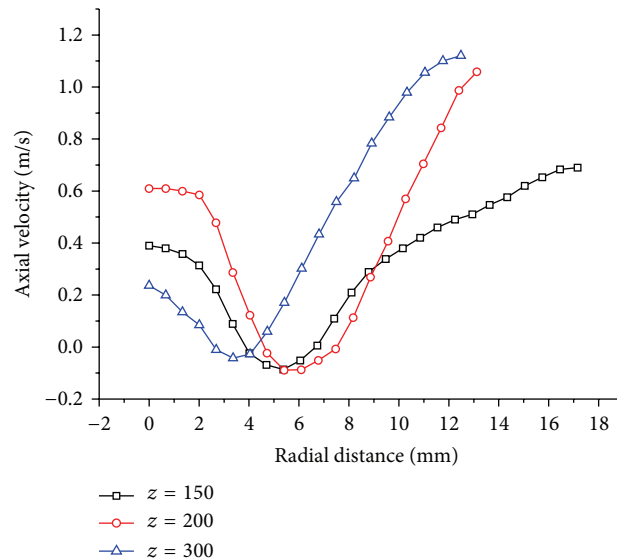


FIGURE 6: Axial velocity distribution.

obtained, and the specific results are shown in Figures 5, 6, and 7.

6. Analysis of Computing Result

6.1. Turbulent Kinetic Energy. The turbulent kinetic energy distribution in hydrocyclone was shown in Figure 7. It can be seen that the turbulent kinetic energy was higher near the small conical wall and the overflow in the LES than the RSM simulation, in which there was nearly no higher turbulence kinetic energy generated except from the small cone section. This is because, if we want to get more accurate calculation of turbulent kinetic energy information, the boundary layer flow should be enough computed. As the LES method

had enough solutions to its boundary layer, the turbulent kinetic energy generated in the hydrocyclone was predicted relatively accurate. However the RSM method simulated the boundary layer flow by logarithmic ratio which has lost the whole generated information of the turbulent kinetic energy. Therefore, the LES method has more advantages for the prediction of the turbulent kinetic energy of flow field in hydrocyclone than the RSM method.

6.2. The Vorticity Distribution. The vorticity distribution in hydrocyclone was shown in Figure 8. We can see from this figure that there were significant nonzero values in the LES to predict the vorticity near the wall, which appeared to be alternate variation in space and constituted a small scale

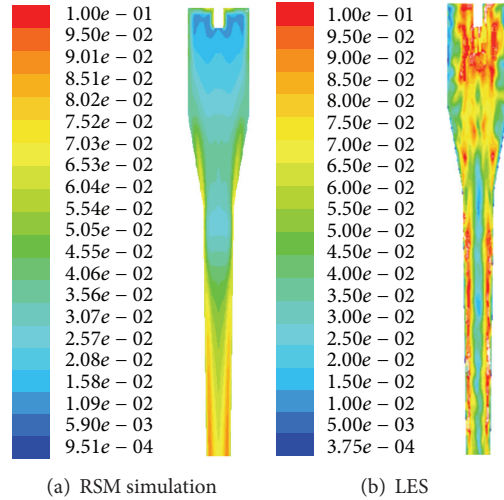


FIGURE 7: Turbulent kinetic energy distribution in hydrocyclone.

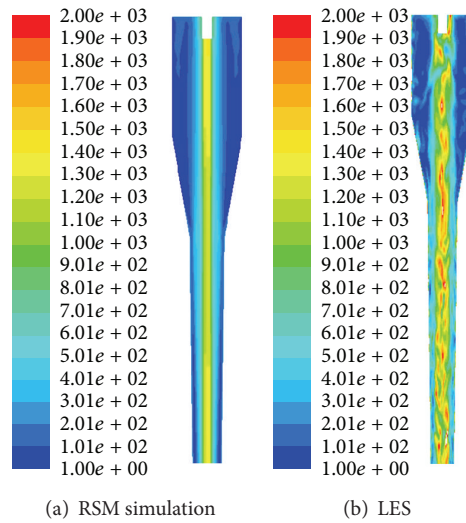


FIGURE 8: The vorticity distribution in hydrocyclone.

vortex structure. With the development of direction of flow to the center, the scale of the vortex increased gradually. Considering the vorticity in the RSM simulation, a lot of small scale vortexes structures were lost. The prediction of central vortexes value was less than the LES results. Thus, the LES can solve more vortex structure of flow field than the RSM and get more turbulent flow pulsation information. It is more advanced in terms of catching small scale vortexes, by the reason that Subgrid Scale Model in the LES can accurately describe the movement of small scale vortex.

6.3. The Flow Velocity Analysis

6.3.1. Tangential Velocity. In the velocity field of the hydrocyclone, tangential velocity is predominant, which is an important factor in affecting the separation efficiency. The comparison of RSM simulation results, LES results, and experimental results of the flow field tangential velocity

distribution of the various stations in the hydrocyclone can be seen in Figure 9.

As can be seen from the figure, the velocity distribution was made up of forced vortexes and free vortexes, and the axial symmetry of the tangential velocity distribution was better. The RSM simulation results both had large deviations on numerical values and the distribution to the experiment results, and the differences were bigger especially in the free vortex area. The tangential velocity distribution of the LES results was relatively consistent with the experiment results both on the values and the distribution, and the forced vortexes were largely overlapping.

6.3.2. Axial Velocity. In the velocity field of the hydrocyclone, another important speed is the axial velocity. The comparison of RSM simulation results, LES results, and experimental results of the flow field axial velocity distribution of various stations in the hydrocyclone can be seen in Figure 9. In the

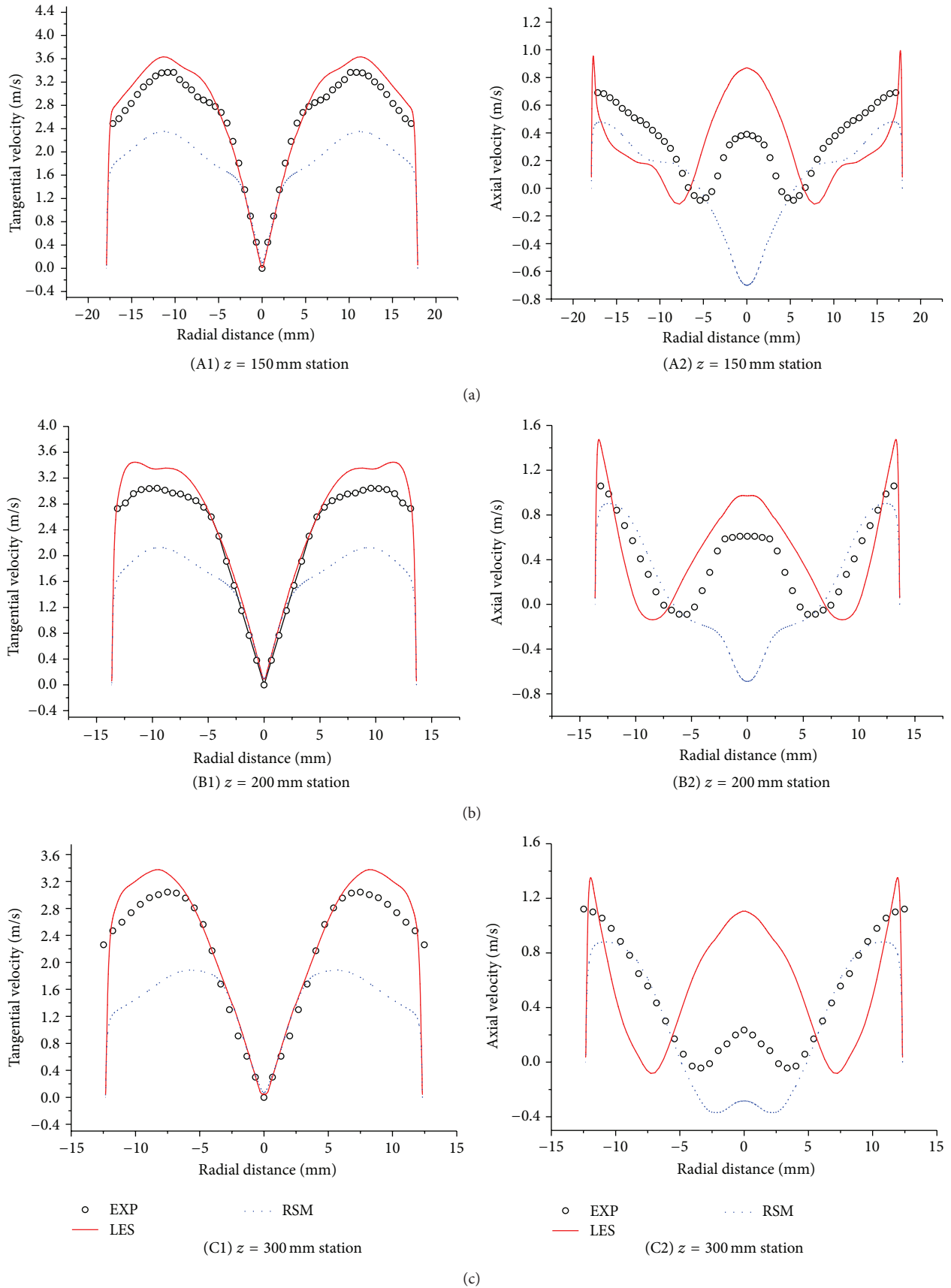


FIGURE 9: Comparison between the tangential and axial velocity at various stations as predicted by the RSM model, the averaged LES results, and the experimental data.

figure, the positive values denote the fluid outflow from the underflow, while the negative value represented the fluid outflow from the overflow. The axial velocity in the hydrocyclone changed from the wall to the center. The maximum value appeared near the wall, with the direction pointing to the underflow outlets. We can see from the numerical size that the distribution regularity of RSM and LES results agreed well with the measured values, and the RSM was more ideal on numerical values near the wall. Opposite results appeared between the RSM and measured values, while the LES was more close to experimental values near the axis. Considering whole fluctuation rule, the LES method was more close to the LDV measured results.

7. The Conclusion

(1) In the calculation of the turbulent kinetic energy and the vorticity of flow field in hydrocyclone, the RSM lost the pulsation characteristics of the small scale vortex structures in spite of solving the boundary layer flow. The LES has the absolute advantages as the Subgrid Scale Model can capture small scale vortex structures more accurately.

(2) The two-dimensional LDV is used to test the flow field of a hydrocyclone, and the velocity distribution of tangential and axial velocities of the various stations in the hydrocyclone under the condition of inlet velocity 0.5 m/s has been got.

(3) During the numerical simulation of velocity field in the hydrocyclone, the RSM simulation results both have some deviations on values and the distribution to the experiment results. The LES results agree well with the LDV results. The simulation results of the LES are superior to the RSM.

Conflict of Interests

There is not any conflict of interests related to this paper.

Acknowledgments

The research was supported by the National Natural Science Foundation of China (11172061) (11402051), Postdoctoral Fund of Heilongjiang Province of China (LBH-Z12273), and Project in Heilongjiang Province Department of Education of China (ky120444).

References

- [1] K. U. Bhaskar, Y. R. Murthy, M. R. Raju, S. Tiwari, J. K. Srivastava, and N. Ramakrishnan, "CFD simulation and experimental validation studies on hydrocyclone," *Minerals Engineering*, vol. 20, no. 1, pp. 60–71, 2007.
- [2] R. Maddahian, M. Asadi, and B. Farhanieh, "Numerical investigation of the velocity field and separation efficiency of deoiling hydrocyclones," *Petroleum Science*, vol. 9, no. 4, pp. 511–520, 2012.
- [3] J. A. Delgadillo, M. Al Kayed, D. Vo, and A. S. Ramamurthy, "CFD simulations of a hydrocyclone in absence of an air core," *Journal of Mining and Metallurgy, Section B: Metallurgy*, vol. 48, no. 2, pp. 197–206, 2012.
- [4] J. A. Delgadillo and R. K. Rajamani, "A comparative study of three turbulence-closure models for the hydrocyclone problem," *International Journal of Mineral Processing*, vol. 77, no. 4, pp. 217–230, 2005.
- [5] J. A. Delgadillo and R. K. Rajamani, "Exploration of hydrocyclone designs using computational fluid dynamics," *International Journal of Mineral Processing*, vol. 84, no. 1–4, pp. 252–261, 2007.
- [6] S. Schmidt, H. Blackburn M, and M. Rudman, "Impact of outlet boundary conditions on the flow properties within a cyclone," in *Proceedings of the 15th Australasian Fluid Mechanics Conference*, pp. 13–17, Sydney, Australia, 2004.
- [7] F. J. Souza and A. S. Neto, "Preliminary results of large eddy simulations of a hydrocyclone," *Revista de Engenharia Térmica*, vol. 3, no. 2, pp. 168–173, 2004.
- [8] J. Zhang, Z. Wang, and Y. Xu, "Large eddy simulation of flow field in a liquid-liquid hydrocyclone," *Chemical Engineering & Machinery*, vol. 40, no. 3, pp. 335–339, 2013.
- [9] W. W. Kim and S. Menon, "Application of the localized dynamic subgrid-scale model to turbulent wall-bounded flows, 35th Aerospace Sciences Meeting, Reno, Nev, USA," Tech. Rep., AIAA-97-0210, American Institute of Aeronautics and Astronautics, 1997.

Research Article

Improved Reliability-Based Optimization with Support Vector Machines and Its Application in Aircraft Wing Design

Yu Wang,¹ Xiongqing Yu,¹ and Xiaoping Du²

¹College of Aerospace Engineering, Nanjing University of Aeronautics and Astronautics, Nanjing 210016, China

²Department of Mechanical and Aerospace Engineering, Missouri University of Science and Technology, Rolla, MO 65409, USA

Correspondence should be addressed to Yu Wang; wangyu@nuaa.edu.cn

Received 25 September 2014; Revised 20 January 2015; Accepted 13 April 2015

Academic Editor: Marc Dahan

Copyright © 2015 Yu Wang et al. This is an open access article distributed under the Creative Commons Attribution License, which permits unrestricted use, distribution, and reproduction in any medium, provided the original work is properly cited.

A new reliability-based design optimization (RBDO) method based on support vector machines (SVM) and the Most Probable Point (MPP) is proposed in this work. SVM is used to create a surrogate model of the limit-state function at the MPP with the gradient information in the reliability analysis. This guarantees that the surrogate model not only passes through the MPP but also is tangent to the limit-state function at the MPP. Then, importance sampling (IS) is used to calculate the probability of failure based on the surrogate model. This treatment significantly improves the accuracy of reliability analysis. For RBDO, the Sequential Optimization and Reliability Assessment (SORA) is employed as well, which decouples deterministic optimization from the reliability analysis. The improved SVM-based reliability analysis is used to amend the error from linear approximation for limit-state function in SORA. A mathematical example and a simplified aircraft wing design demonstrate that the improved SVM-based reliability analysis is more accurate than FORM and needs less training points than the Monte Carlo simulation and that the proposed optimization strategy is efficient.

1. Introduction

There are many uncertainties encountered in both of the aircraft manufacturing process and its subsequent flight operation. The physical properties of materials are uncertain. Manufacturing errors produce the aerodynamic shape and structural dimensions different from the original design [1]. Furthermore, the load on the aircraft is not constant during operation. Fuel is consumed continually during cruise; thus, flight parameters keep changing. After an aircraft has been produced, some parameters sometimes need to be adjusted for a new type. If these uncertainties are considered in the conceptual design, the aircraft performance will be more reliable than deterministic design [2], and both of the risk and cost in the design will be reduced.

Reliability analysis is the key part of reliability-based design optimization (RBDO). Reliability is the probability of success. In physics-based reliability, the status of success is specified by limit-state functions, which are derived from

physics principles [3]. Let the limit-state function be $g(\mathbf{X})$, where \mathbf{X} is a vector of random variables with length n . If the event of success is specified by $g(\mathbf{X}) \geq 0$, then the failure event is $g(\mathbf{X}) < 0$. Consequently, the probability of failure is computed by

$$p_f = \Pr \{g(\mathbf{X}) < 0\} = \int_{g(\mathbf{X}) < 0} f(\mathbf{x}) d\mathbf{x}, \quad (1)$$

where $f(\mathbf{x})$ is the joint probability density function (PDF) of \mathbf{X} .

Since it is difficult to analytically evaluate the probability integral, many approximation methods have been developed. Among them, the First Order Reliability Method (FORM) [4–6] is commonly used. The FORM linearizes the limit-state function $g(\mathbf{X})$ at the Most Probable Point (MPP), which in the standard normal space has the highest probability of producing the value of limit-state function. Then, (1) becomes a linear combination of normal variables. Since only the first

order derivatives of $g(\mathbf{X})$ and some basic information are needed, the FORM is efficient. Its accuracy, however, may not be satisfactory for highly nonlinear limit-state functions.

Several methods are available to improve the accuracy of the FORM. One of the methods is the Second Order Reliability Method (SORM) [7]. The SORM provides a second order approximation to $g(\mathbf{X})$ at the MPP. As a result, it is generally more accurate than the FORM. The MPP-based importance sampling [8, 9] is another alternative method. Random samples are drawn from distributions whose center is shifted to the MPP. A relatively small sample size can then produce a good estimation of the probability of failure. The other strategy is to approximate the safety-failure boundary $g(\mathbf{X}) = 0$ at the MPP with higher accuracy. In the point-fitting method [10], a piecewise paraboloid surface is built with the fitting points selected from each side of MPP along both forward and backward directions of each random variable. Similarly, response surface modeling has also been used to create a surrogate model for the limit-state function at the MPP [11, 12]. A surrogate model can be created using artificial neural network [13] as well.

Recently, another strategy, the support vector machine (SVM) [14] method, has been introduced in reliability analysis. SVM is a statistical classification method. As indicated in [15], reliability analysis can be viewed as a classification problem where SVM is applicable. Examples of using SVM include the fast Monte Carlo simulation (MCS) [16], the limit-state function identification for discontinuous responses and disjoint failure domains [17], SVM-based MCS [18], and virtual SVM for high-dimensional problems [19]. It is worthwhile to further study SVM for reliability analysis and RBDO.

The conventional approach for solving a reliability-based design optimization problem is to employ a double-loop strategy in which the analysis and the synthesis are nested in such a way that the synthesis loop performs the reliability analysis iteratively for meeting the probabilistic constraints. As the double-loop strategy may be computationally infeasible, various single loop strategies have been studied to improve its efficiency. The method ‘‘approximately equivalent deterministic constraints’’ creates a link between a probabilistic design and a safety-factor based design [20]. The reliability constraints are formulated as deterministic constraints that approximate the condition of the MPP for reliability analysis [21]. A single loop method, Sequential Optimization and Reliability Assessment (SORA), is a very efficient method for RBDO [22]. In this method, optimization and reliability analysis are decoupled from each other; no reliability analysis is required within optimization and the reliability analysis is only conducted after the optimization. Hence, the design is quickly improved from cycle to cycle and the computational efficiency is improved significantly. However, because of FORM employed in SORA based on the limit-state function linearization, its precision may not be high enough for the highly nonlinear problem.

In this work, the accuracy of SVM-based reliability analysis was improved firstly. In addition to the training points around the MPP, the gradient of a limit-state function at the MPP was included in approximating the limit-state

function, to guarantee that the surrogate model not only passes through the MPP but also is tangent to the limit-state function at the MPP. And importance sampling is used to estimate the probability of failure based on the surrogate model. Then, the improved SVM-based reliability analysis was integrated into SORA for wing optimization. Results of the two examples showed that this strategy is more accurate than before with a moderately increased computational cost.

2. FORM, IS, and SVM

In this section, the three methods used in this work are reviewed. The methods include the First Order Reliability Method (FORM), importance sampling (IS), and support vector machines (SVM).

2.1. First Order Reliability Method (FORM). In this work, we assume all random variables in \mathbf{X} are independent. FORM involves the following three steps.

(1) *Transformation of Random Variables into Standard Normal Variables.* The original random variables $\mathbf{X} = (X_1, X_2, \dots, X_n)$ (in the X -space) are transformed into random variables $\mathbf{U} = (U_1, U_2, \dots, U_n)$ (in the U -space) whose elements follow a standard normal distribution. The transformation is given by [23]

$$u_i = \Phi^{-1} [F_i(x_i)], \quad (i = 1, 2, \dots, n), \quad (2)$$

where $F_i(x_i)$ is the cumulative distribution function (CDF) of X_i and Φ^{-1} is the inverse CDF of a standard normal variable.

(2) *Search the Most Probable Point (MPP).* The MPP is the point at the limit-state $g(\mathbf{U}) = 0$, and, at the MPP, the PDF of \mathbf{U} is at its maximum. Maximizing the joint PDF of \mathbf{U} and noting that a contour of the PDF of \mathbf{U} is a concentric hypersphere, we obtain the MPP \mathbf{u}^* by solving

$$\begin{aligned} \min_{\mathbf{u}} \quad & \|\mathbf{u}\|, \\ \text{subject to} \quad & g(\mathbf{u}) = 0, \end{aligned} \quad (3)$$

where $\|\cdot\|$ stands for the norm (length) of a vector.

Geometrically, the MPP is the shortest distance point from surface $g(\mathbf{U}) = 0$ to the origin of the U -space. The minimum distance $\beta = \|\mathbf{u}^*\|$ is called the *reliability index*. Then, $g(\mathbf{U})$ is approximated by the first Taylor expansion series at \mathbf{u}^* as

$$g(\mathbf{U}) \approx g(\mathbf{u}^*) + \nabla(\mathbf{u}^*)(\mathbf{U} - \mathbf{u}^*) = \nabla(\mathbf{u}^*)(\mathbf{U} - \mathbf{u}^*), \quad (4)$$

where $\nabla(\mathbf{u}^*)$ is the gradient of g at the MPP and is given by

$$\nabla g(\mathbf{u}^*) = \left(\frac{\partial g(\mathbf{U})}{\partial U_1}, \frac{\partial g(\mathbf{U})}{\partial U_2}, \dots, \frac{\partial g(\mathbf{U})}{\partial U_n} \right) \Big|_{\mathbf{u}^*}. \quad (5)$$

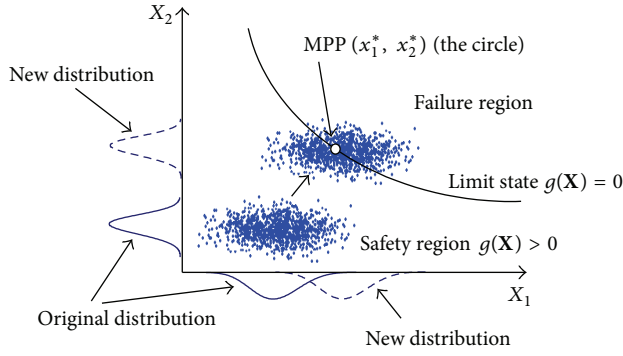


FIGURE 1: Importance sampling.

(c) *Calculate the Probability of Failure.* As shown in (4), $g(\mathbf{U})$ is now a linear combination of normal variables. As a result, $p_f = \Pr\{g < 0\}$ can be easily computed by

$$p_f = P\{g(\mathbf{X}) < 0\} = \Phi(-\beta), \quad (6)$$

where Φ is the CDF of a standard normal variable.

2.2. Importance Sampling (IS). The FORM is commonly used due to its good balance between accuracy and efficiency. For highly nonlinear limit-state functions, however, the accuracy may not be good enough. IS can be used to improve accuracy.

The probability of failure in (1) can be rewritten as

$$p_f = \int_{-\infty}^{+\infty} I(\mathbf{x}) f(\mathbf{x}) d\mathbf{x}, \quad (7)$$

where $I(\cdot)$ is an indicator function and is defined as

$$I(\mathbf{x}) = \begin{cases} 1, & \text{if } g(\mathbf{x}) \leq 0, \\ 0, & \text{otherwise.} \end{cases} \quad (8)$$

p_f is therefore the expectation of $I(\mathbf{x})$; namely,

$$p_f = E\{I(\mathbf{x})\}, \quad (9)$$

where E denotes an expectation. With the direct Monte Carlo simulation (MCS), p_f can be estimated by averaging $I(\mathbf{x})$:

$$p_f = \frac{1}{N} \sum_{i=1}^N I(\mathbf{x}_i) = \frac{N_f}{N}, \quad (10)$$

where \mathbf{x}_i ($i = 1, 2, \dots, N$) are the samples drawn from the joint probability density $f(\mathbf{x})$ and N_f is the number of failures.

A large sample size N is required when p_f is small because the chance of getting samples in failure region is small. IS draws samples from a new set of distributions such that more samples will be in the failure region. One strategy is to shift the mean values of the random variables to the MPP. As shown in Figure 1, all the samples (the lower cloud) generated from the original distributions of X_1 and X_2 are in the safe region. They do not contribute to the probability

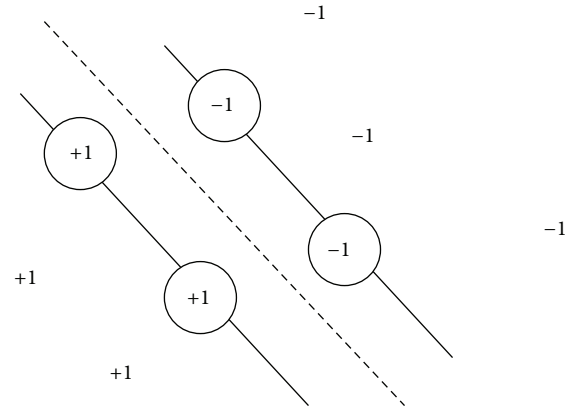


FIGURE 2: Marginal classifiers along with support vectors [27].

estimation. After the mean values are shifted to the MPP, sufficient samples are now in the failure region.

Let the importance sampling density be $h(\mathbf{x})$, which is obtained by shifting the means of $f(\mathbf{x})$ to the MPP. Then, p_f is estimated by

$$\begin{aligned} p_f &= \int I(\mathbf{x}) f(\mathbf{x}) d\mathbf{x} = \int \left[I(\mathbf{x}) \frac{f(\mathbf{x})}{h(\mathbf{x})} \right] h(\mathbf{x}) d\mathbf{x} \\ &\approx \frac{1}{N} \sum_{i=1}^N I(\mathbf{x}_i) \frac{f(\mathbf{x}_i)}{h(\mathbf{x}_i)}. \end{aligned} \quad (11)$$

As shown in Figure 1, IS obtains a significant number of samples in the failure region with the same sample size. Because the indicator function $I(\mathbf{x})$ of a failure point is 1.0, there are a significant number of nonzero terms in the summation in (11). However, it is very difficult for the direct MCS to generate failure samples and the terms in (10) are almost zero. As a result, no estimation of p_f can be produced. Then, more samples are needed. Therefore, IS more efficient than the direct MCS.

2.3. Support Vector Machine (SVM). The SVM method has been primarily used for solving both linear and nonlinear classification problems in statistics. Because in reliability analysis there are two states, either safety or failure, SVM is also applicable for reliability analysis. Recently, several studies on SVM in reliability analysis have been reported [16–18]. The basics of SVM are briefly reviewed in this subsection.

For a linear limit-state function, SVM classifies training data (samples) into two classes, typically represented by “+1” or “-1,” depending on whether the sample belongs to safety or failure region. Two parallel hyperplanes are obtained by maximizing their distance, as shown in Figure 2. There are no samples between the hyperplanes. They therefore separate the samples into safety and failure groups. The points (the circles in the figure) passed by these hyperplanes are called support vectors (SV). The center hyperplane, which lies in half the distance from both hyperplanes, is actually used as the safety-failure boundary [17, 24].

This center hyperplane is the surrogate model for $g(\mathbf{X})$ at the limit-state $g(\mathbf{X}) = 0$ and is represented by

$$y = \mathbf{w} \cdot \mathbf{X} + b, \quad (12)$$

where \mathbf{w} is a weight vector, $\mathbf{w} \cdot \mathbf{X}$ is the dot (inner) product of \mathbf{w} and \mathbf{X} , and b is the bias. And one outer hyperplane follows

$$\mathbf{w} \cdot \mathbf{X} + b = +1 \quad (13)$$

and the other hyperplane satisfies

$$\mathbf{w} \cdot \mathbf{X} + b = -1. \quad (14)$$

Then, the distance between the two hyperplanes is $2/(\mathbf{w} \cdot \mathbf{w})$. As mentioned previously, the distance must be maximized. Because we can minimize $(1/2)\mathbf{w} \cdot \mathbf{w}$. To make sure there are no training points between the two hyperplanes, we need to add the following constraint to the optimization model [24]:

$$y_i (\mathbf{w} \cdot \mathbf{x}_i + b) \geq 1, \quad (15)$$

where \mathbf{x}_i ($i = 1, 2, \dots, m$) is the vector of training points and m is the number of training points. y_i is +1 if \mathbf{x}_i is in the safety region and -1 otherwise.

The optimization model is then given by

$$\begin{aligned} \min_{\mathbf{w}} \quad & \frac{1}{2} \mathbf{w} \cdot \mathbf{w}, \\ \text{s.t.} \quad & y_i (\mathbf{w} \cdot \mathbf{x}_i + b) \geq 1, \quad (i = 1, 2, \dots, m). \end{aligned} \quad (16)$$

The optimization is a quadratic programming problem, and it is usually converted into a Lagrangian dual problem [25, 26]. The dual optimization model is

$$\begin{aligned} \max_{\lambda} \quad & L = \sum_{i=1}^m \lambda_i - \frac{1}{2} \sum_{i,j=1}^m \lambda_i \lambda_j y_i y_j \mathbf{x}_i \cdot \mathbf{x}_j, \\ \text{s.t.} \quad & \sum_{i=1}^n y_i \lambda_i = 0, \\ & 0 \leq \lambda_i, \quad i = 1, 2, \dots, m, \end{aligned} \quad (17)$$

where λ is the Lagrangian multiplier.

Once λ is obtained, the weight vector in (12) can be computed by

$$\mathbf{w} = \sum_{i=1}^m \lambda_i y_i \mathbf{x}_i. \quad (18)$$

According to Karush-Kuhn-Tucker conditions, only the support vectors have non-zero Lagrangian multipliers [27], that is, only the SV appear in the optimum result [25]. Therefore, the bias b in (12) can be determined by SV with $\lambda_j > 0$:

$$b = y_j - \sum_{i=1}^m \lambda_i y_i \mathbf{x}_i \cdot \mathbf{x}_j. \quad (19)$$

For nonlinear limit-state functions, hypersurfaces must be generated. To do so, we can simply replace the dot product $\mathbf{x}_i \cdot \mathbf{x}_j$ in (17) with the following kernel function:

$$K(\mathbf{x}_i, \mathbf{x}_j) = \boldsymbol{\varphi}(\mathbf{x}_i) \cdot \boldsymbol{\varphi}(\mathbf{x}_j), \quad (20)$$

where $\boldsymbol{\varphi}(\mathbf{x})$ is the feature function of \mathbf{x} , which is used to map the original variable into a higher-dimensional space called the feature space. In the N -dimensional feature space, \mathbf{x} is represented by $(\varphi_1(\mathbf{x}), \varphi_2(\mathbf{x}), \dots, \varphi_N(\mathbf{x}))$. It is noted that the kernel function is the dot product of the two feature functions. And the most popular kernel functions are Gaussian kernel and polynomial kernel, which are defined as

$$K(\mathbf{x}_i, \mathbf{x}_j) = \exp\left(\frac{-\|\mathbf{x}_i - \mathbf{x}_j\|^2}{2\sigma^2}\right), \quad (21)$$

$$K(\mathbf{x}_i, \mathbf{x}_j) = (1 + \mathbf{x}_i \cdot \mathbf{x}_j)^d, \quad (22)$$

respectively. Although the feature function $\boldsymbol{\varphi}(\mathbf{x})$ appears in (20), it will not be used directly.

Then, the simplified (surrogate) model for the limit-state function is

$$y = \mathbf{w} \cdot \boldsymbol{\varphi}(\mathbf{X}) + b = \sum_{i=1}^m \lambda_i y_i K(\mathbf{x}_i, \mathbf{X}) + b. \quad (23)$$

3. Improved SVM Method for Reliability Analysis

As discussed above, MPP-based importance sampling (IS) is more accurate than the FORM. But it may still require a significant number of samples for high accuracy. To further improve the accuracy with balanced efficiency, we propose to integrate the FORM, SVM, and IS. To use the full information of the MPP, we also use the gradient of $g(\mathbf{U})$ at the MPP in the U -space. With the additional information of the gradient, the SVM surrogate model will be more accurate. We call this method SVM-MPP-G method. Its procedure is as follows:

- (1) FORM: search the MPP \mathbf{u}^* ;
- (2) IS: generate samples at the MPP;
- (3) SVM: create a surrogate model $\hat{g}(\mathbf{U})$ for the limit-state function $g(\mathbf{U}) = 0$ based on the IS samples and the gradient of $g(\mathbf{U})$ at the MPP in the U -space;
- (4) IS or MCS: perform IS or MCS around the MPP to evaluate the probability of failure p_f with $\hat{g}(\mathbf{U})$.

The flowchart of the method is shown in Figure 3. The details of the steps are provided below.

3.1. Step 1: MPP Search. The MPP is identified with the model in (3). Nonlinear optimization algorithms can be used to solve the model. A specialized search algorithm, however, may be more efficient than optimization. In this work, we use the robust MPP search algorithm, the improved HRLF algorithm, denoted by iHRLF. The algorithm is proposed by Zhang and

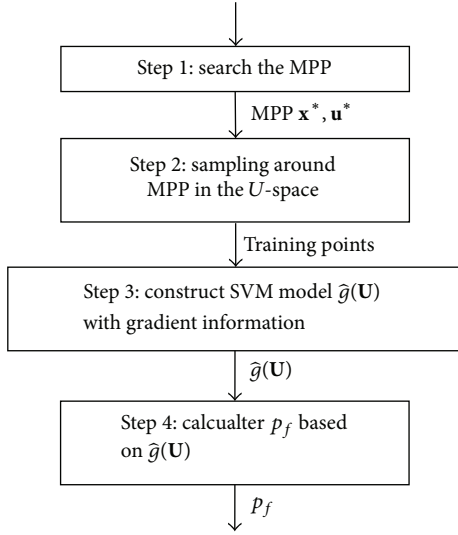


FIGURE 3: Flowchart of the proposed method.

der Kiureghian [28]. iHRLF is efficient; it is also globally convergent because it can converge to a local MPP from any starting point. The algorithm is summarized below.

In iteration $k + 1$, the MPP is updated by

$$\mathbf{u}_{k+1} = \mathbf{u}_k + \alpha \mathbf{d}_k, \quad (24)$$

where the search direction \mathbf{d}_k is given by

$$\mathbf{d}_k = \frac{\nabla g(\mathbf{u}_k) \mathbf{u}_k^T - g(\mathbf{u}_k) \nabla g_y(\mathbf{u}_k) - \mathbf{u}_k}{\|\nabla g_y(\mathbf{u}_k)\|^2}, \quad (25)$$

where $\nabla g(\mathbf{u}_k) = (\partial g / \partial U_1, \partial g / \partial U_2, \dots, \partial g / \partial U_n)_{\mathbf{u}_k}$.

The step size α is determined by minimizing a merit function

$$m(\mathbf{u}) = \frac{1}{2} \|\mathbf{u}\| + c |g(\mathbf{u})| \quad (26)$$

in which the constant c should satisfy

$$c > \frac{\|\mathbf{u}\|}{\|\nabla g(\mathbf{u})\|}. \quad (27)$$

Practically, searching for the step size α terminates once the merit function is sufficiently reduced. The following rule is employed to find α :

$$\alpha = \max_{h \in \mathbb{N}} \{b^h \mid m(\mathbf{u}_k + b^h \mathbf{d}_k) - m(\mathbf{u}_k) < 0\}, \quad b > 0. \quad (28)$$

In this paper, $b = 0.5$ and $c = 2\|\mathbf{u}_k\| / \|\nabla g(\mathbf{u}_k)\| + 10$ are used.

Equation (28) indicates that $\alpha = h$ is the first integer such that the merit function $m(\mathbf{u}_k + b^h \mathbf{d}_k)$ is less than the previous merit function $m(\mathbf{u}_k)$.

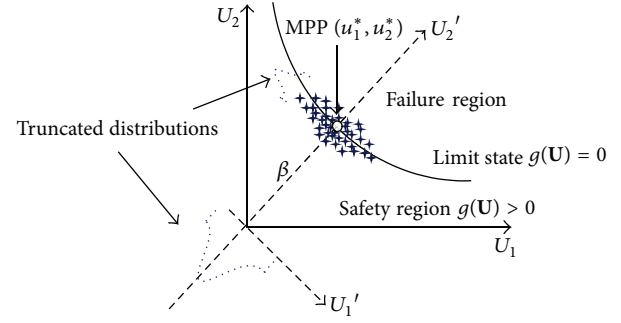


FIGURE 4: Sampling strategy.

If the distance between two consecutive points \mathbf{u}_{k+1} and \mathbf{u}_k is less than a small value ε ; namely, $\|\mathbf{u}_{k+1} - \mathbf{u}_k\| \leq \varepsilon$, the procedure stops. The result is the MPP \mathbf{u}^* in the U -space. The MPP \mathbf{x}^* in the X -space can be obtained by the inverse transformation based on (2)

$$\mathbf{x}_i^* = F_{x_i}^{-1}[\Phi(u_i^*)], \quad (i = 1, 2, \dots, n). \quad (29)$$

3.2. Step 2: Sampling around the MPP. We are interested in creating the limit-state boundary accurately. Since the MPP has the highest probability density at the limit-state, we particularly desire higher accuracy around the MPP. To this end, we draw samples around the MPP. To further improve the sampling efficiency, we also use the gradient information of the limit-state function at the MPP so that the samples will be closer to the limit-state boundary. Since the gradient is a byproduct of the MPP search, no further computations are needed for its use.

To easily draw samples around the MPP, we perform sampling in the U -space. The sampling distributions are standard normal ones, but their means are shifted to the MPP. If the samples are drawn from the sampling distributions directly, they will form a symmetric hypersphere around the MPP. Some of them may be far away from the limit-state boundary. To make them close to the boundary, we shrink the sampling distributions in the gradient direction. To make the samples closer to the MPP, we also truncate the distributions. As shown in Figure 4, more samples are in the vicinity of the MPP with the truncation and shrinking.

To implement the idea, we first rotate coordinates (U_1, U_2, \dots, U_n) into a new set of coordinates $(U'_1, U'_2, \dots, U'_n)$, so that the last coordinate U'_n (U'_2 in the figure) is coincident with the vector from the origin to the MPP. In another word, U'_n is colinear with the gradient of $g(\mathbf{U})$ at the MPP. In the new linear U' -space, the coordinates of the MPP become $[0, \dots, 0, \beta]$. This treatment makes the shrinking easier.

We actually draw samples in the rotated U' -space. The distributions are standard normal distributions for U'_i ($i = 1, 2, \dots, n-1$); namely, $U'_i \sim N(0, 1)$ ($i = 1, 2, \dots, n-1$). The distribution of U'_n is also a normal distribution with its mean being β ; namely, $U'_n \sim N(\beta, 1)$. To make the samples close to the limit-state boundary, we truncate all the distributions. Suppose the PDF of U'_i ($i = 1, 2, \dots, n$) is $\phi_{U'_i}(u)$ and U'_i lies within the interval $(\mu_i - \Delta_i, \mu_i + \Delta_i)$, $\Delta_i > 0$, where Δ_i is the

distance between the mean value and one of the truncated tails; the truncated PDF [29] is then given by

$$\phi_{U'_i}^t(u') = \begin{cases} \frac{\phi_{U'_i}(u')}{\Phi_{U'_i}(\mu_i + \Delta_i) - \Phi_{U'_i}(\mu_i - \Delta_i)}, & \text{if } \mu_i - \Delta_i < u' < \mu_i + \Delta_i, \\ 0, & \text{otherwise,} \end{cases} \quad (30)$$

where $\Phi_{U'_i}(u')$ is the CDF of U'_i .

For U'_i ($i = 1, 2, \dots, n-1$), we use the same distance Δ_i ($i = 1, 2, \dots, n-1$) to shrink the distribution. In the gradient direction in the U'_n -axis, we truncate the distribution of U'_n with a smaller distance Δ_n ; namely, $\Delta_n < \Delta_i$ ($i = 1, 2, \dots, n-1$). Generally, the distances $\Delta_1 = 1.0$ and $\Delta_2 = 0.15 \sim 0.25$ could be taken.

Because of its good efficiency, we also use Latin Hypercube Sampling (LHS) [30] instead of the direct Monte Carlo sampling. In general, 10~25 times the number of random variables could be taken as the number of sampling points. After the samples of \mathbf{U}' are generated, they need to be transformed into the U -space. If each sample point is represented by a row vector, an orthogonal transformation is implemented by

$$\mathbf{U} = \mathbf{U}'\mathbf{R}, \quad (31)$$

where \mathbf{R} is the rotation matrix. It could be computed with the gradient information of the limit-state function at the MPP, which has been obtained during the MPP searching. The matrix \mathbf{R} is derived from another matrix \mathbf{R}_0 with the Gram-Schmidt orthogonalization. \mathbf{R}_0 is given by

$$\mathbf{R}_0 = \begin{bmatrix} \mathbf{I}_{n-1} & 0 \\ \alpha_1 \alpha_2 \cdots \alpha_{n-1} & \alpha_n \end{bmatrix}, \quad (32)$$

where \mathbf{I}_{n-1} is an $(n-1) \times (n-1)$ identity matrix, and the last row of \mathbf{R}_0 is a unit vector defined as follows:

$$\boldsymbol{\alpha} = \frac{\mathbf{u}^*}{\|\mathbf{u}^*\|}. \quad (33)$$

Then, \mathbf{R} can be generated from \mathbf{R}_0 with the following Gram-Schmidt orthogonalization procedure: let the rows of \mathbf{R}_0 and \mathbf{R} be \mathbf{r}_{0i} and \mathbf{r}_i ($i = 1, 2, \dots, n$), respectively. Consider

$$\begin{aligned} \mathbf{r}_n &= \mathbf{r}_{0n}, \\ \mathbf{r}'_k &= \mathbf{r}_{0k} - \sum_{j=k+1}^n \frac{\mathbf{r}_j \mathbf{r}'_{0k}}{\mathbf{r}_j \mathbf{r}'_j} \mathbf{r}_j, \\ \mathbf{r}_k &= \frac{\mathbf{r}'_k}{\|\mathbf{r}'_k\|}, \quad k = n-1, n-2, \dots, 1. \end{aligned} \quad (34)$$

Therefore, we could obtain the training points in the U -space with (31).

3.3. Step 3: Surrogate Model Construction. With the training points obtained above, we now construct the SVM surrogate model $\hat{g}(\mathbf{U})$ for $g(\mathbf{U})$. $\hat{g}(\mathbf{U})$ is not approximated for actual value of $g(\mathbf{U})$. Just the limit-state functions $\hat{g}(\mathbf{U}) = 0$ is similar to $g(\mathbf{U}) = 0$ in the vicinity of the MPP. Different from the traditional SVM methods, this method incorporates the gradient information at the MPP in the optimization model. This allows us to use the full information obtained during the MPP search.

For nonlinear limit-state functions, as discussed in Section 2.3, a feature function $\boldsymbol{\varphi}(\mathbf{x})$ ($\boldsymbol{\varphi}(\mathbf{U})$ in the following discussions) is used to accommodate the nonlinearity. As shown in (23), the approximated limit-state function is given by

$$y = \hat{g}(\mathbf{U}) = \mathbf{w} \cdot \boldsymbol{\varphi}(\mathbf{U}) + b. \quad (35)$$

The derivative of $\hat{g}(\mathbf{U})$ with respect to U_p ($p = 1, 2, \dots, n$) is [31]

$$\left. \frac{\partial \hat{g}}{\partial U_p} \right|_{\mathbf{U}=\mathbf{u}^*} = \mathbf{w} \cdot \boldsymbol{\varphi}'_p(\mathbf{u}^*) = c_p e, \quad (36)$$

where $\mathbf{c} = \nabla g(\mathbf{u}^*) = (\partial g(\mathbf{U})/\partial U_1, \partial g(\mathbf{U})/\partial U_2, \dots, \partial g(\mathbf{U})/\partial U_n)|_{\mathbf{u}^*}$ is the gradient of limit-state function at the MPP and e is the proportionality factor. $e = (\mathbf{w} \cdot \boldsymbol{\varphi}'_h(\mathbf{u}^*))/c_h$, and $|c_h| = \max\{|c_1|, |c_2|, \dots, |c_n|\}$.

We add (36) into the original optimization problem in (16) as additional linear constraints. The new optimization model then becomes

$$\begin{aligned} \min_{\mathbf{w}} \quad & \frac{1}{2} \mathbf{w} \cdot \mathbf{w} \\ \text{s.t.} \quad & y_i [\mathbf{w} \cdot \boldsymbol{\varphi}(\mathbf{u}_i) + b] \geq 1, \quad i = 1, 2, \dots, m, \\ & \left. \frac{\partial g}{\partial u_p} \right|_{\mathbf{U}=\mathbf{u}^*} = \mathbf{w} \cdot \boldsymbol{\varphi}'_p(\mathbf{u}^*) = c_p e, \\ & p = 1, 2, \dots, n. \end{aligned} \quad (37)$$

The Lagrangian function of the dual problem changes to

$$\begin{aligned} L = \frac{1}{2} \mathbf{w} \cdot \mathbf{w} - \sum_{i=1}^m \lambda_i \{ y_i [\mathbf{w} \cdot \boldsymbol{\varphi}(\mathbf{u}_i) + b] - 1 \} \\ - \sum_{p=1}^n \gamma_p \left[\mathbf{w} \cdot \boldsymbol{\varphi}'_p(\mathbf{u}^*) - c_p \frac{\mathbf{w} \cdot \boldsymbol{\varphi}'_h(\mathbf{u}^*)}{c_h} \right] \end{aligned} \quad (38)$$

and $\boldsymbol{\gamma} = [\gamma_1, \gamma_2, \dots, \gamma_n]$. λ_i ($i = 1, 2, \dots, 3$) should be nonnegative. y_i is +1 if $g(\mathbf{u}_i)$ is positive and -1 otherwise. Given the

Karush-Kuhn-Tucker (KKT) complementary conditions [27] for maximizing L , the following equations hold:

$$\frac{\partial L}{\partial \mathbf{w}} = \mathbf{w} - \sum_{i=1}^m \lambda_i \gamma_i \boldsymbol{\varphi}(\mathbf{u}_i) - \sum_{p=1}^n \gamma_p \left[\boldsymbol{\varphi}'_p(\mathbf{u}^*) - \frac{c_p \boldsymbol{\varphi}'_h(\mathbf{u}^*)}{c_h} \right] = 0, \quad (39)$$

$$\mathbf{w} = \sum_{i=1}^m \lambda_i \gamma_i \boldsymbol{\varphi}(\mathbf{u}_i) + \sum_{p=1}^n \gamma_p \left[\boldsymbol{\varphi}'_p(\mathbf{u}^*) - \frac{c_p \boldsymbol{\varphi}'_h(\mathbf{u}^*)}{c_h} \right], \quad (40)$$

$$\frac{\partial L}{\partial b} = -\sum_{i=1}^m \lambda_i \gamma_i = 0, \quad (41)$$

$$\frac{\partial L}{\partial \gamma_p} = \mathbf{w} \cdot \boldsymbol{\varphi}'_p(\mathbf{u}^*) - c_p \frac{\mathbf{w} \cdot \boldsymbol{\varphi}'_h(\mathbf{u}^*)}{c_h} = 0, \quad (42)$$

$p = 1, 2, \dots, n; p \neq h.$

Plugging (40) into (38) yields

$$L = -\frac{1}{2} \sum_{i,j=1}^m \lambda_i \lambda_j \gamma_i \gamma_j \boldsymbol{\varphi}(\mathbf{u}_i) \cdot \boldsymbol{\varphi}(\mathbf{u}_j) + \sum_{i=1}^m \lambda_i + \frac{1}{2} \sum_{p,q=1}^n \gamma_p \gamma_q \left[\boldsymbol{\varphi}'_q(\mathbf{u}^*) \cdot \boldsymbol{\varphi}'_p(\mathbf{u}^*) - \frac{2c_q}{c_h} \boldsymbol{\varphi}'_h(\mathbf{u}^*) \cdot \boldsymbol{\varphi}'_p(\mathbf{u}^*) + \frac{c_p c_q \boldsymbol{\varphi}'_h(\mathbf{u}^*) \cdot \boldsymbol{\varphi}'_h(\mathbf{u}^*)}{c_h^2} \right]. \quad (43)$$

Because

$$\boldsymbol{\varphi}(\mathbf{u}_i) \cdot \boldsymbol{\varphi}(\mathbf{u}_j) = K(\mathbf{u}_i, \mathbf{u}_j), \quad (44)$$

$$\boldsymbol{\varphi}'_q(\mathbf{u}^*) \cdot \boldsymbol{\varphi}'_p(\mathbf{u}^*) = \frac{\partial^2 K(\mathbf{u}_i, \mathbf{u}_j)}{\partial x_{jp} \partial x_{iq}} \Big|_{\mathbf{u}_i=\mathbf{u}_j=\mathbf{u}^*} = K''_{pq}(\mathbf{u}^*, \mathbf{u}^*), \quad (45)$$

then

$$L = -\frac{1}{2} \sum_{i,j=1}^m \lambda_i \lambda_j \gamma_i \gamma_j K(\mathbf{u}_i, \mathbf{u}_j) + \sum_{i=1}^m \lambda_i + \frac{1}{2} \sum_{p,q=1}^n \gamma_p \gamma_q \left[K''_{qp}(\mathbf{u}^*, \mathbf{u}^*) - \frac{2c_q}{c_h} K''_{hp}(\mathbf{u}^*, \mathbf{u}^*) + \frac{c_p c_q K''_{hh}(\mathbf{u}^*, \mathbf{u}^*)}{c_h^2} \right]. \quad (46)$$

And plugging (40) into (42) yields

$$\sum_{i=1}^m \lambda_i \gamma_i \left[\boldsymbol{\varphi}(\mathbf{u}_i) \cdot \boldsymbol{\varphi}'_p(\mathbf{u}^*) - \frac{c_p}{c_h} \boldsymbol{\varphi}(\mathbf{u}_i) \cdot \boldsymbol{\varphi}'_h(\mathbf{u}^*) \right] + \sum_{q=1}^n \gamma_q \left[\boldsymbol{\varphi}'_q(\mathbf{u}^*) \cdot \boldsymbol{\varphi}'_p(\mathbf{u}^*) - \frac{c_p \boldsymbol{\varphi}'_q(\mathbf{u}^*) \cdot \boldsymbol{\varphi}'_h(\mathbf{u}^*)}{c_h} - \frac{c_q \boldsymbol{\varphi}'_h(\mathbf{u}^*) \cdot \boldsymbol{\varphi}'_p(\mathbf{u}^*)}{c_h} + \frac{c_p c_q \boldsymbol{\varphi}'_h(\mathbf{u}^*) \cdot \boldsymbol{\varphi}'_h(\mathbf{u}^*)}{c_h^2} \right] = 0, \quad p = 1, 2, \dots, n, p \neq h.$$

With (45) and

$$\boldsymbol{\varphi}(\mathbf{u}_i) \cdot \boldsymbol{\varphi}'_p(\mathbf{u}^*) = \frac{\partial K(\mathbf{u}_i, \mathbf{u}_j)}{\partial x_{jp}} \Big|_{\mathbf{u}_j=\mathbf{u}^*} = K'_p(\mathbf{u}_i, \mathbf{u}^*), \quad (48)$$

the additional constraints become

$$\sum_{i=1}^m \lambda_i \gamma_i \left[K'_p(\mathbf{u}_i, \mathbf{u}^*) - \frac{c_p}{c_h} K'_h(\mathbf{u}_i, \mathbf{u}^*) \right] + \sum_{q=1}^n \gamma_q \left[K''_{qp}(\mathbf{u}^*, \mathbf{u}^*) - \frac{c_p K''_{qh}(\mathbf{u}^*, \mathbf{u}^*)}{c_h} - \frac{c_q K''_{hp}(\mathbf{u}^*, \mathbf{u}^*)}{c_h} + \frac{c_p c_q K''_{hh}(\mathbf{u}^*, \mathbf{u}^*)}{c_h^2} \right] = 0, \quad p = 1, 2, \dots, n, p \neq h. \quad (49)$$

Then, the dual problem is

$$\begin{aligned} \min \quad & \frac{1}{2} \sum_{i,j=1}^m \lambda_i \lambda_j \gamma_i \gamma_j K(\mathbf{u}_i, \mathbf{u}_j) - \sum_{i=1}^m \lambda_i - \frac{1}{2} \sum_{p,q=1}^n \gamma_p \gamma_q \left[K''_{qp}(\mathbf{u}^*, \mathbf{u}^*) - \frac{2c_q}{c_h} K''_{hp}(\mathbf{u}^*, \mathbf{u}^*) + \frac{c_p c_q K''_{hh}(\mathbf{u}^*, \mathbf{u}^*)}{c_h^2} \right], \\ \text{s.t.} \quad & \sum_{i=1}^m \gamma_i \lambda_i = 0, \\ & \sum_{i=1}^m \lambda_i \gamma_i \left[K'_p(\mathbf{u}_i, \mathbf{u}^*) - \frac{c_p}{c_h} K'_h(\mathbf{u}_i, \mathbf{u}^*) \right] \end{aligned}$$

$$\begin{aligned}
& + \sum_{q=1}^n \gamma_q \left[K''_{qp}(\mathbf{u}^*, \mathbf{u}^*) - \frac{c_p K''_{qh}(\mathbf{u}^*, \mathbf{u}^*)}{c_h} - \frac{c_q K''_{hp}(\mathbf{u}^*, \mathbf{u}^*)}{c_h} + \frac{c_p c_q K''_{hh}(\mathbf{u}^*, \mathbf{u}^*)}{c_h^2} \right] = 0, \quad p = 1, 2, \dots, n, \quad p \neq h, \\
& \lambda_i \geq 0, \quad i = 1, 2, \dots, m.
\end{aligned} \tag{50}$$

Because $\hat{g}(\mathbf{U})$ should pass through the MPP \mathbf{u}^* , we can use $\hat{g}(\mathbf{u}^*) = 0$ to find the bias b . Using $\hat{g}(\mathbf{u}^*) = \mathbf{w} \cdot \boldsymbol{\varphi}(\mathbf{u}^*) + b = 0$ and (40), we obtain

$$\begin{aligned}
b &= -\mathbf{w} \cdot \boldsymbol{\varphi}(\mathbf{u}^*) \\
&= -\sum_{i=1}^m \gamma_i \lambda_i K(\mathbf{u}^*, \mathbf{u}_i) \\
&\quad - \sum_{p=1}^n \gamma_p \left[K'_p(\mathbf{u}^*, \mathbf{u}^*) - \frac{c_p K'_h(\mathbf{u}^*, \mathbf{u}^*)}{c_h} \right].
\end{aligned} \tag{51}$$

The approximated limit-state function is then given by

$$\begin{aligned}
\hat{g}(\mathbf{U}) &= \mathbf{w} \cdot \boldsymbol{\varphi}(\mathbf{U}) + b = \sum_{i=1}^m \lambda_i \gamma_i [K(\mathbf{U}, \mathbf{u}_i) \\
&\quad - K(\mathbf{u}^*, \mathbf{u}_i)] \\
&\quad + \sum_{p=1}^n \gamma_p \left\{ [K'_p(\mathbf{U}, \mathbf{u}^*) - K'_p(\mathbf{u}^*, \mathbf{u}^*)] \right. \\
&\quad \left. - \frac{c_p [K'_h(\mathbf{U}, \mathbf{u}^*) - K'_h(\mathbf{u}^*, \mathbf{u}^*)]}{c_h} \right\}.
\end{aligned} \tag{52}$$

3.4. Step 4: Probability Evaluation. Once $\hat{g}(\mathbf{U})$ is available, a reliability analysis method can be used to estimate the probability of failure p_f . Since $\hat{g}(\mathbf{U})$ is cheaper to compute, we can afford a large number of function calls to maintain higher accuracy. We can therefore use importance sampling (IS) or the direct Monte Carlo simulation. If IS is selected, the probability of failure is computed with (11).

4. Integration of SORA and SVM Method for Reliability Analysis

A typical model of a probabilistic design is given by

$$\begin{aligned}
& \text{Minimize: } f(\mathbf{d}, \mathbf{X}, \mathbf{P}), \\
& \text{Design Variable: } \mathbf{d}, \boldsymbol{\mu}_X, \\
& \text{Subject to: } \Pr\{g_t(\mathbf{d}, \mathbf{X}, \mathbf{P}) \geq 0\} \geq R_t, \\
& \quad \quad \quad t = 1 \sim T,
\end{aligned} \tag{53}$$

where f is an objective function, \mathbf{d} is the vector of deterministic design variables, \mathbf{X} is the vector of random design variables, \mathbf{P} is the vector of random design parameters,

$\Pr\{g_t(\mathbf{d}, \mathbf{X}, \mathbf{P}) \geq 0\} \geq R_t$, $t = 1 \sim T$, are constraint functions, R_t are the desired probabilities of constraint satisfaction, and T is the number of constraints. The design variables are \mathbf{d} and the means ($\boldsymbol{\mu}_X$) of the random design variables \mathbf{X} .

4.1. Sequential Optimization and Reliability Assessment (SORA). The conventional reliability-based optimization employs a double-loop strategy. The outer loop is to solve the optimization problem, and the inner loop is for reliability analysis. The total number of function evaluations will be huge. However, the SORA method decouples the reliability analysis and optimization completely.

In SORA, an equivalent model to the probabilistic constraints in (53) with performance measure approach is given by

$$g_t^R(\mathbf{d}, \mathbf{X}, \mathbf{P}) \geq 0, \quad t = 1 \sim T, \tag{54}$$

where g^R is the R -percentile of $g(\mathbf{d}, \mathbf{X}, \mathbf{P}) \geq 0$; namely,

$$\Pr\{g(\mathbf{d}, \mathbf{X}, \mathbf{P}) \geq g^R\} = R. \tag{55}$$

It indicates that the probability of $g(\mathbf{d}, \mathbf{X}, \mathbf{P})$ greater than or equal to the R -percentile g^R is exactly equal to the desired reliability R . Using the inverse MPP search algorithm, the optimum solution MPP \mathbf{u}_{MPP} can be identified and the desired R percentile is evaluated by

$$g^R = g(\mathbf{u}_{\text{MPP}}) = g(\mathbf{x}_{\text{MPP}}, \mathbf{p}_{\text{MPP}}). \tag{56}$$

Then, the design model (1) is rewritten as

$$\begin{aligned}
& \text{Minimize: } f(\mathbf{d}, \mathbf{X}, \mathbf{P}), \\
& \text{Design Variable: } \mathbf{d}, \boldsymbol{\mu}_X, \\
& \text{Subject to: } g_t^R(\mathbf{d}, \mathbf{X}_{\text{MPP}t}, \mathbf{P}_{\text{MPP}t}) \geq 0, \\
& \quad \quad \quad t = 1 \sim T.
\end{aligned} \tag{57}$$

The concept of SORA method is shown in Figure 5. The optimization in the first cycle is just a deterministic optimization. Then, the reliability analysis is implemented for the deterministic optimum solution to locate the MPP that corresponds to the desired R level. In Cycle 2, the constraints are modified to shift the MPP onto the deterministic boundary to help insure the feasibility of the probabilistic constraint. The new constraints are

$$g_t(\mathbf{d}, \boldsymbol{\mu}_X - \mathbf{s}_t, \mathbf{p}_{\text{MPP}}) \geq 0, \tag{58}$$

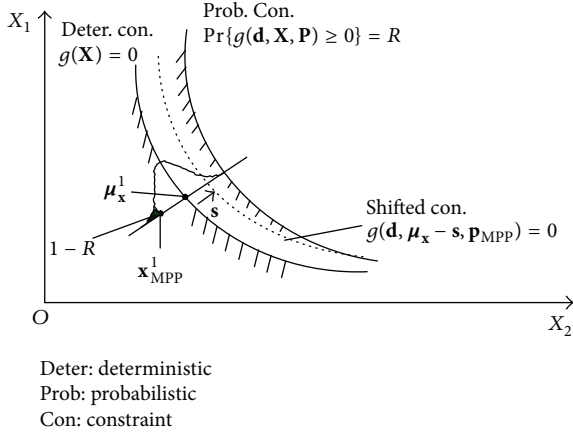


FIGURE 5: Shifting constraint boundary [22].

where \mathbf{s} is the shifting vector as $\mathbf{s}_t = \boldsymbol{\mu}_x^1 - \mathbf{x}_{MPPt}^1$. The superscript 1 means the first cycle.

The reliabilities of those violated probabilistic constraints will improve remarkably using this MPP shifting strategy. After the optimization in Cycle 2, the reliability assessment of Cycle 2 is conducted to find the updated MPPs and to check the design feasibility. If some probabilistic constraints are still not satisfied, the procedure is repeated cycle by cycle until the objective converges and the reliability requirement is achieved when all the shifting distances become zero. Since the SORA method requires much less optimization iterations and reliability assessments to converge, the overall efficiency is high.

4.2. Integration of SORA and Improved Reliability Analysis.

FORM is employed in SORA for reliability analysis. To improve the precision of reliability-based optimization for the highly nonlinear problem, we integrated the improved SVM-based reliability analysis into SORA. The flowchart of this optimization strategy is provided in Figure 6. Firstly, the SORA is operated to find the optimal solution, which satisfies the constraint requirement with the FORM for reliability analysis. Then, the optimal solution is verified by the improved SVM-based reliability analysis. If the approximation for the constraint in SORA could satisfy the accuracy requirement, the procedure stops. Otherwise, the SORA performs again to search a better result in feasible region after reliability index modification, until all the constraints satisfy the reliability requirement and the accuracy is satisfied. The details of the procedure are provided below.

4.2.1. SORA. SORA is the first step in the optimization procedure. The optimal solution $\{\mathbf{d}^{SORA}, \boldsymbol{\mu}_x^{SORA}\}$ and its MPP location \mathbf{u}_{MPP} are found, which satisfy the requirement of reliability R with the FORM for reliability analysis.

Performance measure approach is used in SORA, the R percentile of optimal solution g^R is greater than or equal 0. If g^R is equal to 0, it means the constraint is active. If g^R is greater than 0, it means the constraint is inactive; that is, the design could move towards the constraint more.

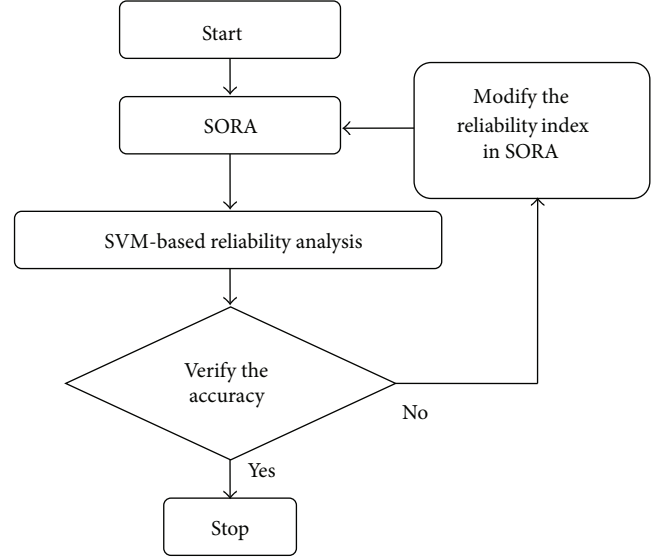


FIGURE 6: Integration of SORA and improved reliability analysis.

4.2.2. SVM-Based Reliability Analysis and Check Accuracy.

After SORA, the optimal solution $\{\mathbf{d}^{SORA}, \boldsymbol{\mu}_x^{SORA}\}$ is verified by the improved SVM-based reliability analysis, and its reliability R_{SVM} is achieved. Then, R_{SVM} should be compared to the required reliability R to check the accuracy of linearization approximation in SORA.

If the verification results show that accuracies of reliability analysis satisfy the requirement, namely, $\|R_{SVM} - R\|/R$ is little enough, the procedure stops. If not, the SORA performs again to search a better result in feasible region after reliability index modification, until all the constraints satisfy the reliability requirement.

4.2.3. Reliability Index Modification in SORA. SORA is based on the FORM for reliability analysis. β_{SORA} indicates the reliability index corresponding to the desired reliability R in SORA, which is used to search the inverse MPP. Therefore, the reliability index is modified in the optimization instead of the reliability R . The new β_{SORA} in the next iteration is given by

$$\beta_{SORA}^{New} = \beta_{SORA} \cdot \frac{\beta}{\beta_{SVM}}, \quad (59)$$

where β_{SVM} is a generalized reliability index, evaluated with the reliability R_{SVM} as follows:

$$\beta_{SVM} = \Phi^{-1}(R_{SVM}). \quad (60)$$

Then, the SORA method is operated again with the new β_{SORA} and starts searching at last optimal solution. Since the new optimization is just to search a better design for a higher accuracy of reliability analysis based on the last optimal solution, only several iterations are needed for convergence.

5. Examples

5.1. Example 1-A: Two-Dimensional Function. In this mathematical example, the optimization problem is defined by

$$\begin{aligned}
& \text{Minimize: } f = -(X_1 + X_2), \\
& \text{Design variables: } X_1, X_2, \\
& \text{Subject to: } \Pr \{g = X_1^2 + X_2^2 - 2X_1X_2 - \sqrt{2}(X_1 + X_2) + 6 < 0\} < 1.0 \times 10^{-3},
\end{aligned} \tag{61}$$

where X_1 and X_2 follow the standard normal distribution. Their design intervals are $[-4, 4]$.

According to [32], the number of training points is gradually increased around the MPP used to create the SVM surrogate models with gradient information for this optimal design. Then, a second order polynomial kernel ($d = 2$) and 50 training points could be used for this two-dimensional nonlinear problem. For making the training points closer to the limit-state boundary, these points are generated with truncated normal distributions in rotated U' -space. A larger truncation for U'_2 than that for U'_1 is used to shrink the samples in the U'_2 direction. The distances are $\Delta_1 = 1.0$ and $\Delta_2 = 0.25$, respectively.

The SORA method is operated to solve this probabilistic optimization followed by the improved SVM-based reliability analysis and modification. Because the proposed SORA + SVM method relies on random samples, the optimization procedure runs 5 times with different random seed numbers to ensure a meaningful comparison.

The results of the first step SORA with $P_{f,\text{SORA}} < 1.0 \times 10^{-3}$ are shown in Line 2 of Table 1. The optimal solutions are $(-0.638, -0.638)$ and the objective is $f = 1.276$. Take the first SORA + SVM optimization procedure as an example. After verification by the improved SVM-based reliability analysis, the probability of failure of the optimal design in SORA is $P_{f,\text{SVM}} = 3.48 \times 10^{-4}$. Not only does it meet the requirements of reliability, but there is a surplus. The design point could be closer to the constraint boundary. It is necessary to modify the reliability index and operate SORA again to search for a better result in the feasible region. After 3 iterations, the final optimal solutions are given in Line 3 of Table 1. It shows that a smaller objective is found in the feasible region by the improved sequential optimization strategy. During the SVM construction in this example, 3 or 4 support vectors are derived.

Monte Carlo simulation is chosen as a benchmark for the comparison of results of these two optimization strategies ((1) only SORA; (2) SORA + SVM). A large sample size of 10^8 is used for each of MCS run. As depicted in Table 1, the error of $P_{f,\text{SORA}}$ is 189.9%. That is because FORM used in SORA just linearizes the limit-state function at the MPP. However, this problem is nonlinear. The error of $P_{f,\text{SVM}}$ for the same design point analyzed with SVM is just 0.8%. After 3 iterations with modifications of the reliability index, the minimum objective $f = -0.318$ is achieved. And, in the last iteration, SORA is operated with $P_{f,\text{SORA}} < 2.78 \times 10^{-3}$ for correcting the error of FORM.

The results of other SORA + SVM optimization procedures with different random seed numbers are listed in Lines 4–7 of Table 1. These optimal solutions are very close to the

first one. The maximum error of $P_{f,\text{SVM}}$ is 6.38% compared to Monte Carlo simulation, and the minimum is only -1.96% .

5.2. Example 2-A: Light Aircraft Wing. For an aircraft wing design, the differences between design and real flight are mainly due to uncertainties in the structural geometry, material properties, operation conditions, and so on. Reliability-based design for the wing structure could reduce the risk and cost. In this subsection, the structure of a light aircraft wing is optimized with the proposed reliability-based optimization strategy [33]. The structural design aims to reduce structural weight by selecting the proper size of structural components to meet the requirements on allowable stresses, deformation limitations, and others.

The basic design requirements for the aircraft are that the takeoff weight of the aircraft is around 700 kg, the flight attitude is about 3000 m, the cruise speed is around 200 km/h, and the external shape of the wing is rectangular. The structure model of the wing is shown in Figure 7. The aspect ratio is 8.0; the reference area is 10 m^2 ; and maximum thickness to chord ratio of the airfoil is 12%. The wing is structurally divided into 7 sections along the wingspan. Each section is a single box beam that consists of several components including the spar caps, the front shear web, the rear shear webs, and the skin. For each section, the bending stress in the spars, the shear stress in the skin, the shear stress in the front and rear webs, and the wing twist deformation are calculated using the beam theory [34].

The wing structure is subject to the aerodynamic loads. Since the light aircraft flies at a subsonic speed and its wing span ratio is relatively large, the lifting line method is used to predict the aerodynamic characteristics, including lift distributions, lift coefficients, and induced drag. The aerodynamic lift distributions are represented by a cubic polynomial function with the coefficients $[0.52544, -0.33753, -1.04033, -1.30315]$. The total drag is the sum of induced drag and parasite drag. In this problem, the parasite drag coefficient is assumed to be 0.015.

In this structural optimization problem, the objective is to minimize the structural weight of the aircraft wing W . The areas of spar caps at each section can be different while the thickness of the skin at each section remains the same. There are 10 design variables $\mathbf{X} = (X_1, X_2, \dots, X_{10})$, where X_i ($i = 1, 2, \dots, 7$) is the area of spar cap in section and X_8, X_9, X_{10} are the thickness of the skin, the front web, and the rear web, respectively. These design variables and their lower and upper bounds are given in Table 2. Because of the manufacturing error, the design variables are supposed to follow the normal distribution, and the coefficient of variation is 0.05. Moreover, considering the uncertainty of flight condition, two parameters are supposed to be normal

TABLE 1: Results of the mathematical example.

	X_1	X_2	f	$P_{f,MCS}$	$P_{f,SORA}$	$P_{f,SVM}$	Error _{SORA}	Error _{SVM}
SORA	-0.6380	-0.6380	1.276	3.45×10^{-4}	1.00×10^{-3}	3.48×10^{-4}	189.9%	0.8%
SORA + SVM1	0.1590	0.1590	-0.318	1.01×10^{-3}	2.78×10^{-3}	9.74×10^{-4}	177.2%	3.5%
SORA + SVM2	0.1615	0.1615	-0.3230	1.02×10^{-3}	2.79×10^{-3}	1.00×10^{-3}	173.53%	-1.96%
SORA + SVM3	0.1703	0.1703	-0.3407	1.05×10^{-3}	2.89×10^{-3}	1.01×10^{-3}	175.24%	-3.81%
SORA + SVM4	0.1437	0.1437	-0.2874	0.94×10^{-3}	2.58×10^{-3}	1.00×10^{-3}	174.47%	6.38%
SORA + SVM5	0.1509	0.1509	-0.3017	0.97×10^{-3}	2.66×10^{-3}	1.00×10^{-3}	173.10%	2.67%

TABLE 2: Design variables of wing.

Design variables	X_1, X_2, \dots, X_7 (mm ²)	X_8 (mm)	X_9 (mm)	X_{10} (mm)	W (kg)	g^R
Lower value	50.0	1.0	1.0	1.0	—	—
Upper value	700.0	2.0	1.0	2.0	—	—
Origin design	300.0	1.5	1.5	1.5	88.529	1.125
Optimal design	50, 56.5, 125.6, 221.0, 341.4, 483.8, 642.3	1.0	1.0	1.0	63.975	0.965

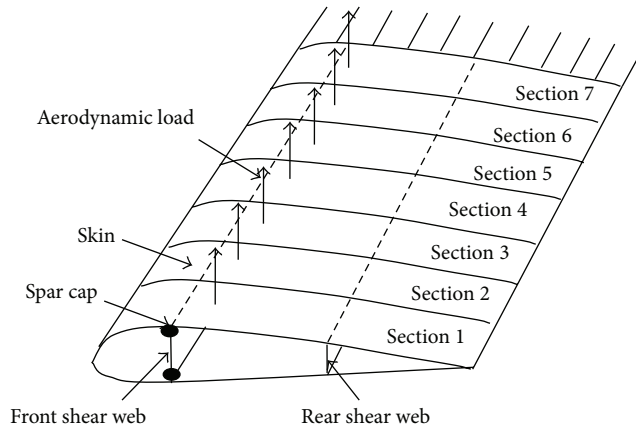


FIGURE 7: The wing structure model [33].

random variables including the flight speed $V \sim N(200, 20)$ and the flight altitude $H \sim N(3000, 300)$.

This optimization problem contains eleven constraints. The bending stresses in the spar cap for each section σ_i ($i = 1, 2, \dots, 7$) should be less than the bending strength of the material S_1 . The maximum shear stress in the skin τ_{skin} should be less than the shear strength of the skin S_2 . The shear stress in the front web τ_{fw} and the shear stress in the rear web τ_{rw} should be less than the shear strength of the spar web S_3 . $[S_1, S_2, S_3]$ is given by $[450, 200, 200]$ MPa. θ is the twist deformation of the wing under the aerodynamic loads, and the allowable twist deformation is a random parameter with $\theta_0 \sim N(2, 0.2)$. The required reliability of this probabilistic constraint is 0.9987 corresponding to a reliability index $\beta = 3$.

Then, the reliability-based wing optimization problem is modeled as

$$\begin{aligned}
 &\text{Given: } H \sim N(3000, 300), V \sim N(200, 20), \theta_0 \sim N(2, 0.2), \\
 &\text{Design variables: } \mathbf{X} = (X_1, X_2, \dots, X_{10}), \text{ coefficient of variation is } 0.05, \\
 &\text{Minimize: } W, \\
 &\text{Subject to: } \Pr \{g = \theta_0 - \theta \geq 0\} \geq 0.9987, \\
 &\quad S_1 - \sigma_i \geq 0, \quad (i = 1, 2, \dots, 7), \\
 &\quad S_2 - \tau_{skin} \geq 0, \\
 &\quad S_3 - \tau_{fw} \geq 0, \quad S_3 - \tau_{rw} \geq 0.
 \end{aligned} \tag{62}$$

The structural optimization of wing is solved by the SORA method with $\beta = 3$ ($R = 0.9987$) at first. The optimal design is listed in Table 2 as well. The weight of wing is reduced. As

shown in the table, the R percentile of optimal solution g^R is 0.965, larger than 0. It indicates that the reliability for this constraint is larger than the required one, and the constraint

TABLE 3: Reliability analysis of optimal solution.

	R_{SORA}	R_{SVM}	$P_{f,\text{SORA}}$	$P_{f,\text{SVM}}$	$P_{f,\text{MCS}}$	Error _{SORA}	Error _{SVM}
SORA + SVM1	0.99870	0.99869	1.30×10^{-3}	1.31×10^{-3}	1.36×10^{-3}	-4.41%	-3.68%
SORA + SVM2	0.99870	0.99866	1.30×10^{-3}	1.34×10^{-3}	1.36×10^{-3}	-4.41%	-1.47%
SORA + SVM3	0.99870	0.99871	1.30×10^{-3}	1.29×10^{-3}	1.36×10^{-3}	-4.41%	-5.15%
SORA + SVM4	0.99870	0.99858	1.30×10^{-3}	1.42×10^{-3}	1.36×10^{-3}	-4.41%	4.41%
SORA + SVM5	0.99870	0.99870	1.30×10^{-3}	1.30×10^{-3}	1.36×10^{-3}	-4.41%	-4.41%

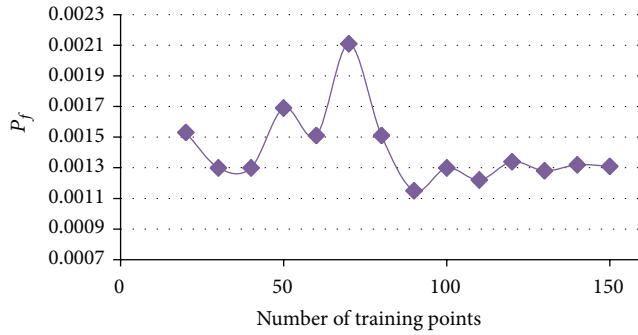


FIGURE 8: Convergence test.

is not active. The improved SVM-based reliability analysis is used to verify the accuracy. Gaussian kernel function ($\sigma = 10$) is chosen in this problem.

Before verification of the optimal design of SORA, we gradually increase the number of training points around the MPP used to create the SVM surrogate models with gradient information for this optimal design. Figure 8 depicts the process of convergence. As shown in the figure, when the number of training points is larger than 100, the fluctuation of curve trends to be gentle. Therefore, 120 training points are used to construct the SVM surrogate models.

The improved SVM-based reliability analysis result is $R_{\text{SVM}} = 0.99869$, which is quite close to the required R . It demonstrates that the FORM in the SORA for reliability analysis satisfies the accuracy requirement. The modification for β and further searching are not needed.

Reliability of the optimal design was analyzed with the improved SVM-based reliability analysis method for 5 times with different random seed numbers to ensure a meaningful comparison. During the SVM construction in this example, 11–17 support vectors are derived. Monte Carlo simulation with 10^6 sample points is also used as a benchmark for the comparison of results of these two optimization strategy for this example. The comparison results are given in Table 3. Since the required reliability is very close to 1, the probability of failure P_f is chosen for comparison in order to reflect the accuracy of the two methods more clearly. As shown in the table, both the errors of SORA (based on FORM) and the improved SVM-based reliability analysis are very small. The error of SORA is only -4.41%. The largest error of the improved SVM-based reliability analysis is -5.15%, and the smallest is only -1.47%. It indicates that the constraint function for the twist deformation of wing is linear in this problem. And the error of the improved SVM-based

reliability analysis is quite small. It declares that the accuracy of this method is high, and it could be applied in both of the linear and nonlinear problems.

In this wing design example, the original function evaluates 438 times in SORA and 558 times in the SORA + SVM. The reliability analysis based on SVM surrogate model runs quite fast. If the Monte Carlo simulation is used to verify the accuracy of SORA, 10^6 sample points are needed. Therefore, computational cost of the proposed optimization strategy is moderate.

6. Conclusion

In this work, a reliability analysis method based on SVM (support vector machine) and MPP (Most Probable Point) is proposed. SVM is employed to create a surrogate model of the limit-state function at the MPP. The gradient information at the MPP is used to guarantee that the surrogate model passes through the MPP and that the surrogate model is tangent to the limit-state function at the MPP. This can greatly improve the sampling efficiency and improve the accuracy of the surrogate model.

Then, the SORA (Sequential Optimization and Reliability Assessment) and SVM-based reliability analysis are integrated. The SORA decoupled the traditional double-loop reliability optimization into a single loop strategy. SVM-based reliability analysis is used to amend the error from linear approximation for limit-state function in SORA.

The mathematical example demonstrates that SVM-based reliability analysis is more accurate than the FORM (in SORA) and more efficient than the direct Monte Carlo simulation. The proposed reliability-based optimization is applied to a simplified wing structure design under these uncertainties as well. Results show that the weight of the wing is reduced and that all deterministic and probabilistic constraints are satisfied. These examples indicate that accuracy of the proposed SVM-based reliability analysis is high for either linear or nonlinear problem. And the proposed optimization strategy is accurate and its computational cost is moderate.

There are, however, some potential problems associated with the MPP-based SVM method. If multiple MPPs exist, the method could be remedied by incorporating the multiple MPPs in the SVM implementation. Similar to the other SVM methods, it is not straightforward to determine the parameters for a kernel function, for example, the order of a polynomial kernel and the standard deviation of a Gaussian kernel. If the dimension, or the number of random variables, is large, the MPP-based SVM method may not be as good

as the MPP-based importance sampling method because a large number of training points will be required to generate an accurate surrogate model.

Nomenclature

b :	Bias
c :	Gradient of limit-state function at the MPP
d :	Vector of deterministic design variables
e :	Proportionality factor
F :	Cumulative distribution function
f :	Joint probability density function; objective function
g^R :	R -percentile of $g(\mathbf{X}) \geq 0$
$g(\mathbf{X})$:	Limit-state function in X space
$g(\mathbf{U})$:	Limit-state function in U space
$\hat{g}(\mathbf{U})$:	Approximated limit-state function in U space
H :	Flight altitude
h :	Importance sampling density
I :	Indicator function
$K(\mathbf{x}_i, \mathbf{x}_j)$:	kernel function
L :	Lagrangian function
m :	Number of samples
n :	Length of vector of random variables
N :	Number of samples; standard normal distribution
\mathbf{p} :	Vector of random design parameters
P_f :	Probability of failure
Pdf:	Probability density function
R :	Reliability
R_t :	Desired probability of constraint satisfaction
\mathbf{R} :	Rotation matrix
\mathbf{s} :	Shifting vector
S_1 :	Bending strength
S_2, S_3 :	Shear strength
\mathbf{u}^* :	MPP in U space
\mathbf{U} :	Vector of random variables in U space
U_i :	i th random variable in U space
V :	Flight speed
\mathbf{w} :	Weight vector
W :	Structural weight of the aircraft wing
\mathbf{X} :	Vector of random variables in X space
X_i :	i th random variable in X space
y_i :	i th output
β :	Reliability index
μ :	Mean value of the random design variable
σ :	Parameter in Gaussian kernel, bending stress
λ, γ :	Lagrangian multiplier
Φ :	Standard normal distribution
$\varphi(\mathbf{x})$:	Feature function
∇g :	Gradient of g
Δ :	Truncated interval
τ :	Shear stress
θ :	Twist deformation of the wing.

Conflict of Interests

The authors declare that there is no conflict of interests regarding the publication of this paper.

Acknowledgments

This work is supported by the Intelligent Systems Center at Missouri University of Science and Technology and the University of Missouri Research Board (7116), the National Natural Science Foundation of China (11432007), and the Fundamental Research Funds for the Central Universities (NUAA NS2015098). The supports are gratefully acknowledged.

References

- [1] T. Zang, M. J. Hemsch, M. W. Hilburger et al., "Needs and opportunities for uncertainty-based multidisciplinary design methods for aerospace vehicles," NASA Report TM-2002-211462, 2002.
- [2] M. Allen and K. Maute, "Reliability-based design optimization of aeroelastic structures," *Structural and Multidisciplinary Optimization*, vol. 27, no. 4, pp. 228–242, 2004.
- [3] S. Mahadevan, "Physics-based reliability models," in *Reliability-Based Mechanical Design*, T. A. Cruse, Ed., pp. 197–232, Dekker, New York, NY, USA, 1997.
- [4] A. M. Hasofer and N. C. Lind, "Exact and invariant second-moment code format," *ASCE Journal of the Engineering Mechanics Division*, vol. 100, no. 1, pp. 111–121, 1974.
- [5] R. Rackwitz and B. Flessler, "Structural reliability under combined random load sequences," *Computers & Structures*, vol. 9, no. 5, pp. 489–494, 1978.
- [6] M. Shinozuka, "Basic analysis of structural safety," *Journal of Structural Engineering*, vol. 109, no. 3, pp. 721–740, 1983.
- [7] L. Tvedt, "Distribution of quadratic forms in normal space—application to structural reliability," *Journal of Engineering Mechanics*, vol. 116, no. 6, pp. 1183–1197, 1990.
- [8] Y. Shin, "Improving probabilistic damage tolerance analysis for inspection optimization: possibilistic-probabilistic approach," in *Proceedings of the 12th AIAA/ISSMO Multidisciplinary Analysis and Optimization Conference*, Victoria, Canada, September 2008.
- [9] F. Li and T. Wu, "An importance sampling based approach for reliability analysis," in *Proceedings of the 3rd Annual IEEE Conference on Automation Science and Engineering (CASE '07)*, pp. 956–961, IEEE, Scottsdale, Ariz, USA, September 2007.
- [10] A. Der Kiureghian, H.-Z. Lin, and S.-J. Hwang, "Second-order reliability approximations," *ASCE Journal of Engineering Mechanics*, vol. 113, no. 8, pp. 1208–1225, 1987.
- [11] B. D. Youn and K. K. Choi, "A new response surface methodology for reliability-based design optimization," *Computers and Structures*, vol. 82, no. 2-3, pp. 241–256, 2004.
- [12] P. R. Adduri and R. C. Penmetsa, "Confidence bounds on component reliability in the presence of mixed uncertain variables," *International Journal of Mechanical Sciences*, vol. 50, no. 3, pp. 481–489, 2008.
- [13] J. E. Hurtado and D. A. Alvarez, "Neural-network-based reliability analysis: a comparative study," *Computer Methods in Applied Mechanics and Engineering*, vol. 191, no. 1-2, pp. 113–132, 2001.

- [14] V. N. Vapnik, *The Nature of Statistical Learning Theory*, Springer, New York, NY, USA, 1995.
- [15] J. E. Hurtado, "An examination of methods for approximating implicit limit state functions from the viewpoint of statistical learning theory," *Structural Safety*, vol. 26, no. 3, pp. 271–293, 2004.
- [16] C. M. Rocco and J. A. Moreno, "Fast Monte Carlo reliability evaluation using support vector machine," *Reliability Engineering and System Safety*, vol. 76, no. 3, pp. 237–243, 2002.
- [17] A. Basudhar, S. Missoum, and A. H. Sanchez, "Limit state function identification using Support Vector Machines for discontinuous responses and disjoint failure domains," *Probabilistic Engineering Mechanics*, vol. 23, no. 1, pp. 1–11, 2008.
- [18] H.-S. Li, Z.-Z. Lü, and Z.-F. Yue, "Support vector machine for structural reliability analysis," *Applied Mathematics and Mechanics*, vol. 27, no. 10, pp. 1295–1303, 2006.
- [19] H. Song, K. K. Choi, I. Lee, L. Zhao, and D. Lamb, "Adaptive virtual support vector machine for reliability analysis of high-dimensional problems," *Structural and Multidisciplinary Optimization*, vol. 47, no. 4, pp. 479–491, 2013.
- [20] Y. T. Wu, Y. Shin, R. Sues, and M. Cesare, "Safety-factor based approach for probabilistic-based design optimization," in *Proceedings of the 42nd AIAA/ASME/ASCE/AHS/ASC Structures, Structural Dynamics and Materials Conference and Exhibit*, Seattle, Wash, USA, 2001.
- [21] X. Chen, T. K. Hasselman, and D. J. Neill, "Reliability based structural design optimization for practical applications," in *Proceedings of the 38th AIAA/ASME/ASCE/AHS/ASC Structures, Structural Dynamics and Materials Conference and Exhibit and AIAA/ASME/AHS Adaptive Structural Forum*, pp. 2724–2732, Kissimmee, Fla, USA, April 1997.
- [22] X. Du and W. Chen, "Sequential optimization and reliability assessment method for efficient probabilistic design," *Journal of Mechanical Design*, vol. 126, no. 2, pp. 225–233, 2004.
- [23] M. Rosenblatt, "Remarks on a multivariate transformation," *Annals of Mathematical Statistics*, vol. 23, pp. 470–472, 1952.
- [24] B. C. Lovell and C. J. Walder, "Support vector machines for business application," in *Business Applications and Computational Intelligence*, chapter 14, Idea Group, Hershey, Pa, USA, 2006.
- [25] B. Schölkopf, "Statistical learning and Kernel methods," Tech. Rep. MSR-TR-2000-23, Microsoft Research, 2000.
- [26] N. Cristianini and J. Shawe-Taylor, *An Introduction to Support Vector Machines*, Cambridge University Press, Cambridge, UK, 2000.
- [27] O. Ivanciuc, "Applications of support vector machines in chemistry," *Reviews in Computational Chemistry*, vol. 23, pp. 291–400, 2007.
- [28] Y. Zhang and A. der Kiureghian, "Two improved algorithms for reliability analysis," in *Proceedings of the 6th IFIP WG7.5 Working Conference on Reliability and Optimization of Structural Systems*, Assisi, Italy, September 1994.
- [29] N. L. Johnson and S. Kotz, *Continuous Univariate Distributions—Volume 1*, John Wiley & Sons, New York, NY, USA, 1970.
- [30] R. L. Iman, J. C. Helton, and J. E. Campbell, "An approach to sensitivity analysis of computer models, Part 1. Introduction, input variable selection and preliminary variable assessment," *Journal of Quality Technology*, vol. 13, no. 3, pp. 174–183, 1981.
- [31] M. Lazaro, I. Santamaria, F. Perez-Cruz, and A. Artes-Rodriguez, "Support vector machine for the simultaneous approximation of a function and its derivative," in *Proceedings of the IEEE 13th Workshop on Neural Networks for Signal Processing (NNSP '03)*, pp. 189–198, Toulouse, France, September 2003.
- [32] Y. Wang, X. Yu, and X. Du, "Reliability analysis with SVM and gradient information at MPP" in *Proceedings of the 7th China-Japan-Korea Joint Symposium on Optimization of Structural and Mechanical Systems*, Huangshan, China, June 2012.
- [33] X. Yu and X. Du, "Reliability-based multidisciplinary optimization for aircraft wing design," *Structure and Infrastructure Engineering: Maintenance, Management, Life-Cycle Design and Performance*, vol. 2, no. 3-4, pp. 277–289, 2006.
- [34] D. H. Allen and W. E. Haisler, *Introduction to Aerospace Structural Analysis*, John Wiley & Sons, New York, NY, USA, 1984.

Research Article

Improved Genetic Algorithm with Two-Level Approximation Method for Laminate Stacking Sequence Optimization by Considering Engineering Requirements

Haichao An, Shenyang Chen, and Hai Huang

School of Astronautics, Beihang University, XueYuan Road No. 37, Haidian District, Beijing 100191, China

Correspondence should be addressed to Shenyang Chen; chenshenyan@buaa.edu.cn

Received 25 September 2014; Accepted 30 December 2014

Academic Editor: Marc Dahan

Copyright © 2015 Haichao An et al. This is an open access article distributed under the Creative Commons Attribution License, which permits unrestricted use, distribution, and reproduction in any medium, provided the original work is properly cited.

Laminated composites have been widely applied in aerospace structures; thus optimization of the corresponding stacking sequences is indispensable. Genetic algorithms have been popularly adopted to cope with the design of stacking sequences which is a combinatorial optimization problem with complicated manufacturing constraints, but they often exhibit high computational costs with many structural analyses. A genetic algorithm using a two-level approximation (GATLA) method was proposed previously by the authors to obtain the optimal stacking sequences, which requires significantly low computational costs. By considering practical engineering requirements, this method possesses low applicability in complicated structures with multiple laminates. What is more, it has relatively high dependence on some genetic algorithm control parameters. To address these problems, now we propose an improved GA with two-level approximation (IGATLA) method which includes improved random initial design, adaptive penalty fitness function, adaptive crossover probability, and variable mutation probability, as well as enhanced validity check criterion for multiple laminates. The efficiency and feasibility of these improvements are verified with numerical applications, including typical numerical examples and industrial applications. It is shown that this method is also able to handle large, real world, industrial analysis models with high efficiency.

1. Introduction

Due to the advantages of high strength-to-weight and high stiffness-to-weight ratios, laminated composites have been stimulated for wide use in aerospace structures. Optimization design of the corresponding stacking sequences is indispensable to make efficient use of the material properties [1–5]. For practical laminated structures, however, the basic ply thicknesses are fixed and the available choices of fiber orientation angles are limited to a small set of angles, such as 0° , $\pm 45^\circ$, and 90° . Because of these manufacturing constraints, stacking sequence design then becomes a combinatorial problem of choosing the fiber direction from a permissible set for each ply.

Genetic algorithm (GA) has been preferred extensively to solve this problem [2–4, 6–8] which proves to be well suited for the stacking sequence optimization. With their random nature, genetic algorithms (GAs) could produce a variety

of alternative designs with similar performance in repeated runs [9], providing the designer with a choice of alternatives. However, one major disadvantage of GAs is that they involve high computational costs in the evaluation of chromosomes. So many studies have concentrated on improving GA's efficiency [3, 9–15]. Among these improvements, approximation concepts with the use of lamination parameters combined with GA have been preferred [11, 13, 16]. With lamination parameters, the problems are simplified and computational costs can be effectively reduced. However, specific programming needs to be developed for structural response analyses and optimal designs are limited to particular laminate configurations [17], consequently restricting their utility in practical engineering applications when lamination parameters are applied.

In a recent study, we have proposed a genetic algorithm using a two-level approximation (GATLA) [18] method for optimizing laminates stacking sequences. Essentially,

this approach adopts an optimization strategy that the genetic algorithm is integrated within the sequential approximation optimization problems, without using any intermediate variables. This strategy involves only low computational costs and many near optimal solutions could be easily obtained.

For practical engineering stacking sequence optimizations, more than two laminates need to be optimized simultaneously, as practical aerospace structural components usually comprise multiple panels and the stacking sequences of them can remarkably affect structural mechanical properties like strength and stiffness performances [5, 19]. Even though the GATLA method has been deemed to be able to deal with the optimizations of multiple laminates in simple structures [18], it has not been extended to practical engineering optimizations with multiple laminates. Moreover, the standard GA used in the strategy has relatively high dependence on some genetic parameters, which brings the burden of determining control parameters to the designers or users. Additionally, computational efficiency is another main factor when dealing with optimization problems, especially for large-scale structures. Although the power of the proposed method is undeniable, it seems that there is still space for efficiency improvements.

Thus, in the present study, the main objective is to further improve the performance of this strategy and make it more applicable to address practical engineering problems efficiently. Firstly, the initial design point which was produced randomly was enhanced. Meanwhile, the standard genetic algorithm inside GATLA was modified with a new penalty scheme as well as adaptive crossover probability and variable mutation probability. Moreover, validity check criterion for individual designs when dealing with multiple laminates was also enhanced to further improve the algorithm performance. All of these improvements were firstly verified with numerical examples, and this new strategy was further applied in industrial engineering problems. Significant improvements were obtained with the utilization of these improvements, and the results also showed that this approach could be applied to complicated structures and obtain reasonable stacking sequences with good efficiency.

2. GATLA Method

The basic principles of GATLA method will be briefly described in this section. For more details the reader could refer to the literature [18].

2.1. Problem Formulation. To implement the optimization procedure, a ground laminate with arbitrarily given number of plies and permissible orientations, such as 0° , $\pm 45^\circ$, and 90° , is needed before calculation. The corresponding discrete 0/1 variables will decide whether the ply in the ground laminate should be retained or not, and a continuous thickness variable is set for each layer. The concept of ground laminate is similar to the concept of ground structure proposed in truss topology optimization [20]. By determining the existence and absence of truss elements in

the ground structure, the optimal layout may be obtained. Back to the present study, some plies might be deleted firstly during the discrete-variable optimization. Furthermore, by increasing the ply thickness after the continuous-variable optimization, several plies might be added. Therefore, by deleting and adding plies to the ground laminate, the optimal stacking sequences could be obtained. The thickness variables seem redundant; however, from lots of calculations, the results of problems considering thickness variables are much better than those without thickness variables, which have been demonstrated in [18]. Based on the ground laminate sequence, the optimization problem can be formulated as follows:

$$\begin{aligned} \min \quad & f(X) \\ \text{s.t.} \quad & g_j(X) \leq 0, \quad j = 1, \dots, m \\ & \alpha_i x_i^L + (1 - \alpha_i) x_i^b \leq x_i, \quad i = 1, \dots, n \quad (1) \\ & x_i \leq \alpha_i x_i^U + (1 - \alpha_i) x_i^b \\ & \alpha_i = 0 \quad \text{or} \quad \alpha_i = 1, \end{aligned}$$

where X is the vector of ply thickness variables, α is the vector of discrete 0/1 variables which represent the existence of each ply, n denotes the total number of plies in the ground laminate, m is the number of constraints, $f(X)$ is the objective function, $g_j(X)$ is the j th constraint function, x_i^U and x_i^L are the upper and lower bounds on the i th thickness variable x_i , respectively, and x_i^b is a very small value (usually $0.01 x_i^L$) used to represent the thickness value of a removed ply. For example, if the ground laminate is given as $[(0/\pm 45/90)_{10}]_s$, the total number of plies is 80, and by considering symmetry there are 40 thickness variables ($X = \{x_1, x_2, \dots, x_{40}\}^T$) and 40 discrete variables ($\alpha = \{\alpha_1, \alpha_2, \dots, \alpha_{40}\}^T$). It can be seen that the symmetry constraint can be readily achieved by optimizing only one half of the laminate, and the other half would be obtained symmetrically. If the balanced requirement that the number of $+45^\circ$ plies should be equal to the number of -45° plies is also considered, it can be realized by enforcing the thickness variables of adjacent $+45^\circ$ and -45° plies in the ground laminate to link together. Moreover, it can be observed that the ply angles in the ground laminate should be selected from the permissible small set of angles. In the end of the optimization, the obtained optimal ply thicknesses need to be rounded to meet the requirement that the ply thickness should be integral multiples to the fixed basic ply thickness. To alleviate matrix cracking problems, it is also required that, in the laminate, there should be no more than four contiguous plies with the same fiber orientation, and it is realized with the use of a penalty term in the objective function, which is to be shown in (8). As for the structural response constraints, $g_j(X)$, they are incorporated into the objective function via penalty functions.

2.2. Global Optimization Strategy. The global optimization strategy is introduced based on problem (1). To solve this

problem, firstly, a first-level approximate problem is constructed using the branched multipoint approximate (BMA) function, which is a piecewise function with two branches for conditions when the corresponding ply exists or is absent, respectively. In the p th stage, the first-level approximate problem can be stated as follows:

$$\begin{aligned} \min \quad & f^{(p)}(X) \\ \text{s.t.} \quad & g_j^{(p)}(X) \leq 0, \quad j = 1, \dots, J_1 \\ & \alpha_i x_{i(p)}^L + (1 - \alpha_i) x_i^b \leq x_i, \quad i = 1, \dots, n \end{aligned} \quad (2)$$

$$\begin{aligned} & x_i \leq \alpha_i x_{i(p)}^U + (1 - \alpha_i) x_i^b \\ & \alpha_i = 0 \text{ or } \alpha_i = 1, \\ & x_{i(p)}^U = \min \{x_i^U, \tilde{x}_{i(p)}^U\}, \end{aligned} \quad (3)$$

$$x_{i(p)}^L = \max \{x_i^L, \tilde{x}_{i(p)}^L\}, \quad (4)$$

where $\tilde{x}_{i(p)}^U$ and $\tilde{x}_{i(p)}^L$ are the move limits of x_i at the p th stage, $f^{(p)}(X)$ and $g_j^{(p)}(X)$ are the approximate functions for objective and constraint functions in the p th stage, respectively, which are created by using the BMA function with the information of the primal functions and their corresponding derivatives at multiple known points, and J_1 is the number of active constraints of the original problem (1). The BMA functions take the forms as follows:

$$w^{(p)}(X) = \sum_{t=1}^H \left\{ w(X_t) + \sum_{i=1}^n \tilde{w}_{i,t}(X) \right\} h_t(X), \quad (5)$$

where

$$\tilde{w}_{i,t}(X) = \begin{cases} \frac{1}{r_{o,t}} \frac{\partial w(X_t)}{\partial x_i} x_{it}^{1-r_{o,t}} (x_i^{r_{o,t}} - x_{it}^{r_{o,t}}) & \text{if } \alpha_i = 1 \\ \frac{1}{r_{m,t}} \frac{\partial w(X_t)}{\partial x_i} (1 - e^{-r_{m,t}(x_i - x_{it})}) & \text{if } \alpha_i = 0, \end{cases} \quad (6)$$

$$h_t(X) = \frac{\bar{h}_t(X)}{\sum_{l=1}^H \bar{h}_l(X)}, \quad t = 1, \dots, H,$$

$$\bar{h}_l(X) = \prod_{\substack{s=1 \\ s \neq l}}^H (X - X_s)^T (X - X_s),$$

where $w^{(p)}(X)$ represents the objective function $f^{(p)}(X)$ or the constraint function $g_j^{(p)}(X)$, X_t is the t th known point, and H is the number of points to be counted, bounded previously by H_{\max} . The exponents $r_{o,t}$ and $r_{m,t}$ ($t = 1, \dots, H$) are adaptive parameters used to control the nonlinearity of

the approximation, which can be obtained from the following equations:

$$\begin{aligned} \min \quad & \sqrt{\sum_{k=1}^H \left\{ w(X_k) - w(X_t) - \sum_{i=1}^n \tilde{w}_{i,t}(X_t) \right\}^2} \\ \text{s.t.} \quad & r_o^L \leq r_{o,t} \leq r_o^U, \quad r_m^L \leq r_{m,t} \leq r_m^U, \quad t = 1, \dots, H. \end{aligned} \quad (7)$$

Since the first-level approximate problem involves both continuous and discrete variables, an optimization strategy is then proposed. Discrete variables (0/1 variables which represent the existence of each ply in the ground laminate) are optimized through GA based on the first-level approximation problem, and when calculating the fitness of the population continuous thickness variables of composite laminate layers are optimized (this procedure is named size optimization hereinafter) by solving the dual problem of the second-level approximation, which could significantly reduce the gene code length in the GA and improve the optimization efficiency and accuracy.

The standard GA is used here. During the process of GA, a constrained problem using an exterior penalty function is established firstly as follows:

$$F_1 = \phi^{n_c} \left[f(X^*) + R \sum_{j=1}^{J_2} (\max \{g_j(X^*), 0\})^q \right], \quad (8)$$

where ϕ^{n_c} is treated as a penalty term in the objective function to enforce the requirement that there should be no more than four contiguous plies with the same fiber orientation, which is to alleviate matrix cracking problems; n_c is the exponent of the power, and it represents the number of stacks violating the 4-ply contiguity constraint; $\phi = (10/9)^{0.5}$ is the penalty parameter for this manufacturing constraint; R is the penalty factor, q denotes the penalty exponent (taken as 1 in this work), and $f(X^*)$ and $g_j(X^*)$ are the objective value and constraint values with respect to the optimal thicknesses of given stacking sequences, which are obtained from the process of solving a second-level approximate problem.

By randomly deleting plies from the given ground laminate, an initial population is generated at the beginning of GA [18]. Each individual in the population represents a stacking sequence design, and related ply thickness variables are optimized when the fitness values are calculated. Corresponding to each individual which means a given ply orientation sequence, discrete variables in the first-level approximate problem are fixed and sizing variables of the plies whose corresponding discrete variables are zero will be removed. The deleted plies and related constraints will not exist. The internal sizing (i.e., ply thickness) optimization problem is then established and to address this problem the second-level approximate problem is formed by expanding the objective function and the constraint functions in

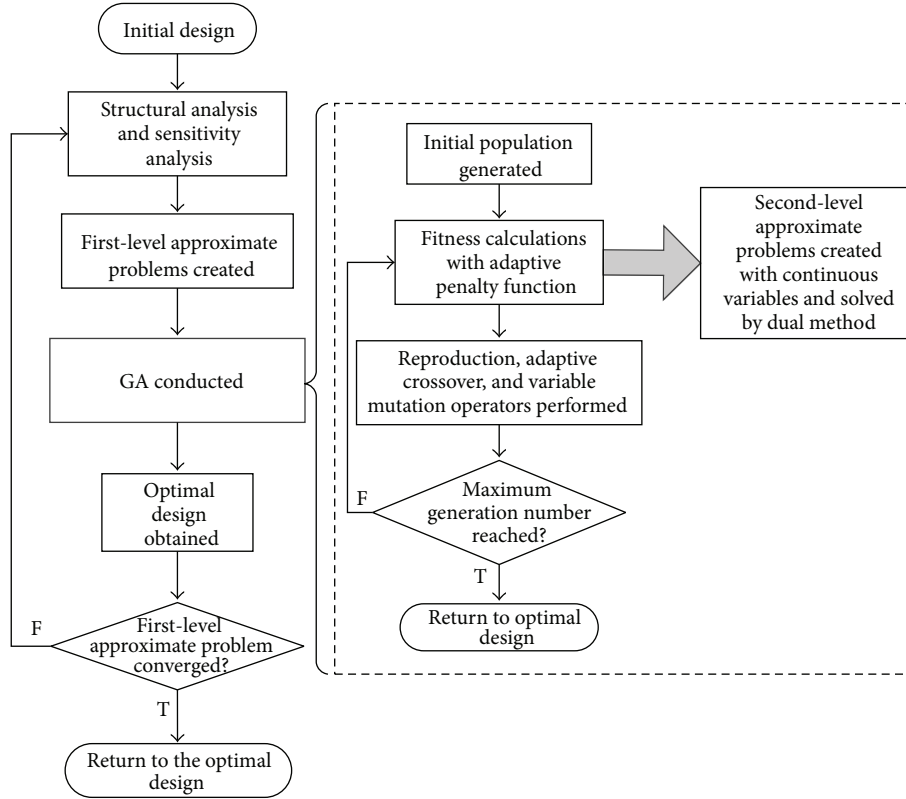


FIGURE 1: Flow chart of global optimization strategy procedure.

the first-level approximate problem into linear Taylor series. In the k th step it is stated as follows:

$$\begin{aligned} \min \quad & f^{(k)}(\bar{X}) = \tilde{f}(\bar{X}_{(k)}) + \sum_{i=1}^I \frac{\partial \tilde{f}(\bar{X}_{(k)})}{\partial \bar{x}_i} (\bar{x}_i - \tilde{x}_{i(k)}) \\ \text{s.t.} \quad & g_j^{(k)}(\bar{X}) = \tilde{g}_j(\bar{X}_{(k)}) \\ & - \sum_{i=1}^I \tilde{x}_{i(k)}^2 \frac{\partial \tilde{g}_j(\bar{X}_{(k)})}{\partial \bar{x}_i} \left(\frac{1}{\bar{x}_i} - \frac{1}{\tilde{x}_{i(k)}} \right) \leq 0, \\ & j = 1, \dots, J_2, \end{aligned} \quad (9)$$

$$\bar{x}_{i(k)}^L \leq \bar{x}_i \leq \bar{x}_{i(k)}^U, \quad i = 1, \dots, I,$$

$$\bar{x}_{i(k)}^U = \min \{x_{i(p)}^U, \tilde{x}_{i(k)}^U\},$$

$$\bar{x}_{i(k)}^L = \max \{x_{i(p)}^L, \tilde{x}_{i(k)}^L\},$$

where $f^{(k)}(\bar{X})$ is the objective function at the k th step, $g_j^{(k)}(\bar{X})$ is the constraint function, $\tilde{f}(\bar{X}_{(k)})$ and $\tilde{g}_j(\bar{X}_{(k)})$ are obtained from the approximate expressions in (2), $\tilde{x}_{i(k)}^U$ and $\tilde{x}_{i(k)}^L$ are the move limits at the k th step, and $\bar{x}_{i(k)}^U$ and $\bar{x}_{i(k)}^L$ are the upper and lower bounds at the k th step.

Dual method is then utilized to deal with the second-level approximate problem. When the second-level approximate

problem converges, the fitness of the population could be obtained and genetic algorithm operators are executed to solve the first-level approximate problem. After that, the design variables and the corresponding structural parameters are modified for the next full structural analysis and sensitivity analysis, and then go to the next design cycle.

The flow chart of the strategy is schematically demonstrated in Figure 1. In the end of the optimization procedure, the optimized ply thicknesses are rounded to meet the requirement that they should be integral multiples to the fixed basic ply thickness, and the layers with small value thickness x_i^b will be removed. The standard GA mentioned previously is replaced with improvement schemes, as shown in Figure 1, which will be described in the next section.

3. Improvements to GATLA Method

3.1. Improved Random Initial Design. As stated in Section 2, the optimization process starts from the arbitrarily given ground laminate, with limited orientations and excessive plies. To produce an initial design based on the ground laminate, in the original GATLA method, each ply in the ground laminate is randomly deleted with a relatively high level of probability, for example, 0.9 or larger. Here, this probability is defined as the deleted-ply percentage for the initial design, designated DPID. However, this random operation will probably produce a design with zero plies kept, or in a slightly better condition, with one or two plies retained in the

ground laminate. Even if the probability to delete each ply is given a smaller value, the case that zero or very few plies are kept is possible to happen.

In order to avoid the producing of the initial design with few plies, here, this random design process is improved. Firstly, the deleted-ply percentage for the initial design, that is, DPID, is multiplied by the total number of plies in the ground laminate, and the obtained product value is rounded to nearest integer. Next, each ply in the ground laminate is randomly deleted as before with the given probability. The number of removed plies is counted, and this amount is then compared with the obtained product value. If the amount of deleted plies is less than the rounded product value, this random produced design is identified as an appropriate initial design. Otherwise, if the number of deleted plies is larger, which means too many plies have been deleted from the ground laminate or even no ply is retained, this produced design then adds plies one by one until the amount of deleted plies is fewer than the rounded product value to be identified as an appropriate initial design. For example, when the ground laminate is $[(0/\pm 45/90)_{10}]_s$ and DPID is given as 0.9, the number of removed plies from the ground laminate should not be more than 72, that is, 80×0.9 . If the generated initial design is $[0/\pm 45/0/90/\pm 45]_s$, the number of kept plies is 14, and that of the removed plies is 66. So this design could be identified as an appropriate initial design to go to the next optimization step. However, if the random produced design is $[0/\pm 45]_s$, the amount of deleted plies is then 74, which is larger than 72. Then add plies to this design to generate an appropriate one that meets the requirement. For instance, $[0/\pm 45/0]_s$ gets valid after adding 0-degree layer to the original design.

3.2. New Penalty Scheme in Objective Function. Optimization problems with constraints must be transformed into unconstrained ones as GA is an unconstrained optimization method. In the original GATLA, an exterior penalty function is used to achieve this. As is formulated in (8), penalty control parameters R and q are predefined constants and need to be adjusted according to different optimization problems. The appropriate selection of these parameters plays a crucial role in determining the computational efficiency.

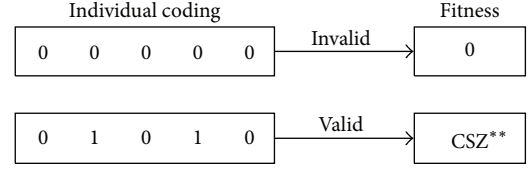
Though various specific penalty schemes have been proposed (see the introduction in [21]), Barbosa and Lemonge developed an adaptive penalty function without any type of user defined penalty parameter. The objective function proposed with an adaptive penalty is written as

$$F(X^*) = \begin{cases} f(X^*) & \text{if } X^* \text{ is feasible,} \\ \bar{f}(X) + \sum_{j=1}^m k_j g_j(X^*) & \text{otherwise,} \end{cases} \quad (10)$$

where

$$\bar{f}(X) = \begin{cases} f(X^*) & \text{if } f(X^*) > \langle f(X) \rangle, \\ \langle f(X) \rangle & \text{otherwise,} \end{cases} \quad (11)$$

$$k_j = \langle f(X) \rangle \frac{\bar{g}_j}{\sum_{l=1}^m [\bar{g}_l]^2},$$



**CSZ: calculated by size optimization

FIGURE 2: One example to illustrate original criterion.

and $\langle f(X) \rangle$ represents the average value of the objective function $f(X)$ over current population, $g_j(X^*)$ is the violation of the j th constraint of the individual design corresponding to X^* , \bar{g}_j is the violation of the j th constraint averaged over the current population, and m is the number of total constraints.

The main feature of this penalty scheme, besides being adaptive and not requiring any predefined parameter, is to automatically define a different penalty coefficient which varies along the run according to the feedback received from the evolutionary process for each constraint. The adaptive scheme also relieves the user from the burden of having to determine, by trial and error, sensitive parameters to cope with every new constrained optimization problem.

Based on this approach, an alternative penalty function was proposed in [22], which also has the same features as (10). Herein, we utilize the consistent type of this formulation [22] but replace the corresponding exponent (i.e., 3) with Figure 2 based on our numerical studies, as established in (12). Furthermore, the optimal design could be considered as the one with the largest possible constraint margin of all individuals of the same objective function [3]. Therefore, a small fraction of the critical constraint value is subtracted from the objective function when all constraints are satisfied. In the present work, the ultimately new form of the unconstrained objective function with adaptive penalty scheme is defined as follows:

$$F_1 = \begin{cases} \phi^{n_c} \left[f(X^*) + \langle f(X) \rangle \right. \\ \quad \cdot \max \{g_1(X^*), \dots, g_{J_2}(X^*)\} \\ \quad \left. \text{if } X^* \text{ is feasible,} \right. \\ \phi^{n_c} \left\{ \bar{f}(X) + \langle f(X) \rangle \right. \\ \quad \cdot \left[\left(1 + \sum_{j=1}^{J_2} \beta_j g_j(X^*) \right)^2 - 1 \right] \\ \quad \left. \text{otherwise,} \right. \end{cases} \quad (12)$$

where

$$\beta_j = \frac{\bar{g}_j}{\sum_{l=1}^{J_2} \bar{g}_l}, \quad (13)$$

and β_j is the violation percent of the j th constraint in the current population. $\phi = (10/9)^{0.5}$ is retained to enforce the 4-ply contiguity constraint and n_c is the total number of same-orientations plies in excess of the four contiguously same-orientation plies. $\varepsilon = 0.001$ is employed here and we add $\langle f(X) \rangle$ to guarantee the small fraction ε is neither too small nor too large with respect to the object function value, which makes the function more adaptive. $g_j(X^*) \leq 0$ when the j th constraint is satisfied and $g_j(X^*) > 0$ otherwise. The new objective function established here could automatically adjust the penalty to the infeasible designs from generation to generation and enhance the search capability to obtain a global optimum or get close to it. This adaptive penalty function enables two control parameters, R and q in (8), not to be given any more.

3.3. Adaptive Crossover and Variable Mutation Probabilities.

In GA, crossover is used to produce new generation by combining a portion of each parent's genetic string and mutation is adopted to add or delete genes by introducing small changes in children created by crossover. The efficiency of GA is often sensitive to the probabilities of crossover and mutation (hereafter referred to as P_c and P_m , resp.) [4], and the choice of both of them critically affects the performance as they are fixed constants in the standard GA. In practice, it is ideal to vary P_c and P_m adaptively by GA itself. Srinivas and Patnaik [23] proposed a method with adaptive probabilities of crossover and mutation to realize the twin goals of maintaining diversity in the population and sustaining the convergence capacity of GA. Moreover, an improved version of adaptive crossover and mutation operators was proposed by Ren and San [24]. The modified expression for P_c is as follows and is utilized in this paper:

$$P_c = \begin{cases} P_{c1} - \frac{(P_{c1} - P_{c2})(f' - f_{ave})}{f_{max} - f_{ave}} & f' \geq f_{ave} \\ P_{c1} & f' < f_{ave} \end{cases} \quad (14)$$

where f_{max} is the maximum fitness value in the population, f_{ave} is the average fitness value in every population, and f' is the larger of the fitness values of the solutions to be crossed. In addition, we set $P_{c1} = 0.9$ and $P_{c2} = 0.6$ for each optimization problem. The modified formulation increases P_c of the individuals with the highest fitness value up to P_{c2} , making the best individual no longer in a stagnant state.

The modified expression for P_m proposed by Ren and San [24] is similar to that in (14), where f' is replaced by f , which is the fitness of an individual. Thus, it means the calculation increases by obtaining the fitness of the current population generated after the crossover operator. Actually, it was observed that the use of relatively high mutation rates at the start of the GA-runs could be an efficient aim at preventing premature convergence [25]. Thereafter, a very simple formulation to reduce the probability of mutation in geometric progression proposed by Leite and Topping [25] is adopted in this paper. By giving the initial probability of

mutation P_{mi} and the final probability of mutation P_{mf} , the coefficient for the reduction of the mutation rate at each generation is determined by

$$r_m = \sqrt[\text{MaxG}]{\frac{P_{mf}}{P_{mi}}}, \quad (15)$$

where MaxG is the maximum number of generations. In this study, we set $P_{mi} = 0.1$ and $P_{mf} = 0.001$ for each optimization problem. Thus, P_c and P_m do not need to be predefined anymore.

3.4. Enhanced Validity Check Criterion for Multiple Laminates.

As is stated in Section 2, the optimization procedure is conducted by adding or deleting plies in the given ground laminate. In the process of GA, with the randomness of the initial population and GA operators, there may be some infeasible designs with invalid coding due to the excess removal of plies. Some individuals of these designs may be able to meet all the constraints after size optimization, that is, solving the second-level approximate problems. However, for designs with seriously overmuch removal of plies, even after the size optimization, they may remain serious constraint violations, consequently affecting the convergence to some extent. So there is no more need to perform the second-level approximation to these individuals and their fitness values could be directly set to be zero, which could improve the algorithm efficiency as a result. With regard to this, in GATLA, a validity check criterion was put forward for each individual coding. The criterion is that, for each encoded design, when the value of deleted plies is less than a certain percentage relative to corresponding ground laminate, this individual coding can be considered as valid and size optimization afterwards is conducted to achieve the fitness calculation; otherwise, this coding is identified to be invalid and zero is diametrically given to its fitness value without further size optimization. The ratio for this earlier stated judgment is defined as the maximum percentage permissible to delete layers, designated as FITP in [18] and this paper. This parameter should be initially given on the basis of ground laminate layers to guarantee the optimal design included. To illustrate this judgmental procedure, an example is shown in Figure 2. The number of plies in a ground laminate is 5, FITP = 0.8, and the coding is considered valid when the deleted plies are fewer than 4 (i.e., 5×0.8).

However, deficiency could occur during the implementation of multiple laminates optimization. For example, if there are two laminates as design domain, one of them may be encoded with [000000] among the population, and the other's coding could be [111010]. Apparently there are 12 plies in the ground laminate, and 8 plies are deleted for this individual. If FITP was given to be 0.8, this coding is identified to be valid according to the original criterion mentioned previously, for 8 is less than 9.6 (i.e., 12×0.8). But no plies are reserved in the first laminate, and obviously this design should be considered invalid. With another three designs, this condition is shown in Figure 3.

Here, in order to overcome this shortcoming, the validity check criterion especially for multiple laminates is enhanced.

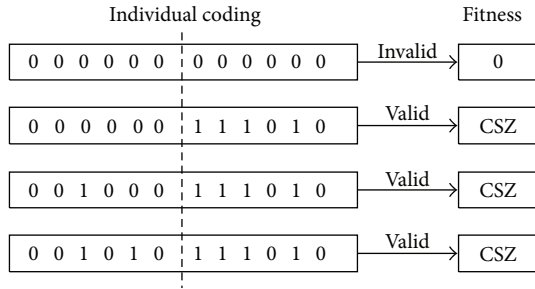


FIGURE 3: Coding judgment using original criterion.

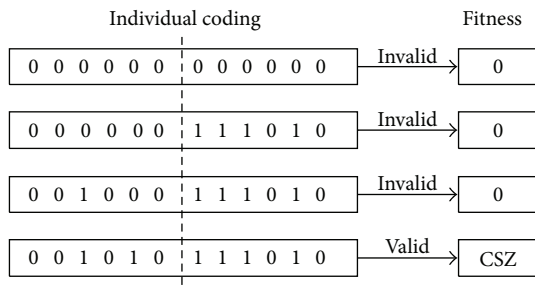


FIGURE 4: Coding judgment using enhanced criterion.

First of all, the original criterion (OC) is implemented to the laminates one by one. When the coding design for each laminate is determined as valid, this individual could possess final validity identification. For the design with two laminates previously mentioned, according to the enhanced criterion (EC), less than 4.8 (i.e., 6×0.8) plies should be removed in each laminate to be judged as valid. See Figure 4 to describe this scheme. It can be easily seen that both original and enhanced criteria are identical for dealing with just one laminate design. These validity checks essentially mean rejecting some designs out of the second-level optimization to improve the algorithm performance.

4. Numerical Examples

Numerical examples are conducted in this section to test the improvements by comparing with the original GATLA method. As the GA is a stochastic process, the algorithm performance will be evaluated in terms of reliability and normalized computation price. In this study, the indicator of the normalized price is the average number of evaluations of the structural analysis divided by the reliability of reaching a practical optimum after 200 independent runs here, while the reliability is defined as the fraction of runs that produced a practical optimum during the 200 repeated runs.

4.1. A Composite Cone-Cylinder Structure. The first example deals with the optimization of symmetric stacking sequences of a composite cone-cylinder structure, as shown in Figure 5, which consists of two composite parts: a conic part and a cylindrical part. The dimensions are $r = 60$ mm, $R = 100$ mm, $a = 100$ mm, and $b = 200$ mm. The two ends of

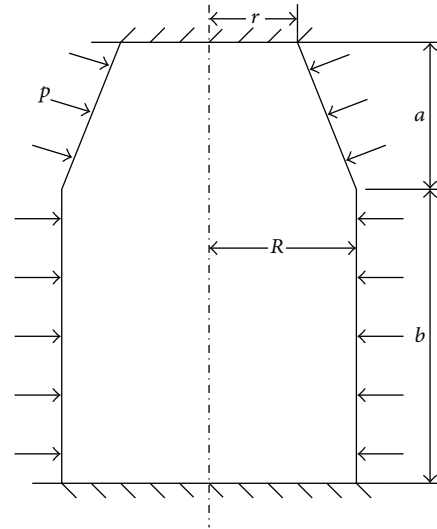


FIGURE 5: Dimensions of cone-cylinder structure.

the structure are fixed, with outer surfaces under a pressure of $p = 0.3$ Mpa. The material is shown in Table 1, and the 0° fiber direction is along the longitudinal direction of the cone and cylinder. The objective is to minimize the weight of the whole structure. The constraints are $f_1 \geq 1700$ Hz and $\lambda_1 \geq 6$, where f_1 is the first-order frequency of the structure and λ_1 is the critical buckling factor, respectively.

The ground laminates were given as $[(0/45/-45)_{10}]_s$ for the conic part and $[(0/45/-45/90)_7/0/45]_s$ for the cylindrical part. Due to the restrictions on the manufacturing process in which the thickness of one layer could not be lower than t , the lower and upper bounds on ply thickness were set as $x_i^L = t$ and $x_i^U = 4t$, and the thickness of a removed ply was $x_i^b = 0.01t$. In addition, DPID = 0.95 and FITP = 0.8. The best designs are known with 6 plies for the conic part and 8 plies for the cylindrical part, both referring to half of the laminates. The practical optima for this problem are designed as the feasible designs within $2.5t$ -ply weights of the cylindrical part for half of both laminates of the global optimum. Some stacking sequences of the practical optima obtained with the proposed strategy are shown in Table 2, with ply thicknesses not rounded. As for the rounded results, they are not discussed in this section when making comparisons between methods.

The performance of the original method (GATLA) and GATLA method with the improvements described previously (IGATLA) was compared based on different population sizes and maximum generation numbers. With 200 runs for each case, the optimization results are shown in Table 3, and, in the GATLA method, the standard GA was used with $P_c = 0.95$ and $P_m = 0.05$, $R = 0.1$. From the results in Table 3, it could be seen that the computation costs could be significantly reduced, and the reliability is increased to a high level of around 90%. For example, in the population size of 20 and maximum generations of 60, the normalized computation price is reduced about 75.4% while the reliability is increased by 21%.

TABLE 1: Material properties.

Property	Example 1	Example 2	Value	Example 4	Example 5
Young's modulus, E_1	128 Gpa	138 Gpa	127.59 Gpa	135 Gpa	160 Gpa
Young's modulus, E_2	13 Gpa	11 Gpa	13.03 Gpa	9.12 Gpa	9.0 Gpa
Shear modulus, G_{12}	6.4 Gpa	6.5 Gpa	6.41 Gpa	5.67 Gpa	4.8 Gpa
Poisson's ratio, ν_{12}	0.3	0.28	0.3	0.31	0.36
Ply thickness, t	0.127 mm	0.125 mm	0.127 mm	0.12 mm	0.08 mm
Density, ρ	1600 kg/m ³	1600 kg/m ³	1577.8 kg/m ³	1600 kg/m ³	1600 kg/m ³

TABLE 2: Practical optima of cone-cylinder structure.

Laminate Co: conic part Cy: cylindrical part	Ply	Weight, kg	f_1 , Hz	λ_b
$[-45_2/0/45/0/45]_s$	(Co)—[12]	0.5622	1713.0	6.0637
$[-45/90/0/45/-45/45/0_2]_s$	(Cy)—[16]			
$[0/45/0/45/-45_2/0]_s$	(Co)—[14]	0.5623	1735.4	6.5342
$[90_2/-45/0/45/-45/45/0]_s$	(Cy)—[16]			
$[45_2/0/-45/45_2/-45]_s$	(Co)—[14]	0.5623	1702.2	6.9326
$[90/-45/90/0/45/0/-45/0]_s$	(Cy)—[16]			
$[45_2/0/45/0/-45/45]_s$	(Co)—[14]	0.5723	1738.1	6.9188
$[90/45/-45/0/45/-45/45/0]_s$	(Cy)—[16]			
$[45_2/-45_2/0/45]_s$	(Co)—[12]	0.5403	1709.2	5.9711
$[90/45/0/-45_2/0/45/0]_s$	(Cy)—[16]			
$[45/-45_2/45/-45/0]_s$	(Co)—[12]	0.5914	1715.1	6.2208
$[-45/45/-45/90/45/90/0_2/45]_s$	(Cy)—[18]			
$[-45/0_2/-45/0/-45/0]_s$	(Co)—[14]	0.6134	1710.1	6.8836
$[0/-45/90/45/90/45/-45_2/0]_s$	(Cy)—[18]			
$[0/45/-45/0/-45/0/-45_2]_s$	(Co)—[16]	0.5843	1742.9	6.5043
$[90/45/-45/0/-45/0/45/0]_s$	(Cy)—[16]			

4.2. *A Two-Patch Panel.* The second example for a two-patch panel stacking sequence optimization [26] is selected to further demonstrate the efficiency of IGATLA method, with minimum weight as objective and critical buckling factor not less than 0.76 as constraint under the loading $N_x = 25$ N/mm. This structure consists of three laminates, two identical laminates along the edges, shown in Figure 6. The plate is simply supported on its edges and all four external edges remain straight. The composite material properties are also shown in Table 1. The best designs have been known with 24 plies for the exterior laminate and 8 plies for the interior part. The practical optima here are defined as the feasible designs within $2t$ -ply weights for one half of the exterior/interior laminate of the global optimum. 200 independent optimization runs are performed to show the computational performance.

Starting with $[(0/45/-45)_5]_s$ and $[(-45/45/90)_2]_s$ as the ground laminates for the exterior and interior part, respectively, the optimization is conducted with 200 repeated runs, where the population size and maximum generation number are both 100; DPID = 0.28 and FITP = 0.96. Table 4 lists several practical optima obtained with GATLA method.

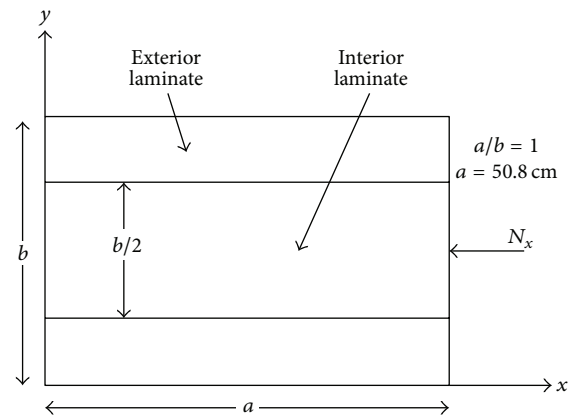


FIGURE 6: Geometry and loading of the considered two-patch panels.

It shows that this strategy is effective in dealing with stacking sequence optimization and more near optimal designs can be provided for the designer. Table 5 compares the efficiency

TABLE 3: Computational performance comparison.

Population size	Maximum generation number	Normalized computation price		Reliability	
		GATLA	IGATLA	GATLA	IGATLA
20	60	36.05	8.89	0.69	0.90
80	60	21.96	11.18	0.80	0.87
120	60	24.61	11.84	0.79	0.85
120	100	20.87	10.64	0.92	0.89

TABLE 4: Practical optima of composite panels.

	Laminate Ex: exterior part In: interior part	Plies	Weight, kg (B/A)	Critical buckling factor (B/A)
Case 1	[0/45/-45/0/-45/45/0/45/-45/0/-45] ₂ s [90/45/90] ₂ s	(Ex)—[24] (In)—[08]	0.8258/0.8258	0.76/0.76
Case 2	[0/45/0/45/-45/0/-45/0/-45/0/-45/45]s [-45/90/-45/90]s	(Ex)—[24] (In)—[08]	0.8343/0.8258	0.73/0.72
Case 3	[0 ₂ /45/-45/0/45/-45/0 ₂ /45/-45/0]s [90/45/-45/90]s	(Ex)—[24] (In)—[08]	0.8258/0.8258	0.74/0.74
Case 4	[0/45/-45/0/45/-45/0 ₂ /45/-45/0/45]s [-45/90/-45/45/90]s	(Ex)—[24] (In)—[10]	0.8774/0.8774	0.77/0.77
Case 5	[0/-45/0/45/-45/0/45/-45/0/-45/0/-45]s [-45/45/90/-45/90]s	(Ex)—[24] (In)—[10]	0.8774/0.8774	0.78/0.78
Reference [26]	[(-45/45) ₂ /45/0/-45/0 ₃]s [90/-45/45/90]s	(Ex)—[24] (In)—[08]	0.8258	0.81 [#] /0.76 ^{##}

A: after rounding, B: before rounding; #: critical buckling factor in reference, and ##: value given by Nastran.

TABLE 5: Computational performance comparison.

Methods	Normalized computation price	Reliability
GATLA	17.80	0.97
IGATLA	8.56	1.00
Reference [26]	25	

of the GATLA and IGATLA methods, as well as the number of finite element analysis in [26]. It can be seen that whether with improvements or not the GATLA approach exhibits lower computational costs, and by directly dealing with stacking sequences and thicknesses of each ply no intermediate variables like lamination parameters in [26] are used. Additionally, with the improvements in the GATLA method, the normalized computational cost is reduced from 17.80 to 8.56. So the computational cost saves 51.9% with these improvements. It could be concluded that noticeable improvements in the computational cost are obtained, and meanwhile a higher level of feasibility is achieved.

5. Engineering Applications

5.1. A Missile Rudder Structure Component Design. The first industrial application is to design the stacking sequence of a structural component from the missile rudder, which is to show the applicability of optimizing practical structures. The simplified geometry model and its dimensions are shown

in Figure 7, and the length units are all millimeter, that is, mm. The semicircle region with a radius of 21.6 mm at the bottom is fixed, and a uniform distributed force with the total value of 5000 N is applied along the red line, 72 mm away from the bottom edge. The applied force is perpendicular to the surface of the composite plate. The properties of the composite materials are also shown in Table 1, and the 0-degree fibre direction is along the y direction. The objective is to minimize the weight of the composite plate. The constraint is that the maximum displacement of the whole structure should not be more than 3 mm.

The optimization parameters are $x_i^L = t$, $x_i^U = 4t$, $x_i^b = 0.01t$, DPID = 0.95, and FITP = 0.9. Three optimization cases are studied based on three different ground laminates: [(0/±45/90)₂₅]s (Case 1), [(±45/0/90)₂₅]s (Case 2), and [(0/±45/90)₂₀]s (Case 3). In Case 1, there are 100 continuous thickness variables and 100 discrete variables. For Case 2, the number of design variables is equal to that of Case 1. The difference between them is the sequences in the ground laminates. Compared with Cases 1 and 2, fewer variables are involved in Case 3, that is, 80 thickness variables and 80 discrete variables. Considering the balanced constraint, the thickness variables of adjacent +45° and -45° plies are linked together in all three cases. The population size N and generation number MaxG are 100 and 150, respectively. The optimization results obtained from the three cases are summarized in Table 6, where the thickness-rounded design results and not rounded designs are the same.

TABLE 6: Summary of practical designs.

Case	Optimum designs	Plies	Weight, kg	Maximum displacement, mm	Iteration number
1	$[\pm 45/90/0/\pm 45]_2/0/(\pm 45)_2/0/\pm 45/90/0/(\pm 45)_2/90/(\pm 45)_2/90/(\pm 45/90/0/\pm 45)]_s$	80	0.5031	3.01	9
	$[90/0_2/90/\pm 45/0/90/\pm 45/0/(\pm 45)_2/90/0_2/(\pm 45/90/0_2/90_2/(\pm 45/90)_2)]_s$	80	0.5031	3.04	10
	$[\pm 45/90/0/90/\pm 45/0_2/90/0_2/(\pm 45)_2/90/0_2/(\pm 45)_2/90/(\pm 45)_3/90/\pm 45/90_2/0/90/0]_s$	80	0.5031	3.05	14
2	$[(\pm 45)_2/0/90/\pm 45/0/(\pm 45)_2/90/(\pm 45/0_2/90/\pm 45)_2/(\pm 45)_3/90/0/90/0/\pm 45/0/90/0]_s$	80	0.5031	3.02	9
	$[(\pm 45)_2/90/\pm 45/0/(\pm 45)_2/90/(\pm 45)_2/0/(\pm 45/0_2/90/(\pm 45)_2/0/(\pm 45/90)_2)]_s$	80	0.5031	3.03	14
	$[(\pm 45)_2/0/\pm 45/90/0/90/(\pm 45)_2/0/(\pm 45)_2/0/90/0/(\pm 45)_5/0/(\pm 45)_2/90/\pm 45]_s$	80	0.5031	3.05	9
3	$[0/\pm 45/90/\pm 45/0/90/\pm 45/90/0/90/(\pm 45)_2/0/(\pm 45)_3/0/\pm 45/0/90/\pm 45/90_2/(\pm 45/90/0_2/\pm 45)]_s$	80	0.5031	2.99	8
	$[\pm 45/0_2/90/(\pm 45)_2/90/0/\pm 45/0/\pm 45/90/0/\pm 45/90/0_2/90/0_2/90_2/0/90/0_2]_s$	80	0.5031	3.00	14
	$[\pm 45/90/0/(\pm 45)_3/90/0/90_2/0/\pm 45/0/90/\pm 45/0/90/0_2/90/0_2/90_2/0_2/0_2]_s$	80	0.5031	3.02	13

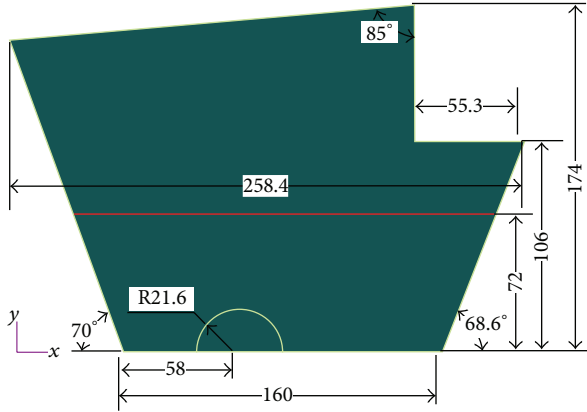


FIGURE 7: Geometry model and its dimensions of a missile rudder structure component.

TABLE 7: Load cases.

Load case	Overloading, g	
	Transverse	Longitudinal
1	1.80	-5.40
2	1.65	-8.85
3	1.65	-5.85
4	1.35	-10.50

With certain errors allowed, these results are acceptable, providing alternatives for the designer. Moreover, it can be seen that the proposed method is also effective starting with different ground laminates, which shows its robustness and applicability in dealing with practical structures.

5.2. *A Satellite Structure Design.* To further verify the practicality of the developed optimization system in engineering applications, the stacking sequences of the main cylinder in a satellite are optimized to provide the designer with a choice of alternatives. All of the calculations are conducted in a computer with CPU 3.30 GHz/RAM 8.00 G.

A satellite structure is composed of two parts: the main structure platform and the payload cabin. It is connected with the launch vehicle through a joint ring in the bottom of the main structure platform. In the main structure platform, a main cylinder with a conic part and a cylindrical part is designed, the stacking sequence of which needs to be optimized. The stiffness of the whole satellite should satisfy the requirement that the first-order natural transverse frequency, f_1 , is not lower than 15 Hz. Meanwhile, the design should also meet the stability demand that under each launch condition load, listed in Table 7, the critical buckling factor should not be less than 1.5.

Based on the primal design of the satellite structure, an FE (finite element) model was established with Patran, and the FE model of the main structure platform is shown in Figure 8, with a side panel and payload cabin removed. The main cylinder is also shown in Figure 8. Based on the connecting interface between the satellite and launch vehicle, the boundary condition is to fix the bottom of the joint ring.

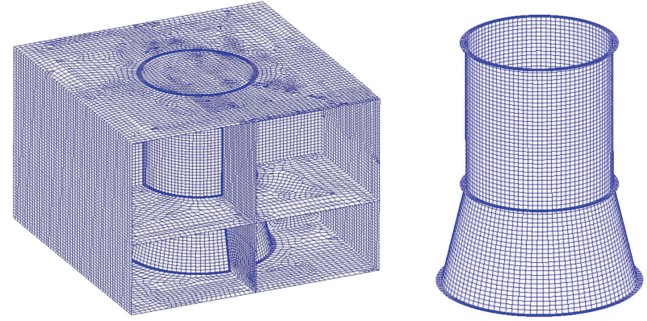


FIGURE 8: FE model of main structure platform in satellite structure.

In the optimization calculation, the ground laminate was given as $[(0/\pm 45/90)_5]_s$ for the cylindrical part, with $[(0/\pm 45)_6]_s$ for the conic part. And 0° fiber direction is along the longitudinal direction of the main cylinder. For the composite material properties in the design space, they are listed in Table 1. Considering the balanced constraint requirement that the number of $+45^\circ$ plies should be equal to the number of -45° plies, the thickness variables of adjacent $+45^\circ$ and -45° plies are enforced to link together here. The population size and maximum generation number in GA are 80 and 60, respectively. Among the constraints, the first-order natural transverse frequency, f_1 , and critical buckling factor under Load Case 4, $\lambda_{b,4}$, are set as constraint functions which will be satisfied automatically during the optimum calculation. Critical buckling factors under the other three load cases act as measurements to verify the optimized structure. The objective is to seek the minimum weight. Table 8 shows several optimization results of the stacking sequences with ply thicknesses not rounded. As the deleted plies with $0.01t$ -thickness are removed completely here for structural analyses in Table 8, a few critical buckling factors are a bit less than 1.5.

According to the results shown in Table 8, the stacking sequences are redesigned next by rounding the thicknesses and adding one or more plies if needed to meet the design requirements. The redesigned results are presented in Table 9, and it can be found that the stiffness and the stability of the final solutions basically satisfy all the design constraints, which provided guidelines to the detailed design of the satellite structure. Besides, as could be seen in Table 8, less than twenty-five structural analyses were implemented during the whole process for these five result cases, which means that this optimization strategy can supply reasonable solutions efficiently even for large-scale engineering problem.

6. Conclusions

By considering practical engineering requirements, the genetic algorithm using a two-level approximation devised in previous work for stacking sequence optimization was improved in the present study, and the performance was investigated with more typical numerical examples and industrial applications. With these improved optimization

TABLE 8: Summary of stacking sequence designs.

	Laminate Co: conic part Cy: cylindrical part	Plies	Weight of main cylinder, kg	f_1 , Hz	$\lambda_{b,4}$	Number of structural analyses	CPU cost, h
Case 1	[45/-45/90 ₂]s [45/-45/0/45/-45/0]s	(Cy)—[08] (Co)—[12]	3.068	17.335	1.4425	6	1.15
Case 2	[90 ₂ /45/-45]s [0/45 ₃ /-45 ₃ /0 ₂]s	(Cy)—[08] (Co)—[18]	3.254	17.423	1.4664	15	2.95
Case 3	[90/45 ₂ /-45 ₂]s [0/45 ₂ /-45 ₂ /0 ₂]s	(Cy)—[10] (Co)—[14]	3.096	17.625	1.5598	23	4.51
Case 4	[45/-45/90 ₂]s [0/45/-45/0/45/-45]s	(Cy)—[08] (Co)—[12]	3.250	17.335	1.6774	20	4.01
Case 5	[45/-45/90 ₂]s [45 ₃ /-45 ₃ /0 ₂]s	(Cy)—[08] (Co)—[16]	3.279	17.544	1.4190	11	2.18

TABLE 9: Redesigned stacking sequence results.

	Laminate Co: conic part Cy: cylindrical part	Plies	Weight of main cylinder, kg	f_1 , Hz	Critical buckling factors			
					$\lambda_{b,1}$	$\lambda_{b,2}$	$\lambda_{b,3}$	$\lambda_{b,4}$
Case 1	[45/-45/90 ₂ /0]s [45/-45/0 ₂ /45/-45/0]s	(Cy)—[09] (Co)—[14]	3.110	17.361	1.9392	1.5705	1.9589	1.5188
Case 2	[90 ₂ /45/-45]s [0/45 ₃ /-45 ₃ /0 ₂]s	(Cy)—[08] (Co)—[18]	3.434	17.576	1.9129	1.5794	1.9457	1.4702
Case 3	[90/45 ₂ /-45 ₂]s [0/45 ₂ /-45 ₂ /0 ₂]s	(Cy)—[10] (Co)—[14]	3.268	17.903	1.8887	1.6462	1.9672	1.5914
Case 4	[45/-45/90 ₂ /0]s [0/45/-45/0/45/-45/0]s	(Cy)—[09] (Co)—[14]	3.110	17.361	1.9081	1.7142	1.9920	1.6837
Case 5	[45/-45/90 ₂ /0]s [45 ₃ /-45 ₃ /0 ₂]s	(Cy)—[09] (Co)—[16]	3.351	17.417	2.0974	1.7528	2.1539	1.6881

strategies including improved random initial design, adaptive penalty fitness function, adaptive crossover probability, and variable mutation probability, as well as enhanced validity check criterion for multiple laminates, significantly higher computational efficiency and reliability than before have been obtained, which also relieve the designers from the burden of determining several control parameters. Meanwhile, a wealth of near optimal designs could be produced easily as well. By applying this strategy in practical engineering problems, it has been found that reasonable stacking sequences have been obtained, and this method is capable of conducting practical engineering optimizations efficiently to provide the designer with a choice of alternatives.

Conflict of Interests

The authors declare that there is no conflict of interests regarding the publication of this paper.

Acknowledgment

The authors acknowledge the support of this research work received from the National Natural Science Foundation of China (Grant no. 11102009).

References

- [1] H. Fukunaga and H. Sekine, "Stiffness design method of symmetric laminates using lamination parameters," *AIAA Journal*, vol. 30, no. 11, pp. 2791–2793, 1992.
- [2] R. Le Riche and R. T. Haftka, "Optimization of laminate stacking sequence for buckling load maximization by genetic algorithm," *AIAA journal*, vol. 31, no. 5, pp. 951–956, 1993.
- [3] R. le Riche and R. T. Haftka, "Improved genetic algorithm for minimum thickness composite laminate design," *Composites Engineering*, vol. 5, no. 2, pp. 143–161, 1995.
- [4] B. Liu, R. T. Haftka, M. A. Akgün, and A. Todoroki, "Permutation genetic algorithm for stacking sequence design of composite laminates," *Computer Methods in Applied Mechanics and Engineering*, vol. 186, no. 2–4, pp. 357–372, 2000.
- [5] A. Todoroki and M. Sekishiro, "New iteration fractal branch and bound method for stacking sequence optimizations of multiple laminates," *Composite Structures*, vol. 81, no. 3, pp. 419–426, 2007.
- [6] J. H. Park, J. H. Hwang, C. S. Lee, and W. Hwang, "Stacking sequence design of composite laminates for maximum strength using genetic algorithms," *Composite Structures*, vol. 52, no. 2, pp. 217–231, 2001.
- [7] M. Cho and S. Y. Rhee, "Layup optimization considering free-edge strength and bounded uncertainty of material properties," *AIAA Journal*, vol. 41, no. 11, pp. 2274–2282, 2003.

- [8] M. Shakeri, M. H. Yas, and M. Ghasemi Gol, "Optimal stacking sequence of laminated cylindrical shells using genetic algorithm," *Mechanics of Advanced Materials and Structures*, vol. 12, no. 4, pp. 305–312, 2005.
- [9] S. Nagendra, D. Jestin, Z. Gürdal, R. T. Haftka, and L. T. Watson, "Improved genetic algorithm for the design of stiffened composite panels," *Computers and Structures*, vol. 58, no. 3, pp. 543–555, 1996.
- [10] G. Soremekun, Z. Gürdal, R. T. Haftka, and L. T. Watson, "Improving genetic algorithm efficiency and reliability in the design and optimization of composite structures," Tech. Rep. TR-96-13, Department of Computer Science, Virginia Polytechnic Institute and State University, Blacksburg, Va, USA, 1996.
- [11] B. Liu, R. T. Haftka, and M. A. Akgün, "Composite wing structural optimization using genetic algorithms and response surfaces," in *Proceedings of the 7th AIAA/USAF/NASA/ISSMO Symposium on Multidisciplinary Analysis and Optimization*, pp. 1–12, St. Louis, Mo, USA, 1998.
- [12] V. B. Gantovnik, Z. Gürdal, and L. T. Watson, "A genetic algorithm with memory for optimal design of laminated sandwich composite panels," *Composite Structures*, vol. 58, no. 4, pp. 513–520, 2002.
- [13] A. Todoroki and T. Ishikawa, "Design of experiments for stacking sequence optimizations with genetic algorithm using response surface approximation," *Composite Structures*, vol. 64, no. 3-4, pp. 349–357, 2004.
- [14] P. Kere and J. Lento, "Design optimization of laminated composite structures using distributed grid resources," *Composite Structures*, vol. 71, no. 3-4, pp. 435–438, 2005.
- [15] C. H. Park, W. I. Lee, W. S. Han, and A. Vautrin, "Improved genetic algorithm for multidisciplinary optimization of composite laminates," *Computers and Structures*, vol. 86, no. 19-20, pp. 1894–1903, 2008.
- [16] K. Yamazaki, "Two-level optimization technique of composite laminate panels by genetic algorithms," in *Proceedings of the 37th AIAA/ASME/ASCE/AHS/ASC Structures, Structural Dynamics, and Materials Conference and Exhibit*, pp. 1882–1887, AIAA, Salt Lake City, Utah, USA, 1996.
- [17] H. Ghiasi, D. Pasini, and L. Lessard, "Optimum stacking sequence design of composite materials Part I: constant stiffness design," *Composite Structures*, vol. 90, no. 1, pp. 1–11, 2009.
- [18] S. Chen, Z. Lin, H. An, H. Huang, and C. Kong, "Stacking sequence optimization with genetic algorithm using a two-level approximation," *Structural and Multidisciplinary Optimization*, vol. 48, no. 4, pp. 795–805, 2013.
- [19] A. Todoroki and M. Sekishiro, "Stacking sequence optimization to maximize the buckling load of blade-stiffened panels with strength constraints using the iterative fractal branch and bound method," *Composites Part B: Engineering*, vol. 39, no. 5, pp. 842–850, 2008.
- [20] M. Ohsaki, "Genetic algorithm for topology optimization of trusses," *Computers & Structures*, vol. 57, no. 2, pp. 219–225, 1995.
- [21] H. J. C. Barbosa and A. C. C. Lemonge, "A new adaptive penalty scheme for genetic algorithms," *Information Sciences*, vol. 156, no. 3-4, pp. 215–251, 2003.
- [22] X. Liu, G. Cheng, J. Yan, and L. Jiang, "Singular optimum topology of skeletal structures with frequency constraints by AGGA," *Structural and Multidisciplinary Optimization*, vol. 45, no. 3, pp. 451–466, 2012.
- [23] M. Srinivas and L. M. Patnaik, "Adaptive probabilities of crossover and mutation in genetic algorithms," *IEEE Transactions on Systems, Man and Cybernetics*, vol. 24, no. 4, pp. 656–667, 1994.
- [24] Z.-W. Ren and Y. San, "Improved adaptive genetic algorithm and its application research in parameter identification," *Journal of System Simulation*, vol. 18, no. 1, pp. 41–43, 2006.
- [25] J. P. B. Leite and B. H. V. Topping, "Improved genetic operators for structural engineering optimization," *Advances in Engineering Software*, vol. 29, no. 7–9, pp. 529–562, 1998.
- [26] F.-X. Irisarri, M. M. Abdalla, and Z. Gürdal, "Improved shepard's method for the optimization of composite structures," *AIAA Journal*, vol. 49, no. 12, pp. 2726–2736, 2011.

Research Article

Reliability-Based Topology Optimization Using Stochastic Response Surface Method with Sparse Grid Design

Qinghai Zhao,¹ Xiaokai Chen,¹ Zheng-Dong Ma,² and Yi Lin³

¹*Collaborative Innovation Center of Electric Vehicles in Beijing, School of Mechanical Engineering, Beijing Institute of Technology, Beijing 100081, China*

²*Department of Mechanical Engineering, University of Michigan, Ann Arbor, MI 48105, USA*

³*Beijing Automotive Technology Center, Beijing 100081, China*

Correspondence should be addressed to Xiaokai Chen; chenxiaokai@263.net

Received 18 July 2014; Revised 11 November 2014; Accepted 27 November 2014

Academic Editor: Chao Jiang

Copyright © 2015 Qinghai Zhao et al. This is an open access article distributed under the Creative Commons Attribution License, which permits unrestricted use, distribution, and reproduction in any medium, provided the original work is properly cited.

A mathematical framework is developed which integrates the reliability concept into topology optimization to solve reliability-based topology optimization (RBTO) problems under uncertainty. Two typical methodologies have been presented and implemented, including the performance measure approach (PMA) and the sequential optimization and reliability assessment (SORA). To enhance the computational efficiency of reliability analysis, stochastic response surface method (SRSM) is applied to approximate the true limit state function with respect to the normalized random variables, combined with the reasonable design of experiments generated by sparse grid design, which was proven to be an effective and special discretization technique. The uncertainties such as material property and external loads are considered on three numerical examples: a cantilever beam, a loaded knee structure, and a heat conduction problem. Monte-Carlo simulations are also performed to verify the accuracy of the failure probabilities computed by the proposed approach. Based on the results, it is demonstrated that application of SRSM with SGD can produce an efficient reliability analysis in RBTO which enables a more reliable design than that obtained by DTO. It is also found that, under identical accuracy, SORA is superior to PMA in view of computational efficiency.

1. Introduction

The subject for optimal structural topologies under uncertainty is very important, challenging, and attractive for researchers. The field of structural topology optimization has become matured since the pioneering work by Bendsoe and Kikuchi [1]. Details of various proposed methodologies can be found in comprehensive reviews and text books [2–4]. The aim of the optimization process is to obtain a material distribution within a fixed design domain, so as to optimize the specified structural response subjected to prescribed constraints. However, most of the optimization problems are established in deterministic manner where the designs are carried out without considering the variations observed in geometry and material property as well as external loads due to inherent uncertainty. Consequently, optimum design obtained by the so-called deterministic topology optimization (DTO) may represent unreasonable reliability level.

Hence, reliability-based topology optimization (RBTO) has emerged which achieves optimal topologies while quantitatively measuring the effects of uncertainty by means of probability constraints.

The state-of-the-art topology optimization methodologies have been applied for obtaining optimized reliable designs of structures and mechanisms considering uncertainties. Density-based method taking into account loading and material uncertainties has been demonstrated for microelectromechanical systems (MEMS) [5], for geometrically nonlinear structures [6]. A level set based approach for compliant mechanisms under uncertainties exhibited by loads, material properties, and member geometries has been reported by Zhang and Ouyang [7]. Recently, topology optimization with uncertainties has been demonstrated for the bidirectional evolutionary structural optimization (BESO) in the design for electrothermal compliant mechanisms [8] and for a vehicle's hood reinforcement [9]. Although the RBTO is a rapidly

expanding active research field, topology optimization integration with probability constraint is still quite challenging, that is, the numerical difficulty for direct estimation failure probability. Such difficulties have motivated the development of various uncertainty propagation methods, such as Monte-Carlo simulation (MCS) method [10], the first and second order reliability methods (FORM/SORM) [11], response surface method (RSM) [12], and the stochastic response surface method (SRSM) [13].

MCS is the most comprehensively used sampling method but the required time and resources can be expensive due to a tremendous number of repeated analyses, especially for general structures with low failure probability. In order to improve efficiency maintaining simplicity, two recommended approaches based on FORM to the failure probability calculation are developed, the reliability index approach (RIA) [14] and its inverse, the more efficient performance measure approach (PMA) [15]. In Maute and Frangopol [5], a robust formulation of RBTO based on the PMA has been presented to account for uncertainties. A comparison study between RIA and PMA has been summarized for RBTO formulation [16], where the results clearly show that PMA has better convergence and efficiency than RIA. In general, the FORM-based RBTO approaches estimate the structure reliability (via reliability index) within the topology optimization algorithm and are referred to as nested-loop (or double-loop) methods. However, empirical evidence suggests that such double-loop approaches lead to substantially high computational cost and weak convergence stability, especially involving virtual simulation models (i.e., finite element models). To overcome these difficulties, some authors proposed different methods to solve RBTO problems seeking for simplification and efficiency formulations. The so-called hybrid (or concurrent) RBTO method has been proposed by Kharmanda and Olhoff [17], where reliability analysis is decoupled from optimization procedures and carried out at the beginning of the optimization loops, followed by equivalent DTO. Luo et al. [18] introduced the fuzzy set theory into multiobjective topology optimization, in which the uncertainties of the objection function and constraints are described by using nonlinear membership functions. A reliability-based topology optimization method using a nonprobabilistic multiellipsoid convex model has been proposed by Luo et al. [19], where the model represents uncertainty of bounded parameters. The theories of a single-loop method for component reliability-based topology optimization (CRBTO) and system reliability-based topology optimization (SRBTO) have been developed by Silva et al. [20] and by Nguyen et al. [21], respectively. The proposed methodology is compatible with existing topology optimization software and suitable for practical applications.

The available reliability analysis using FORM/SORM is conveniently performed with known limit state function. However, in many practical complex structures, the relationship between output response and input data does not exist. Therefore, several surrogate methods, such as the response surface method (RSM) and the Kriging method, are used to approximate the implicit limit state function by a surrogate model. RBTO using standard response surface method has been performed by Yoo et al. [22], where much fewer

experimental points are required compared to traditional response surface method. A comparison study between the standard response surface method and Kriging method can be found in Eom et al. [23]. There are not many works focusing on design of experiments (DOE), although it is a key issue for surrogate methods implementation in RBTO.

In this paper, two RBTO methodologies are presented, implemented on several numerical examples, including performance measure approach (PMA) and sequential optimization and reliability assessment (SORA). Topology optimization method is solved by the solid isotropic microstructure with penalty (SIMP) method. Reliability analysis is carried out by FORM, where the limit state function is approximated by the stochastic response surface method (SRSM). Design of experiment (DOE) is generated by sparse grid design (SGD), which was proven to be an effective and special discretization technique. The proposed approaches are capable of solving a wide range of problems, but the focus of this paper is to be limited to minimum-volume optimization problems for a detailed description. Monte-Carlo simulations are also performed to verify the accuracy of the failure probabilities computed by the proposed approach.

The paper is organized as follows. In Section 2, the basic formulation of RBTO is presented, followed by the selected methodologies including PMA and SORA. Descriptions of the SRSM and SGD are briefly discussed in Sections 3 and 4, respectively. The flowchart and procedure of PMA and SORA are presented in Section 5. Numerical results and discussion for RBTO methodologies and DTO are illustrated in Section 6. Finally, the conclusion of the paper is provided in Section 7.

2. Reliability-Based Topology Optimization

In general, RBTO problems are formulated as follows:

$$\begin{aligned} \min_{\boldsymbol{\rho}} \quad & C(\boldsymbol{\rho}) \\ \text{s.t.} \quad & \Pr [G_i(\boldsymbol{\rho}, \mathbf{X}) \leq 0] \leq P_{f_i}^T \quad i = 1, \dots, m \\ & \boldsymbol{\rho}_{\min} \leq \boldsymbol{\rho} \leq \boldsymbol{\rho}_{\max}, \end{aligned} \quad (1)$$

where $\boldsymbol{\rho}$ is the vector of design variables (i.e., the element densities), defined as independent deterministic variables with the upper bounds $\boldsymbol{\rho}_{\max}$ and lower bounds $\boldsymbol{\rho}_{\min}$, \mathbf{X} is the vector of random variables (i.e., loads and material property) with the realizations being noted \mathbf{x} , $C(\cdot)$ is the objective function, $G_i(\cdot)$, $i = 1, \dots, m$, is the i th limit state function or performance function, $\Pr[\cdot]$ is the probability operator, $P_{f_i}^T$ is the target failure probability for the i th constraint, and m is the number of probabilistic constraints. To evaluate the failure probability, the safe region is defined as $G_i(\boldsymbol{\rho}, \mathbf{X}) > 0$, the failure region as $G_i(\boldsymbol{\rho}, \mathbf{X}) < 0$, and the limit state function as $G_i(\boldsymbol{\rho}, \mathbf{X}) = 0$. The failure probability for each constraint may be obtained by evaluating the multidimensional integral as follows:

$$P_{f_i} = \Pr [G_i(\boldsymbol{\rho}, \mathbf{X}) \leq 0] = \int \cdots \int_{G_i(\boldsymbol{\rho}, \mathbf{X}) \leq 0} f_{\mathbf{X}}(\mathbf{x}) d\mathbf{x}, \quad (2)$$

where P_{f_i} is the failure probability and $f_{\mathbf{X}}(\mathbf{x})$ is the joint probability density function (PDF) of random variables \mathbf{X} . In practice, it is difficult and even impossible to compute this integral exactly. In this paper, FORM is adopted for reliability analysis because of its efficiency and simplicity. The key concept of FORM is to find the most probable point (MPP), which is defined as the point on the limit state function closest to the origin in the normalized space transformed from the physical space through the Rosenblatt or the Nataf transformations. By FORM approximation, the failure probability and the allowable failure probability are evaluated by

$$P_{f_i}^T \approx \Phi(-\beta_i^T), \quad P_{f_i} \approx \Phi(-\beta_i), \quad (3)$$

where $\Phi(\cdot)$ is the standard cumulative distribution function (CDF) and β_i^T is the target reliability index for the i th constraint and the reliability index β [24], which is a reliability measurement defined as the distance between the MPP and the origin. By applying the Rosenblatt or the Nataf transformations, random vector \mathbf{X} is transformed to a vector of normalized and independent Gaussian \mathbf{U} (zero means and unit variance), expressed as $\mathbf{U} = T(\mathbf{X})$ or $\mathbf{X} = T^{-1}(\mathbf{U})$. Based on the above transformation, the limit state function is correspondingly defined as

$$G_i(\boldsymbol{\rho}, \mathbf{X}) = G_i(\boldsymbol{\rho}, T^{-1}(\mathbf{U})) = g_i(\boldsymbol{\rho}, \mathbf{U}), \quad (4)$$

where g_i is the i th limit state function in the normalized space.

2.1. Performance Measure Approach (PMA) for RBTO. In this paper, PMA is used as a reference comparison method for SORA. By using PMA formulation, the RBTO is expressed as

$$\begin{aligned} \min_{\boldsymbol{\rho}} \quad & C(\boldsymbol{\rho}) \\ \text{s.t.} \quad & G_i^P(\boldsymbol{\rho}, \mathbf{x}_i^*) \geq 0 \quad i = 1, \dots, m \\ & \boldsymbol{\rho}_{\min} \leq \boldsymbol{\rho} \leq \boldsymbol{\rho}_{\max}, \end{aligned} \quad (5)$$

where G_i^P is the target performance with respect to the i th limit state function calculated at the MPP denoted as \mathbf{x}_i^* in physical space or \mathbf{u}_i^* in normalized space, which can be found by the inverse reliability analysis, given as

$$\begin{aligned} \min_{\mathbf{u}} \quad & g_i(\mathbf{u}) \\ \text{s.t.} \quad & \|\mathbf{u}\| = \beta_i^T. \end{aligned} \quad (6)$$

As the inverse reliability analysis is an optimization procedure by itself, the RBTO is a typical double-loop strategy, where the outer loop is an optimization problem in terms of design variables $\boldsymbol{\rho}$ and the inner loop for reliability analysis in terms of random variables \mathbf{X} .

2.2. Sequential Optimization and Reliability Assessment (SORA) for RBTO. Initiated by Du and Chen [25], this

approach decouples the RBTO model into a series of cycles of DTO and reliability analysis. In each cycle, DTO and reliability analysis are decoupled from each other and reliability analysis is only conducted after the DTO. SORA for RBTO can be expressed as

$$\begin{aligned} \min_{\boldsymbol{\rho}} \quad & C(\boldsymbol{\rho}^k) \\ \text{s.t.} \quad & G_i(\boldsymbol{\rho}^k, \mathbf{x}_i^{k-1}) \geq 0 \quad i = 1, \dots, m \\ & \boldsymbol{\rho}_{\min} \leq \boldsymbol{\rho}^k \leq \boldsymbol{\rho}_{\max}, \end{aligned} \quad (7)$$

where k indicates the end cycle of each deterministic topology optimization and \mathbf{x}_i^{k-1} is the MPP in physical space with respect to the i th limit state in the $(k-1)$ th cycle, given by the transformation of $\mathbf{u}_i^{*(k-1)}$. By the given current optimal design $\boldsymbol{\rho}^{*(k)}$, the next MPP $\mathbf{u}_i^{*(k)}$ is obtained by the inverse reliability analysis, defined as

$$\begin{aligned} \min_{\mathbf{u}} \quad & g_i(\boldsymbol{\rho}^{*(k)}, \mathbf{u}) \\ \text{s.t.} \quad & \|\mathbf{u}\| = \beta_i^T. \end{aligned} \quad (8)$$

The advantage of the SORA formulation is that the number of reliability analyses will be significantly reduced as it is equal to the number of cycles. The entire optimization process is repeated until the deterministic topology optimization becomes convergent and reliability requirements are satisfied.

3. Stochastic Response Surface Method

The stochastic response surface method (SRSM) is the most widely used surrogate method in structural reliability analysis, which can be viewed as a conceptual extension of classical deterministic response surface method [26]. The SRSM approximates the true limit state function through series expansions of standard random variables which is typically a k th order Hermite orthogonal polynomial with undetermined coefficients. Consider

$$\begin{aligned} g(\mathbf{u}) = & a_0 \Gamma_0 + \sum_{i_1=1}^d a_{i_1} \Gamma_1(u_{i_1}) \\ & + \sum_{i_1=1}^d \sum_{i_2=1}^{i_1} a_{i_1 i_2} \Gamma_2(u_{i_1}, u_{i_2}) \\ & + \sum_{i_1=1}^d \sum_{i_2=1}^{i_1} \sum_{i_3=1}^{i_2} a_{i_1 i_2 i_3} \Gamma_3(u_{i_1}, u_{i_2}, u_{i_3}) + \dots, \end{aligned} \quad (9)$$

where $\{u_i\}_{i=1}^{\infty}$ is a set of independent normalized random variables, a_0, a_{i_1}, \dots are deterministic coefficients to be estimated, $g(\mathbf{u})$ is the approximated limit state function, and Γ_i are Hermite polynomials of degree p , given by

$$\Gamma_p(u_{i_1}, \dots, u_{i_p}) = (-1)^p e^{1/2} \mathbf{u}^T \mathbf{u} \frac{\partial^p}{\partial u_{i_1} \dots \partial u_{i_p}} e^{-1/2} \mathbf{u}^T \mathbf{u}, \quad (10)$$

where \mathbf{u} is the vector of p independent normal random variables $\{u_i\}_{i=1}^p$, which represent the input uncertainties. Furthermore, the Hermite polynomials defined on $\{u_i\}_{i=1}^p$ are orthogonal with respect to an inner product defined as the expectation of the product of two random variables [13]. Thus,

$$E[\Gamma_p \Gamma_q] = 0 \quad \text{iff } \Gamma_p \neq \Gamma_q. \quad (11)$$

Applying the least square method, the coefficients $\mathbf{b} = [a_0, a_1, \dots, a_p]$ can be calculated by minimizing the square of error expressed as follows:

$$\min J(\mathbf{b}) = \|\bar{\mathbf{g}} - \mathbf{A}\mathbf{b}\|^2, \quad (12)$$

where $\bar{\mathbf{g}}(\mathbf{u})$ is the corresponding real function evaluated at a set of sampling points. The analytical solution can be expressed as

$$\mathbf{b} = (\mathbf{A}^T \mathbf{A})^{-1} \mathbf{A}^T \bar{\mathbf{g}}, \quad (13)$$

where \mathbf{A} is the matrix of bases at the sampling points, defined as

$$\mathbf{A} = \begin{bmatrix} \Gamma_0(u_1) & \Gamma_1(u_1) & \cdots & \Gamma_p(u_1) \\ \Gamma_0(u_2) & \Gamma_1(u_2) & \cdots & \Gamma_p(u_2) \\ \vdots & \vdots & \ddots & \vdots \\ \Gamma_0(u_N) & \Gamma_1(u_N) & \cdots & \Gamma_p(u_N) \end{bmatrix}. \quad (14)$$

Therefore, one key issue when applying SRSM for structural reliability analysis is to choose a suitable design of experiment to generate sampling points.

4. Sparse Grid Design

The sparse grid design is a special discretization technique, which can be traced back to the Smolyak algorithm [27]. It is based on hierarchical basis, a representation of a discrete function space which is equivalent to the conventional nodal basis, and a sparse tensor product construction [28]. The one-dimensional difference quadrature formula is defined as

$$\Delta_k^1(f) = (Q_k^1 - Q_{k-1}^1)(f), \quad \text{with } Q_0^1(f) = 0. \quad (15)$$

Then, the Smolyak quadrature formula for d -dimensional functions f with level $l \in N$ is given by

$$Q_l^d(f) = \sum_{|\mathbf{k}| \leq l+d} (\Delta_{k_1}^1 \otimes \cdots \otimes \Delta_{k_d}^1)(f). \quad (16)$$

Note that $|\mathbf{k}|$ denotes the summation of the multi-indices ($|\mathbf{k}| = k_1 + \cdots + k_d$). Alternatively, the above formula can be written as

$$Q_l^d(f) = \sum_{l+1 \leq |\mathbf{k}| \leq l+d} (-1)^{l+d-|\mathbf{k}|} \cdot \binom{d-1}{l+d-|\mathbf{k}|} \cdot (Q_{k_1}^1 \otimes \cdots \otimes Q_{k_d}^1)(f). \quad (17)$$

To compute $Q_l^d(f)$, specific tensor product rules of sparse grid are needed, defined as

$$U_l^d = \bigcup_{l+1 \leq |\mathbf{k}| \leq l+d} (U_{k_1}^1 \otimes \cdots \otimes U_{k_d}^1), \quad (18)$$

where U_l^i denote the one-dimension support nodes, which can be obtained by univariate quadrature algorithms, such as Newton-Cotes, Gauss quadrature, and Clenshaw-Curtis rules [29].

In this paper, the Clenshaw-Curtis type sparse grid design H^{CC} is constructed, with equidistant nodes for polynomial interpolation. Here, the u_k^i are defined as

$$u_k^i = \begin{cases} \frac{(i-1)}{(m_k-1)} & \text{for } i = 1, \dots, m_k, \text{ if } m_k > 1 \\ 0.5 & \text{for } i = 1, \text{ if } m_k = 1, \end{cases} \quad (19)$$

where

$$m_k = \begin{cases} 1 & \text{if } k = 1 \\ 2^{k-1} + 1 & \text{if } k > 1. \end{cases} \quad (20)$$

Figure 1 illustrates the grids H^{CC} obtained using the Clenshaw-Curtis rule of dimensions $d = 2$ and $d = 3$ with level $l = 2$.

5. Flowchart and Procedure of RBTO

The flowcharts of the RBTO/PMA and RBTO/SORA methods are provided in Figure 2. For example, the strategy of SORA contains two parts: "equivalent" deterministic optimization and independent reliability analysis. At first, the topology optimization problem is formulated based on SIMP method and solved by using the method of moving asymptotes (MMA) with standard settings [30]. To ensure manufacturability and mesh independence, the mesh-independent density filtering is applied to eliminate the appearance of numerical instabilities [31]. Then, the reliability analysis is implemented at the deterministic optimum solution to locate the MPP that satisfies the desired target reliability index, where the SRSM approximates the true limit state function by regression analysis of the least square method, combined with SGM adopted to generate the experimental sample points based on random variables. The new deterministic optimization model is constructed based on the MPP while the stop criterion is not satisfied. Next procedure cycle is running until the stopping criterion is convergent.

6. Numerical Examples

6.1. The MBB Beam. In the first example, consider the popular MBB beam depicted in Figure 3. The dimensions of the beam are $L = 90$ mm and $H = 30$ mm and the thickness is $t = 1$ mm. Young's modulus $E_0 = 2.10 \times 10^5$ MPa and Poisson's ratio $\nu = 0.30$ are assumed. An external load $F = 100$ N is applied. Design domain is discretized by 2700 (90×30) four-node bilinear finite elements. Random variables are chosen

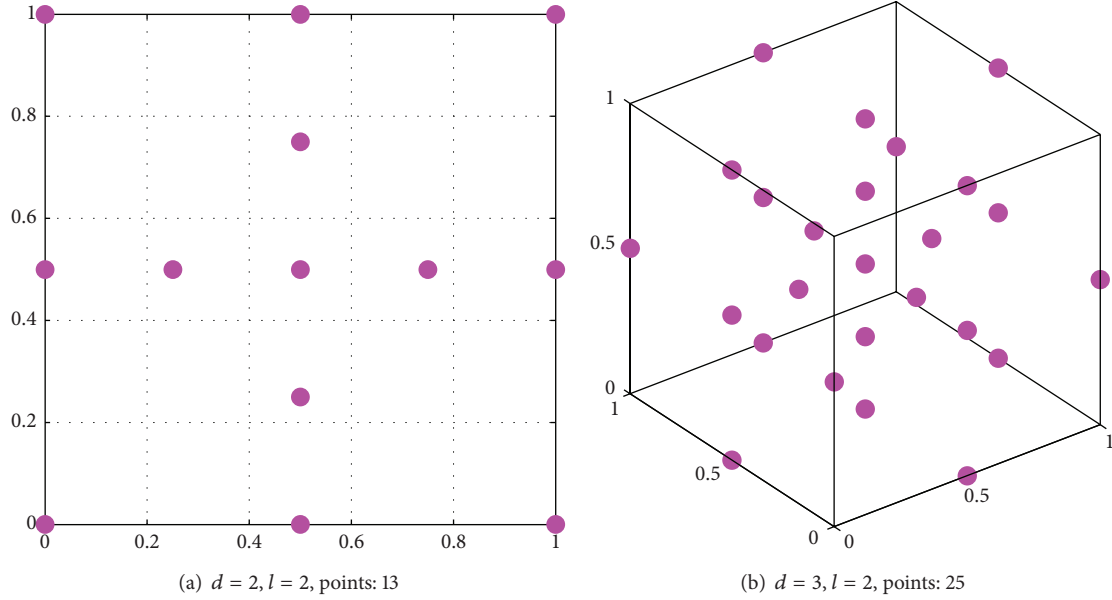


FIGURE 1: The Clenshaw-Curtis type sparse grid design.

TABLE 1: Comparison of topology optimization design results.

Approach	Volume/volume fraction (mm ²)/%	Reliability index (β)	Computing time (s)	Design point	
				E_0 /MPa	F/N
DTO	1047.19/38.78	—	314.74	—	—
PMA	1351.48/50.05	3.002	1655.11	1.59×10^5	117.68
SORA	1351.48/50.05	3.002	493.58	1.59×10^5	117.68

as Young's modulus E_0 and external load F . Each variable is assumed to be normally distributed and has 10% standard deviation of the mean value.

RBTO problems are formulated as follows:

$$\begin{aligned}
 & \min_{\boldsymbol{\rho}} V \\
 & \text{s.t. } \Pr [G(\boldsymbol{\rho}, \mathbf{X}) \leq 0] \leq P_f^T = 0.135\% \quad (21) \\
 & \quad \boldsymbol{\rho}_{\min} \leq \boldsymbol{\rho} \leq \boldsymbol{\rho}_{\max},
 \end{aligned}$$

where V is the volume and the limit state function is defined as $G = \delta_{\max} - \delta$. δ is the actual displacement and δ_{\max} is the allowable displacement assigned as 0.140 mm. The probability of constraint violation is less than 0.135%, which means that the target reliability index is equal to 3.0.

The optimal topologies obtained by DTO and RBTO approaches are presented in Figures 4 and 5, respectively. The optimization results obtained from each approach are summarized in Table 1, including volume/volume fraction, reliability index, computing time, and design point. The reliability index is calculated by 10,000 Monte-Carlo simulations. And the coefficients of SRSM to construct limit state functions at some iteration during PMA and SORA procedures are given in Tables 2 and 3, respectively, where u_1 and u_2 are the normalized values of Young's modulus E_0 and applied load F , respectively.

TABLE 2: Approximated limit state function constructed by SRSM in PMA.

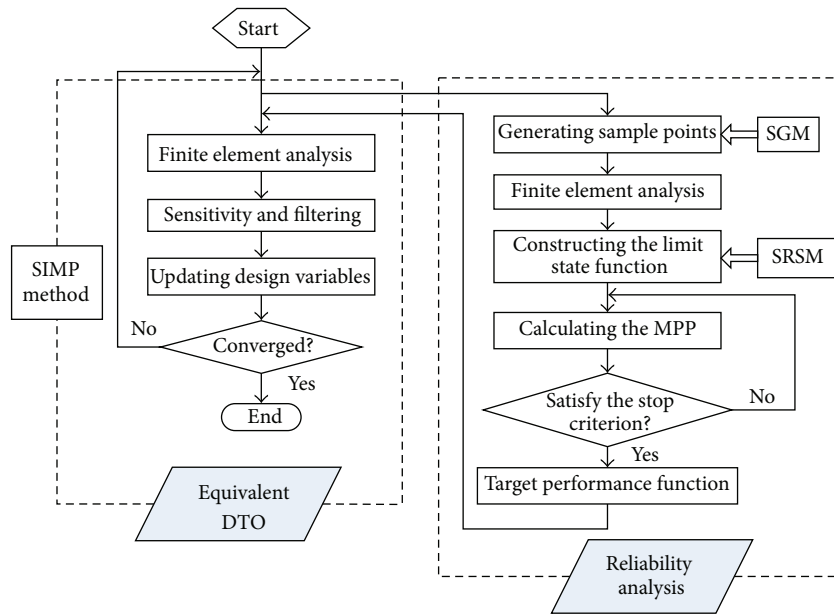
Iteration	a_0	a_1	a_2	a_3	a_4	a_5
1	-2.5006	0.3782	-0.3661	-0.0381	0.0381	-0.0004
2	-0.3879	0.1500	-0.1451	-0.0151	0.0151	-0.0001
3	0.2686	0.0790	-0.0765	-0.0080	0.0080	-0.0001
\vdots	\vdots	\vdots	\vdots	\vdots	\vdots	\vdots
101	0.2484	0.0812	-0.0786	-0.0082	0.0082	-0.0001
102	0.2484	0.0812	-0.0786	-0.0082	0.0082	-0.0001
103	0.2484	0.0812	-0.0786	-0.0082	0.0082	-0.0001

Approximated limit state function: $g(\mathbf{u}) = a_0 + a_1 u_1 + a_2 u_2 + a_3 (u_1^2 - 1) + a_4 u_1 u_2 + a_5 (u_2^2 - 1)$.

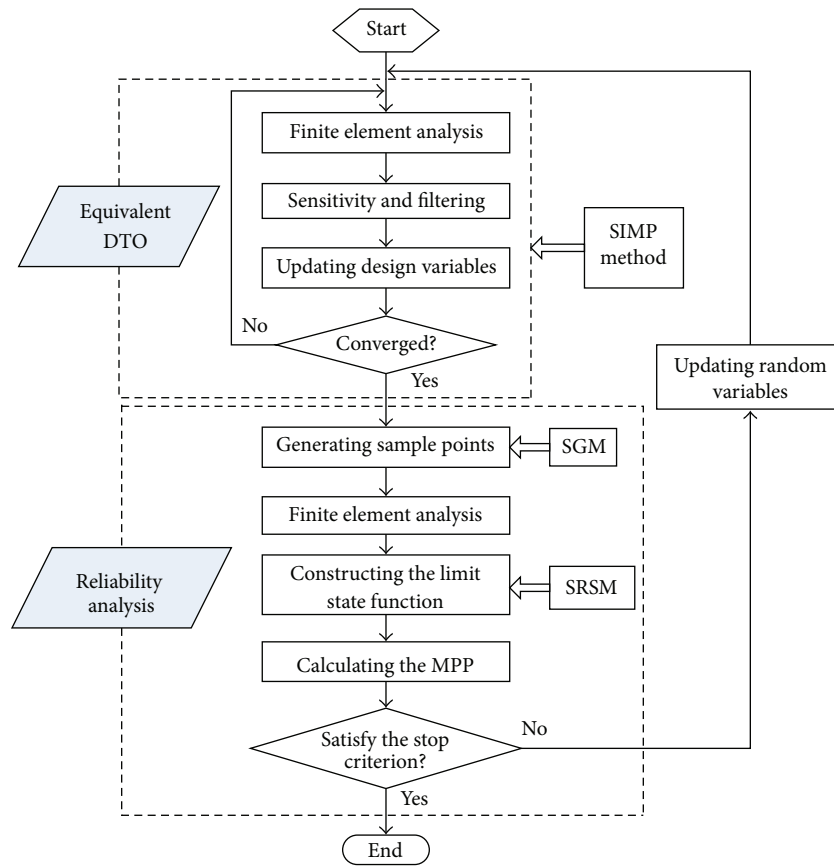
TABLE 3: Approximated limit state function constructed by SRSM in SORA.

Iteration	a_0	a_1	a_2	a_3	a_4	a_5
1	-0.0102	0.1092	-0.1057	-0.0110	0.0110	-0.0001
2	0.2484	0.0812	-0.0786	-0.0082	0.0082	-0.0001

From the comparison of the results, the optimal solutions obtained by RBTOs have different topologies from those obtained by DTO with the application of SRSM with SGD in reliability analysis, as shown in Figures 4 and 5. As the results listed in Table 1 show, RBTOs use more material than DTO by



(a) PMA



(b) SORA

FIGURE 2: The flowchart of RBTO.

TABLE 4: Comparison of topology optimization design results.

Approach	Volume/volume fraction (mm ²)/%	Reliability index (β)	Computing time (s)	Design point		
				E_0 /MPa	F_x /N	F_y /N
DTO	918.59/25.52	—	971.31	—	—	—
PMA	1345.49/37.37	3.003	8266.06	5.62×10^4	171.53	116.15
SORA	1345.49/37.37	3.003	2296.5	5.62×10^4	171.53	116.15

TABLE 5: Approximated limit state function constructed by SRSM in PMA.

Iteration	a_0	a_1	a_2	a_3	a_4	a_5	a_6	a_7	a_8	a_9
1	-1.9135	0.3228	-0.2885	-0.3034	-0.0326	0.0306	-0.0144	0.0000	-0.0152	0.0322
2	-0.2137	0.1345	-0.1099	-0.1366	-0.0136	0.0117	-0.0055	0.0000	-0.0068	0.0145
⋮	⋮	⋮	⋮	⋮	⋮	⋮	⋮	⋮	⋮	⋮
170	0.3517	0.0718	-0.0624	-0.0693	-0.0073	0.0066	-0.0031	-0.0000	-0.0035	0.0073
171	0.3517	0.0718	-0.0624	-0.0693	-0.0073	0.0066	-0.0031	-0.0000	-0.0035	0.0073

Approximated limit state function: $g(\mathbf{u}) = a_0 + a_1u_1 + a_2u_2 + a_3u_3 + a_4(u_1^2 - 1) + a_5u_1u_2 + a_6(u_2^2 - 1) + a_7u_2u_3 + a_8(u_3^2 - 1) + a_9u_1u_3$.

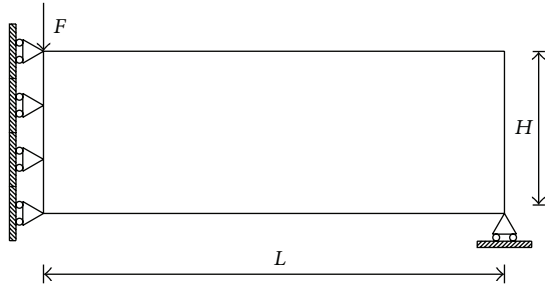


FIGURE 3: The design domain of the MBB beam.

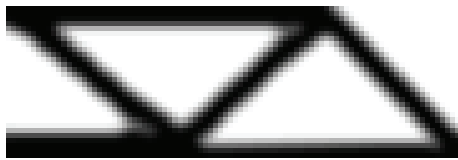


FIGURE 4: Resulting topology of DTO.

11.27%, improving the reliability index up to 3.002. It can also be seen from the results listed in Table 1 that SORA seems to be more efficient than PMA, with the evidence in computing time and the number of reliability analyses, as presented in Tables 1, 2, and 3.

6.2. The Loaded Knee Structure. Next, the loaded knee structures with multiple load cases are depicted in Figure 6. The dimensions of the structure are $L = 60$ mm and the thickness is $t = 1$ mm. Young's modulus $E_0 = 7.10 \times 10^4$ MPa and Poisson's ratio $\nu = 0.33$ are assumed. Two external load cases, $F_x = 150$ N and $F_y = 100$ N, are applied on the midpoint of the right edge, respectively. Design domain is discretized by 3600 (60×60) four-node elements. Random variables are chosen as Young's modulus E_0 and external loads F_x and F_y . Each variable is assumed to be normally distributed and has

10% standard deviation of the mean value. It should be noted that sampling points generated by SGD are extended to three dimensions in this example.

In this example, the objective function is volume, and the limit state function is defined as $G = c_{\max} - c$. c is the sum of compliance for the two load cases, and c_{\max} is the allowable compliance and is assigned to 40 N·mm. The target reliability index is set to 3.0.

The optimal topologies obtained by DTO and RBTO approaches are presented in Figures 7 and 8, respectively. The optimization results obtained from each approach are summarized in Table 4, including volume/volume fraction, reliability index, computing time, and design point. The reliability index is calculated by Monte-Carlo simulations. And the coefficients of SRSM to construct limit state functions at some iteration during PMA and SORA procedures are given in Tables 5 and 6, respectively, where u_1 and u_2 are the normalized values of Young's modulus E_0 and applied loads F_x and F_y , respectively.

From the comparison of the results, the application of SRSM with SGD in RBTO enables different topologies from that obtained by DTO, as shown in Figures 7 and 8. RBTOs use more material by 11.85% than DTO, corresponding with the reliability index rising to 3.003, as the results listed in Table 4. It can also be seen from the results listed in Table 4 that there is practically no difference in the optimum volume obtained by SORA and PMA. However, the number of reliability analyses for SORA significantly reduces to 3, compared with that for PMA which rises to 171. Based on the result, it also concluded that SRSM has good performance in reliability analysis and that SGD is able to generate reasonable sampling points.

6.3. Heat Conduction Problem. Here, the extended heat conduction problem is considered, as shown in Figure 9. The dimensions of the structure are $L = 80$ mm and the thickness is $t = 1$ mm. The thermal conductivity $k_0 = 0.4$ W/(mm·K) is

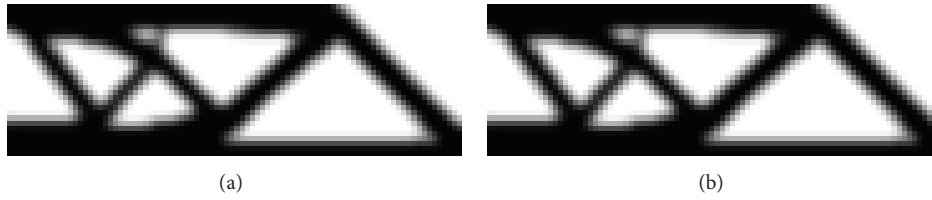


FIGURE 5: Resulting topologies of RBTO: (a) PMA; (b) SORA.

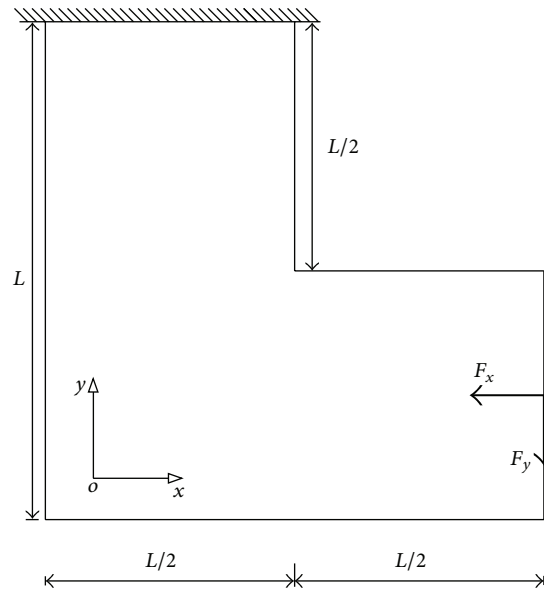


FIGURE 6: Design domain of the loaded knee structure.



FIGURE 7: Resulting topology of DTO.

TABLE 6: Approximated limit state function constructed by SRSM in SORA.

Iteration	a_0	a_1	a_2	a_3	a_4	a_5	a_6	a_7	a_8	a_9
1	-0.0199	0.1130	-0.0971	-0.1101	-0.0114	0.0103	-0.0048	-0.0000	-0.0055	0.0117
2	0.3531	0.0717	-0.0623	-0.0691	-0.0072	0.0066	-0.0031	0.0000	-0.0035	0.0073
3	0.3517	0.0718	-0.0624	-0.0693	-0.0073	0.0066	-0.0031	-0.0000	-0.0035	0.0073

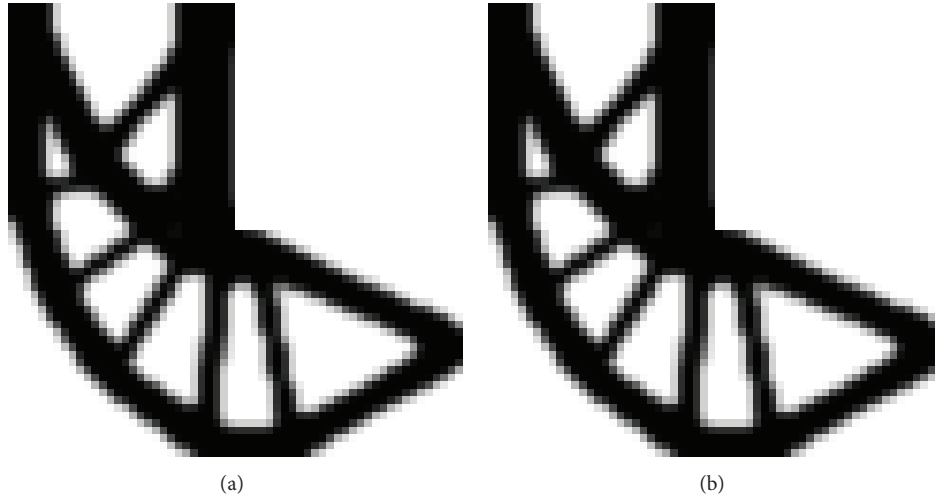


FIGURE 8: Resulting topologies of RBTO: (a) PMA; (b) SORA.

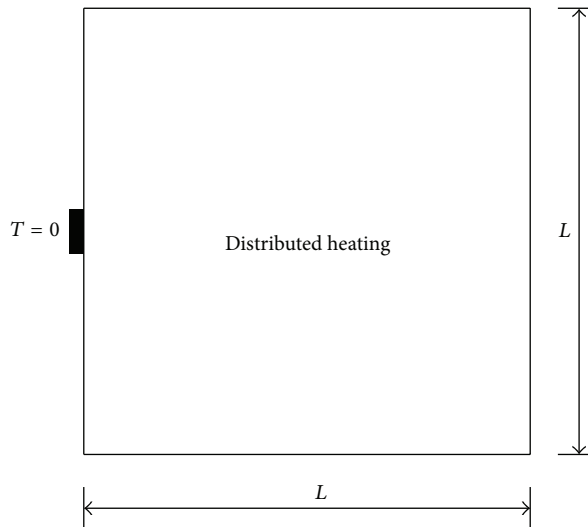


FIGURE 9: Design domain of the loaded knee structure.

assumed. The square plate is evenly heated by constant heat source $Q = 0.001 \text{ W/mm}^2$ and the temperature of the center of the left edge is set to 0. Design domain is discretized by 6400 (80×80) four-node elements. Random variables are chosen as thermal conductivity k_0 and constant heat source Q . Each variable is assumed to be normally distributed and has 10% standard deviation of the mean value.

In this example, the objective function is volume, and the limit state function is defined as $G = \varphi_{\max} - \varphi$. φ is the dissipation of heat transport potential capacity, and φ_{\max} is the allowable dissipation of heat transport potential capacity and is assigned to 500 W. The target reliability index is set to 3.0.

The optimal topologies and temperature contours obtained by DTO and RBTOs are presented in Figures 10 and 11, respectively. The optimization results obtained from each approach are summarized in Table 7, including volume/volume fraction, reliability index, computing time, and design

point. The reliability index is calculated by Monte-Carlo simulations. And the coefficients of SRSM to construct limit state functions at some iteration during PMA and SORA procedures are given in Tables 8 and 9, respectively, where u_1 and u_2 are the normalized values of thermal conductivity k_0 and constant heat source Q , respectively.

It can be found that the application of SRSM with SGD in RBTO also has well-behaved heat conduction problem. From the comparison of the results, the optimal solutions obtained by RBTO have different topologies from those obtained by DTO, as shown in Figure 10. As the results listed in Table 7 show, RBTOs use more material than DTO by 6.84%, improving the reliability index by up to 3.003. It can also be seen from the results listed in Table 7 that the optimum volume obtained by SORA and PMA is identical. However, SORA seems to be more efficient than PMA, as the number of reliability analyses significantly reduces, as presented in Tables 8 and 9.

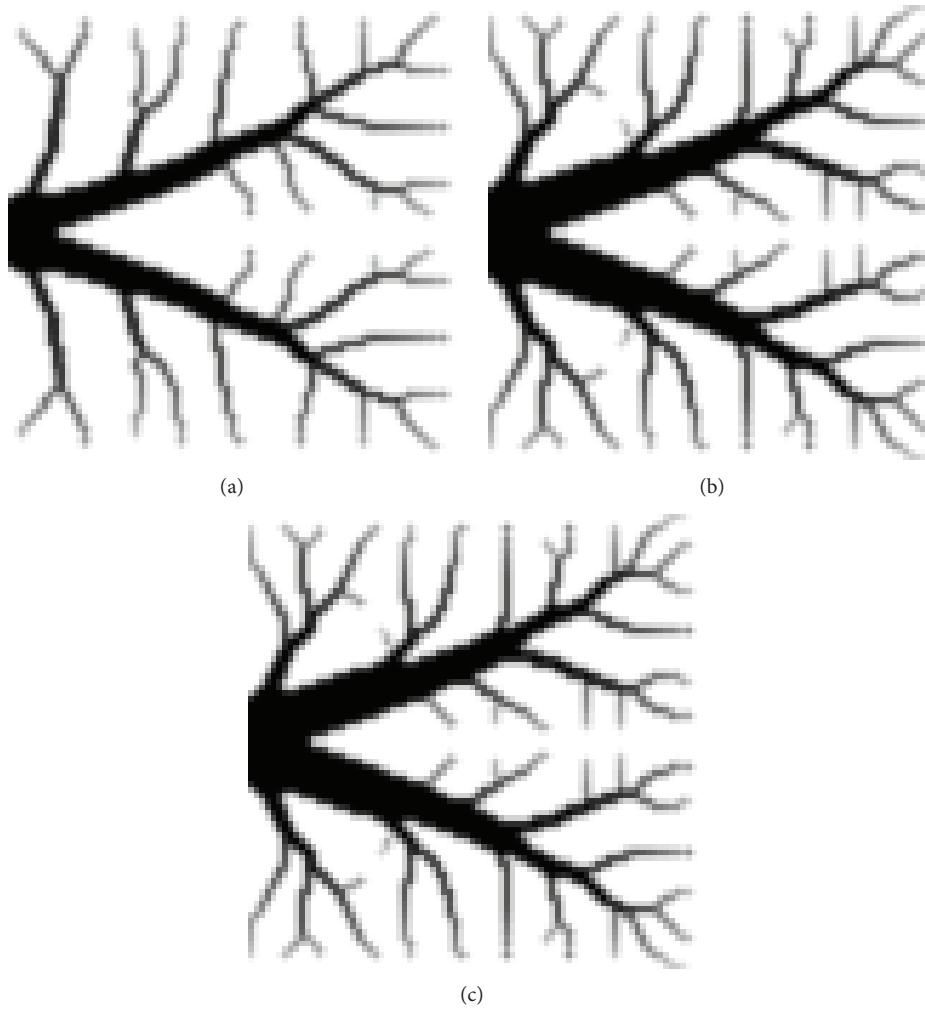


FIGURE 10: Resulting topologies: (a) DTO; (b) PMA; (c) SORA.

TABLE 7: Comparison of topology optimization design results.

Approach	Volume/volume fraction (mm ²)/%	Reliability index (β)	Computing time (s)	Design point	
				$k_0/W/(mm \cdot K)$	$Q/W/mm^2$
DTO	1112.7409/17.39	—	144.75	—	—
PMA	1551.0111/24.23	3.003	2697.55	0.332	1.25×10^{-3}
SORA	1551.0111/24.23	3.003	400.45	0.332	1.25×10^{-3}

TABLE 8: Approximated limit state function constructed by SRSM in PMA.

Iteration	a_0	a_1	a_2	a_3	a_4	a_5
1	-0.6505	0.1861	-0.3425	-0.0188	0.0356	-0.0174
2	-0.1788	0.1329	-0.2446	-0.0134	0.0254	-0.0124
\vdots	\vdots	\vdots	\vdots	\vdots	\vdots	\vdots
203	0.3762	0.0703	-0.1294	-0.0071	0.0135	-0.0066
204	0.3762	0.0703	-0.1294	-0.0071	0.0135	-0.0066

Approximated limit state function: $g(\mathbf{u}) = a_0 + a_1 u_1 + a_2 u_2 + a_3 (u_1^2 - 1) + a_4 u_1 u_2 + a_5 (u_2^2 - 1)$.

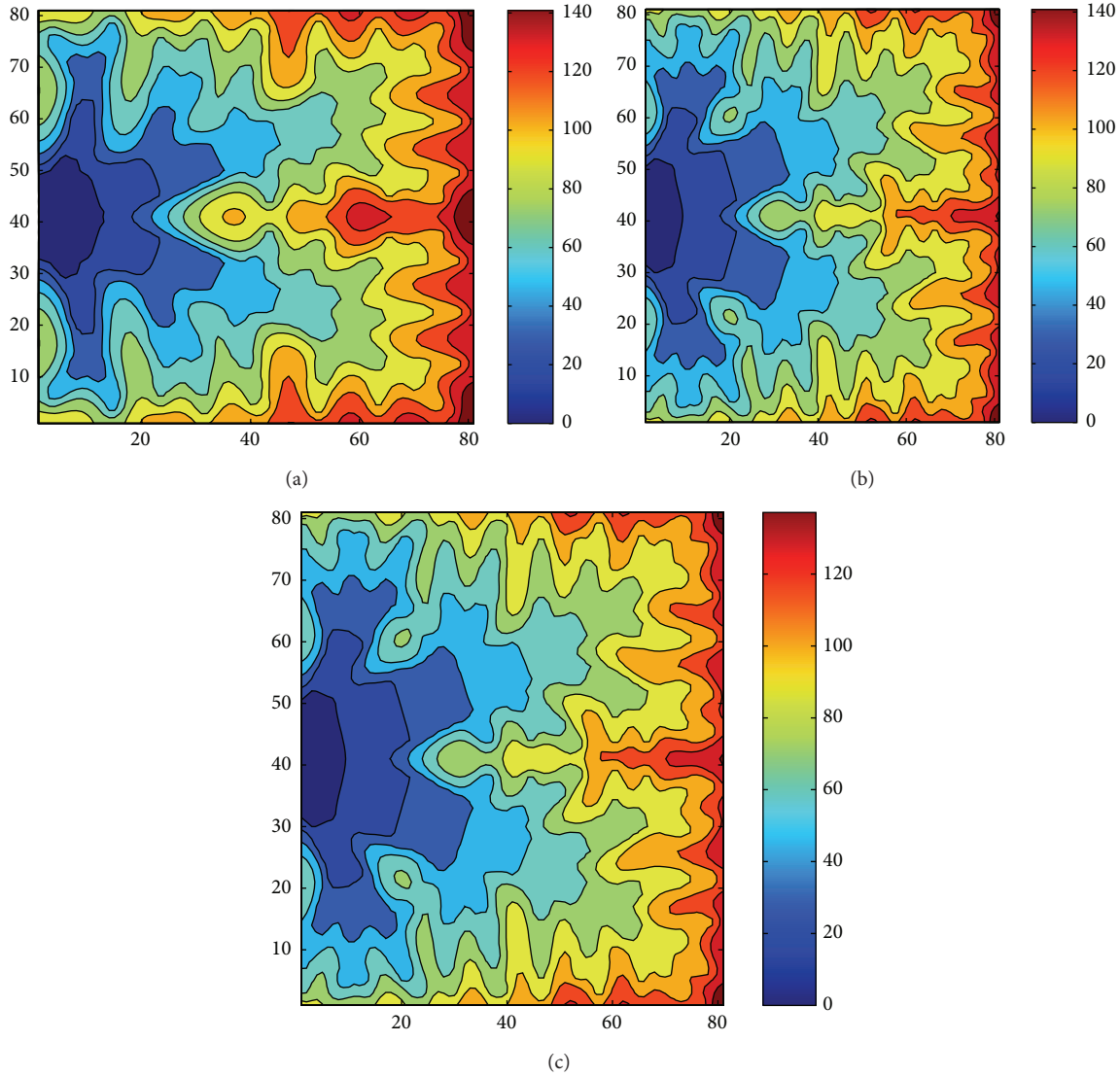


FIGURE 11: Resulting temperature contour: (a) DTO; (b) PMA; (c) SORA.

TABLE 9: Approximated limit state function constructed by SRSM in PMA.

Iteration	a_0	a_1	a_2	a_3	a_4	a_5
1	-0.0182	0.1148	-0.2113	-0.0116	0.0220	-0.0107
2	0.3762	0.0703	-0.1294	-0.0071	0.0135	-0.0066

7. Conclusion

This paper presents a mathematical framework that integrates the reliability concept into topology optimization to solve RBTO problems under uncertainty. Typically, two RBTO methodologies are implemented on several numerical examples including PMA and SORA. To enhance the computational efficiency, reliability analysis is carried out by SRSM and SGD. From the comparison of the numerical results, the following conclusions are obtained.

- (1) SRSM with SGD can produce an efficient reliability analysis in RBTO, where the limit state function is approximated by SRSM, combined with SGD to generate the reasonable sampling points.
- (2) The optimal solutions of RBTO are more reliable than those obtained by DTO, where more material is used and different topologies may be obtained. SORA seems to be more efficient than PMA, as the number of reliability analyses significantly reduces.
- (3) It should be noticed that the computation cost of RBTO is still a challenge, because repeated reliability analysis is required for different sets of variables, especially when involving complex practical structures. One possible extension is integrating more efficient surrogate models and reasonable DOE to improve the numerical efficiency of reliability analysis.

Conflict of Interests

The authors declare that there is no conflict of interests regarding the publication of this paper.

Acknowledgments

This research is supported by National Natural Science Foundation of China (Grant nos. 51275040 and 50905017) and the Programme of Introducing Talents of Discipline to Universities (no. B12022). The authors are also grateful to Krister Svanberg for providing his implementation of the MMA algorithm.

References

- [1] M. P. Bendsøe and N. Kikuchi, "Generating optimal topologies in structural design using a homogenization method," *Computer Methods in Applied Mechanics and Engineering*, vol. 71, no. 2, pp. 197–224, 1988.
- [2] H. A. Eschenauer and N. Olhoff, "Topology optimization of continuum structures: a review," *Applied Mechanics Reviews*, vol. 54, no. 4, pp. 331–389, 2001.
- [3] M. P. Bendsøe and O. S. Sigmund, *Topology Optimization: Theory, Methods and Application*, Springer, Berlin, Germany, 2003.
- [4] Y. M. Xie and G. P. Steven, *Evolutionary Structural Optimization*, Springer, London, UK, 1997.
- [5] K. Maute and D. M. Frangopol, "Reliability-based design of MEMS mechanisms by topology optimization," *Computers and Structures*, vol. 81, no. 8–11, pp. 813–824, 2003.
- [6] Z. Kang and Y. Luo, "Non-probabilistic reliability-based topology optimization of geometrically nonlinear structures using convex models," *Computer Methods in Applied Mechanics and Engineering*, vol. 198, no. 41–44, pp. 3228–3238, 2009.
- [7] X. M. Zhang and G. F. Ouyang, "A level set method for reliability-based topology optimization of compliant mechanisms," *Science in China E: Technological Sciences*, vol. 51, no. 4, pp. 443–455, 2008.
- [8] K.-H. Cho, J.-Y. Park, M.-G. Im, and S.-Y. Han, "Reliability-based topology optimization of electro thermal-compliant mechanisms with a new material mixing method," *International Journal of Precision Engineering and Manufacturing*, vol. 13, no. 5, pp. 693–699, 2012.
- [9] K.-H. Cho, J.-Y. Park, S.-P. Ryu, and S.-Y. Han, "Reliability-based topology optimization based on bidirectional evolutionary structural optimization using multi-objective sensitivity numbers," *International Journal of Automotive Technology*, vol. 12, no. 6, pp. 849–856, 2011.
- [10] R. Y. Rubinstein, *Simulation and the Monte Carlo Method*, John Wiley & Sons, New York, NY, USA, 1981.
- [11] C. Sundararajan, *Probabilistic Structural Mechanics Handbook: Theory and Industrial Applications*, Springer, New York, NY, USA, 1995.
- [12] M. R. Rajashekhar and B. R. Ellingwood, "A new look at the response surface approach for reliability analysis," *Structural Safety*, vol. 12, no. 3, pp. 205–220, 1993.
- [13] S. S. Isukapalli, A. Roy, and P. G. Georgopoulos, "Stochastic response surface methods (SRSMs) for uncertainty propagation: application to environmental and biological systems," *Risk Analysis*, vol. 18, no. 3, pp. 351–363, 1998.
- [14] I. Enevoldsen and J. D. Sørensen, "Reliability-based optimization in structural engineering," *Structural Safety*, vol. 15, no. 3, pp. 169–196, 1994.
- [15] J. Tu, K. K. Choi, and Y. H. Park, "A new study on reliability-based design optimization," *Journal of Mechanical Design (ASME)*, vol. 121, no. 4, pp. 557–564, 1999.
- [16] C. Kim, S. Wang, K.-R. Bae, H. Moon, and K. K. Choi, "Reliability-based topology optimization with uncertainties," *Journal of Mechanical Science and Technology*, vol. 20, no. 4, pp. 494–504, 2006.
- [17] G. Kharmanda, N. Olhoff, A. Mohamed, and M. Lemaire, "Reliability-based topology optimization," *Structural and Multidisciplinary Optimization*, vol. 26, no. 5, pp. 295–307, 2004.
- [18] Z. Luo, L. P. Chen, J. Z. Yang, Y. Q. Zhang, and K. Abdel-Malek, "Fuzzy tolerance multilevel approach for structural topology optimization," *Computers & Structures*, vol. 84, no. 3–4, pp. 127–140, 2006.
- [19] Y. Luo, Z. Kang, Z. Luo, and A. Li, "Continuum topology optimization with non-probabilistic reliability constraints based on multi-ellipsoid convex model," *Structural and Multidisciplinary Optimization*, vol. 39, no. 3, pp. 297–310, 2009.
- [20] M. Silva, D. A. Tortorelli, J. A. Norato, C. Ha, and H. R. Bae, "Component and system reliability-based topology optimization using a single-loop method," *Structural and Multidisciplinary Optimization*, vol. 41, no. 1, pp. 87–106, 2010.
- [21] T. H. Nguyen, J. Song, and G. H. Paulino, "Single-loop system reliability-based topology optimization considering statistical dependence between limit-states," *Structural and Multidisciplinary Optimization*, vol. 44, no. 5, pp. 593–611, 2011.
- [22] K.-S. Yoo, Y.-S. Eom, J.-Y. Park, M.-G. Im, and S.-Y. Han, "Reliability-based topology optimization using successive standard response surface method," *Finite Elements in Analysis and Design*, vol. 47, no. 7, pp. 843–849, 2011.
- [23] Y.-S. Eom, K.-S. Yoo, J.-Y. Park, and S.-Y. Han, "Reliability-based topology optimization using a standard response surface method for three-dimensional structures," *Structural and Multidisciplinary Optimization*, vol. 43, no. 2, pp. 287–295, 2011.
- [24] A. M. Hasofer and N. C. Lind, "An exact and invariant first order reliability format," *ASCE Journal of Engineering Mechanics*, vol. 100, no. 1, pp. 111–121, 1974.
- [25] X. Du and W. Chen, "Sequential optimization and reliability assessment method for efficient probabilistic design," *Journal of Mechanical Design, Transactions of the ASME*, vol. 126, no. 2, pp. 225–233, 2004.
- [26] F. Xiong, W. Chen, Y. Xiong, and S. Yang, "Weighted stochastic response surface method considering sample weights," *Structural and Multidisciplinary Optimization*, vol. 43, no. 6, pp. 837–849, 2011.
- [27] S. A. Smolyak, "Quadrature and interpolation formulas for tensor products of certain classes of functions," *Soviet Mathematics*, vol. 1, no. 4, pp. 240–243, 1963.
- [28] H. Yserentant, "On the multilevel splitting of finite element spaces," *Numerische Mathematik*, vol. 49, no. 4, pp. 379–412, 1986.
- [29] T. Gerstner and M. Griebel, "Numerical integration using sparse grids," *Numerical Algorithms*, vol. 18, no. 3–4, pp. 209–232, 1998.

- [30] K. Svanberg, "The method of moving asymptotes—a new method for structural optimization," *International Journal for Numerical Methods in Engineering*, vol. 24, no. 2, pp. 359–373, 1987.
- [31] O. Sigmund, "Morphology-based black and white filters for topology optimization," *Structural and Multidisciplinary Optimization*, vol. 33, no. 4-5, pp. 401–424, 2007.

Research Article

Improved Genetic Algorithm with Two-Level Approximation for Truss Optimization by Using Discrete Shape Variables

Shen-yan Chen, Xiao-fang Shui, Dong-fang Li, and Hai Huang

School of Astronautics, Beihang University, XueYuan Road No. 37, HaiDian District, Beijing 100191, China

Correspondence should be addressed to Shen-yan Chen; chenshenyan@buaa.edu.cn

Received 25 September 2014; Revised 10 April 2015; Accepted 17 April 2015

Academic Editor: P. Beckers

Copyright © 2015 Shen-yan Chen et al. This is an open access article distributed under the Creative Commons Attribution License, which permits unrestricted use, distribution, and reproduction in any medium, provided the original work is properly cited.

This paper presents an Improved Genetic Algorithm with Two-Level Approximation (IGATA) to minimize truss weight by simultaneously optimizing size, shape, and topology variables. On the basis of a previously presented truss sizing/topology optimization method based on two-level approximation and genetic algorithm (GA), a new method for adding shape variables is presented, in which the nodal positions are corresponding to a set of coordinate lists. A uniform optimization model including size/shape/topology variables is established. First, a first-level approximate problem is constructed to transform the original implicit problem to an explicit problem. To solve this explicit problem which involves size/shape/topology variables, GA is used to optimize individuals which include discrete topology variables and shape variables. When calculating the fitness value of each member in the current generation, a second-level approximation method is used to optimize the continuous size variables. With the introduction of shape variables, the original optimization algorithm was improved in individual coding strategy as well as GA execution techniques. Meanwhile, the update strategy of the first-level approximation problem was also improved. The results of numerical examples show that the proposed method is effective in dealing with the three kinds of design variables simultaneously, and the required computational cost for structural analysis is quite small.

1. Introduction

The optimal design of a truss structure has been an active research topic for many years. Important progress has been made in both optimality criteria and solution techniques. As is well known, the optimal shape design of a truss structure depends not only on its topology but also on the element cross-sectional areas. This inherent coupling of structural shape, topology, and element sections explicitly indicates that the truss shape or topology or sizing optimization should not be performed independently. To date, most researchers focus on the subject of truss shape and sizing optimization [1–3] or topology and sizing optimization [4, 5], while relatively little literature is available on truss shape, topology, and sizing simultaneous optimization [6, 7]. The main obstacle is that shape and topology and sizing variables are fundamentally different physical representations. Combining these three types of variables may entail considerable mathematical difficulties and, sometimes, lead to ill-conditioning problem

because their changes are of widely different orders of magnitude.

GA has been widely applied in truss topology optimization, especially for mixed variable problems. Based on various given problems, many specific GA methods have been proposed [8, 9]. However, they are still not completely satisfactory owing to their high computational cost and unstable reliability, especially for large scale structures [10, 11]. It is, therefore, apparent that the efficiency and reliability of GA retain large space to be improved further.

To improve the efficiency of truss sizing/topology optimization, Dong and Huang [12] proposed a GA with a two-level approximation (GATA), which obtains an optimal solution by alternating topology optimization and size optimization. As the structural analyses are used for building a series of approximate problems and the GA is conducted based on the approximate functions, the computational efficiency is greatly improved and the number of structural analyses can be reduced to the order of tens. Later, Li et al. [5]

improved the GATA to enhance its exploitation capabilities and convergence stability. However, the shape variables are not involved in their research.

In this paper, based on the truss topology and sizing optimization system using GATA [5], a series of techniques were proposed to implement the shape, topology, and sizing optimization simultaneously in a single procedure. Firstly, a new optimization model is established, in which the truss nodal coordinates are taken as shape variables. To avoid calculating sensitivity of shape variables, discrete variables are used by adding the length of the individual chromosome. Therefore, sizing variables are continuous and shape/topology variables are discrete. To solve this problem, a first-level approximate problem is improved for the change of truss shape. Then, GA is used to optimize the individuals which include discrete 0/1 topology variables representing the deletion or retention of each bar and the integer-valued shape variables corresponding to nodal coordinates. Within each GA generation, a nesting strategy is applied in calculating the fitness value of each member [5, 12]. That is, for each member, a second-level approximation method is used to optimize the continuous size variables [5, 12]. In terms of GA, hybrid gene coding strategy is introduced, as well as the improvement of genetic operators. The controlled mutation of shape variables is considered in the generation of initial population. The uniform crossover is implemented for discrete topology variables and shape variables independently. Meanwhile, the first-level approximation problem update strategy was also improved in this paper. The proposed method is examined with typical truss structures and is shown to be quite effective and reliable.

This paper is organized as follows. In Section 2, we describe the optimization formulation for truss sizing/shape/topology optimization. In Section 3, we describe the optimization method GATA and in Section 4 the details of improvements for the optimization method are stated. In Section 5, we present our numerical examples and the algorithm performance and conclusion remarks are given in Sections 6 and 7, respectively.

2. Problem Formulation

The truss sizing/shape/topology optimization problem is formulated in (1). Here, three kinds of design variables are defined as follows.

- (1) *Sizing Variables.* $X = \{x_1, x_2, \dots, x_n\}^T$ is the size variable vector, with x_i ($i = 1, 2, \dots, n$) denoting the cross-sectional area of bar members in i th group and n denoting the number of groups.
- (2) *Shape Variables.* $Y = \{y_1, y_2, \dots, y_m\}^T$ is the shape variable vector, and m is the number of shape variables; $y_e = y_{e,d}$ ($d = 1, \dots, p_e$) denotes the identifier number within the possible coordinates set $\{y_{e,1}, \dots, y_{e,p_e}\}$, and p_e is the number of possible coordinates of e th shape variable.
- (3) *Topology Variables.* $\alpha = \{\alpha_1, \alpha_2, \dots, \alpha_n\}^T$ is the topology variable vector. If $\alpha_i = 0$, members in i th group

are removed, and x_i is set to a very small value x_i^b , which is generally calculated as 10^{-4} multiplied by the initial value of x_i ; if $\alpha_i = 1$, members in i th group are retained, and x_i is optimized between the upper bound x_i^U and the lower bound x_i^L :

$$\begin{aligned}
 \text{Find } & X = \{x_1, x_2, \dots, x_n\}^T, \\
 & Y = \{y_1, y_2, \dots, y_m\}^T, \\
 & \alpha = \{\alpha_1, \alpha_2, \dots, \alpha_n\}^T, \\
 \text{min } & W = \sum_{i=1}^n \alpha_i f_i(X) \\
 \text{s.t. } & \beta_j g_j(X) \leq 0 \quad j = 1, \dots, k - v, \\
 & g_j(X) \leq 0 \quad j = k - v + 1, \dots, k, \\
 & \alpha_i x_i^L + (1 - \alpha_i) x_i^b \leq x_i \quad i = 1, \dots, n, \\
 & x_i \leq \alpha_i x_i^U + (1 - \alpha_i) x_i^b, \\
 & \alpha_i = 0 \text{ or } \alpha_i = 1, \\
 & y_e = y_{e,d} \in \{y_{e,1}, \dots, y_{e,p_e}\} \\
 & d = 1, \dots, p_e; \quad e = 1, \dots, m,
 \end{aligned} \tag{1}$$

where W is the total weight of the truss structure and $f_i(X, Y)$ denotes the weight of i th group. $g_j(X, Y)$ represents j th constraint in the model, which could be constraints of element stresses, node displacements, mode frequency, or buckling factor. k denotes the total number of constraints, and v is the number of frequency or bulking constraints. If some bar members are removed, the corresponding constraints are eliminated, such as the stress constraints of the removed members. Thus, β_j indicates whether the respective constraint is eliminated; if $\beta_j = 0$, j th constraint is eliminated; otherwise if $\beta_j = 1$, j th constraint is retained.

To facilitate describing the optimization model, a truss structure is taken as an example, which is shown in Figure 1. y coordinate of node 1 could be 100, 120, 140, and 160, while x coordinate of node 2 could be 200, 240, and 280. It is required that the coordinate variation of node 1 and node 2 is independent and that node 1 should be symmetric with node 3 along the dotted line, which means that there are two independent shape variables. In addition, the cross-sectional dimension of each bar element is required to be optimized independently and each bar element is allowed to be deleted or retained, which means that there are 7 size variables and 7 topology variables.

3. Optimization Method

3.1. The First-Level Approximate Problem. To solve problem (1) which is always implicit, a first-level problem is constructed to transform $f_i(X)$ and $g_j(X)$ into a sequence of

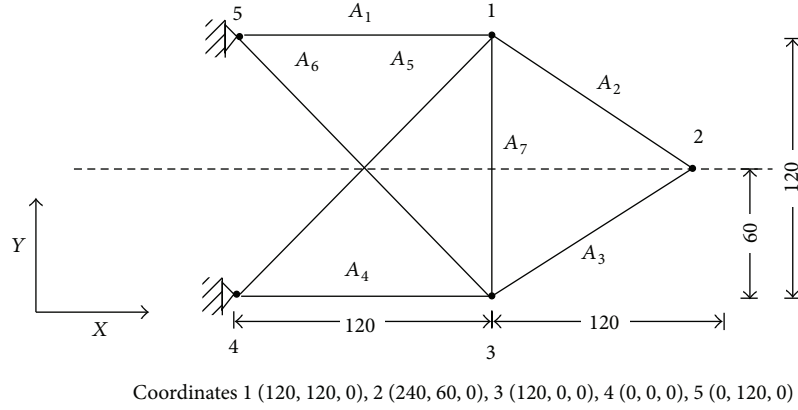


FIGURE 1: Seven-bar truss and node coordinates.

nonlinear explicit approximate functions. In p th stage, the approximate explicit problem can be stated as

$$\begin{aligned}
 &\text{Find } X = \{x_1, x_2, \dots, x_n\}^T, \\
 &Y = \{y_1, y_2, \dots, y_m\}^T, \\
 &\alpha = \{\alpha_1, \alpha_2, \dots, \alpha_n\}^T, \\
 &\min W = \sum_{i=1}^n \alpha_i f_i^{(p)}(X) \\
 &\text{s.t. } \beta_j g_j^{(p)}(X) \leq 0 \quad j = 1, \dots, J_1, \\
 &g_j^{(p)}(X) \leq 0 \quad j = J_1 + 1, \dots, J, \\
 &\alpha_i x_{i(p)}^L + (1 - \alpha_i) x_i^b \leq x_i \quad i = 1, \dots, n, \\
 &x_i \leq \alpha_i x_{i(p)}^U + (1 - \alpha_i) x_i^b, \\
 &\alpha_i = 0 \text{ or } \alpha_i = 1, \\
 &y_e = y_{e,d} \in \{y_{e,1}, \dots, y_{e,p_e}\} \\
 &d = 1, \dots, p_e; \quad e = 1, \dots, m,
 \end{aligned} \tag{2}$$

$$x_{i(p)}^U = \min \{x_i^U, \bar{x}_{i(p)}^U\}, \tag{3}$$

$$x_{i(p)}^L = \max \{x_i^L, \bar{x}_{i(p)}^L\}, \tag{4}$$

where $x_{i(p)}^U$ and $x_{i(p)}^L$ are upper and lower bounds of size variable x_i at p th stage; $\bar{x}_{i(p)}^U$ and $\bar{x}_{i(p)}^L$ are the moving limits of x_i at p th stage; $g_j^{(p)}(X)$ are j th approximate constraint function at p th stage, which is constructed as follows. First, structural and sensitivity analysis are implemented at the point $X_{(p)} = \{x_{1(p)}, x_{2(p)}, \dots, x_{n(p)}\}^T$ to obtain the constraint response. Second, the results of structural and sensitivity analysis are

used to construct a branched multipoint approximate (BMP) function ((5)–(8)) [5, 12]:

$$g_j^{(p)}(X) = \sum_{t=p-(H-1)}^p \left\{ g_j(X_t) + \sum_{i=1}^n \tilde{g}_{j,i,t}(X) \right\} h_t(X), \tag{5}$$

$$\tilde{g}_{j,i,t}(X) = \begin{cases} \frac{1}{r_{o,t}} \frac{\partial g_j(X_t)}{\partial x_i} x_{it}^{1-r_{o,t}} (x_i^{r_{o,t}} - x_{it}^{r_{o,t}}), & \text{if } \alpha_i = 1 \\ \frac{1}{r_{m,t}} \frac{\partial g_j(X_t)}{\partial x_i} (1 - e^{-r_{m,t}(x_i - x_{it})}), & \text{if } \alpha_i = 0, \end{cases} \tag{6}$$

$$h_t(X) = \frac{\bar{h}_t(X)}{\sum_{l=1}^H \bar{h}_l(X)} \quad t = 1, \dots, H, \tag{7}$$

$$\bar{h}_l(X) = \prod_{s=1, s \neq l}^H (X - X_s)^T (X - X_s), \tag{8}$$

$$\begin{aligned}
 &\min \sqrt{\left\{ \sum_{z=1}^H g_j(X_z) - g_j(X_t) - \tilde{g}_{j,i,t}(X_t) \right\}^2} \\
 &\text{s.t. } -5 \leq r_{o,t} \leq 5, \\
 &\quad -5 \leq r_{m,t} \leq 5,
 \end{aligned} \tag{9}$$

$$t = 1, \dots, H,$$

where X_t is t th known point, H is the number of points to be counted, and $H = \min\{p, H_{\max}\}$. When the number of known points is larger than H_{\max} (always set as 5), only the last H_{\max} points are counted; $h_t(X)$ is a weighting function, which is defined in (7)–(8); $r_{o,t}$ and $r_{m,t}$ are the adaptive parameter controlling the nonlinearity of $g_j^{(p)}(X)$, which are determined by solving the least squares parameter estimation in (9). When $t = 1$, $r_{o,t} = -1$ and $r_{m,t} = 3.5$. For more details of BMP function, please see the work by Dong and Huang (2004) [12]. Though problem (2) is explicit, it involves topology and shape variables which cannot be directly solved by mathematical programming method. Thus a GA is implemented for explicit mixed variables problem (2).

3.2. GA to Deal with Mixed Variables Problem. GA is used to generate and operate on sequences of mixed variables vector $S = \{y_1, y_2, \dots, y_m, \alpha_1, \alpha_2, \dots, \alpha_n\}^T$ representing the truss shape and topology, in which α_i ($i = 1, \dots, n$) is 0/1 variables and y_d ($d = 1, \dots, m$) is integer-valued variable. Based on the optimum vector S_{p-1}^* obtained in the last iteration, the GA generates an initial population randomly, in which the vector $S_{l,k,p}$ ($k = 1$) represents l th individual in k th generation at p th iteration of the first-level approximate problem. Then, for every individual in the current generation, the optimal size variables vector $X_{l,k,p}^*$ is obtained by solving a second-level approximation problem, which will be described later in Section 3.3. To reduce the structural analyses, the objective value $W^{(p)}(X_{l,k,p}^*)$ is calculated accurately with analytic expressions, and the constraint value $g_j^{(p)}(X_{l,k,p}^*)$ is calculated with approximate functions ((5)–(9)). Then, $W^{(p)}(X_{l,k,p}^*)$ and $g_j^{(p)}(X_{l,k,p}^*)$ are used to calculate the fitness of individual $X_{l,k,p}^*$ with penalty function method (10). For more details of penalty functions, please see work by Li et al. (2014) [5]. Consider

$$\begin{aligned} \text{penal}(X_{l,k,p}^*) &= \overline{W}' \sum_{j=1}^{J_1} \frac{|\overline{g}_j|}{\sum_{j=1}^{J_1} \overline{g}_j} v_j(X_{l,k,p}^*), \\ \text{fitness}(X_{l,k,p}^*) &= \{f_{\max}^p - (W^{(p)}(X_{l,k,p}^*) + \text{penal}(X_{l,k,p}^*))\} \\ &\cdot \left(1 + \frac{M_{\text{crit}}}{J_1}\right). \end{aligned} \quad (10)$$

After the fitness value of all the members in the initial generation is calculated, the genetic selection, crossover, and mutation operators work on the vector $S_{l,k,p}$ in sequence based on the individual fitness value $\text{fitness}(X_{l,k,p}^*)$ to generate the next generation ($k = k + 1$). The different genetic operations on 0/1 variables vectors $\alpha = \{\alpha_1, \alpha_2, \dots, \alpha_n\}^T$ and integer-valued variables vectors $Y = \{y_1, y_2, \dots, y_m\}^T$ will be described in Section 4. When the maximum generation ($\max G$) is reached, the optimum vectors S_p^* and X_p^* are obtained for the next iteration ($p = p + 1$) of the first-level approximate problem.

3.3. The Second-Level Approximate Problem. After constructing first-level approximate problem (2) and implementing GA to generate sequences of vector $S_{l,k,p}$, original problem (1) is transformed to an explicit problem with continuous size variables only. To improve the computational efficiency, a second-level approximate problem is constructed using linear Taylor expansions of reciprocal design variables [5, 12]. In m th step, the second-level approximate problem is stated in

$$\begin{aligned} \min W^{(m)}(\overline{X}) \\ = \overline{W}(\overline{X}_{(m)}) + \sum_{d=1}^D \frac{\partial \overline{W}(\overline{X}_{(m)})}{\partial \overline{x}_d} (\overline{x}_d - \overline{x}_{d(m)}) \end{aligned}$$

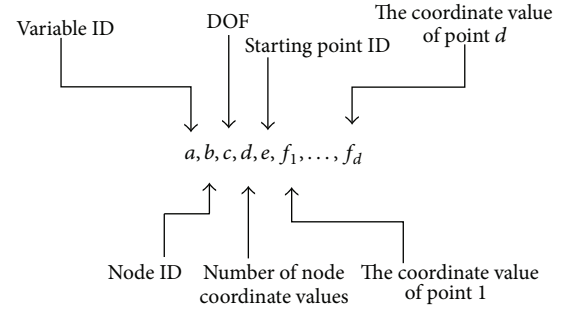


FIGURE 2: The definition of shape variables.

$$\begin{aligned} \text{s.t. } g_j^{(m)}(\overline{X}) \\ = \tilde{g}_j(\overline{X}_{(m)}) \\ - \sum_{d=1}^D \tilde{x}_{d(m)}^2 \frac{\partial \tilde{g}_j(\overline{X}_{(m)})}{\partial \tilde{x}_d} \left(\frac{1}{\tilde{x}_d} - \frac{1}{\tilde{x}_{d(m)}} \right) \leq 0 \\ j = 1, \dots, J_2, \\ \overline{x}_{d(m)}^L \leq \tilde{x}_d \leq \overline{x}_{d(m)}^U \quad d = 1, \dots, D, \end{aligned} \quad (11)$$

where $W^{(m)}(\overline{X})$ is the approximate objective value and $g_j^{(m)}(\overline{X})$ is the approximate value of j th constraint in m th step; $\overline{x}_{d(m)}^U$ and $\overline{x}_{d(m)}^L$ are move limits of \overline{X}_d and $\overline{x}_{d(m)}^U$ and $\overline{x}_{d(m)}^L$ are upper and lower bounds of x_d in m th step. After constructing the second-level approximate problem, a dual method and a BFGS are used to seek the optimal size variable $X_{l,k,p}^*$ [5, 12].

4. Improvements in GATA for Adding Shape Variables

To facilitate describing the improvements for adding shape variables in GATA, the truss structure in Figure 1 is also taken as an example.

4.1. Definition of Shape Variables and Variable Link. In problem (1), $Y = \{y_1, y_2, \dots, y_m\}^T$ is the shape variable vector; $y_e = 1 \sim p_e$ ($e = 1, 2, \dots, m$) denotes the identifier number of the possible coordinates. Each shape variable is defined with an array. As shown in Figure 2, a represents the identifier number of shape variables; b is the identifier number of the nodes to be moved; c means the direction of coordinate, which could be 1 or 2 or 3, corresponding to x - or y - or z -axis coordinate, respectively; d is the number of possible discrete coordinate values of node d ; e denotes the identifier number of node coordinates of the initial truss structure; $\{f_1, f_2, \dots, f_d\}$ denotes the discrete coordinate set of node b , or variable a , and $f_1 \leq f_2 \leq \dots \leq f_d$ (or $f_1 \geq f_2 \geq \dots \geq f_d$). The shape variables can be linked with each other; that is, some node coordinates could vary with a given relation, such as symmetric variation. The definition of shape variable link relation is explained in Figure 3. a represents the identifier

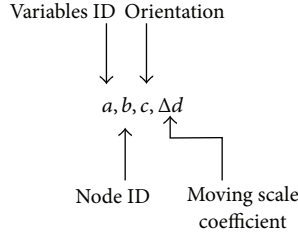


FIGURE 3: The link method of shape variables.

number of shape variables; b is the identifier number of the nodes that is expected to link; c denotes the direction of coordinate which is expected to link, $c = 1$ or 2 or 3 , corresponding to x - or y - or z -axis coordinate, respectively; Δd is defined as a moving scaling factor, which means that the linked coordinate value is $\Delta d \cdot x$ when the coordinate value of shape variable a is x ; $\Delta d = -1$ for symmetric nodes. According to the shape variable definition rules described above, the shape variables of node 1 and node 2 could be defined as follows:

- 1, 1, 2, 4, 2, 100, 120, 140, 160,
- 2, 2, 1, 3, 2, 200, 240, 280.

The node 3 is symmetric with node 1 along the dotted line in Figure 1; thus, a sentence should be defined to describe the shape variable link relationship; that is,

- 1, 3, 2, -1.

The definitions of shape variables and variable link are further explained in Figures 2 and 3, respectively.

4.2. GA Execution Process

4.2.1. Hybrid Coding Strategy of Shape and Topology Variables.

In GATA, discrete variables are optimized through GA. After introducing the discrete shape variables, the string of genes should include the information of both topology variables and shape variables. Decimal coding is adopted for nodal positions, while the topology variables keep using binary format. The gene of each individual could be written as $S = y_1 y_2 \cdots y_m \alpha_1 \alpha_2 \cdots \alpha_n$ where $y_1 y_2 \cdots y_m$ and $\alpha_1 \alpha_2 \cdots \alpha_n$ represent the code of shape variables and topology variables, respectively. For instance, there are 2 shape variables and 7 topology variables in the truss of Figure 1; the gene of an individual is 1-3-1-1-1-1-0-1, which means the first shape variable taking the 1st coordinate in {100, 120, 140, 160} and the second shape variable taking the 3rd coordinate in {200, 240, 280}. The corresponding truss configuration is shown in Figure 4.

4.2.2. Generation of the Initial Population. The generation mechanism of the initial population is updated for involving shape variables. At the first/initial calling of GA, the initial population of the designs is generated randomly. Once the optimal members of the population have been obtained, the initial population of the next generation is generated

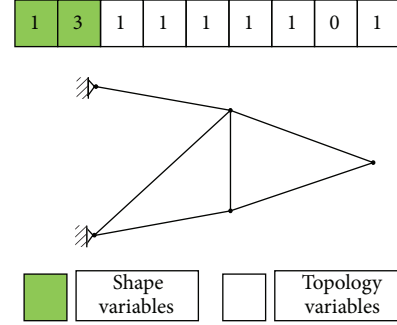


FIGURE 4: Example of individual gene code.

according to the elite of former generations of the GA. That is to say, from the second calling of the GA, the initial population consists of three parts: (1) there are the optimal individuals of the former generations; (2) members which are generated according to the optimal individuals of the last generation; that is, y_i ($i = 1, \dots, m$) sequentially mutate under control with a low probability (Section 4.2.4), while α_i will approach 0 with a greater probability if the corresponding optimal size variable x_i is small; (3) the mutation of y_i is the same as that in (2), while α_i mutate randomly with a given low probability. The mutation control technique of shape variables will be explained in Section 4.2.4.

According to our calculation experience, the population size and maximum evolutionary generation should exceed twice the total design variables. If it is more than 100, then it will take 100.

4.2.3. Roulette-Wheel Selection. Roulette-wheel selection is used to select a father design and a mother design from the parent generation, which is easy to be executed. Suggesting that the population size is M , the fitness value of i th individual in k th generation is F_i ; then the probability of individual i to be selected in the next generation is

$$P_{is} = \frac{F_i}{\sum_{i=1}^M F_i} \quad (12)$$

It can be seen from (12) that the individual of higher fitness value has greater probability to be selected. The fitness value of each individual is obtained using (10), as described in Section 3.2.

4.2.4. Uniform Crossover. Uniform crossover is popularly applied in the GA since it could produce better individuals and has lower probability to break good individuals. Since decimal coding is adopted for nodal coordinates, while the topology variables keep using binary format, crossover operator could not be carried on between these two kinds of code. Uniform crossover which operates gene by gene is implemented to the two areas independently. Before crossover, two individuals are selected randomly as mother and father chromosomes. Then, for each gene, a random value r within $0 \sim 1$ is generated. Let $x_1 =$ value of gene from the mother and let $x_2 =$ value of gene from the father. Let $y_1 =$ value of gene from the first child and let $y_2 =$ value of gene

from the second child. For 0/1 topology genes and integer-valued shape genes,

$$\begin{aligned} y_1 &= x_1, \\ y_2 &= x_2, \\ &\text{if } r > P_c \\ y_1 &= x_2, \\ y_2 &= x_1, \\ &\text{if } r \leq P_c, \end{aligned} \quad (13)$$

where P_c is the crossover probability. Repeat this process until a new population is generated with N individuals.

4.2.5. Controlled Uniform Mutation of Shape Variables. Uniform mutation and controlled uniform mutation are implemented for 0/1 topology genes and integer-valued genes, respectively. For each gene, a random number r between zero and one is generated. If $r \leq P_{\text{mutate}}$ (mutating probability), the gene is mutated. For 0/1 valued topology genes, the gene is mutated to its allelomorph ($0 \rightarrow 1, 1 \rightarrow 0$). For an integer-valued coordinate gene, a controlled mutation technique is implemented to limit the mutation range, which could decrease the numerical instability induced by the large change of coordinates and improve the accuracy of the first-level approximation functions.

Two parameters are included in the control mutation technique, which are mutation probability P_m and move limit P_{move} . Mutation operation is implemented to each point of shape gene sequentially with P_m . First, if a particular point needs to mutate, let us assume that the number of coordinate positions with respect to this shape variable is d and the present identifier number is e , and then the upper limit UP_{mute} and lower limit DO_{mute} of allowable mutation range are obtained as

$$\begin{aligned} UP_{\text{mute}} &= \begin{cases} \min([d \cdot P_{\text{move}}] + e, d) & d \cdot P_{\text{move}} \geq 1 \\ \min(1 + e, d) & d \cdot P_{\text{move}} \leq 1, \end{cases} \\ DO_{\text{mute}} &= \begin{cases} \max([e - d \cdot P_{\text{move}}], 1) & d \cdot P_{\text{move}} \geq 1 \\ \max(e - 1, 1) & d \cdot P_{\text{move}} < 1. \end{cases} \end{aligned} \quad (14)$$

Note that $[x]$ denotes the maximum integer not larger than x .

Then, an integer between UP_{mute} and DO_{mute} will be generated as the mutation result. Normally, $P_m = 0.001 \sim 0.5$ and $P_{\text{move}} = 0.3 \sim 0.5$.

4.3. Update Strategy of the First-Level Approximation Problem.

In p th iteration process of GATA for truss shape and topology optimization, the results of the structural and sensitivity analysis at X_p are used to construct the first-level approximation problem using the multipoint approximation function. After introducing the shape variables, the truss shape $Y = \{y_1, y_2, \dots, y_m\}^T|_p$ might be different from that in

the last iteration. Therefore, it is necessary to update the first-level approximation problem, so as to make it correspond to the present shape. The update strategy of the first-level approximation problem is then modified as follows. If the shape code of the optimal individual is inconsistent with that of the last iteration, a new first-level approximation problem will be built, and the number of known points H will be set as 1; else the first-level approximation problem is consistent with the last iteration and increases the number of known points H . The update strategy of the first-level approximate problem in the whole optimization process is emphasized in the algorithm flowchart (Figure 5).

4.4. Algorithm Flowchart. The flowchart of the IGATA (Improved Genetic Algorithm with Two-Level Approximation) for truss size/shape/topology optimization is shown in Figure 5. After getting the optimal X_p^* from the GA, a convergence criterion in (15) is used to determine whether the first-level approximate problem is terminated. Here, ε_1 is size variables convergence control parameter, ε_3 is weight convergence control parameter, ε_2 is the constraints control parameter, and p_{max} is the maximum iterative number for first-level approximate problem. The computational cost of IGATA is low because the first-level approximate techniques reduce the number of structural analyses significantly and the second-level approximate techniques reduce the number of the design variables significantly [5, 12]:

$$\begin{aligned} \left| \frac{x_{ip} - x_{i(p-1)}}{x_{i1}} \right| &\leq \varepsilon_1 \quad (i = 1, 2, \dots, n), \\ g_{\text{max}}(X_p) &= \max(g_1(X_p), \dots, g_m(X_p)) \leq \varepsilon_2 \\ &\text{or } p = p_{\text{max}}, \end{aligned} \quad (15)$$

$$\left| \frac{W(X_p) - W(X_{p-1})}{W(X_p)} \right| \leq \varepsilon_3.$$

5. Numerical Examples

5.1. Ten-Bar Truss. The ten-bar truss has been studied by Rajan [6], as shown in Figure 6. The unit of length is inch. Node 6 is the original point. The length of bars 1, 2, 3, 4, 5, and 6 is 360 in. Nodes 4 and 6 are separately applied to a force of 100000 lb. Young's modulus is $E = 10^7$ Psi and material density is 0.1 lb/in.³. The section area of each bar is taken as independent variable, which is originally 10 in.² and is permitted to vary between 1 in.² and 34 in.². y coordinates of nodes 1, 3, and 5 are taken as independent shape variables. The moveable range of y coordinate is 180 in. to 1000 in. Discrete coordinates are preset for the shape variables, as shown in Table 1. The shape variables and link relation are defined as definition. Therefore, there are 10 size variables, 10 topology variables, and 3 shape variables in all. The stress of each bar should not exceed $\pm 25,000$ Psi.

The parameters of GA are set as follows: population size 30, evolution generations 35, crossover probability 0.8, and mutation probability 0.05. The optimized solution of

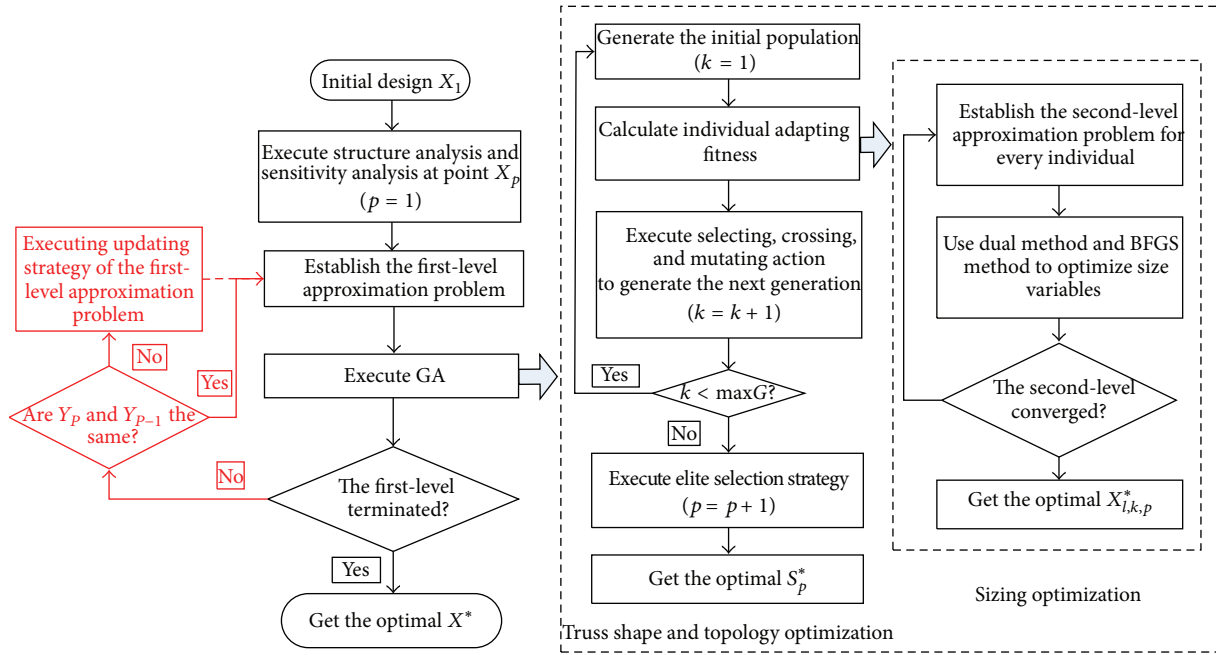


FIGURE 5: The flowchart of the present approach.

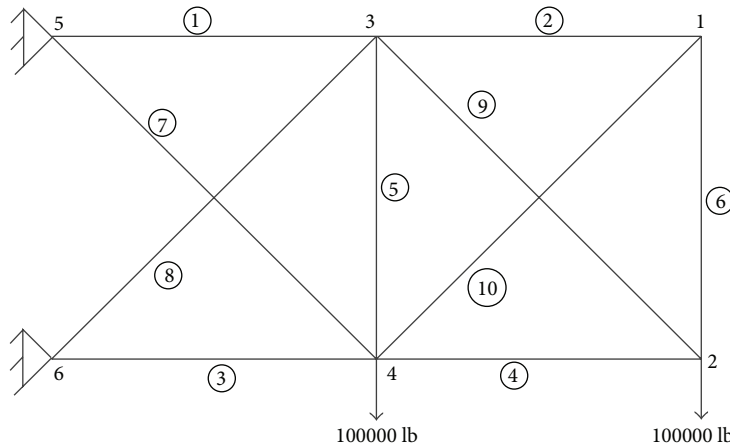


FIGURE 6: Ten-bar truss structure.

the shape, topology, cross-sectional areas, structural weight, and constraint obtained by the present approach is listed in Table 2, for comparison with [6]. It is seen from Table 2 that the critical constraint is very close to the boundary and the optimal weight of this paper is 3173 lb, which is lower than the result of [6] by 81 lb. The optimized shape and topology configuration are contrasted in Figure 7. The iteration history is shown in Figure 8. It is seen that the optimized solution is obtained after only 4 iterations. This example demonstrated the validity and efficiency of the proposed method.

5.2. Twelve-Bar Truss. A twelve-bar truss has been studied by Zhang et al. [13], as shown in Figure 9. The unit of length is mm. The structural symmetry should be kept in the design process. Young's modulus is $E = 1000 \text{ Pa}$ and material

density is 1 kg/mm^3 . The section area of each bar is taken as independent variable, which is originally 10 mm^2 , and is permitted to vary between 1 mm^2 and 100 mm^2 . x and y coordinates of nodes 2 and 5 are taken as independent shape variables. The moveable range of x coordinate is 0 mm to 50 mm, and the moveable range of y coordinate is 0 to ∞ . Discrete coordinates are preset for the shape variables, as shown in Table 3. The shape variables and link relation are defined as definition. Therefore, there are 12 size variables, 12 topology variables, and 4 shape variables in all. The stress of each bar should not exceed $\pm 450 \text{ Pa}$.

The parameters of GA are set as follows: population size 50, evolution generations 50, crossover probability 0.9, and mutation probability 0.05. The optimized solution of the shape, topology, cross-sectional areas, structural weight,

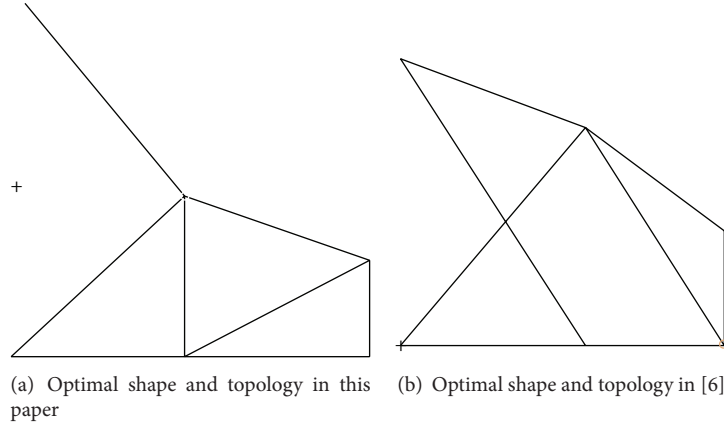


FIGURE 7: The optimized shape and topology of ten-bar truss structure.

TABLE 1: Shape variables and coordinates identifier number.

S.V. ID	Coord.	Position number and corresponding coordinates							
		1	2	3	4	5	6	7	8
1	y_1	360	610	687	760	787	810	860	1000
2	y_3	300	330	360	450	540	554	560	
3	y_5	180	187	190	200	210	230	260	360

Note: S.V. are shape variables.

TABLE 2: Comparison of optimized design of ten-bar planar truss.

Variable	Initial design	Present paper	Reference [6]
y_1	360	180	186.5
y_3	360	330	554.5
y_5	360	687	786.9
A_1	10	21.6	9.9
A_2	10	1.0	9.4
A_3	10	12.6	11.5
A_4	10	12.6	1.5
A_5	10	4.4	0
A_6	10	17.1	12.0
A_7	10	0	11.5
A_8	10	2.6	3.6
A_9	10	0	0
A_{10}	10	1.0	10.4
Struc. analyses		20	—
Weight (lb)		3173.0	3254.0
Critical constraint		2.1×10^{-4}	—

and constraint obtained by the present approach is listed in Table 4, for comparison with [13]. The optimized shape and topology configuration are contrasted in Figure 10. The iteration history is shown in Figure 11. It is seen that the final structural weight is 1023 kg, which is lower than the result in [13] by 109 kg, and the critical constraint is very close to the boundary. The optimized solution is obtained after only 4 iterations. This example demonstrated the validity and efficiency of the proposed method.

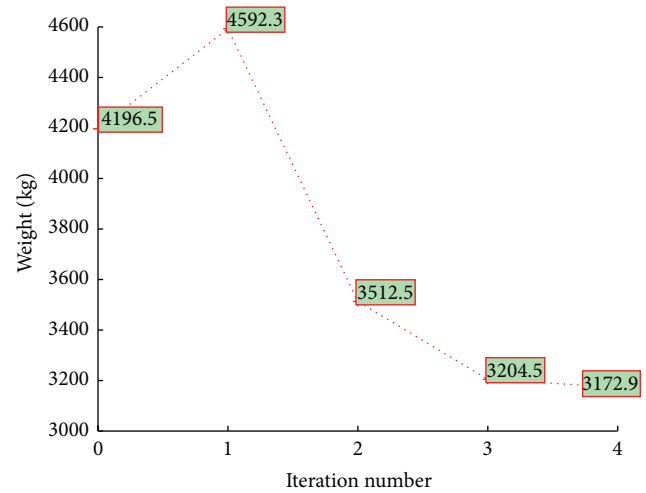


FIGURE 8: Iteration history of ten-bar truss.

TABLE 3: Shape variables and coordinates identifier number of 12-bar planar truss.

S.V. ID	Coord.	Position number and corresponding coordinates						
		1	2	3	4	5	6	7
1	x_1	5	10	15	20	25		
2	x_2	30	35	40	45			
3	y_1	2	5	10	15	20	25	30
4	y_2	2	5	10	15	20	25	30

6. Algorithm Performance

Consider the example of ten-bar truss in Section 5, with population size and maximum generations (maxG) set from 10 to 100, respectively, which is shown in Figure 12, while other parameters remain as given before. At each parameter set point, 100 independent runs of IGATA are executed. Since there are 100-parameter set points, IGATA is executed in a total of 10,000 times. For each parameter set point, the average weight is shown in Figure 13.

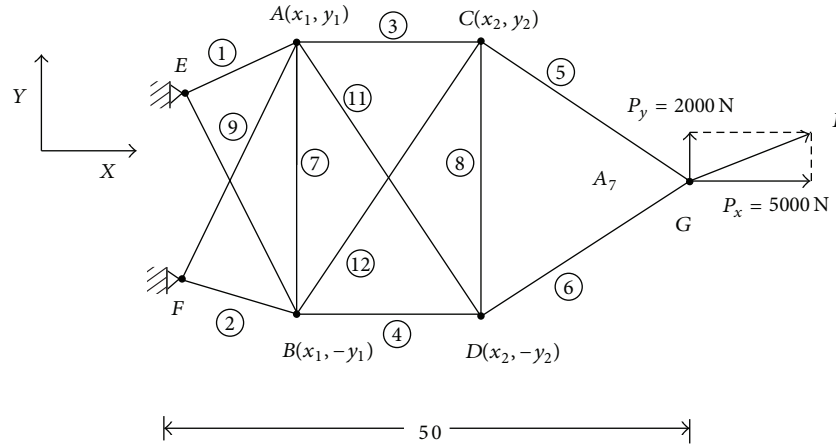


FIGURE 9: Twelve-bar truss structure.

TABLE 4: Comparison of optimized design of twelve-bar planar truss.

Variable	Initial design	Present paper	Reference [13]
x_1	15	10	31.18
x_2	30	35	38.30
y_1	15	10	9.21
y_2	15	5	7.28
A_1	10	4.11	1.00
A_2	10	15.90	14.50
A_3	10	1.13	1.98
A_4	10	14.73	10.60
A_5	10	1.17	2.10
A_6	10	12.88	10.80
A_7	10	0	1.46
A_8	10	1.00	1.00
A_9	10	3.23	5.73
A_{10}	10	1.74	2.51
A_{11}	10	2.59	1.00
A_{12}	10	0	1.00
Struc. analyses		17	—
Weight (kg)		1023.3	1132.6
Critical constraint		2.1×10^{-4}	—

It can be seen from Figure 13 that the minimum weight is 2800 lb, which is less than the weight of the initial structure by 32.6%. To describe the efficiency of the IGATA involving size/shape/topology variables, we counted the number of the results that are lower than 3254 lb, which is the optimal result in [6]. It can be seen that 8 results with lower weight are obtained within the 100-parameter set points.

As compared with the IGATA only including size and topology variables [5], the algorithm performance in this paper is not so satisfactory. To test the reason for this situation, continuous shape variables instead of discrete variables were used in the hybrid coding strategy in GA. The results of repeated tests show that the algorithm performance does not improve obviously. Thus the main reason may not lie in

the continuity of shape variables but lie in the quality of the first-level approximation function induced by the shape variables. When executing GA in p th iteration process of IGATA for truss shape and topology optimization, the objective and constraint approximation functions of the optimal individual from the last iteration are used, which do not change along with the structure shape, although controlled mutation has been implemented.

To improve the accuracy and efficiency of IGATA, we will use continuous shape variables and add sensitivity information of shape variables in the first-level approximation problem in the subsequent work.

7. Conclusion

In this paper, aiming at simultaneous consideration of sizing, shape, and topology optimization of truss structures, a design method IGATA is presented, which is based on the truss sizing and topology optimization method GATA. The shape variables are involved by using GA and are considered as discrete to avoid the sensitivity calculation, through which the computational cost is decreased significantly. A comprehensive model is established for involving the three kinds of design of variables, in which the shape variables are corresponding to a set of discrete node coordinates. GA is used to solve the first-level approximate problem which involves sizing/shape/topology variables. When calculating the fitness value of each member in the current generation, a second-level approximation method is used to optimize the continuous size variables. The definition, link, and code of the shape variables are presented, and the crossover and mutation of the decimal/binary mix-coding population are realized. The update strategy of the first-level approximation problem is also improved for the cases when the truss shapes are different from the neighbor iterations, so as to ensure that the truss shape is corresponding with the approximation problem. The results of numerical example demonstrated the validity of the method. Moreover, truss optimization problem with sizing/shape/topology variables can be treated effectively with the proposed method.

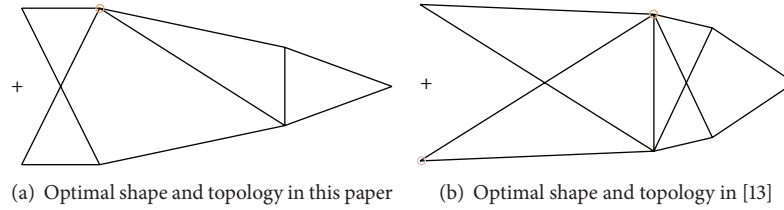


FIGURE 10: The optimized shape and topology of twelve-bar truss structure.

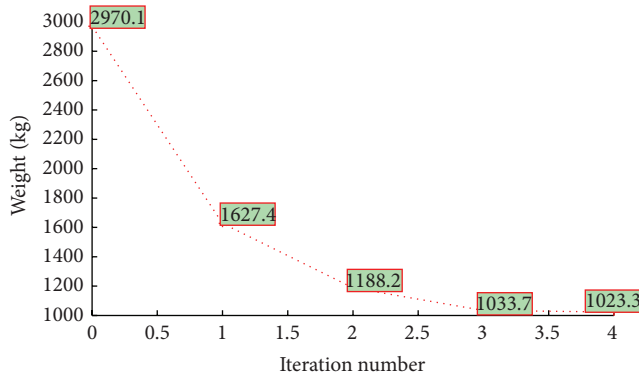


FIGURE 11: Iteration history of twelve-bar truss.

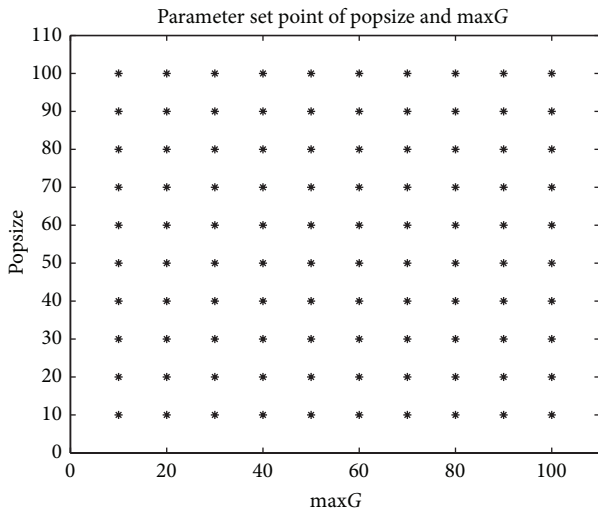


FIGURE 12: GA parameters set point.

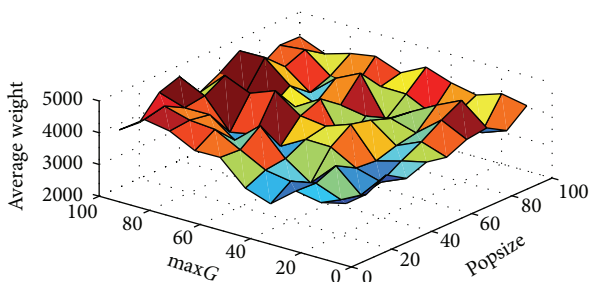


FIGURE 13: Average weight at each set point.

Nomenclature

X :	Size variable vector
x_i :	Cross-sectional area of bar members in i th group
Y :	Shape variable vector
y_e :	Identifier number within the possible coordinates set $[y_{e,1}, \dots, y_{e,p_e}]$
a :	Topology variable vector
W :	Total weight of the truss structure
$f_i(X, Y)$:	The weight of i th group
$g_j(X, Y)$:	j th constraint
k :	The total number of constraints
v :	The number of frequency constraints.

Conflict of Interests

The authors declare that there is no conflict of interests regarding the publication of this paper.

Acknowledgment

This research work is supported by the National Natural Science Foundation of China (Grant no. 11102009), which the authors gratefully acknowledge.

References

- [1] L. Wei, T. Tang, X. Xie, and W. Shen, "Truss optimization on shape and sizing with frequency constraints based on parallel genetic algorithm," *Structural and Multidisciplinary Optimization*, vol. 43, no. 5, pp. 665–682, 2011.
- [2] D. Wang, W. H. Zhang, and J. S. Jiang, "Truss optimization on shape and sizing with frequency constraints," *AIAA Journal*, vol. 42, no. 3, pp. 622–630, 2004.
- [3] O. Sergeyev and Z. Mróz, "Sensitivity analysis and optimal design of 3D frame structures for stress and frequency constraints," *Computers and Structures*, vol. 75, no. 2, pp. 167–185, 2000.
- [4] R. Su, X. Wang, L. Gui, and Z. Fan, "Multi-objective topology and sizing optimization of truss structures based on adaptive multi-island search strategy," *Structural and Multidisciplinary Optimization*, vol. 43, no. 2, pp. 275–286, 2011.
- [5] D. Li, S. Chen, and H. Huang, "Improved genetic algorithm with two-level approximation for truss topology optimization," *Structural and Multidisciplinary Optimization*, vol. 49, no. 5, pp. 795–814, 2014.

- [6] S. D. Rajan, "Sizing, shape, and topology design optimization of trusses using genetic algorithm," *Journal of Structural Engineering*, vol. 121, no. 10, pp. 1480–1487, 1995.
- [7] R. J. Balling, R. R. Briggs, and K. Gillman, "Multiple optimum size/shape/topology designs for skeletal structures using a genetic algorithm," *Journal of Structural Engineering*, vol. 132, no. 7, Article ID 015607QST, pp. 1158–1165, 2006.
- [8] P. Hajela and E. Lee, "Genetic algorithms in truss topological optimization," *International Journal of Solids and Structures*, vol. 32, no. 22, pp. 3341–3357, 1995.
- [9] H. Kawamura, H. Ohmori, and N. Kito, "Truss topology optimization by a modified genetic algorithm," *Structural and Multidisciplinary Optimization*, vol. 23, no. 6, pp. 467–472, 2002.
- [10] W. Tang, L. Tong, and Y. Gu, "Improved genetic algorithm for design optimization of truss structures with sizing, shape and topology variables," *International Journal for Numerical Methods in Engineering*, vol. 62, no. 13, pp. 1737–1762, 2005.
- [11] K. Sawada, A. Matsuo, and H. Shimizu, "Randomized line search techniques in combined GA for discrete sizing optimization of truss structures," *Structural and Multidisciplinary Optimization*, vol. 44, no. 3, pp. 337–350, 2011.
- [12] Y. Dong and H. Huang, "Truss topology optimization by using multi-point approximation and GA," *Chinese Journal of Computational Mechanics*, vol. 21, no. 6, pp. 746–751, 2004.
- [13] Z. Zhang, W. Yao, and L. Zhou, "Study on size and shape collaborative optimization method of truss structure," *Advances in Aeronautical Science and Engineering*, vol. 3, no. 2, pp. 138–143, 2012.

Research Article

Reliability Analysis of High Rockfill Dam Stability

Ping Yi, Jun Liu, and Chunlei Xu

School of Civil Engineering, Dalian University of Technology, Dalian 116024, China

Correspondence should be addressed to Ping Yi; yiping@dlut.edu.cn

Received 11 September 2014; Accepted 17 April 2015

Academic Editor: Rafael J. Villanueva

Copyright © 2015 Ping Yi et al. This is an open access article distributed under the Creative Commons Attribution License, which permits unrestricted use, distribution, and reproduction in any medium, provided the original work is properly cited.

A program 3DSTAB combining slope stability analysis and reliability analysis is developed and validated. In this program, the limit equilibrium method is utilized to calculate safety factors of critical slip surfaces. The first-order reliability method is used to compute reliability indexes corresponding to critical probabilistic surfaces. When derivatives of the performance function are calculated by finite difference method, the previous iteration's critical slip surface is saved and used. This sequential approximation strategy notably improves efficiency. Using this program, the stability reliability analyses of concrete faced rockfill dams and earth core rockfill dams with different heights and different slope ratios are performed. The results show that both safety factors and reliability indexes decrease as the dam's slope increases at a constant height and as the dam's height increases at a constant slope. They decrease dramatically as the dam height increases from 100 m to 200 m while they decrease slowly once the dam height exceeds 250 m, which deserves attention. Additionally, both safety factors and reliability indexes of the upstream slope of earth core rockfill dams are higher than that of the downstream slope. Thus, the downstream slope stability is the key failure mode for earth core rockfill dams.

1. Introduction

Rockfill dams are commonly used geotechnical infrastructures for water management. One of the critical aspects of rockfill dam design is stability analysis, that is, the computation of safety factors (Chen and Morgenstern 1983 [1]; Janbu 1973 [2]). A deterministic approach is traditionally utilized for this analysis. However, as natural materials, rockfill and earth core exhibit large uncertainties in their shear strength parameters, dry bulk density, and other pertinent properties, which cannot be handled in the traditional deterministic methods. Therefore, the application of probabilistic reliability concepts to the stability analysis of dams has drawn increasing attention over the past two decades (Wolff 1996 [3]; Bureau 2003 [4]; Yanmaz and Beser 2005 [5]). Duncan (2000) [6] pointed out that the reliability analysis offers a useful supplement to conventional stability analyses, because the resultant reliability index contains more information than the deterministic safety factor.

The limit equilibrium method (LEM) and the strength reduction method (SRM) on the basis of the finite element method (FEM) or finite difference method (FDM) are currently popular methods among engineers for slope stability

analysis (Hassan and Wolff 1999 [7]; Griffiths and Fenton 2004 [8]). Whether LEM or SRM is used, the stability analysis of rockfill dams is a time-consuming process and the calculated safety factor is an implicit function of basic variables, such as materials' shear strength parameters and dry bulk density. Then in the reliability analysis, the performance function is implicit and many iterations of calculating the safety factor have to be performed to obtain the reliability index. Therefore, despite its potential value, reliability theory has not been widely adopted in geotechnical engineering because of huge computational cost.

The response surface method (RSM) has been developed to deal with implicit performance functions and Xu and Low (2006) [9] utilized RSM combined with FEM to calculate the reliability index of slopes. However, the surrogate performance function from the RSM may cause a deviation from the exact model (Luo et al. 2012 [10]). When no such surrogate performance function is used, most previous reports have utilized the mean value first-order second-moment (FOSM, Hassan and Wolff 1999 [7]) method or its extension, the point-estimate method (Rosenblueth 1975 [11]), to calculate the approximate reliability index of slope stability. In some papers, the distributions of the random variables are not

mentioned at all, and the reliability index is calculated by the performance function's mean value divided by its standard deviation (Duncan 2000 [6]). In others, two expressions are given based on the normal distribution and the lognormal distribution (Liang et al. 1999 [12]). However, it is well known in reliability analysis that different values of the reliability index might be obtained for different mathematical forms of the same limit state function when FOSM is used (Hasofer and Lind 1974 [13]). Baecher and Christian (2003) [14] have studied such problem in geotechnical engineering. Accordingly, the first-order reliability method (FORM) is recommended and has gradually been accepted by researchers despite its complexity (Babu and Srivastava 2010 [15]). In this paper, FORM is utilized.

Although there are some commercial software programs, for example, PLAXIS (FEM) and FLAC (FDM), for the slope stability analysis, software package combining the slope stability and reliability analysis is rare (Cho 2009 [16]). In this paper, a self-developed program 3DSTAB, which integrates slope stability analysis and reliability analysis, is introduced. LEM is employed in this program to calculate safety factors and FORM, more precisely, the HL-RF iterative algorithm, is utilized to compute reliability indices. Three examples reported in recent literature are studied and the comparisons prove the validity and accuracy of 3DSTAB. Then two typical kinds of rockfill dams, that is, concrete faced rockfill dams and earth core rockfill dams, are considered. Rockfill dams with different heights over 100 m and different slope ratios are analyzed to study the relationships of the safety factors and reliability indices to the dam height and dam slope ratio parameter.

2. Reliability Analysis

To perform the reliability analysis of the slope stability of dams, a performance function or limit state function, $g(\mathbf{x})$, should be defined to identify the failure state ($g(\mathbf{x}) < 0$) and safety state ($g(\mathbf{x}) > 0$), where $\mathbf{x} = (x_1, x_2, \dots, x_n)$ is a random variable vector. The following formulation of the performance function (Phoon 2008 [17]) is widely utilized and adopted in this paper:

$$g(\mathbf{x}) = g(x_1, x_2, \dots, x_n) = F_s(x_1, x_2, \dots, x_n) - 1.0, \quad (1)$$

where F_s is the safety factor and the prescribed acceptable safety factor is 1.0 (Liang et al. 1999 [12]). The probability of failure can be defined as

$$P_f = P(g(\mathbf{x}) < 0) = \int_{g(\mathbf{x}) \leq 0} f(\mathbf{x}) \, d\mathbf{x} \quad (2)$$

in which $f(\mathbf{x})$ is the joint probability density function of \mathbf{x} . Because the multidimensional integral in (2) can be very difficult and nearly impossible, the reliability index β is generally calculated in engineering, and the failure probability is estimated by

$$P_f \approx \Phi(-\beta); \quad (3)$$

$\Phi(\cdot)$ is the standard normal cumulate distribution function.

In slope stability reliability analysis, most previous reports have utilized FOSM (Hassan and Wolff 1999 [7]) method or its extension, the point-estimate method (Rosenblueth 1975 [11]), to calculate the reliability index to avoid heavy computational burden. However when FOSM is used, different values of the reliability index might be obtained for different mathematical forms of the same limit state function (Hasofer and Lind 1974 [13]) and Baecher and Christian (2003) [14] have studied such problem in geotechnical engineering. Accordingly, FORM has gradually been accepted by researchers despite its complexity (Babu and Srivastava 2010 [15]).

In FORM, the original random vector \mathbf{x} is transformed to a standard Gaussian vector \mathbf{u} firstly, expressed as $\mathbf{x} = \mathbf{T}(\mathbf{u})$ (Hohenbichler and Rackwitz 1981 [18]) and the performance function $g(\mathbf{x}) = g(\mathbf{T}(\mathbf{u})) = G(\mathbf{u})$. Then the reliability index β is the minimum distance from the coordinate origin to the limit state surface in \mathbf{u} -space, and its computation is formulated as the following optimization problem:

$$\begin{aligned} \min \quad & \|\mathbf{u}\| \\ \text{s.t.} \quad & G(\mathbf{u}) = 0 \\ \text{so that} \quad & \beta = \|\mathbf{u}^*\|, \end{aligned} \quad (4)$$

where \mathbf{u}^* is the design point on the limit state surface in \mathbf{u} -space. The design point can be located by various optimization algorithms, such as the gradient projection (GP) method, the augmented Lagrangian (AL) method, and the sequential quadratic programming (SQP) method (Val et al. 1996 [19]). Among various methods that have been evaluated for application on structural reliability, an iterative algorithm, the HL-RF algorithm (Hasofer and Lind 1974 [13], Rackwitz and Flessler 1978 [20]), is found to be very efficient as it requires the least amount of storage and computation in each step in comparison with other methods (Liu and der Kiureghian 1991 [21]). The HL-RF algorithm computes the reliability index by the following iterative formulas:

$$\begin{aligned} \beta^k &= \frac{G(\mathbf{u}^k) - (\nabla_{\mathbf{u}} G(\mathbf{u}^k))^T \mathbf{u}^k}{\|\nabla_{\mathbf{u}} G(\mathbf{u}^k)\|}, \\ \mathbf{u}^{k+1} &= -\beta^k \frac{\nabla_{\mathbf{u}} G(\mathbf{u}^k)}{\|\nabla_{\mathbf{u}} G(\mathbf{u}^k)\|}. \end{aligned} \quad (5)$$

The iteration is completed when the absolute change of the design points between two subsequent iterations is smaller than a prescribed small quantity, for example, 0.001. The HL-RF algorithm can generally obtain the results with enough accuracy after some iterations and is utilized in this paper.

3. 3DSTAB Program

The slope stability analysis and reliability analysis are combined in the self-developed program 3DSTAB. LEM, which has received wide acceptance because of its simplicity, is utilized to calculate the slope stability safety factor. FORM, more precisely, the HL-RF iterative algorithm, is utilized to compute the reliability index.

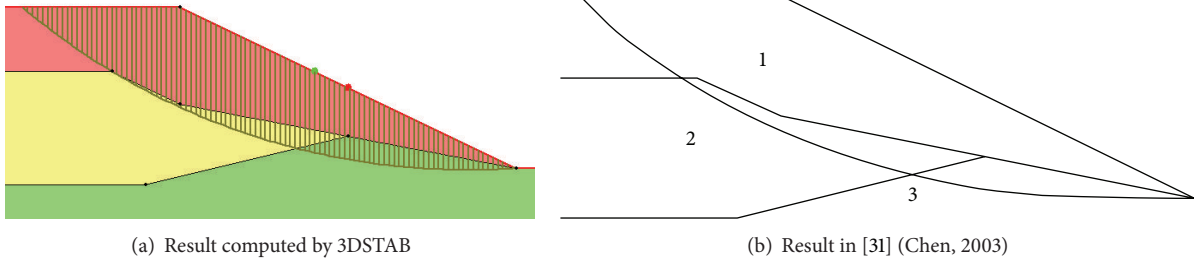


FIGURE 1: Comparison of the critical slip circles in the example of a multilayered soil slope.

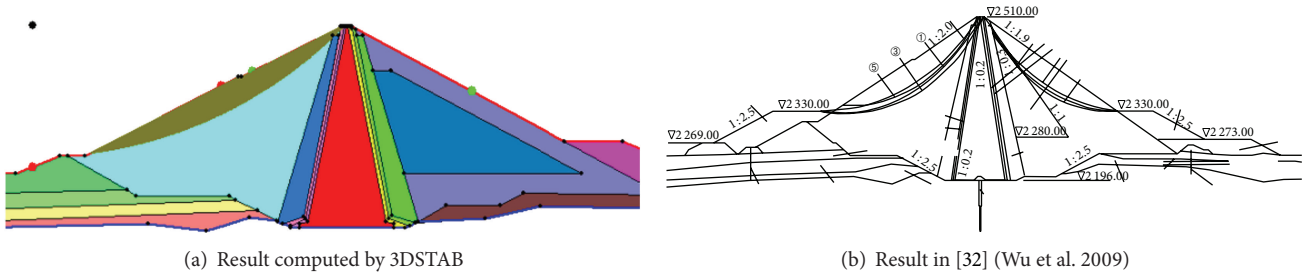


FIGURE 2: Comparison of the critical slip circles of the Shuangjiangkou core-wall rockfill dam.

The Bishop method (Bishop 1955 [22]), simple Janbu method (Janbu 1968 [23]), or the global analysis method (Zheng 2009 [24], Zheng 2012 [25]) can be chosen under static conditions. Although the program can perform 2D and 3D slope stability analyses, just 2D analysis is performed in this paper because Duncan (1996) [26] pointed out that the safety factors resulting from 3D analyses are normally greater than those from 2D analyses. To calculate the safety factor of the slope stability, mean values are assigned to the variables and the particle swarm optimization (PSO) method is applied to search the critical slip surface, which is referred to as the critical deterministic surface (Li et al. 2007 [27]). In reliability analysis, the critical slip surface is searched, and the corresponding safety factor is determined for every realization of the random variables in every iteration. Several iterations are needed to calculate the reliability index through the HL-RF algorithm. The critical slip surface for the final realization, \mathbf{u}^* , is referred to as the critical probabilistic slip surface. Some previous papers only calculated the reliability index β corresponding to the critical deterministic surface (Calle 1985 [28]; Honjo and Kuroda 1991 [29]). However, some researchers have shown that these two kinds of slip surfaces do not generally coincide (Liang et al. 1999 [12]; Hassan and Wolff 1999 [7]). Here, we calculate β corresponding to the critical probabilistic surface. However, when the derivative $\nabla_{\mathbf{u}}G(\mathbf{u}^k)$ is computed by the finite difference method in every iteration, we do not search the critical slip surface anymore, and the previous critical slip surface is saved and utilized. This kind of sequential approximation strategy is widely utilized in structural optimization and reliability-based optimization (Yi et al. 2008 [30]).

To prove the accuracy and validity of 3DSTAB, three examples that have recently appeared in literature are restudied and compared. The examples include an example of multilayered soil (Chen 2003 [31]), the Shuangjiangkou core-wall rockfill dam with a height of 314 m (Wu et al. 2009 [32]) and the Nuozhadu core-wall rockfill dam with a height of 261.5 m (L.-H. Chen and Z.-Y. Chen 2007 [33]). The computational models and the statistical information of the random parameters are the same as those in the corresponding literature. The comparisons of the critical slip circles are shown in Figures 1–3. The safety factors and the reliability indices are listed in Table 1. The figures and the table show that the results computed by 3DSTAB program are similar to the results reported in other publications and are accurate and reliable.

4. Stability Reliability Analysis of High Rockfill Dams

As natural materials, rockfill and earth core exhibit large uncertainties. In this paper, the dry bulk densities and shear strength parameters, including the linear strength parameters of earth core material and the nonlinear strength parameters of rockfill material, are taken as random variables. Based on the statistical properties of the random variables reported in literature, stability reliability analyses of two typical kinds of rockfill dams with different heights over 100 m and different slope ratios are performed using the self-developed program 3DSTAB. The effects of dam height and slope ratio on

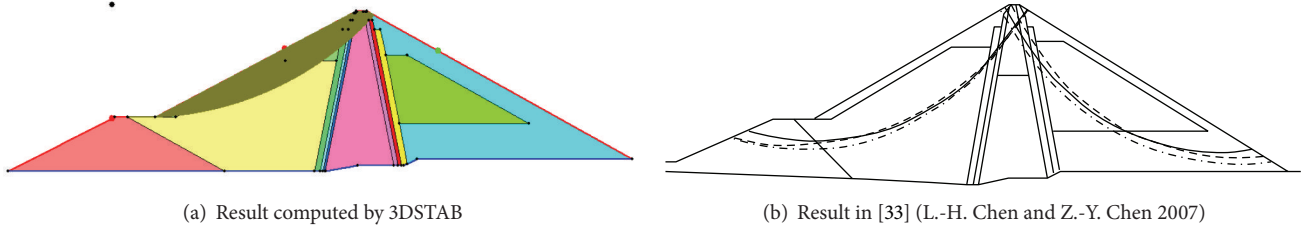


FIGURE 3: Comparison of the critical slip circles of the Nuozhadu core-wall rockfill dam.

TABLE 1: Comparison of stability analyses of the three examples.

	Results computed by 3DSTAB		Results in the literature	
	F_s	β	F_s	β
Multilayered soil slope	1.525	5.121	1.500	4.963
Shuangjiangkou core-wall rockfill dam	1.813	5.353	—	5.573
Nuozhadu core-wall rockfill dam	1.949	4.185	1.888	—

the safety factor and the reliability index of concrete faced rockfill dams and earth core rockfill dams are discussed.

4.1. Statistical Properties of Random Variables. The linear Mohr-Coulomb failure criterion is conventionally utilized to perform dam stability analyses as follows:

$$\tau_f = c + \sigma_n \tan \Phi \quad (6)$$

in which τ_f is the peak shear strength, σ_n is the effective normal stress, c is the cohesion or snap-in force, and Φ is the internal frictional angle. However, the results of many large-scale triaxial tests indicate that Mohr failure envelopes for rockfill exhibit significant nonlinearity, particularly under low and medium normal stresses. And the slope failure of a rockfill dam is just generally associated with relatively low normal stresses (Indraratna et al. 1993 [34]). Thus, the nonlinearity of the Mohr-Coulomb failure criterion cannot be neglected. Duncan (1980) [35] proposed that the drained friction angle Φ of rockfill can be evaluated from the following logarithmic expression:

$$\Phi = \Phi_0 - \Delta\Phi \log\left(\frac{\sigma_3}{P_a}\right) \quad (7)$$

in which σ_3 is the smallest principal stress, P_a is the atmospheric pressure, Φ_0 is the value of Φ when σ_3 is equal to P_a , and $\Delta\Phi$ is the reduction of Φ corresponding to a 10-fold increase in σ_3 . This logarithmic nonlinear shear strength criterion is widely utilized in China (Bai and Cui 1994 [36]; Lu and Yin 2004 [37]), and the Chinese “Design Code for Rolled Earth-rock Fill Dams” (SL274-2001) [38] recommends that the logarithmic expression (7) should be utilized to describe the nonlinear shear strength of rough grain materials, such as rockfill.

In this paper, we consider earth core material to have linear shear strength expressed in (6) and the main and

TABLE 2: Statistical information of earth core.

	γ (kN/m ³)	c (kN/m ³)	Φ (°)
Mean value μ	20.7	23.0	30.3
Standard deviation σ	1.3	2.8	1.3
Variation coefficient δ (%)	6.3	12.2	4.3
Distribution type	Normal	Lognormal	Lognormal

subrockfill material to have the logarithmic nonlinear shear strength expressed in (7). The shear strength parameters in these expressions and the dry bulk density, γ , are taken as random parameters and their statistical information, which is reported by Xu (2010) [39], is listed in Tables 2 and 3. Because considering correlations between the parameters would only marginally increase the slope stability and its reliability (Babu and Srivastava 2010 [15]; Wu et al. 2009 [32]), the correlations are not considered here, and the obtained results are thus relatively conservative.

From Tables 2 and 3, we can see that most of the stochastic variables obey normal distribution. It has been pointed out that a normally distributed variable is defined on the real number space \mathbf{R} , and negative values may be given to a parameter that is positive in nature, such as Φ_0 . This would give an unreasonable lower value to the reliability index (Liang et al. 1999 [12]). The situation will be worse when the variation coefficient of the parameter is not small. So a truncated normal distribution is adopted in this study for all normally distributed parameters to avoid sampling negative values (Most and Knabe 2010 [40]). The upper limit is $\mu + 3\sigma$, and the lower limit is the larger one of $\mu - 3\sigma$ and zero, in which μ is the mean value and σ is the standard deviation.

4.2. Stability Reliability Analysis. Two kinds of rockfill dams, that is, concrete faced rockfill dams and earth core rockfill

TABLE 3: Statistical information of rockfill.

	Main rockfill			Subrockfill		
	γ (kN/m ³)	Φ_0 (°)	$\Delta\Phi$ (°)	γ (kN/m ³)	Φ_0 (°)	$\Delta\Phi$ (°)
Mean value μ	21.0	51.2	8.2	20.8	48.8	9.4
Standard deviation σ	0.8	4.3	3.2	0.7	4.6	2.3
Variation coefficient δ (%)	3.8	8.4	39.0	3.3	9.4	24.5
Distribution type	Normal	Normal	Normal	Normal	Normal	Normal

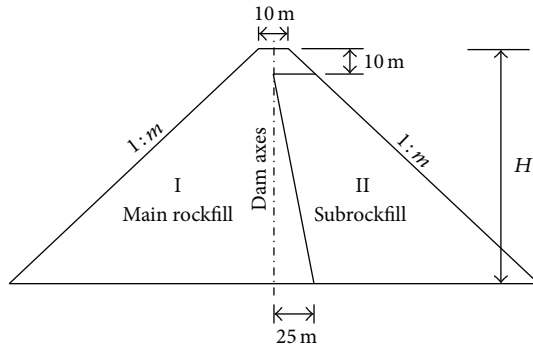
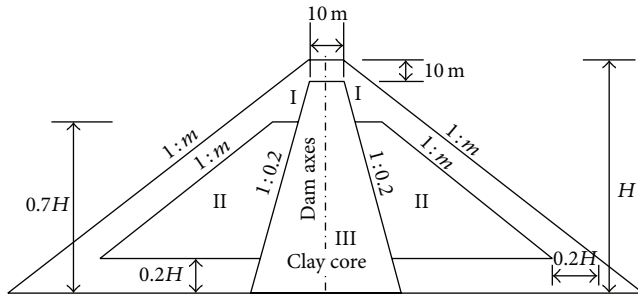


FIGURE 4: Cross section of a concrete faced rockfill dam.



Note: the width of the clay core wall is 6 m when the dam height is 100 m or 150 m

FIGURE 5: Cross section of an earth core rockfill dam.

dams, are analyzed and their typical cross-sectional shapes are shown in Figures 4 and 5. The dam height H varies from 100 m to 350 m in intervals of 50 m. The slope ratio is expressed as 1: m , where m can be 1.3, 1.4, 1.5, or 1.6 for concrete faced rockfill dams and 1.8, 1.9, or 2.0 for earth core rockfill dams, respectively. Cushion zone and transition zone are ignored due to little effect on slope stability. The Bishop method is utilized to calculate safety factors under static conditions. The number of soil strips is $(m * H + 20)$, and the soil strip width is less than 1.0 m. The reliability index is computed through the HL-RF iterative algorithm with a maximum of 20 iterations.

The water level is set to the maximum pool level. The stability of the downstream slope is considered for concrete faced rockfill dams. The safety factors and reliability indices at different heights (H) and slope ratio parameters (m) are shown in Figure 6. For earth core rockfill dams, the stabilities

of both the upstream and downstream slopes under steady-state seepage conditions are calculated. The results are shown in Figures 7 and 8.

Figure 6 shows that the safety factors of the downstream slopes of concrete faced rockfill dams range from 1.34 to 1.85 and the reliability indices range from 1.60 to 5.67. Both quantities decrease as the dam height (H) increases, as mentioned by Cao and Chen (1991) [41]. At the same time, both quantities decrease as the slope ratio parameter (m) decreases; that is, the safety factors and the reliability indices decrease as the dam slope becomes steeper. This corresponds with the fact that the higher and the steeper dams are, the more dangerous they become. It should be noted in Figure 6 that when the dam height is relatively low (i.e., from 100 m to 200 m), the safety factors and the reliability indices decrease dramatically as the dam height increases. Strangely, when the dam height (H) exceeds 250 m, the safety factors and the reliability indices decrease very slowly with further increases of the dam height. The stability reliability analyses of both the upstream and downstream slopes of earth core rockfill dams present the same behavior, and this deserves extra attention.

Figures 7 and 8 show the safety factors and reliability indices of the upstream and downstream slopes of earth core rockfill dams, respectively. These quantities also decrease as the dam height (H) increases and the slope factor (m) decreases. The safety factors of the upstream slopes of earth core rockfill dams range from 1.80 to 2.35, and the reliability indices range from 4.03 to 11.52. The ranges are from 1.70 to 2.23 for F_s and from 3.20 to 8.37 for β of downstream slopes. Both the safety factors and reliability indices of the upstream slopes of earth core rockfill dams are higher than those of the downstream slopes. Thus, the stability of the downstream slope is the key failure mode of earth core rockfill dams.

Figures 6 to 8 also show that the safety factors and reliability indices of earth core rockfill dams are higher than those of concrete faced rockfill dams. This is mainly because earth core rockfill dams considered here have relatively gentle slopes compared to concrete faced rockfill dams.

It should be pointed out that the reliability indices in this section are a bit small, especially for dams higher than 250 m. This happens because the statistical parameters reported by Xu (2010) [39] are the statistical results from 44 dams in China, and their divergences are relatively larger than those of a single dam. However, the behavior of the quantities is more important than their specific values.

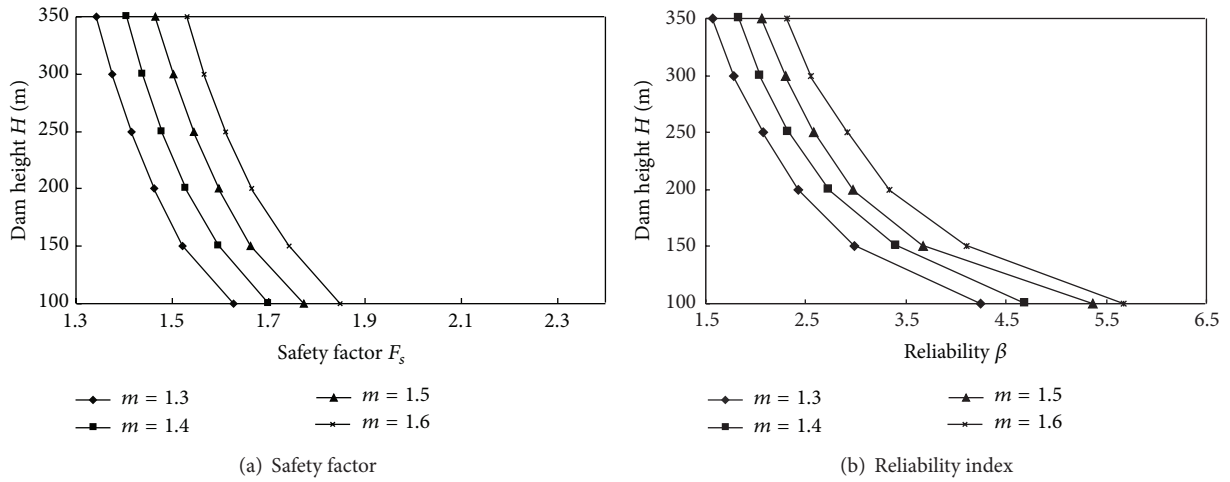


FIGURE 6: Safety factors and reliability indices of downstream slopes of concrete faced rockfill dams.

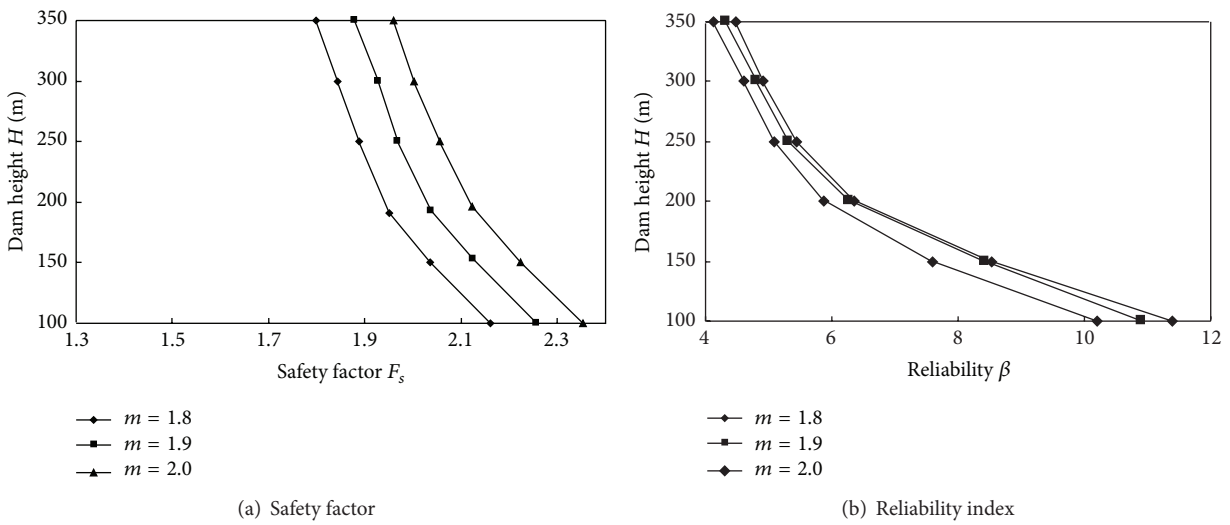


FIGURE 7: Safety factors and reliability indices of upstream slopes of earth core dams.

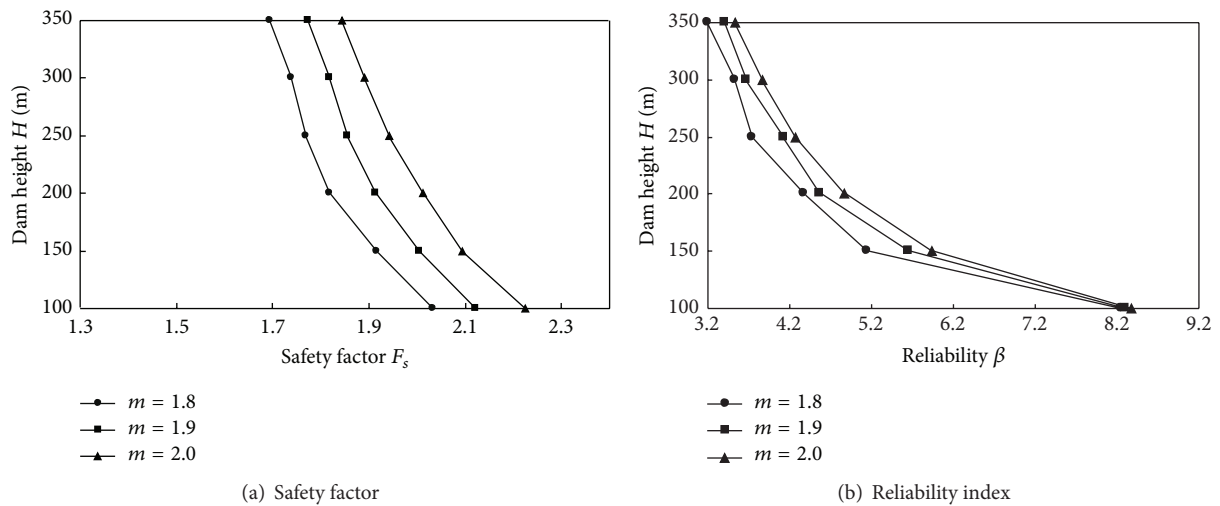


FIGURE 8: Safety factors and reliability indices of downstream slopes of earth core rockfill dams

5. Conclusions

(1) A self-developed program 3DSTAB combining the slope stability analysis and reliability analysis is introduced. In this program, LEM is utilized to calculate the safety factor of the critical slip surface under static conditions. FORM, more precisely, the HL-RF iterative algorithm, is utilized to compute the reliability index corresponding to the critical probabilistic surface. When the derivatives of the performance function are calculated by the finite difference method in every iteration, a sequential approximation strategy is utilized. In other words, we do not search the critical slip surface under this circumstance, and the previous critical slip surface is saved and used, which improves the efficiency notably. Three examples reported in recent literature are studied and the comparisons prove the accuracy and validity of 3DSTAB.

(2) The dry bulk densities and shear strength parameters, including the linear strength parameters of earth core material and the nonlinear strength parameters of rockfill material, are taken as random variables. The truncated normal distribution is used for all normally distributed parameters to prevent negative sampling values. Because considering correlations between the parameters would only marginally increase the slope stability and its reliability, the correlations are not considered in this paper.

(3) Using the self-developed program 3DSTAB, the stability reliability analyses of concrete faced rockfill dams and earth core rockfill dams with different heights over 100 m and different slope ratios are performed. The results show that both the safety factors and reliability indices decrease as the dam's slope increases at a constant dam height and as the dam height increases at a constant slope ratio. More precisely, they decrease dramatically as the dam height increases from 100 m to 200 m, while decrease slowly once the dam height exceeds 250 m, which deserves extra attention.

Both the safety factors and reliability indices of the upstream slopes of earth core rockfill dams are higher than those of the downstream slopes. Thus, the stability of the downstream slope is the key failure mode of earth core rockfill dams.

Conflict of Interests

The authors declare that there is no conflict of interests regarding the publication of this paper.

Acknowledgments

This work is funded by the Key Project of Chinese National Programs for Fundamental Research and Development (2015CB057703), the National Natural Scientific Foundation of China (51138001), and the Fundamental Research Funds for the Central Universities (DUT14ZD206), which are gratefully acknowledged.

References

- [1] Z.-Y. Chen and N. R. Morgenstern, "Extensions to the generalized method of slices for stability analysis," *Canadian Geotechnical Journal*, vol. 20, no. 1, pp. 104–119, 1983.
- [2] N. Janbu, "Slope stability computation," in *Embankment-Dam Engineering*, R. C. Hirschfeld and S. J. Poulos, Eds., pp. 47–86, John Wiley & Sons, New York, NY, USA, 1973.
- [3] T. F. Wolff, "Probabilistic slope stability in theory and practice," in *Proceedings of the Uncertainty in the Geologic Environment: From Theory to Practice*, pp. 419–433, ASCE, Madison, Wis, USA, July–August 1996.
- [4] G. J. Bureau, "Dams and appurtenant facilities," in *Earthquake Engineering Handbook*, W. F. Chen and C. Scawthorn, Eds., CRC Press, 2003.
- [5] A. M. Yanmaz and M. R. Beser, "On the reliability-based safety analysis of Porsuk dam," *Turkish Journal of Engineering & Environmental Sciences*, vol. 29, pp. 309–320, 2005.
- [6] J. M. Duncan, "Factors of safety and reliability in geotechnical engineering," *Journal of Geotechnical and Geoenvironmental Engineering*, vol. 126, no. 4, pp. 307–316, 2000.
- [7] A. M. Hassan and T. F. Wolff, "Search algorithm for minimum reliability index of earth slopes," *Journal of Geotechnical and Geoenvironmental Engineering*, vol. 125, no. 4, pp. 301–308, 1999.
- [8] D. V. Griffiths and G. A. Fenton, "Probabilistic slope stability analysis by finite elements," *Journal of Geotechnical and Geoenvironmental Engineering*, vol. 130, no. 5, pp. 507–518, 2004.
- [9] B. Xu and B. K. Low, "Probabilistic stability analyses of embankments based on finite-element method," *Journal of Geotechnical and Geoenvironmental Engineering*, vol. 132, no. 11, pp. 1444–1454, 2006.
- [10] X. F. Luo, X. Li, J. Zhou, and T. Cheng, "A Kriging-based hybrid optimization algorithm for slope reliability analysis," *Structural Safety*, vol. 34, no. 1, pp. 401–406, 2012.
- [11] E. Rosenblueth, "Point estimates for probability moments," *Proceedings of the National Academy of Sciences of the United States of America*, vol. 72, no. 10, pp. 3812–3814, 1975.
- [12] R. Y. Liang, O. K. Nusier, and A. H. Malkawi, "A reliability based approach for evaluating the slope stability of embankment dams," *Engineering Geology*, vol. 54, no. 3-4, pp. 271–285, 1999.
- [13] A. M. Hasofer and N. C. Lind, "Exact and invariant second-moment code format," *Journal of the Engineering Mechanics Division*, vol. 100, no. 1, pp. 111–121, 1974.
- [14] G. B. Baecher and J. T. Christian, *Reliability and Statistics in Geotechnical Engineering*, John Wiley & Sons, Chichester, UK, 2003.
- [15] G. L. S. Babu and A. Srivastava, "Reliability analysis of earth dams," *Journal of Geotechnical and Geoenvironmental Engineering*, vol. 136, no. 7, pp. 995–998, 2010.
- [16] S. E. Cho, "Probabilistic stability analyses of slopes using the ANN-based response surface," *Computers and Geotechnics*, vol. 36, no. 5, pp. 787–797, 2009.
- [17] K.-K. Phoon, *Reliability-Based Design in Geotechnical Engineering*, Taylor and Francis, New York, NY, USA, 2008.
- [18] M. Hohenbichler and R. Rackwitz, "Non-normal dependent vectors in structural safety," *Journal of Engineering Mechanics*, vol. 107, no. 6, pp. 1227–1239, 1981.
- [19] D. Val, F. Bljager, and D. Yankelevsky, "Optimization problem solution in reliability analysis of reinforced concrete structures," *Computers & Structures*, vol. 60, no. 3, pp. 351–355, 1996.

- [20] R. Rackwitz and B. Flessler, "Structural reliability under combined random load sequences," *Computers & Structures*, vol. 9, no. 5, pp. 489–494, 1978.
- [21] P.-L. Liu and A. der Kiureghian, "Optimization algorithms for structural reliability," *Structural Safety*, vol. 9, no. 3, pp. 161–177, 1991.
- [22] A. W. Bishop, "The use of the slip circle in the stability analysis of slopes," *Géotechnique*, vol. 5, no. 1, pp. 7–17, 1955.
- [23] N. Janbu, "Slope stability computations," Soil Mechanics and Foundation Engineering Report, The Technical University of Norway, Trondheim, Norway, 1968.
- [24] H. Zheng, "Eigenvalue problem from the stability analysis of slopes," *Journal of Geotechnical and Geoenvironmental Engineering*, vol. 135, no. 5, pp. 647–656, 2009.
- [25] H. Zheng, "A three-dimensional rigorous method for stability analysis of landslides," *Engineering Geology*, vol. 145–146, pp. 30–40, 2012.
- [26] J. M. Duncan, "State of the art: limit equilibrium and finite-element analysis of slopes," *Journal of Geotechnical Engineering*, vol. 122, no. 7, pp. 577–596, 1996.
- [27] L. Li, S. Chi, G. Lin et al., "Search for the critical slip surface using mixed version of particle swarm optimization algorithms," *Industrial Construction*, vol. 37, no. 2, pp. 55–59, 2007 (Chinese).
- [28] E. O. F. Calle, "Probabilistic analysis of stability of earth slopes," in *Proceedings of the 11th International Conference on Soil Mechanics and Foundation Engineering*, pp. 809–812, Balkema, San Francisco, Calif, USA, August 1985.
- [29] Y. Honjo and K. Kuroda, "A new look at fluctuating geotechnical data for reliability design," *Soils and Foundations*, vol. 31, no. 1, pp. 110–120, 1991.
- [30] P. Yi, G. Cheng, and L. Jiang, "A sequential approximate programming strategy for performance-measure-based probabilistic structural design optimization," *Structural Safety*, vol. 30, no. 2, pp. 91–109, 2008.
- [31] Z. Y. Chen, *Soil Slope Stability Analysis: Theory, Methods and Programs*, Water Pub Press, Beijing, China, 2003, (Chinese).
- [32] Z. Y. Wu, J. K. Chen, W. L. Xu, B. Wen, and P. Zhang, "Research on methodology of reliability analysis of high rock-fill dam slope stability using nonlinear strength indexes and its engineering application," *Chinese Journal of Rock Mechanics and Engineering*, vol. 28, no. 1, pp. 130–137, 2009 (Chinese).
- [33] L.-H. Chen and Z.-Y. Chen, "Effect of nonlinear strength of rockfill on slope stability of high earth-rock dam," *Rock and Soil Mechanics*, vol. 28, no. 9, pp. 1807–1810, 2007 (Chinese).
- [34] B. Indraratna, L. S. S. Wijewardena, and A. S. Balasubramaniam, "Large-scale triaxial testing of grey wacke rockfill," *Geotechnique*, vol. 43, no. 1, pp. 37–51, 1993.
- [35] J. M. Duncan, "Strength, stress-strain and bulk modulus parameters for finite element analyses of stresses and movements in soil masses," Tech. Rep., The University of California, Berkeley, Calif, USA, 1980.
- [36] S. T. Bai and Y. H. Cui, "The mechanical properties of rockfill," *Journal of Hydroelectric Engineering*, vol. 58, no. 3, pp. 21–30, 1994 (Chinese).
- [37] Q. F. Lu and Z. Z. Yin, "Effect of strength nonlinearity on slope stability of high rockfill dam," *Chinese Journal of Rock Mechanics and Engineering*, vol. 23, no. 16, pp. 2708–2711, 2004 (Chinese).
- [38] The Professional Standards Compilation Group of People's Republic of China, *Design Code for Rolled Earth-Rock Fill Dams (SL274-2001)*, China Water Power Press, Beijing, China, 2002, (Chinese).
- [39] C. Xu, *Study on Reliability of Slope Stability of High Rockfill Dam*, Dalian University of Technology, Dalian, China, 2010, (Chinese).
- [40] T. Most and T. Knabe, "Reliability analysis of the bearing failure problem considering uncertain stochastic parameters," *Computers and Geotechnics*, vol. 37, no. 3, pp. 299–310, 2010.
- [41] K. M. Cao and Z. W. Chen, "The stability analysis of rockfill dam using non-linear strength criterion," *Water Resources and Hydropower Engineering*, vol. 8, no. 9, pp. 37–42, 1991 (Chinese).

Research Article

Structural Response Analysis under Dependent Variables Based on Probability Boxes

Z. Xiao and G. Yang

State Key Laboratory of Advanced Design and Manufacturing for Vehicle Body, College of Mechanical and Vehicle Engineering, Hunan University, Changsha 410082, China

Correspondence should be addressed to G. Yang; yanggang@hnu.edu.cn

Received 29 October 2014; Revised 16 March 2015; Accepted 7 April 2015

Academic Editor: Alessandro Palmeri

Copyright © 2015 Z. Xiao and G. Yang. This is an open access article distributed under the Creative Commons Attribution License, which permits unrestricted use, distribution, and reproduction in any medium, provided the original work is properly cited.

This paper considers structural response analysis when structural uncertainty parameters distribution cannot be specified precisely due to lack of information and there are complex dependencies in the variables. Uncertainties in parameter are quantified by probability boxes (p -boxes) and dependence among uncertain parameters is modeled by copula. To calculate uncertainty structural response, a sampling-based method is proposed. In this method, a sampling strategy is used to sample random intervals from dependent p -boxes according to the copula theory and the metamodel-based optimization method is applied to solve a range of structural interval response problems. Two types of errors are presented to evaluate the error of different p -boxes. Four numerical examples are investigated to demonstrate the effectiveness of the present method.

1. Introduction

Traditional quantification of the uncertainties existing in a system and the corresponding calculation of uncertainty propagation are generally based on the probability model, in which random distributions are used to describe the uncertainty. Unfortunately, for practical engineering problems, sufficient experimental samples are not always available or sometimes very expensive to obtain. Thus alternative imprecise probabilities have been proposed, including the interval theory [1], the evidence theory [2], and probability boxes (p -boxes) [3]. The focus of this paper is on p -boxes, which are more expressive generalization of both traditional probability distributions and interval representations. The p -box incorporates facilities from probability theory for modeling correlations and dependencies and from interval analysis expressing ignorance by expressing interval bounds on the cumulative distribution function (CDF) for a random variable [4]. On the other hand, the p -box has a clear behavioral interpretation and therefore is easy acceptable for practicing engineers [5].

In the field of uncertainty analysis based on p -boxes, a lot of exploratory work has been reported in theoretical and

application aspects. For example, Williamson and Downs [6] proposed an algorithm to compute binary arithmetic operations (addition, subtraction, multiplication, and division) on pairs of independent discrete p -boxes for risk assessment. Karanki et al. [7] used the two-phase Monte Carlo simulation to calculate the multiplication of two p -boxes for the safety assessment. Bruns [8] compared three uncertainty propagation methods to find the appropriate computational methods for propagating p -boxes through the black box engineering models. Zhang et al. [9–11] combined the interval finite element analysis (FEA) and the interval sampling method and proposed an interval Monte Carlo (IMC) method for structural analysis with p -boxes which are defined by distributions with interval parameters. Bai et al. [12] developed a numerical method to compute the linear elastic static and dynamic response of structures with epistemic uncertainty represented by evidence variables, which integrated the moment concept and finite element method and also suited to p -boxes variables. Ghosh and Olewnik [13] improved the performance of the two-phase Monte Carlo simulation by replacing the outer loop by optimization algorithms and replacing the inner loop by the sparse grid numerical integration.

Among the above-mentioned methods, they focused on discussing uncertainty propagation of independent p -boxes. However, the complex dependencies are common in physical systems and can have profound impacts on the numerical results of calculations [14–16]. Ferson et al. [17] illustrated several methods which are used to model the dependence among variables that are cannot be generalized easily for use with p -boxes and proposed that copulas could represent easily the dependence in p -boxes. Based on the analysis, they presented an approach known as the dependency bounds convolution (DBC) method. The DBC method could calculate the propagation of dependent p -boxes whose dependence is expressed by given parametric copula. Despite the fact that DBC is useful for a sequence of basic arithmetic operations or elementary function with a small number of uncertain variables, it must overcome some obstacles for application in engineering design. Among these problems, the low efficiency difficulty seems to be the severest one. The Cartesian product method is applied in the DBC, which can impose significant computational burden.

In this paper, a computational method is proposed to propagate dependent p -boxes through structural model, where dependence in p -boxes is described by copula. By the copula sampling technique, the input epistemic uncertainties represented by p -boxes are transformed into a range of intervals. The metamodel-based optimization is employed as the solver to calculate the structural response with input intervals. A mathematical function has been tested to show the procedure and the efficiency of the proposed method and then three structural numerical examples are investigated by the present method.

2. Probability Boxes Theory under Dependence

2.1. Probability Boxes. A p -box is a class of distribution functions delimited by an upper and a lower bound which collectively represent the epistemic uncertainty about the distribution function of a random variable. Let \mathbf{D}^P denote the space of distribution functions on the real numbers \mathfrak{R} . A p -box will be defined as

$$\mathbf{D}^P = \{F(x) : \forall x \in \mathfrak{R}, \underline{F}(x) \leq F(x) \leq \overline{F}(x)\}, \quad (1)$$

where $\underline{F}(x), F(x), \overline{F}(x) : \mathfrak{R} \rightarrow [0, 1]$, $\underline{F} = P(X \leq x)$, and $\overline{F} = P(X \leq x)$ are the lower and upper bounds of a p -box, which is also written as $[\overline{F}, \underline{F}]$.

There are several ways to construct p -boxes, depending on the type of information available. In this paper, p -boxes are constructed based on 95% confidence intervals on the parameters of a known distribution type. The distribution types are determined on the basis of the theoretical knowledge or previous experience.

2.2. Describing Dependence in Probability Boxes with Copula. Now, consider the dependence in p -boxes which can be

described by copulas. A copula is a multivariate probability distribution for which the marginal probability of each variable is uniformly distributed. By Sklar's theorem [18], copulas are simply the dependence functions that knit together marginal distributions to form their joint distribution. Consider a random vector (X_1, X_2, \dots, X_d) with CDFs $(F_1(x_1), F_2(x_2), \dots, F_d(x_d))$ which are represented by p -boxes in this paper, the multivariate cumulative distribution function can be written as

$$H(x_1, x_2, \dots, x_d) = C(F_1(x_1), F_1(x_2), \dots, F_d(x_d)), \quad (2)$$

where C is a multivariate copula.

2.3. Dependency Bounds Convolution Method. Ferson et al. [17] firstly used dependency bounds convolution method to calculate binary arithmetic operations on pairs of dependent discrete Dempster-Shafter structures. This method mainly contains discretization of the p -boxes and Cartesian product. Consider that $f : \mathbf{X} \rightarrow Y$, $\mathbf{X} = (X_1, X_2)$ are two dependent p -boxes connected by copula function $C(X_1, X_2)$, and Y is the response quantity. The p -boxes X_1 and X_2 are discretized into M focal elements, which are represented by $\{([a_i^L, a_i^R], p_i)\}$ ($i = 1, 2, \dots, M$) and $\{([b_j^L, b_j^R], q_j)\}$ ($j = 1, 2, \dots, M$), respectively. By Yager's Cartesian product, the response quantity in the (i, j) th focal element can be defined by an interval $[z_l^L, z_l^R]$, where $l = M * (i - 1) + j$. The probability mass r_l associated with the (i, j) th focal element can be calculated by

$$r_l = C(P_i, Q_j) - C(P_{i-1}, Q_j) - C(P_i, Q_{j-1}) + C(P_{i-1}, Q_{j-1}), \quad (3)$$

where P_i and Q_j are the cumulative masses, $P_i = \sum_{k=1}^i p_k$ and $Q_j = \sum_{k=1}^j q_k$. The result is written as focal elements $\{([z_l^L, z_l^R], r_l)\}$ ($l = 1, 2, \dots, M^2$) which can be transferred into a p -box by

$$\overline{F}(z) = \sum_{z_l^L \leq z} r_l, \quad (4)$$

$$\underline{F}(z) = \sum_{z_l^R < z} r_l,$$

where $\overline{F}(z)$ and $\underline{F}(z)$ are upper bound and lower bound, respectively.

3. Structural Response Analysis

Using p -boxes to quantify the structural parameters, the structural response will be also a p -box variable. In this section, we will develop an efficient response analysis method for structures by combining p -box theory and the optimization method.

3.1. Sampling Random Intervals from the Dependent p -Boxes. By virtue of Sklar's theorem [18], pseudorandom samples can

be generated from (2). That is, given a procedure to generate a sample (u_1, u_2, \dots, u_d) from the copula C , the required sample can be constructed as

$$\begin{aligned} & (x_1, x_2, \dots, x_d) \\ &= (F_1^{-1}(u_1), F_2^{-1}(u_2), \dots, F_d^{-1}(u_d)), \end{aligned} \quad (5)$$

where F_i^{-1} ($i = 1, 2, \dots, n$) are quasi-inverse function of CDF and (x_1, x_2, \dots, x_d) are a sample from a random vector (X_1, X_2, \dots, X_d) . So the random intervals in accordance with the dependent probability boxes can be generated by following two steps.

The first is to generate a sample from copula. There are lots of algorithms which can generate a sample from a specified copula function [19]. As conditional method may be applied for every chosen copula, it is used as the sample method and illustrated in this section. Just to explain this method in a simple way, let us assume a bivariate copula C in which all of its parameters are known and pairs (u, v) need to be generated from bivariate copula function $C(u, v)$. Two independent uniform $(0, 1)$ variates u and t are generated, and then $v = c_u^{(-1)}(t)$, where $c_u^{(-1)}(t)$ denotes a quasi-inverse of $c_u(v)$ which equals the partial derivative of the copula $\partial C(u, v)/\partial u$.

The other step is to compute dependent random intervals from p -boxes. Suppose that (u_1, u_2, \dots, u_d) are a sample from the copula C and $([\bar{F}_1(x_1), \underline{F}_1(x_1)], [\bar{F}_2(x_2), \underline{F}_2(x_2)], \dots, [\bar{F}_d(x_d), \underline{F}_d(x_d)])$ are their CDFs. For each u_i and corresponding to $[\bar{F}_i(x_i), \underline{F}_i(x_i)]$, a random interval is generated:

$$x_i^I = [x_i^L, x_i^R] = [\bar{F}_i^{-1}(u_i), \underline{F}_i^{-1}(u_i)], \quad (6)$$

where x_i^I is random interval from $[\bar{F}_i(x_i), \underline{F}_i(x_i)]$. The superscript I represents the interval distribution parameters and the superscripts L and R , respectively, represent the lower and upper bounds of interval. \bar{F}_i^{-1} and \underline{F}_i^{-1} denote the quasi-inverse function of upper and lower bounds of a p -box. Thus using (u_1, u_2, \dots, u_d) will simulate a range of dependent intervals $(x_1^I, x_2^I, \dots, x_d^I)$.

Zhang et al. [9] presented an IMC method for sampling intervals from the independent p -boxes. When random variables contain both dependent and independent p -boxes, the present sampling method and the IMC method can be used to perform random sampling for dependent and independent p -boxes, respectively.

3.2. Metamodel-Based Interval Analysis. Through above section sampled treatments, a range of interval vectors is acquired from p -boxes. Consider the vector \mathbf{x} of uncertain parameters defined to be contained within an interval vector (or hypercube) \mathbf{x}^I . Interval vectors sampling m times from p -boxes are represented as \mathbf{x}_k^I ($k = 1, 2, \dots, m$). For a practical engineering problem, the input-output relationship between these parameters and the output quantity of interest is represented by the function $f(\cdot)$ applied on these parameters.

The interval analysis for the function is numerically equivalent to solving the following equation:

$$y_k^s = (y_k | (\mathbf{x}_k \in \mathbf{x}_k^I) (y_k = f(\mathbf{x}_k^I))), \quad (7)$$

where y_k^s contains all y_k which are obtained from applying the function $f(\cdot)$ on all possible vectors within the interval vector \mathbf{x}_k^I . In many cases, an exact description of y_k^s is extremely difficult to find. Therefore, an interval y_k^I is used to approximate the exact solution y_k^s . For the black box model in the practical engineer problem, solution of y_k^I will make the computational cost extremely expensive [20]. Besides, a great number of repeating interval analyses will be conducted, which will generate unaffordable computational burden. So metamodeling techniques are used to approximate $f(\cdot)$ for improving the computational cost.

To improve the accuracy of metamodel, design of experiments (DOE) should be applied. An experimental design domain can be acquired by truncating the p -box at a probability of α (α is level of significance), which are represented as $[X_i^L, X_i^R] = [\bar{F}_i^{-1}(\alpha), \underline{F}_i^{-1}(1 - \alpha)]$. The vector form is $\mathbf{X}^I = [\mathbf{X}^L, \mathbf{X}^R]$. In this paper, the Latin hypercube design (LHD) method is adopted, which is a space-filling design with constrainedly stratified sampling method. The sample of this method does not increase exponentially with the number of variables. Radial basis function (RBF) [21] is used to approximate the function $f(\cdot)$, which can be expressed as

$$\hat{f}(\mathbf{x}) = \sum_{i=1}^s w_i \varphi(\|\mathbf{x} - \mathbf{x}_i\|), \quad (8)$$

where \mathbf{x}_i is the sampling point selected through LHS, s is the number of sampling points, w_i is mass coefficient, and $\varphi(\cdot)$ is the basis function. The common basis functions include thin-plate spline, Gaussian, and multiquadrics. The metamodel-based solution of y_k^I can be transferred into the following optimization problems:

$$\begin{aligned} y_k^L &= \min \quad \hat{f}(\mathbf{x}_k), \\ &\text{s.t.} \quad \mathbf{x}_k^L \leq \mathbf{x}_k \leq \mathbf{x}_k^R, \\ y_k^R &= \max \quad \hat{f}(\mathbf{x}_k), \\ &\text{s.t.} \quad \mathbf{x}_k^L \leq \mathbf{x}_k \leq \mathbf{x}_k^R, \\ y_k^I &= [y_k^L, y_k^R]. \end{aligned} \quad (9)$$

The gradient-based optimization techniques such as sequential quadratic programming can be used to solve this problem, and the initial point can be selected on the bound point of intervals.

3.3. *Computation of Output Quantity.* Repeating m times interval analysis, we will acquire intervals y_k^I ($k = 1, 2, \dots, m$), which can be transformed into a p -box by [9]

$$P^L \leq P [Y \leq y] \leq P^R \quad (10)$$

with $P^L = (1/m) \sum_{k=1}^m \mathbf{I}[y_k^R \leq y]$ and $P^R = (1/m) \sum_{i=1}^m \mathbf{I}[y_k^L \leq y]$, where \mathbf{I} is the indicator function. Summarizing the above procedure, the present method can be summarized as follows.

Step 1. Collect all p -boxes $\mathbf{X} = (X_1, X_2, \dots, X_n)$ and sample m interval vectors $\mathbf{x}_i^I = (x_{i,1}^I, x_{i,2}^I, \dots, x_{i,n}^I)$ ($i = 1, 2, \dots, m$) from \mathbf{X} by the method in Section 3.1.

Step 2. Conduct the design of experiments with LHS in the experimental design domain $[\mathbf{X}^L, \mathbf{X}^R]$.

Step 3. Construct a RBF response surface for approximating (7).

Step 4. Conduct optimization analysis over each \mathbf{x}_i^I and acquire interval vector y^I .

Step 5. Generate the p -box of the output quantity by (10).

4. Error Analysis

The absolute error and the relative error are popular to measure the accuracy between the experimental data and the true value, which is extended to analysis errors of different p -boxes. In this paper, the absolute errors contain the area error and the boundary error. Suppose that the two p -boxes $A = [\bar{F}_A(x), \underline{F}_A(x)]$ and $B = [\bar{F}_B(x), \underline{F}_B(x)]$; then the left area error and the right area error between two p -boxes are, respectively, calculated by

$$\begin{aligned} S^L &= \int_{-\infty}^{\infty} |\bar{F}_A(x) - \bar{F}_B(x)| dx, \\ S^R &= \int_{-\infty}^{\infty} |\underline{F}_A(x) - \underline{F}_B(x)| dx. \end{aligned} \quad (11)$$

The area error between two p -boxes is defined as the sum of the left area error and the right area error, which is written as $S = S^L + S^R$. As the area error cannot reflect the discrepancy of boundary between two p -boxes, the discrepancy of the boundary is used as the boundary error. Plotting a line with the cumulative probability α will produce two intersection points with the boundary of a p -box. For $[\bar{F}_A(x), \underline{F}_A(x)]$, two intersection points are $\bar{F}_A^{-1}(\alpha)$ and $\underline{F}_A^{-1}(\alpha)$. Two intersection points of $[\bar{F}_B(x), \underline{F}_B(x)]$ are $\bar{F}_B^{-1}(\alpha)$ and $\underline{F}_B^{-1}(\alpha)$. Thus the boundary error $\Delta L(\alpha)$ is

$$\Delta L(\alpha) = \Delta L_1(\alpha) + \Delta L_2(\alpha), \quad (12)$$

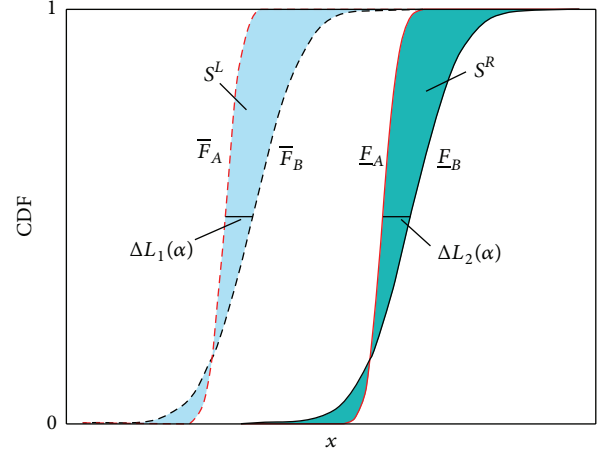


FIGURE 1: Schematic diagram of the area error and the boundary error between $[\bar{F}_A, \underline{F}_A]$ and $[\bar{F}_B, \underline{F}_B]$.

where $\Delta L_1(\alpha) = |\bar{F}_A^{-1}(\alpha) - \bar{F}_B^{-1}(\alpha)|$ and $\Delta L_2(\alpha) = |\underline{F}_A^{-1}(\alpha) - \underline{F}_B^{-1}(\alpha)|$. The illustration of the area error and the boundary area is shown in Figure 1.

The relative error is used for comparing the precision of different p -boxes, which have the relative area error and the relative boundary error. Just to explain the definition, two p -boxes are named, respectively, the relative p -box and the contrastive p -box. The definition of relative area error is the absolute error of two p -boxes dividing the area between two bounds of the relative p -box. Suppose that $[\bar{F}_A, \underline{F}_A]$ and $[\bar{F}_B, \underline{F}_B]$ are taken as the relative p -box and the contrastive p -box, respectively. The relative area error is defined by

$$E_R = 100 * \frac{|S|}{\int_{-\infty}^{\infty} |\bar{F}_A(x) - \underline{F}_A(x)| dx} \%, \quad (13)$$

where S is the area error between two p -boxes. The relative boundary error in the probability value α is computed by

$$E_L(\alpha) = 100 * \frac{|\Delta L(\alpha)|}{|\bar{F}_A^{-1}(\alpha) - \underline{F}_A^{-1}(\alpha)|} \%, \quad (14)$$

where $\Delta L(\alpha)$ is the boundary error between two p -boxes. Two types of error are used to quantify the errors between p -boxes, when the discrepancy of different p -boxes can be distinguished from the figure.

5. Numerical Examples and Discussions

5.1. *Sum of X and Y.* The test function

$$Z = X + Y, \quad (15)$$

where X and Y are random variables represented by dependent p -boxes with the Gaussian copula. The Pearson correlation ρ of the two random variables is 0.3. X is bounded by normal distribution whose means are between 2 and 8

TABLE 1: Uncertain parameters for the 10-bar aluminum truss.

Uncertain variables	Parameter 1 (mean)	Parameter 2 (standard deviation)	Boundary parameter distribution
F_1 (N)	[442800, 44680]	40000	Normal
F_2 (N)	[442800, 44680]	40000	Normal
F_3 (N)	[1709200, 1849200]	40000	Normal
E (Mpa)	68948	[3120, 3350]	Normal

and whose standard deviation is 0.5. Y also is specified by the class of normal distributions with means [15, 20] and standard deviation 1.5. According to the statistics theory, the theoretical cumulative probability of Z can be calculated by the following equations:

$$Z = \int_{-\infty}^z \frac{1}{\sqrt{2\pi(\sigma_1^2 + 2\rho\sigma_1\sigma_2 + \sigma_2^2)}} e^{-(z-\mu_1^I - \mu_2^I)^2 / 2(\sigma_1^2 + 2\rho\sigma_1\sigma_2 + \sigma_2^2)} dz, \quad (16)$$

where $\mu_1^I = [2, 8]$, $\mu_2^I = [15, 20]$, $\sigma_1 = 0.5$, and $\sigma_2 = 1.5$. The numerical boundaries of Z are computed by the Simpson quadrature [22].

As a comparison, the DBC method with a range of the discretization numbers $\mathbf{M} = [10, 20, \dots, 400]$ is adopted to compute this problem here. According to the Cartesian product, \mathbf{M}^2 analyses would be required if two p -boxes are discretized into \mathbf{M} focal elements, respectively. The absolute error values with the theoretical p -boxes under the different discretization number are shown in Figures 2 and 3 by the red line with asterisk markers. Now, use the present method with the sample sizes \mathbf{M}^2 to solve the same problem, and their absolute error values are plotted in Figures 2 and 3 with the blue line with filled circular markers.

From the area error lines in Figure 2, two lines have the obvious convergence procedure with the increasing iterations, while the area error of the present method has the faster convergence procedure. Under the same calculated amount, the circular-marked values are always under the asterisk-marked values. In other words, the present method has more accuracy than the DBC method. Figure 3 shows the boundary error line under three boundary points $\alpha = 0.025, 0.5$, and 0.975 with two different methods. These boundary error lines have the trend of approximate 0 with increasing the calculation time. In three boundary points, the filled circular-marked error lines are always below the asterisk-marked error lines, except little points when $\alpha = 0.5$ that the asterisk-marked values are slightly bigger than the circular-marked lines. Using the present method will produce less error than using the DBC method under the same computation time; thus the present method has more calculation efficiency. For the multiple random variables, this advantage is more obvious. The calculated amount using the DBC method is exponential growth with increasing number of random variables and discretization number. This numerical test demonstrated the validity of the proposed present method. The calculation of structural responses is performed in the following section using the present method.

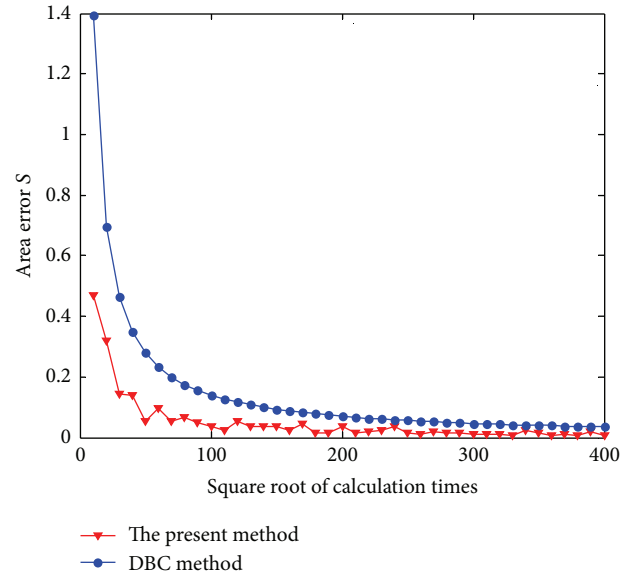


FIGURE 2: Area error lines with the present method and the DBC method.

5.2. A 10-Bar Aluminum Truss. A linear elastic 10-bar aluminum truss [23] is shown in Figure 4. The certain parameters for the 10-bar aluminum truss are the density $\rho = 2768 \text{ kg/m}^3$, the length of the horizontal and vertical bars $L = 9.144 \text{ m}$, and the bars areas $A = 4000 \text{ mm}^2$ ($i = 1, 2, \dots, 10$). The truss is subjected to two vertical forces F_1 and F_2 , and a horizontal force F_3 , which are uncertain variables of the structures. The Young modulus E is treated as the random variables. The interesting system response is d_y , the vertical displacement of the joint 2. The uncertain parameters presented by p -boxes are shown in Table 1.

F_1, F_2, F_3 , and E are truncated with $\alpha = 0.05$ as the design domain of input data. LHS method is applied to generate sampling points and finite element method is used to solve d_y . RBF approximation model is constructed, which can be written as

$$d_y = f(F_1, F_2, F_3, E), \quad (17)$$

where F_2 and F_3 are dependent and the Young modulus E and the force F_1 are independent variables. Dependence in F_2 and F_3 is represented by the Gaussian copula with Pearson coefficient 0.9. The probability bounds of d_y are computed

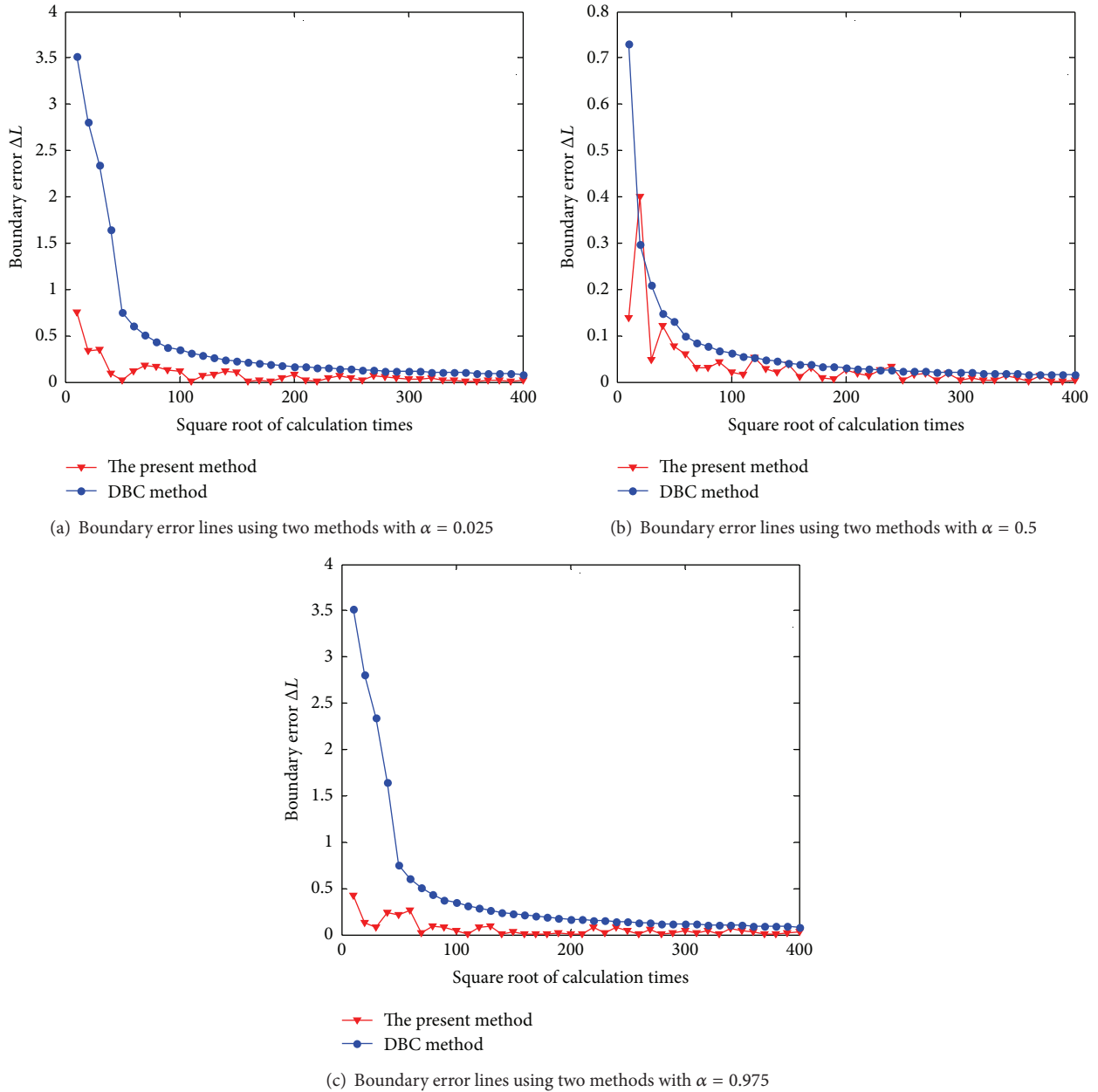


FIGURE 3: Boundary error lines with $\alpha = 0.025, 0.5, \text{ and } 0.975$.

by the present method involving by 10^5 replications. For comparison purpose, we assume that F_1, F_2, F_3 , and E are mutually independent due to lacking enough dependent information. The result of d_y is also calculated by the present method with 10^5 sample size. Two p -boxes of d_y , considering dependent or independent input data are plotted in Figure 5 which are called $[\bar{F}_A, \underline{F}_A]$ and $[\bar{F}_B, \underline{F}_B]$, respectively. $[\bar{F}_A, \underline{F}_A]$ is regarded as the theoretical value and $[\bar{F}_B, \underline{F}_B]$ is taken as proximate value due to lacking enough dependent information. The relative errors between $[\bar{F}_A, \underline{F}_A]$ and $[\bar{F}_B, \underline{F}_B]$ are shown in Table 2. It can be found that the relative area error is 3.43%. When $\alpha = 0.025$ or $\alpha = 0.975$, the boundary error

are 8.24% and 7.85%, respectively. It can be noticed that the relative boundary error is close to zero when $\alpha = 0.5$. From this example, the dependence in the input p -boxes has great impact on probability bounds of structural responses, which is particularly obvious in the tail of probability bounds.

5.3. A 25-Bar Steel Truss. This case is a 25-bar steel truss [24] which is shown in Figure 6. The length of each horizontal or vertical bar is 15.24 m and the cross-sectional area of all bars is 5000 mm^2 . The Poisson ratio is 0.3. The joint 12 is hinge-supported, and the joints 6, 8, and 10 are roller-supported. The joints 7, 9, and 11 are subjected to the vertical loads F_3, F_2 ,

TABLE 2: Relative area error and relative boundary errors between the theoretical p -box and the approximate p -box.

Error type	The theoretical p -box and the approximate p -box
Relative area error	3.43%
Relative boundary error $\alpha = 0.025$	8.24%
Relative boundary error $\alpha = 0.5$	0.01%
Relative boundary error $\alpha = 0.975$	7.85%

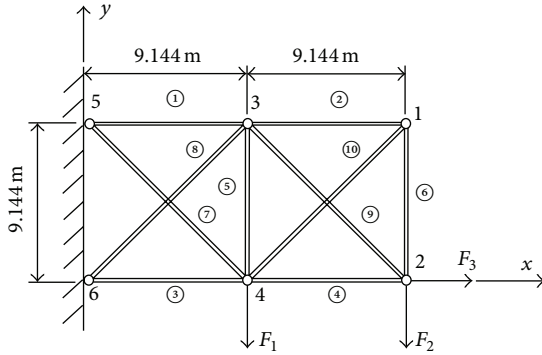


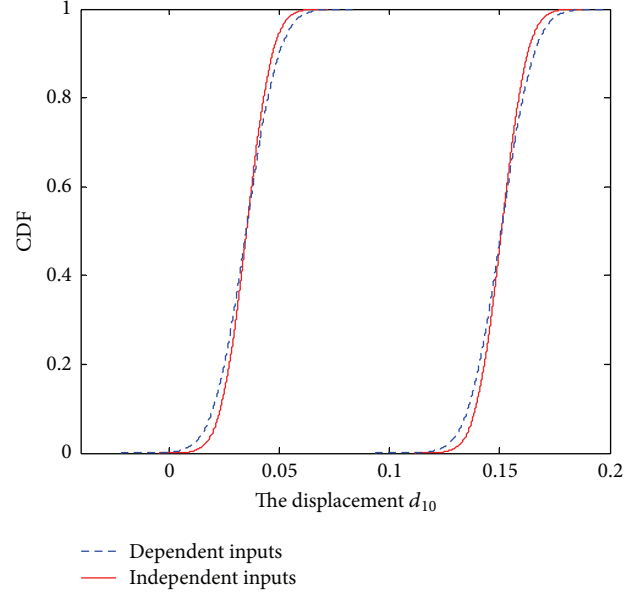
FIGURE 4: A 10-bar aluminum truss.

and F_1 , respectively, and the joint 1 is subjected to a horizontal load F_4 . The forces F_1, F_2, F_3 , and F_4 and the Young modulus E are treated as p -boxes, which are shown in Table 3. The interesting value is the vertical displacement d_3 of the joint 9. RBF is used to replace the finite element model, which can be written as

$$d_3 = f(F_1, F_2, F_3, F_4, E), \quad (18)$$

where F_1, F_2, F_3 , and F_4 and E are truncated at the probability of 0.05 and LHS is used to sample points.

Four cases are designed to analyse the influence from dependence in input variables and shown in Table 4. For cases 1–3, each of two forces is mutually dependent and their copulas are Frank copula. E is regarded as the independent variable. The relatively large correlation coefficient 0.9 for random variables is used. In case 4, five input variables are assumed to be mutually independent. p -boxes of d_3 in four cases are obtained by the present method with 10^4 samples that are shown in Figure 7, where p -boxes of d_3 with the condition in cases 1–3 are taken as the theoretical value and p -box of d_3 with case 4 is used as approximate value. The relative area error between the theoretical value and approximate value is listed in Table 5. By comparing the relative error under different cases, the relative area error or the relative bounds area under case 2 is more than the error under case 1 and case 3. For each case 1–case 3, the relative bounds error for $\alpha = 0.5$ is less than the relative bounds error for $\alpha = 0.05$ or $\alpha = 0.95$, which is very small and


 FIGURE 5: p -boxes of d_{10} with dependent and independent inputs.

nearly 0. Overall, dependence under case 2 has more influence for the structural response of d_3 in this example. This example demonstrates that neglecting the dependence in input variables will produce unpredictable error for bounds of structural response.

5.4. Application to a Taylor Impact Test. Taylor impact tests are often performed to confirm the plastic behavior of a material under severe strain conditions. Extremely high plastic strains and strain rates occur at the crushed end of the rod, resulting in severe local deformation. The experimental data usually consist of measurements of its final deformed profile. As shown in Figure 8, the cylindrical sample total length $L_{\text{initial}} = 3.8$ cm and the diameter $D_{\text{initial}} = 0.76$ cm. Testing material is the high-strength low-alloy (HSLA-100) steel [25]. The modulus of elasticity is taken to be $E = 197$ GPa and the material density $\rho = 7842$ kg/m³. The initial velocity of the sample is 246 m/s. For the Taylor test, the final deformed profile is an important index to evaluate the material performance. Thus in the application the uncertainty response analysis is conducted for the final total length L_{final} and the final diameter D_{final} . To compute the two values, the finite element method is employed, and Zerilli-Armstrong (Z-A) model

$$\sigma = \alpha_1 + \alpha_2 \exp \left[\left(-\alpha_3 + \alpha_4 \ln \frac{\partial \varepsilon}{\partial t} \right) T \right] + \alpha_5 \varepsilon^{\alpha_6} \quad (19)$$

is used for rate-dependent plasticity, where ε is the equivalent plastic strain, σ is resulting stress, and T is the temperature at the start of the experiment. The parameters $\alpha_1 \sim \alpha_6$ are material-specific. The Belytschko-Tsay shell element is used to create finite element model with 2000 elements. The initial temperature T is 298 K. The time duration of the impact process is 20 ms.

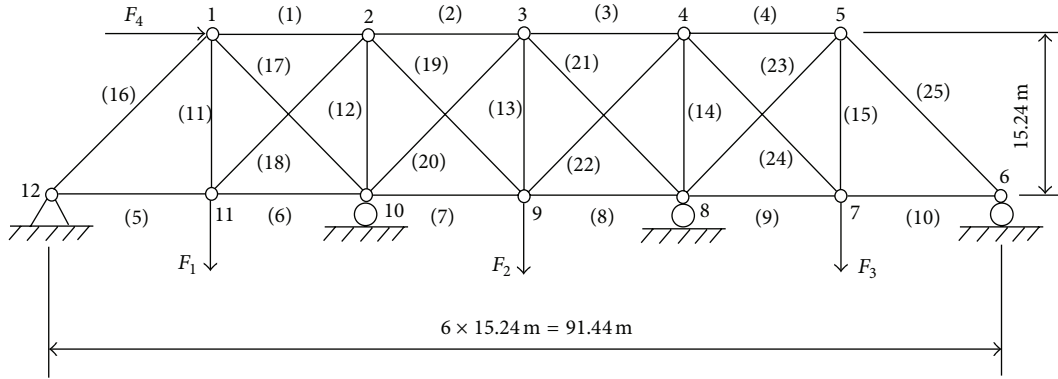


FIGURE 6: A 25-bar steel truss [24].

TABLE 3: Uncertain variables for the 25-bar steel truss.

Uncertain variables	Parameter 1 (mean)	Parameter 2 (standard deviation)	Boundary distribution type
F_1 (N)	[1.679e6, 1.879e6]	$3.2e5$	Normal
F_2 (N)	[2.124e6, 2.324e6]	$3.2e5$	Normal
F_3 (N)	[1.679e6, 1.879e6]	$3.2e5$	Normal
F_4 (N)	[1.234e6, 1.434e6]	$3.2e5$	Normal
E (Mpa)	[1.99949e5, 2.10125e5]	$1.949e3$	Normal

TABLE 4: Four cases under different dependence.

Dependent case number	Dependency and Kendall correlations
Case 1	Kendall coefficient between F_1 and F_2 is $\tau_{1,1} = 0.9$ Kendall coefficient between F_3 and F_4 is $\tau_{1,2} = 0.9$
Case 2	Kendall coefficient between F_1 and F_3 is $\tau_{2,1} = 0.9$ Kendall coefficient between F_2 and F_4 is $\tau_{2,2} = 0.9$
Case 3	Kendall coefficient between F_1 and F_4 is $\tau_{3,1} = 0.9$ Kendall coefficient between F_2 and F_3 is $\tau_{3,2} = 0.9$
Case 4	$F_1, F_2, F_3,$ and F_4 are mutually independent

TABLE 5: Relative area error and relative boundary errors under four cases.

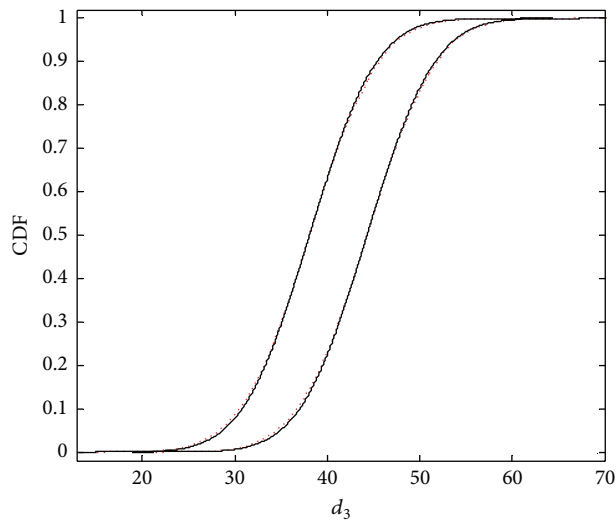
Error type	Case 1 and case 4	Case 2 and case 4	Case 3 and case 4
Relative area error	3.80%	13.62%	3.31%
Relative boundary error $\alpha = 0.025$	11.58%	35.99%	8.39%
Relative boundary error $\alpha = 0.5$	0.46%	0.24%	1.19%
Relative boundary error $\alpha = 0.975$	7.77%	29.81%	12.97%

TABLE 6: Distribution of the random variables for the Taylor test.

Z-A parameters	Distribution parameter 1	Distribution parameter 2	Distribution type
α_1 (MPa)	$\mu_{\alpha_1} = [86.5, 119.5]$	$\sigma_{\alpha_1} = 4.125$	Normal
α_2 (MPa)	$\mu_{\alpha_2} = [922.5, 985.5]$	$\sigma_{\alpha_2} = 7.875$	Normal
α_3 (K^{-1})	$\mu_{\alpha_3} = [3.8e - 4, 4.4e - 4]$	$\sigma_{\alpha_3} = 7.375e - 5$	Normal
α_4 (K^{-1})	$\mu_{\alpha_4} = [1.025e - 4, 1.315e - 4]$	$\sigma_{\alpha_4} = 3.625e - 6$	Normal
α_5 (MPa)	$\mu_{\alpha_5} = [985, 1007]$	$\sigma_{\alpha_5} = 2.75$	Normal
α_6	$\mu_{\alpha_6} = [0.2365, 0.575]$	$\sigma_{\alpha_6} = 0.0026$	Normal

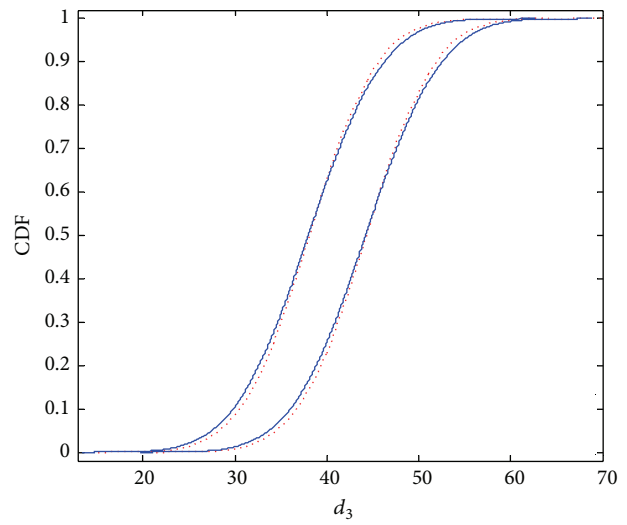
TABLE 7: Correlation coefficient matrix for the Z-A model parameters.

Z-A parameters	α_1	α_2	α_3	α_4	α_5	α_6
α_1	1	-0.083	0.372	0.207	-0.488	0.267
α_2	-0.083	1	0.344	0.311	0.082	0.130
α_3	0.372	0.344	1		0.453	-0.621
α_4	0.207	0.311	0.802	1	0.271	-0.466
α_5	-0.488	0.082	0.453	0.271	1	-0.860
α_6	0.267	0.130	-0.621	-0.466	-0.860	1



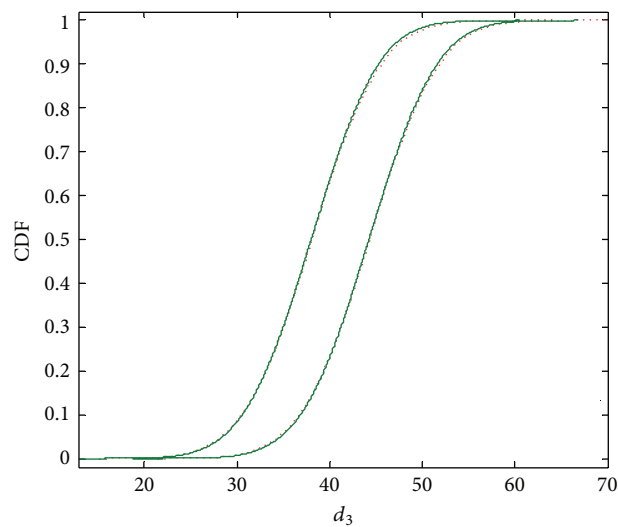
..... p -box in case 4
 — p -box in case 1

(a) p -boxes for d_3 with case 1 and case 4



..... p -box in case 4
 — p -box in case 2

(b) p -boxes for d_3 with case 2 and case 4



..... p -box in case 4
 — p -box in case 3

(c) p -boxes for d_3 with case 3 and case 4

FIGURE 7: p -boxes for d_3 in three cases.

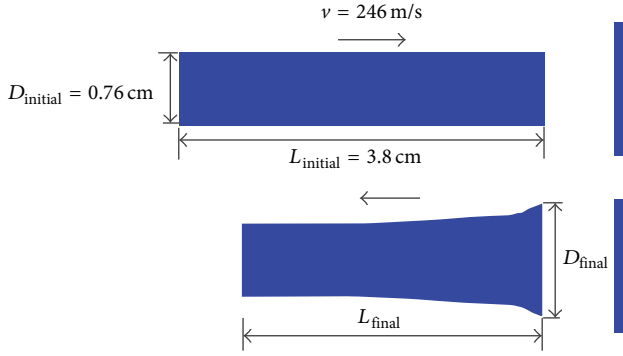
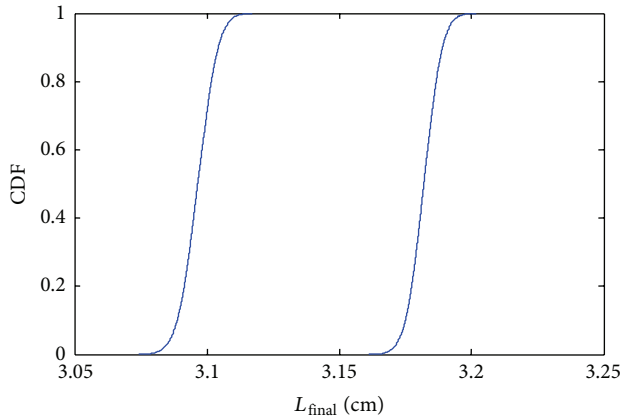


FIGURE 8: Simulating the Taylor impact test.

FIGURE 9: p -boxes of L_{final} .

Due to the manufacturing and measuring errors, Z-A model parameters are thus treated as p -boxes variables, which are given in Table 6. There is dependence in these parameters [26] and their correlation coefficients are given in Table 7.

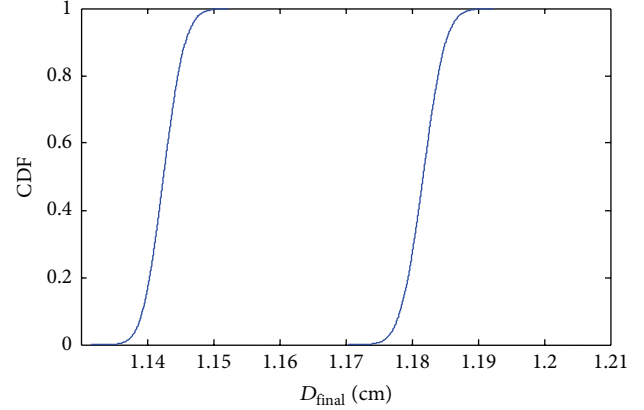
According to the present method, the random variables are truncated at $\alpha = 5e - 4$ firstly. For generating the sample points, LHS method is used. The approximation models of L_{final} and D_{final} are constructed by RBF, which are expressed as

$$\begin{aligned} L_{\text{final}} &= f(\alpha_1, \alpha_2, \alpha_3, \alpha_4, \alpha_5, \alpha_6), \\ D_{\text{final}} &= g(\alpha_1, \alpha_2, \alpha_3, \alpha_4, \alpha_5, \alpha_6). \end{aligned} \quad (20)$$

The analysis results of dependence are plotted in Figures 9 and 10, respectively. From this example, the present method is also effective for the nonlinear model including dependent uncertain parameters.

6. Conclusion

A computational method has been developed for the calculation of the structural responses under uncertain parameters represented by dependent p -boxes. The p -boxes are discretized into a range of intervals based on the copula sampling technique. The calculation of structural response interval is

FIGURE 10: p -boxes of D_{final} .

carried out by the metamodel-based optimization method. The resulting intervals are then assembled into a p -box. The present method takes both the advantages of efficiency of sampling method and the advantage of handling dependent p -boxes of DBC method.

By investigating dependence in the structural uncertainty parameters based on the present method, dependence in the variables cannot be neglected. When the dependent variables are regarded as the independent variables, the probability bound of structural responses will produce error, which are unpredictable and may lead to the failure decision-making. We have demonstrated, through the use of the present method for solving a benchmark problem and three numerical examples, that this method is effective and practical for the structural response analysis.

Conflict of Interests

The authors declare that there is no conflict of interests regarding the publication of this paper.

Acknowledgment

This work is supported by the grant from the Fundamental Research Funds for the Central Universities (Grant no. 227201401203).

References

- [1] R. E. Moore, *Methods and Applications of Interval Analysis*, SAIM Publisher, Philadelphia, Pa, USA, 1979.
- [2] R. R. Yager, J. Kacprzyk, and M. Fedrizzi, *Advances in the Dempster-Shafer Theory of Evidence*, John Wiley & Sons, New York, NY, USA, 1994.
- [3] K. Sentz and S. Ferson, "Combination of evidence in Dempster-Shafer theory," SAND 2002-0835, Sandia National Laboratories, Albuquerque, NM, USA, 2002.
- [4] M. Beer, S. Ferson, and V. Kreinovich, "Imprecise probabilities in engineering analyses," *Mechanical Systems and Signal Processing*, vol. 37, no. 1-2, pp. 4-29, 2013.

- [5] J. M. Aughenbaugh and C. J. J. Paredis, "The value of using imprecise probabilities in engineering design," *Transactions of the ASME, Journal of Mechanical Design*, vol. 128, no. 4, pp. 969–979, 2006.
- [6] R. C. Williamson and T. Downs, "Probabilistic arithmetic. I. Numerical methods for calculating convolutions and dependency bounds," *International Journal of Approximate Reasoning*, vol. 4, no. 2, pp. 89–158, 1990.
- [7] D. R. Karanki, H. S. Kushwaha, A. K. Verma, and S. Ajit, "Uncertainty analysis based on probability bounds (P-Box) approach in probabilistic safety assessment," *Risk Analysis*, vol. 29, no. 5, pp. 662–675, 2009.
- [8] M. C. Bruns, *Propagation of imprecise probabilities through black box models [M.S. thesis]*, Georgia Institute of Technology, Atlanta, Ga, USA, 2006.
- [9] H. Zhang, R. L. Mullen, and R. L. Muhanna, "Interval Monte Carlo methods for structural reliability," *Structural Safety*, vol. 32, no. 3, pp. 183–190, 2010.
- [10] H. Zhang, R. L. Mullen, and R. L. Muhanna, "Finite element structural analysis using imprecise probabilities based on p-box representation," in *Proceedings of the 4th International Workshop on Reliable Engineering Computing 'Robust Design-Coping with Hazards, Risk and Uncertainty'*, pp. 3–5, National University of Singapore, Singapore, March 2010.
- [11] H. Zhang, R. L. Mullen, and R. L. Muhanna, "Structural analysis with probability-boxes," *International Journal of Reliability and Safety*, vol. 6, no. 1–3, pp. 110–129, 2012.
- [12] Y. C. Bai, C. Jiang, X. Han, and D. A. Hu, "Evidence-theory-based structural static and dynamic response analysis under epistemic uncertainties," *Finite Elements in Analysis and Design*, vol. 68, pp. 52–62, 2013.
- [13] D. D. Ghosh and A. Olewnik, "Computationally efficient imprecise uncertainty propagation," *Journal of Mechanical Design*, vol. 135, no. 5, Article ID 051002, 12 pages, 2013.
- [14] W. E. Vesely, F. F. Goldberg, N. H. Roberts, and D. F. Hassl, *Fault Tree Handbook*, U.S. Nuclear Regulatory Commission, Washington, DC, USA, 1987.
- [15] J. W. Hickman, "PRA procedures guide: a guide to the performance of probabilistic risk assessments for nuclear power plants, in two volumes," NUREGCR-2300-V1 and-V2, National Technical Information Service, Washington, DC, USA, 1983.
- [16] K. Hanson and F. Hemez, "Uncertainty quantification of simulation codes based on experimental data," in *Proceedings of the 41st Aerospace Sciences Meeting and Exhibit*, American Institute of Aeronautics and Astronautics, 2003.
- [17] S. Ferson, R. B. Nelsen, J. Hajagos et al., "Dependence in probabilistic modeling, Dempster-Shafer theory, and probability bounds analysis," SAND 2004-3072, Sandia National Laboratories, 2004.
- [18] R. B. Nelsen, *An Introduction to Copulas*, vol. 139 of *Lecture Notes in Statistics*, Springer, Berlin, Germany, 1999.
- [19] U. Cherubini, E. Luciano, and W. Vecchiato, *Copula Methods in Finance*, John Wiley & Sons, New York, NY, USA, 2004.
- [20] D. Moens and M. Hanss, "Non-probabilistic finite element analysis for parametric uncertainty treatment in applied mechanics: recent advances," *Finite Elements in Analysis and Design*, vol. 47, no. 1, pp. 4–16, 2011.
- [21] M. D. Buhmann, *Radial Basis Functions: Theory and Implementations*, vol. 12 of *Cambridge Monographs on Applied and Computational Mathematics*, Cambridge University Press, Cambridge, UK, 2003.
- [22] W. Gander and W. Gautschi, "Adaptive quadrature—revisited," *BIT Numerical Mathematics*, vol. 40, no. 1, pp. 84–101, 2000.
- [23] P. Yi, G. Cheng, and L. Jiang, "A sequential approximate programming strategy for performance-measure-based probabilistic structural design optimization," *Structural Safety*, vol. 30, no. 2, pp. 91–109, 2008.
- [24] C. Jiang, X. Han, and G. R. Liu, "Optimization of structures with uncertain constraints based on convex model and satisfaction degree of interval," *Computer Methods in Applied Mechanics and Engineering*, vol. 196, no. 49–52, pp. 4791–4800, 2007.
- [25] R. L. Martineau, M. B. Prime, and T. Duffey, "Penetration of HSLA-100 steel with tungsten carbide spheres at striking velocities between 0.8 and 2.5 km/s," *International Journal of Impact Engineering*, vol. 30, no. 5, pp. 505–520, 2004.
- [26] K. M. Hanson and F. M. Hemez, "Uncertainty quantification of simulation codes based on experimental data," in *Proceedings of the 41st Aerospace Sciences Meeting and Exhibit*, January 2003.